Electrohydrodynamic Actuators for Propulsion and Flow Control

Ravi Sankar Vaddi

A document

submitted in partial fulfillment of the

requirements for the degree of

Doctor of Philosophy

University of Washington

2021

Reading Committee:

Igor V Novosselov, Chair

Alexander V Mamishev

Alberto Aliseda

Program Authorized to Offer Degree:

Mechanical Engineering

University of Washington

Abstract

Electrohydrodynamic Actuators for Propulsion and Flow Control

Ravi Sankar Vaddi

Chair of the Supervisory Committee:
Research Associate Professor, Igor V Novosselov
Department of Mechanical Engineering

Non-thermal plasma (NTP) actuators have been studied in the context of flow control, noise and drag reduction, lift augmentation, and laminar-turbulent transition control. These actuators have the advantages of simple design, fast response time, and easy integration. However, insights into the interaction between Coulombic forces and fluid motion are needed to improve the performance of NTP devices. This dissertation aims to improve the performance of plasma actuators for aerodynamic flow control applications. Several analytical and empirical contributions are described hereafter. First, an analytical model is derived from the first principles for corona discharge-induced thrust. Second, an empirical model was developed for standard two-electrode dielectric barrier discharge (DBD) actuators relating plasma volume, actuation voltage, discharge current, and momentum injection. The third contribution is a novel DC augmented dielectric barrier discharge (DBD – DCA) actuator. The DBD – DCA with negative DC generates two times greater thrust force compared to standard DBD. We also present the effect of electrode shape on

the thrust augmentation for DBD – DCA over the linear electrode arrangement. The thrust measured quadruples with sawtooth electrode DBD – DCA with negative DC compared to standard DBD. Fourth, the application of an optimized DBD – DCA actuator on a NACA 0012 airfoil; the actuator performances are evaluated in terms of lift and drag coefficients at low angles of attack. The results suggest that DBD – DCA has the best ability to control an aerial vehicle without moving parts.

TABLE OF CONTENTS

LIST OF FIGURES

LIST OF TABLES

ACKNOWLEDGEMENTS

It gives me immense pleasure to express my gratitude to the people who helped me on a wonderful journey, the culmination of this thesis. First and foremost, I would like to say thank you to Dr. Igor Novosselov for introducing me to this fascinating world of electrohydrodynamics, and his mentorship. The constant support and encouragement I have received from him, through the highs and lows of graduate school. I would also like to thank him for allowing me and enabling me to pursue work with other researchers within the academic community and outside.

I would like to thank Prof. Alexander Mamishev for being a 'second' advisor during my Ph.D. I would also like to thank Prof. Mamishev for pushing and demanding in many aspects of my work. I will cherish for a long time the discussion we have had, which on my occasions extended into the realms of arts, history, general technology, philosophy, and politics. He taught me how to manage projects and I was fortunate to collaborate with him on grants.

I would like to thank Prof. Alberto for serving as a mentor during my Ph.D. He helped me learn the basic principles of hot wire anemometry and told me to focus on the fundamentals. I would like to thank Dr. Sawyer Fuller for introducing me to the insect scale robot community at the University of Washington. I would also like to thank Prof. Alberto and Dr. Sawyer welcomed me in their labs and allowed me to use their equipment. I would also like to thank Prof. Dana Dabiri for his contribution of thoughts, advice, and time as a committee member.

For the last five years, I have enjoyed the good company of several members, past and present of Novosselov Research Group - including Yifei Guan, Patrick Fillingham, Justin Davis, Gaurav Mahamuni, Jiayang He, Zhi Yan Chen, Jan Nikolas Knuefer and Anthony Tang. I have pestered most of them for help with my experimental setups on various occasions that I needed additional hands and gladly they obliged! The research discussions that I had with them, especially Yifei and Patrick, gave rise to ideas that eventually shaped this thesis. The lab manager Byron Ockerman has been very resourceful. I am grateful to all the group members for their help and support.

I would like to thank Aerojet Rocketdyne, Aeronautical Testing Service, and Zepher for building the wind tunnel, without which this thesis would not be possible. I am especially grateful

for the thoughts, ideas, and support from Charles Sota. I am grateful for the discussions we have had, while we are working on the wind tunnel. He helped me learn the basic principles of aerodynamics and wind tunnel testing.

I am grateful to the Joint Center for Aerospace Technology Innovation, Aerojet Rocketdyne, Office of Director of National Intelligence ODNI Contract 2017-17073100004, National Institute of Health for their financial support.

I've also, to my surprise, managed to make and keep a fair number of friends in all my years. To Sneha, Vaibhav, Akshay, Rohan, Chinmay, and Prasanna, thanks for checking in on me to see how I was doing. Aditya, Anamol, Rodrigo, and Alicia thanks for surviving your PhDs with me. A special thanks to Rodrigo for a nigh never-ending adventure as well as being one of the thought researchers I know.

I am fortunate to have had some fantastic teachers throughout my student years. I am thankful to all of them, collectively and individually that helped me in getting this far. I would like to express my sincere gratitude to the person I consider as my guru - Prof. Gururaja Rao. I had the incredible opportunity to work under him during my undergraduate years, and he has taken a keen interest in my progress since then. He is a role model to me, and a great source of inspiration.

Finally, I would like to acknowledge my family - my parents Dr. Papayya Sastry and Phani Purna, brother Sasank for their support and encouragement through the years. In addition, I would like to thank my wonderful wife Sai Kruthi for her continued support. Grad school has had its tough moments, I was fortunate enough to have their love and support throughout. I am lucky to have them.

नारायणं नमस्कृत्य नरं चैव नरोत्तमम्।
Narayanam namaskritya naram chava narottamam
देवीं सरस्वतीं व्यासं ततो जयमुदीरयेत्
Devim sarasvatim vyasam tato jayam udirayet
– Śrīmad Bhāgavata Mahā-purāṇa

The supreme Godhead, the best of humans,
The goddess of learning and the great author
After respecting them our words can be successful

Chapter 1. INTRODUCTION

The work presented in this dissertation is motivated by the ever-increasing need for improved methods and technologies for propulsion and control of aerial vehicles [1-4]. Electrohydrodynamic (EHD) or plasma actuators have been demonstrated as remarkable devices for separation control, lift enhancement, and noise reduction. Despite many recent publications on this topic, there remain some basic questions on momentum injection, thrust, and discharge current and the methods to improve them. Improved assessment techniques are necessary for plasma actuators that investigate the relationship between electrical and mechanical quantities. This dissertation examines the design, integration, and testing of electrohydrodynamic thrusters for propulsion and control of aerial vehicle applications by developing empirical and analytical models to measure the thrust force generated by plasma actuators. This work is based on the publications [5-15] by the author.

1.1 INTRODUCTION TO ELECTROHYDRODYNAMIC ACTUATORS

Electrohydrodynamics (EHD) is an interdisciplinary field that describes the interaction of fluids with an electric field. EHD actuators at their heart are simple devices consisting of sharp electrodes separated by an air gap and connected to a high voltage generator to apply the potential between them. When a sufficient potential is applied, an electrical breakdown of air occurs in which ions are generated in the high electric field region near the high voltage electrode, these ions drift towards the grounded cathode. The ions collide with the neutral air molecules, resulting in a macroscopic wind – also known as electrohydrodynamic (EHD) flow or ionic wind.

The success of EHD technology has been limited due to the modest pressure achieved by the EHD actuators; however, in applications with a low-pressure drop, the EHD-driven flow is appropriate. Among the advantages of the EHD approach are the ability to operate at a small scale

without moving parts, straightforward control of the system, and quiet operation. In propulsion applications, corona-induced EHD flow directly converts electric energy into kinetic energy and breaks the size limit associated with moving mechanical parts.

EHD actuators have been used for various applications, including air propulsion [8, 16, 17], boundary layer modification [18-22], plasma-assisted combustion [23, 24], electrostatic precipitation [9, 11, 25], convective cooling [26-31], transition delay [32, 33], noise reduction [34-36], de-icing [37], lift augmentation [38-40], and separation control [2, 41-43]. The transition from the understanding of principles and operation of EHD to the practical application of the technology spans many decades of research. The contributions of this dissertation apply primarily to the use of EHD devices for propulsion and control for aerial vehicles, however, some generalizations can be made to apply the results to other applications.

1.2 Advantages and Disadvantages of EHD Actuators for Aerial Vehicles

EHD air movers were proposed for various industrial applications. Related to aerial vehicle control and propulsion, the earlier reports date to the 1950s, but the first scientific breakthrough did not come until 1968 with Velkoff and Ketchmann [18], and subsequent improvements are made in the design of plasma actuators. EHD actuators have been proposed for use in separation control, lift enhancement, and noise reduction. However, EHD actuators have some drawbacks, including the need for a high voltage power supply, ozone generation, and actuator performance drop with an increase in altitude. This section reviews some of the major advantages and disadvantages of EHD actuators for aerial vehicles. A comparison of different mechanisms for the control of aerial vehicles in theory and implementation is shown in Table 1.1 [2].

Table 1.1. Qualitative comparison between various active flow actuators for aerial vehicles. Δ = Worst, ΔΔΔ = Best

	Suction devices	MEMS or Piezoelectric pumps	EHD actuators
Mech. complexity	Δ	ΔΔ	ΔΔΔ
Control complexity	ΔΔΔ	Δ	ΔΔ
Mech. efficiency	ΔΔ	ΔΔΔ	Δ
Thrust to weight	Δ	ΔΔ	ΔΔΔ
Robustness	Δ	ΔΔ	ΔΔΔ
Altitude performance	ΔΔΔ	ΔΔ	Δ

1.2.1 *Potential advantages of EHD actuators*

Thin profile: One of the main advantages of EHD actuators is their scalability to low profile structures thin profiles where conventional control techniques function poorly. The small size and simple geometry of the plasma actuators ensure minimal disturbances and interferences with the external flow. The absence of mechanical parts in EHD devices enables to initiate flow with the device's thickness of less than a millimeter.

Reliability: In comparison to other actuation techniques for aerial vehicles with moving parts that require regular maintenance. EHD devices can be more reliable, which could lead to low fabrication and maintenance costs; however, special attention needs to be paid to the integrity of the dielectric layer (in DBD) and electronics (high voltage power supplies, etc.) Research into these topics and overall system integration is required.

Weight reduction: The absence of mechanical parts reduces the weight of the aircraft, given that low-weight electronic components can be developed. In civil aviation, the reduced weight allows for increased payload and a decrease in fuel consumption. For fixed-wing aircraft, it allows for fast and high load maneuver.

Low acoustic emission: The acoustic signature of an aircraft results from both powerplant and aerodynamic noise. Aerodynamic noise arises from the airflow around the aircraft fuselage and control surfaces and tends to increase with velocity. To reduce aerodynamic noise, the outer profile of the vehicle is designed to minimize airflow separation and turbulence generation. Plasma actuators can reduce flow separation that leads to aerodynamic during maneuvering.

High mass flow rates: Synthetic jets and piezoelectric pumps are other emerging technologies used for active control. However, on a small scale, these devices do not produce higher flow rates that are advantageous for effective control of aerial vehicles. EHD actuators produce higher flow rates than some of the synthetic and piezoelectric pumps in thin form factors. Moreover, the momentum can be injected over a wide area with a single actuator.

Response time: Plasma actuators have short response times and can be utilized to control unsteady phenomena. In specific scenarios, they could replace control surfaces, such as ailerons and flaps, increasing aircraft maneuverability.

Drag Reduction: Plasma actuators generate thrust and can be used to overcome viscous drag on the airfoil. For an aerial vehicle, the reduced drag allows for a decrease in fuel consumption.

1.2.2 *Disadvantages of EHD actuators*

Low energy conversion: When used for propulsion, ionic wind devices have significant limitations. The ions that are generated travel in the electrical field, colliding with molecules and entraining flow. Conventional pumps, fans, propellers use a solid blade to impart momentum to the airstream, which offers more effective energy transfer. Electrical energy is directly converted into kinetic energy, and the energy conversion is very low (~1-2%). This efficiency can be even lower due to viscous losses in internal flow scenarios.

Generation of toxic gases: Plasma actuators require a breakdown of air; thus, ozone and other reactive oxygen and nitrogen reactive species are formed in the ionization zone. Ozone is corrosive and toxic, so EHD devices need ozone mitigation strategies.

Effect of aerial vehicle speed and altitude: The EHD actuator's efficiency decreases at higher altitudes due to the low air density. The plasma actuator effect decreases with the increase in freestream velocity. However, plasma actuators can be most effective for small-scale UAVs and other low-altitude vehicles.

Stability: EHD actuator performance changes with external operating conditions. When humidity increases, the actuator becomes less stable; this is especially important in corona discharge EHD. In DBD, the surface on which the EHD actuator is mounted can also have a significant influence on the ions being created.

High-voltage requirements: Electric field in the ion creation region should be greater than the breakdown strength of the air, which is around 3 *MV/m*. This requires an operating voltage greater than ~3 kV. AC or pulsed DC power supplies are needed to energize the DBD electrode. EHD

thruster or actuator requires high efficiency (and often compact) high voltage power supply onboard the vehicle. High voltage safety in an EHD actuator is essential, so the design and engineering of the power supply are required to meet the safety standards. However, relatively low power requirements make compact designs feasible.

1.3 Scientific and Technology Challenges

The research presented in this dissertation has several scientific and engineering challenges which can be broadly classified into several categories detailed below.

1.3.1 *Design of EHD actuators*

The working principles, advantages, and disadvantages of EHD actuators can be described in a brief introduction, but the design considerations for aerospace applications are significant. The basic design rules and numerical modeling techniques, available for other well-known technologies, are underdeveloped for EHD flow. The EHD phenomenon has complex, highly coupled and nonlinear parameters such as charge generation and transport rate, bulk flow rate, and electric field strength. Although analytical models have been reported in the literature, they apply only to the simplest geometries and idealized assumptions, and their usefulness for real-world aerospace applications is limited. EHD modeling is heavily dependent on the boundary conditions, which are determined from the experiments. With the limited set of experiments, designing EHD actuators using modeling is difficult.

In the last decade, significant progress has been made in numerical and analytical modeling and design understanding, which is included in this dissertation work.

1.3.2 *Improvement of actuator performance*

The EHD actuator performance for aerospace applications depends on numerous factors, such as the physical dimensions, materials, operating conditions, and EHD actuator location.

1.3.2.1 Physical dimensions

The EHD actuator performance depends on different physical dimensions, including the gap between electrodes and electrode shape. The electric field between the anode and cathode causes the breakdown of air and the bulk flow. A shorter distance between the anode and cathode results in higher electric field strength and higher peak velocity concentrated in a point with a lower operating voltage range. Meanwhile, a longer distance between the anode and cathode results in distributed momentum over a wide area and a higher voltage range.

Regarding the electrode shape, the standard shape is linear for both the anode and cathode; the actuators consist of two rectangular conducting strips separated by a dielectric layer. Shaped electrodes have been introduced, including triangular, serpentine, square, and horseshoe-shaped actuators. In linear electrodes, the EHD force primarily acts in the streamwise direction. With the new geometries, the body force is locally normal to the active electrode edge, resulting in 3D effects.

1.3.2.2 Materials

When choosing the material for electrodes, there are two important parameters to keep in mind: the material and thickness t. Electrodes are typically fabricated using metal foils, and the thickness must be selected in such a way that does not disrupt the boundary layer. For a DBD plasma actuator, the general aim is to lower the capacitance of the actuator. Different dielectric materials

will have a different dielectric constant ε. The capacitance is proportional to ε/t ratio, and the power loss through the dielectric is proportional to the capacitance. Therefore, lowering the capacitance by using thicker dielectrics or more insulating ones decreases the power loss, allowing a higher voltage and higher body force. However, for a given applied voltage, a thinner dielectric may produce higher velocities. The use of thicker dielectric materials with low dielectric constants causes a spreading of the electric field lines on the dielectric surface, lowering the current density and streamer formation.

1.3.2.3 Operating conditions

The position of the EHD actuator on the airfoil can change fluid dynamic characteristics such as laminar to turbulent transition, flow separation/reattachment, turbulence level, which will have different applications based on its position. EHD actuator located on the leading edge will delay the transition. The transition delay affects friction drag, postponing the stall since the turbulent boundary layer can withstand the adverse pressure gradient. Furthermore, the laminar flow has less drag and is more prone to separation at a high angle of attack. The flow reattachment due to co-flow momentum injection into separated flow on a wing allows to improve the aerodynamic characteristics like maximum lift and increase in the angle of attack for the wing. EHD actuator located on the trailing edge can reduce flow separation and change the downwash angle of the airfoil. The change in the downwash angle creates a moment on the aerodynamic center, and it can be used for controlling the airfoil at low angles of attack.

1.3.3 *Integration of actuator on an aerial vehicle*

The path from exploratory study and proof-of-concept experiment to integration in a commercial product is often the most significant effort in technology development. The successful

integration of EHD devices with aircraft requires solving multiple engineering challenges. One must ensure that a plasma actuator meets the requirements for separation control, drag reduction, and lift augmentation, design of the system to optimize the aerodynamic performance, design of a compact high voltage power source for EHD operation, and provide long-term reliability.

1.4 Scope of the Dissertation

Figure 1.1 shows the scope of this dissertation and future work in a visual format. This dissertation is a study into the theory, implementation, and testing of EHD actuators for propulsion and control of aerial vehicles.

Theory: In the area of theory, this dissertation attempts to develop a better understanding of the fundamental principles for EHD actuators. A generalizable analytical model for thrust determination is developed for corona discharge from first principles. The thrust expression can be used to design propulsion systems and can be readily implemented in numerical simulations. The corona discharge thrust model framework is used to develop a semi-analytical model to calculate the discharge current, thrust, momentum injection. The developed empirical model characterizes the dielectric barrier discharge actuator based on the AC inputs. The analytical and empirical models developed for corona discharge and dielectric barrier discharge can be readily applied for determining more realistic boundary conditions in numerical simulations.

Experimental design: Two different EHD actuator concepts are presented in this dissertation: corona-discharge actuator and DBD actuator. The main idea behind the EHD actuators is to induce momentum on the airfoil to control boundary layer flow for augmentation of lift force and the aerial vehicle can be controlled without ailerons, flaps. Corona actuator consists of a high voltage anode and a cathode with a shallow rectangular cavity. As the potential on the anode increases,

there will be a spark-over, which means the electrical breakdown across the electrode separation gap. For DBD actuators, there is a dielectric material between the electrodes to eliminate the sparkover. Corona actuators are better for providing thrust and DBD actuators are for control applications. Various designs of plasma actuators with and without dielectric barrier were fabricated and tested. A design study has been conducted to determine the optimal anode design, distance between anode and cathode. The baseline prototypes or laboratory scale EHD actuators are hand-made using commercial off-the-shelf materials and parts, and a fabrication process is developed. Rigorous tests provide proof of concept validation for EHD actuator performance. Parametric studies are performed to show the interactions between the thrust, energy transfer efficiency, and key design parameters of interest, including anode voltage, geometric factors, and HV electronics.

Development for aerodynamic applications: The road from laboratory scale to commercial product is long, and the full development is outside the scope of this dissertation. However, this dissertation does attempt to present the opportunity of EHD actuators for propulsion and control of aerial vehicles and demonstrates the feasibility of the EHD actuators through design, construction, and testing of a full-scale wing section with an integrated EHD actuator, and then test this device in a low-speed wind tunnel. The EHD actuator performance is characterized in a non-zero free stream environment by test at realistic Reynolds number. Lift, drag, and moment coefficients are determined for a selected 2D wing section with EHD actuators and reviews the challenges on the path to the successful integration of EHD actuators for aerospace applications. In addition, this dissertation attempts to present EHD actuators as propulsion devices for miniature aerial vehicles (insect scale) through design, construction, and demonstrating the lift-off of a centimetre scale aerial vehicle.

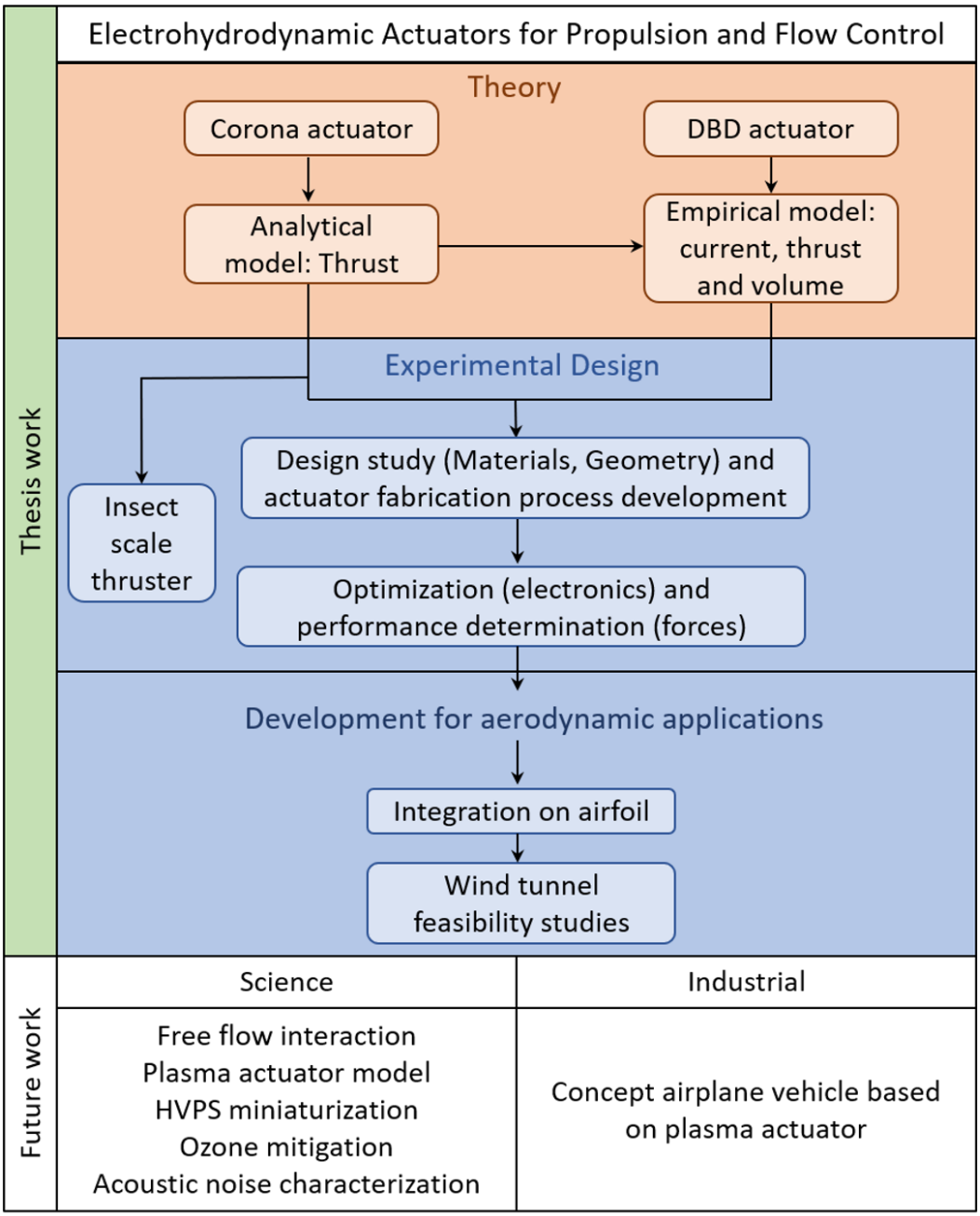

Figure 1.1. Scope of the dissertation and future work.

1.5 Contributions of the Dissertation

This dissertation aims to develop a better understanding of EHD actuator designs and scale-up, provides tools for performance characterization. The author hopes this manuscript would

demonstrate the feasibility of EHD actuators on airfoil for propulsion and control and open doors to the design of UAVs with active EHD flow control. Consequently, specific contributions have been made to assist the research community with the ongoing research and development of plasma actuator technology.

- Formulated an analytical model for thrust force determination from first principles for corona discharge.

- Developed an empirical model for two-electrode DBD actuators relating plasma volume, discharge current, and momentum injection.

- Designed, fabricated, and tested a novel plasma actuator (DBD – DCA) for increased performance.

- Demonstrated the control capability of DBD – DCA on an airfoil at low angles of attack.

1.6 Outline of the Dissertation

This dissertation examines the design, integration, and testing of electrohydrodynamic actuators for propulsion and control of aerial vehicle applications. Chapter 2 of this work entails a brief review of the plasma actuators. The main electrical and geometrical parameters that influence the performance and applications of propulsion and flow control problems are discussed. Chapter 3 presents the experimental study on point to ring corona discharge, the results are compared with analytical and numerical solutions. Chapter 4 discusses the analytical model developed to determine electrohydrodynamic thrust and the model is validated with three independent experimental results. In Chapter 5, the experimental results of a centimeter-scale EHD thruster are presented, and the lift-off of the EHD quad thruster is demonstrated. Chapter 6 discusses the corona

discharge induced wall jet on the conducting and insulating plate for flow control applications. The flow is studied experimentally and numerically to resolve spatiotemporal characteristics of charge density, velocity, and electric field. Chapter 7 discusses the empirical model development for the DBD actuator, including electrical current associated with microdischarges, plasma volume, and wall jet momentum. The presented empirical model characterizes the DBD wall jet momentum and discharge current based only on AC inputs. Chapter 8 demonstrates the advantage of a new DC augmented dielectric barrier discharge (DBD – DCA) on thrust performance and effectiveness compared to the standard two-electrode DBD. Chapter 9 discusses three different electrode shapes for increasing the performance of the DBD – DCA actuator and compares them with linear shape electrodes. In Chapter 10, the best performing DBD – DCA actuator from the flat plate study is installed on a NACA 0012 airfoil, and wind tunnel test results are presented and analyzed. Chapter 11 discusses the influence of particles in EHD systems. A new particle charging method in EHD and a novel aerosol collector based on the EHD particle charging method are presented. Finally, the overall conclusions and lessons learned and proposed road map forward for future research are reported in Chapter 12.

Chapter 2. PLASMA ACTUATORS BACKGROUND

This section presents a brief background on plasma actuators. Two configurations of plasma actuators 1. DC Corona discharge 2. AC DBD actuators are presented with their geometric optimizations and state-of-the-art analytical models. Then the application of plasma actuators to propulsion and control applications for aerial vehicles is presented.

2.1 PLASMA

Plasma is one of the four fundamental states of matter, and the term was introduced by Noble Prize winner Irving Langmuir. It consists of gas either partially or fully ionized. It consists of an equal number of positively charged ions and negatively charged electrons, i.e., it is globally neutral. In nature, plasma can be commonly found in space, as in star cores, solar wind, and lightning. Plasma can be artificially generated by heating a neutral gas or subjecting it to a strong electromagnetic field to the point where the gas becomes electrically conductive. Nowadays, artificially generated plasma is widely used in industrial applications such as surface treatment [44, 45], plasma sterilization [46, 47], plasma cutting [48, 49], plasma screens, neon tubes, and for control and propulsion in the aerospace industry.

The plasma can be classified into thermal and non-thermal depending on the relative temperature of electrons, ions, and neutral molecules. Thermal plasma has ions, electrons, and neutral molecules at the same temperature. Non-thermal plasma has ions and neutral molecules at low temperatures and electrons at higher temperatures. Plasma is called hot if it is fully ionized, or cold if it is partially ionized. Cold plasmas are usually non-thermal plasmas, and they are usually used in technological applications. In this dissertation, only cold plasmas are considered because

the energy supplied to the actuator to induce the flow is used to produce electrons and not to heat the surrounding gas. Two types of plasma discharges can be used for plasma actuators:

(1). Corona Discharge

(2). Dielectric Barrier Discharge

2.2 CORONA DISCHARGE

Corona discharge is an electrical breakdown of air in which ions are generated in the high electric field region near the high energy anode, these ions drift towards the grounded cathode. The mechanism of the corona ionic wind is shown in Figure 2.1. When a high voltage is applied, the neutral air molecules are ionized by the strong electric field at the tip of the corona electrode [50, 51]. In positive corona discharge, electrons are attracted to the high voltage corona electrode, positive ions such as O_2^+ and O^+ drift towards the cathode. As the high-velocity ions repelled from the corona electrode, they collide with the neutral air molecules driving the EHD flow. The ions' acceleration in the electric field and their interaction with the neutral molecules in the ion drift region can be modeled as an external force term (Coulomb force) in the Navier-Stokes equations. A two-part model is required: (i) the description of the ion motion in the electrical field, and (ii) the effect of the ion drift on the neutral gas in the flow acceleration region.

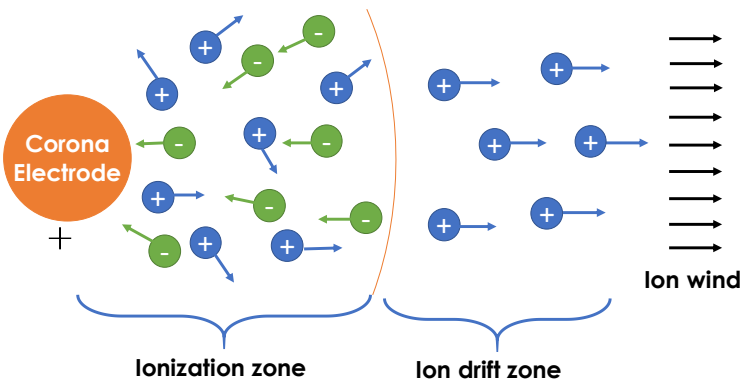

Figure 2.1. Schematic of positive corona discharge.

2.2.1 *Electrical characterization of corona discharge*

The voltage-current ($\varphi - I$) relation during the corona discharge characterizes the ion motion between the electrodes globally. This phenomenon has been studied since the early 20th century. The classic ($\varphi - I$) relationship was derived by Townsend [52] in 1914 as shown in Eq. (2.1) and validated for a coaxial corona configuration

$$I = C\varphi(\varphi - \varphi_o), \tag{2.1}$$

where I is the corona current, φ is the corona voltage, φ_o is the onset corona voltage and C is a fitting parameter. To physically interpret the parameter C, Cooperman showed that $C \propto \mu_b / L_c^2$[53], where μ_b is the ion mobility and L_c is the characteristic length scale. The electrical power of the corona discharge is computed using the Eq. (2.2)

$$P = \varphi I. \tag{2.2}$$

The quadratic relationship has been validated for various corona geometries, such as point-to-pot [54], point-to-plate [55], and point-to-ring [56]. In a point-to ring corona, Giubbilini also demonstrated that the ion current is inversely proportional to the point-to-ring distance [56]. Some

recent studies modify Townsend's quadratic relationship to better describe the $(\varphi - I)$ relationship for different electrode configurations, e.g., point-to-plate [57], point-to-grid [58], sphere-to-plane [59], coaxial cylinders [60, 61], wire-cylinder-plate [62], point-to-ring [56, 63, 64], parallel electrodes [65], multi-electrodes [66], and non-uniform electric fields [67].

2.2.2 *Corona discharge: ionic wind and thrust*

The theoretical aspect of EHD in gas was first investigated by Robinson [68] as shown in Eq.(2.3), who demonstrated the ability of electrostatic blowers to generate velocities up to 4 m/s.

$$v = k\sqrt{\frac{I}{\rho\mu_b}}, \tag{2.3}$$

where k is the geometric parameter, ρ is the gas density, and μ_b us the ion mobility. The concept of electric wind associated with an EHD thrust was first demonstrated in a one-dimensional model showing that the EHD thrust is dependent on the electric pressure [69]. Christenson and Moller have developed an expression for EHD thrust and found that EHD efficiency can be related to ion mobility [70]. Pekker et al. first derived an ideal 1D EHD thruster model for calculating maximum thrust and thrust efficiency from the charge conservation equation and the Mott-Gurney law [71]. Mott-Gurney law describes the relation between maximum electric current density and applied voltage in semiconductors [72]. The current density was shown to vary as $J \propto \varphi(\varphi - \varphi_o)$, in agreement with the Townsend $(\varphi - I)$ relationship [52] in 1914. Since then, the form $I = C\varphi(\varphi - \varphi_o)$ has been widely adopted for corona discharge analysis [55, 73-77]. The thrust induced by the ions $(\varphi - T)$ relationship can be derived based on Townsend's relationship $(\varphi - I)$ [78, 79] and the maximum thrust can be defined based on Mott-Gurney law [78]. Thrust is equal to the Coulomb force acting on the volume of the fluid between anode and cathode,

$$T = \int \rho_e E dV = \int \rho_e E A dx = \int \frac{JAdx}{\mu_b} = \frac{Id}{\mu_b} = \frac{C\varphi(\varphi - \varphi_o)d}{\mu_b}, \quad (2.4)$$

where ρ_e is the charge density, T is the thrust force, E is the electric field and d is the distance between anode and cathode. The thrust efficiency is calculated as given in Eq.(2.5)

$$\frac{T}{P} = \frac{Id}{\mu_b \varphi I} = \frac{d}{\mu_b \varphi}, \quad (2.5)$$

where P is the electrical power consumed by the corona discharge.

2.2.3 *Numerical modeling of corona discharge*

The ions' interaction with the neutral molecules can be modeled as an external force term (Lorentz force) in the Navier-Stokes equations [64, 78]. Insights into the multiphysics nature of the EHD flow are important for understanding this phenomenon. To correctly predict the flow established by this force, the following elements need to be considered: (i) the electric field resulting from the potential difference between the corona and ground electrodes, as well as its modifications due to the space charge in the high ion concentration in the region; (ii) the ion motion in the resulting electric field; (iii) the interaction between the ion drift and the neutral gas in the flow acceleration region; (iv) the viscous and turbulent stresses; and (v) the effects of developing complex flow patterns as a result of the accelerating flow and device geometry. State-of-the-art literature evaluates several corona configurations [80-82]. Numerical modeling has been applied to the design and analysis of electrostatic precipitators (ESP) [83-86] and heat transfer enhancement [28, 87-90]. Previous EHD flow models use an iterative approach to: (i) calculate the electric field and electric force under Kaptzov's hypothesis [91] or Peek's law [92], and (ii) set

a constant space charge on the anode so that the solution matches the cathode current from the experimental data. This method requires multiple iterations and is therefore inefficient.

An issue with the corona discharge operation is the instability of the discharge. One solution is introducing a dielectric barrier discharge, where a dielectric material is inserted between the two electrodes. A direct current (DC) cannot flow through the dielectric material; an AC voltage is required.

2.3 Dielectric Barrier Discharge

Dielectric Barrier Discharge (DBD) actuators consist of two electrodes, usually asymmetrically located, separated by a dielectric material. One of the electrodes is exposed to air (exposed electrode), the other is entirely covered by a dielectric material (encapsulated electrode), as shown in Figure 2.2. The electrodes are powered by alternating current (AC), usually with voltages of the order of 10 kV and frequencies in the order of kHz. The other mode of DBD operation involves applying short and repetitive pulses. Nanosecond DBD (NS-DBD) utilizes pulses that are usually nanosecond wide, and frequency is in the same order as AC voltage. As the current never exceeds a few microamps to milliamps, the power consumption is less.

When a high voltage is applied, the electric field is strongest in the region between the electrodes; the plasma is generated at the active electrode's edge [93-95]. The downstream length (or length) of the electrodes is usually a few millimeters, and different studies have explored the effects of gaps between the electrodes [96-98]. When the electric field exceeds a specific threshold value, known as the breakdown electric field, the air ionizes in the area where the electric potential is larger. Electrons are extracted from the neutral air molecules by leading to air. The electrons released by the exposed electrode travel towards the dielectric layer over the encapsulated

electrode and back over one AC period. In the negative-going half cycle, the electrons are released in the air by the exposed electrode and thus ionize the air. The negatively charged electrons are repelled towards the encapsulated electrode and accumulate on the surface of the dielectric. During the positive half cycle, the electrons on the dielectric layer go back to the exposed electrode. This process is highlighted in Figure 2.3 where both half cycles are illustrated. Through collisions, momentum is transferred to the flow. The plasma is formed as the result of a series of discharges as electrons are transferred onto and off the dielectric surface [99]. The DBD actuator induces a pulsed velocity with the same frequency as the AC voltage [2, 22, 100-103]. The effect of the electrodes' thickness and the dielectric media significantly impacts the actuator's performance [95, 104-107]. A single straight-edged DBD actuator is assumed to produce a two-dimensional flow field due to the spanwise uniform electric field. Other actuator designs have been considered, including serrated electrodes that produce a three-dimensional flow field [108-110].

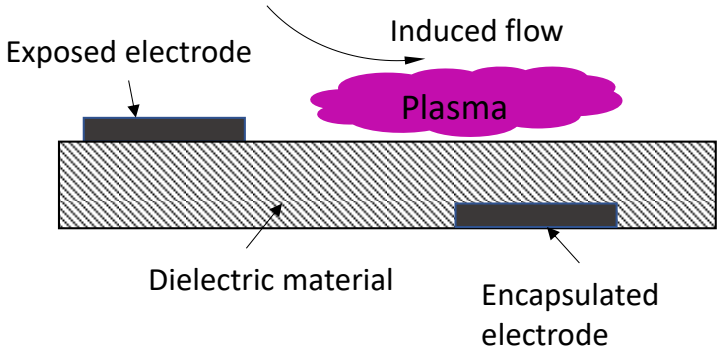

Figure 2.2. Schematic of the dielectric barrier discharge actuator. The exposed electrode indicates a high voltage electrode, and the encapsulated electrode is at the ground.

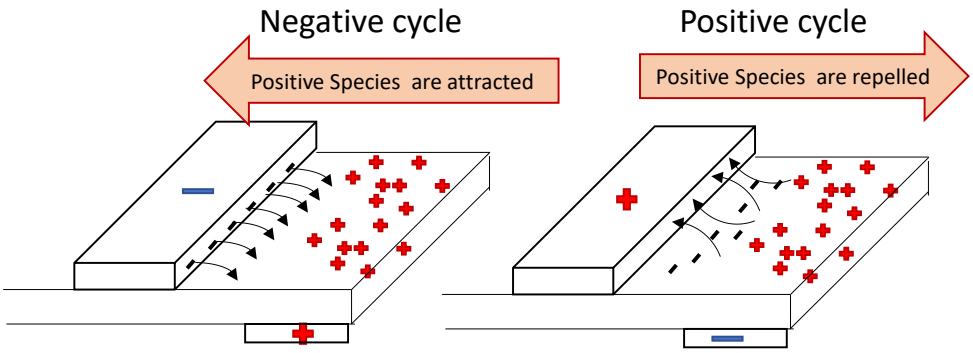

Figure 2.3. Working principle of DBD. The electrons are emitted from the exposed electrode collect on the dielectric surface, to be returned on the subsequent half-cycle of the discharge.

Font [111, 112] suggested that in the negative-going cycle, the electrons are repelled, and positive ions are attracted towards the exposed electrode. The net force is not zero since the positive ions are attracted towards the electrode. The ions are directed towards the exposed electrode. In the positive half cycle, the direction of the electric field is reversed, and the positive ions move from the exposed electrode, the direction of the force is from the exposed to the encapsulated electrode. The magnitude of the body force in the positive-going cycle is much greater than the other half cycle. Thus, the total net direction in a single cycle is towards the encapsulated electrode. The experiments using PIV in one cycle demonstrated that the tangential force oscillates between two positive values [94]. Due to the force applied by the positive ions, emitted from the exposed electrode, the direction of the resultant force is from the upper electrode to the lower electrode. Thus, the net force direction is towards the encapsulated electrode. The theory is suggested by Orlov [113] and is called the push-push theory. Figure 2.4 shows the schematic of both theories. It is still an open question whether both cycles contribute to the momentum [3].

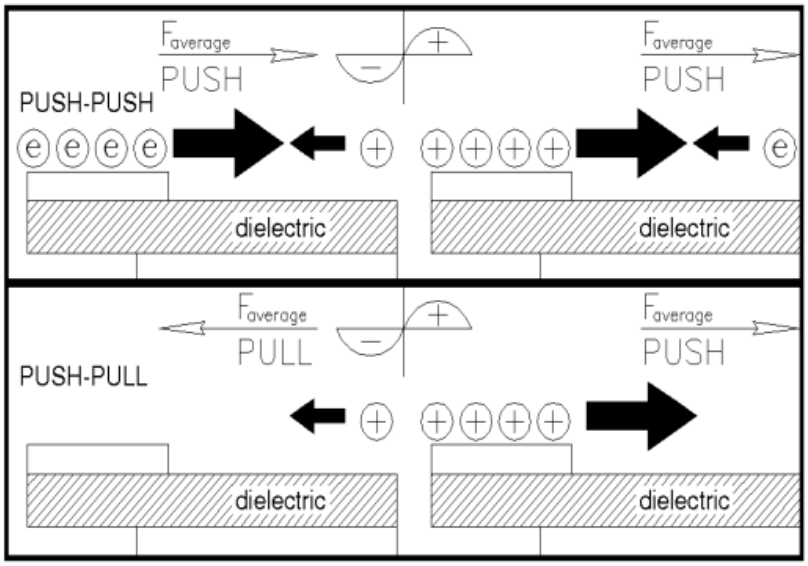

Figure 2.4. Push-push and pull-push theories for dielectric barrier discharge [114].

2.3.1 *Electrical characterization of DBD*

Traditional metrics to characterize plasma actuators' electrical performance include current, power and charge transported. The voltage is measured directly from the output of the power supply unit or utilizing high voltage probes. On the other hand, the current can be measured through a shunt resistance on the ground electrode [94, 115]. Alternatively, an inductive Rogowski coil can be used to measure current [116-118]. A Rogowski coil allows to push the response of the current measurements beyond 100 MHz, which is suitable for microdischarge characterization. Figure 2.5 shows current and voltage measurements of a DBD. A current measurement through a non-intrusive current coil can be viewed as a superposition of low-frequency capacitive current, discharge current, and noise. The capacitive current is often filtered out or ignored because it corresponds to the transiently stored energy in the dielectric or air and not energy transferred to fluid motion [96]. On the other hand, the discharge current indicates the amount of charged species that can participate in the energy transfer to fluid motion. The discharge current comprises

numerous peaks in the positive-going cycle due to streamer propagation with the addition of glow discharge during the negative-going cycle [119]. Figure 2.6 shows the number of microdischarges for positive and negative semi cycles as a function of voltage amplitude.

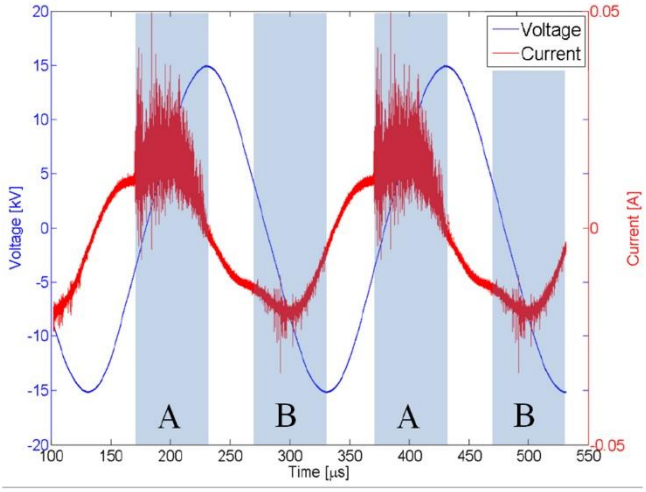

Figure 2.5. Current and voltage measurements of an asymmetric dielectric barrier discharge. Regions A and B indicate the microdischarges [120].

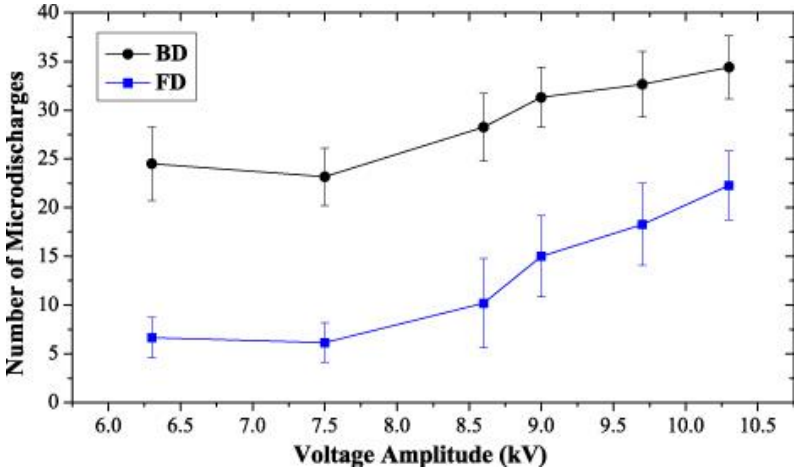

Figure 2.6. Number of microdischarges with respect to voltage amplitude. Here BD is a positive semi cycle, and FD is a negative semi cycle [116].

The electric power W_{elec} can be computed from voltage and current measurements as shown in Eq. (2.6)

$$W_{elec} = \frac{1}{T}\int_0^T \varphi(t) i(t) dt \tag{2.6}$$

where T is the AC period of DBD, $\varphi(t)$ and $i(t)$ are the voltage and current signals. The current and voltage signals have to be measured with a good oscilloscope with high bandwidth, resolution and sampling rate. These conditions are essential for accurate capture of individual discharges that have been shown to occur on average over a 30 ns duration [121]. The high bandwidth and the sampling rate minimize the noise during the current measurements and can be used to compute the time-averaged electrical power [52]. An alternative way to compute the power for DBD is to measure the charge through a capacitor in series between the actuator and the ground [1, 122]. The capacitor integrates the current; with this technique, there is no need to resolve current spikes. A typical voltage-charge curve, which is called the Lissajous figure, and the area enclosed by the curve is the energy dissipated by per period.

The electrical power is typically characterized as a power-law based functions of either f_{AC} and $\varphi(t)$. Some research groups use a quadratic approximation for the power consumption with increasing operating voltage [115, 123, 124]. Other groups have reported exponent values ranging between 2 – 3.5 [99, 122, 125, 126], depending on the geometry. Most research groups found a linear relationship between the power and frequency [94, 115, 124] and Kriegseis found that $W_{elec} \propto {f_{AC}}^{1.5}$ [122].

2.3.2 *DBD: Thrust characteristics*

The thrust of the DBD plasma actuator gives a direct metric to the momentum injected into the flow by the DBD plasma actuator. Several methods have been used for measuring the plasma-induced thrust. Typically, a simplified approach is to use a high-resolution force balance and measure the thrust force directly [127-131] or calculate it from the velocity measurements using pitot tubes, particle image velocimetry (PIV), and laser Doppler velocimetry (LDV). The control volume analysis of the flow field is used to determine the net thrust generated [127, 132, 133]. The thrust force is equal to the net momentum generated by the actuator corrected for the shear force on the surface. Comparison of direct thrust measurements and control volume analysis were performed by Durscher and Roy [127]. Based on their findings, the plate length is an important consideration when comparing direct thrust measurements. Direct thrust measurements can be readily done with an analytical balance with higher resolution, range, and tare. When the actuator is placed on the balance with the jet facing up, the balance reading is the sum of the thrust force and shear forces on the surface. If the shear force is small and can be neglected, then the thrust force is equal to momentum.

The thrust force generated by DBD has a power-law relationship with the voltage $T \propto V^m$ at a given frequency. Several values for m are proposed in the literature for sinusoidal voltage input. Wilkinson [134] found that m = 4.8 fits their data and it is independent of the chemical composition of the dielectric material. Thomas [135] proposed m = 3.5 for low voltage range and m = 2.3 for high voltage range. Similar relation of m = 3.5 was used by Matsuno [131] to fit their data. Zito [136] used four different values of m = 2.2, 3.4, 3.6, and 6.6 to fit their thrust data from micro dielectric barrier discharge actuators. David et al. [128] found a quadratic relationship between the plasma thrust and voltage in log-log space at constant frequencies. These results contrast power

relationships developed in literature which are approximate over a limited voltage range. A generalized empirical/ analytical model is developed based on corona discharge for DBD plasma thrust and found that the thrust has a quadratic relationship with voltage and a power law with frequency [123, 137].

It is important to understand the effect of external factors such as relative humidity, pressure and temperature on the thrust induced by dielectric barrier discharge since these actuators would be installed on aircraft wings. Benard studied the effect of humidity from 40% - 98% RH on velocity and current [138]. The induced velocity increases with air humidity up to RH<55% and then it drops, but the DBD actuator could still work. Relative humidity changes the current peaks as well, decreases the number of current peaks, which means the discharge becomes more filamentary and it is not a uniform glow [139]. The ambient pressure has a significant impact on the performance of the DBD: both on the velocity [140] and discharge intensity [141]. The discharge power and the plasma length increase with a decrease in the pressure [142, 143]; however, the velocity and body force increase with a decrease in pressure, reach a maximum value, and then decrease [142]. Similar observations for body force are observed in the literature [144] over a pressure range of 13-101 kPa and demonstrated the pressure at which thrust is maximized. The factors influencing the pressure at which the thrust was maximized were recently studied, and a generalized formula describing the relationships between pressure, permittivity, dielectric thickness, and operating voltage was derived to determine the thrust [145]. The induced velocity increases linearly with temperature [146]. In the current dissertation, the effects of external factors are not studied, but they can be explored in the future.

2.3.3 *Numerical modeling of DBD*

The effect of plasma actuator on the flow can be modelled through a body force term as shown in Eq. (2.7) into the Navier-Stokes equation

$$\vec{f}_{EHD} = \rho_c \vec{E}, \tag{2.7}$$

where ρ_c is the charge density and $\vec{E}$ is the electric field. The simplest models such as the Shyy model [147], models taking some assumptions like force is assumed to be steady in time, the electric field has a linear spatial distribution in both directions. Another simple model is the one proposed by Suzen & Huang model [148, 149]. Considering relative permittivity properties of the working fluid and actuator materials, the simplified DBD models define the charge density as a one-dimensional boundary condition with a half Gaussian distribution starting at the edge of the ground electrode closest to the active electrode [150]. The half Gaussian charge distribution has been experimentally and numerically investigated, and it is typically presented as a function of x-direction [99, 126, 151-154]. The y-direction is indirectly considered through the Debye length [113, 155]. Another simple model has been proposed by Orlov [156], which models the actuator as a lumped element electrical circuit, made of capacitors, resistors, and diodes, to capture the charge distribution on the surface. These models can significantly reduce the calculation times, especially for complex scenarios or 3D geometries, such as boundary-layer separation control, turbine blades, and channel flow [154, 157-159]. However, these models use guessed parameters like charge density, debye length and this thesis provides empirical relationships for plasma volume and discharge current. Using these empirical relationships, an approximate boundary conditions can be determined for numerical simulations.

2.3.4 *Optimization of DBD*

2.3.4.1 Electrode shape

The linear electrode shape induces direct momentum addition to the boundary layer, and they rapidly lose effectiveness as the flow velocities increase. To increase the actuator performance, different exposed electrode shapes have been tested in the past, with the aim of introducing a three-dimensional flow field. Shapes such as serpentine [108, 160], triangular [42, 43, 161] and square were studied numerically and experimentally in different flow control problems [109, 162]. These actuators can generate spanwise periodic streamwise vortex structures, due to the opposite colliding jets from the electrode edges, as shown in Figure 2.7. These actuators induced a local pinching and a local spreading of fluid along the span of the actuator. One of the most interesting electrode shapes is a triangular (sawtooth, serrated) shaped electrode, consisting of several triangular tips. The electrode can act as a vortex generator because the induced velocity is perpendicular to the edges of the electrode; in addition, it induces direct momentum due to the sharp tips. The induced flow field is composed of wall jets from the tips and vortices generated downstream of the triangular roots. The induced vortices increase the mixing between the free stream and boundary layer, which helps in energizing the boundary layer efficiently. Recently, an optimization study was done on the actuator performance both at a bench and for flow control performance [163, 164] and a height to pitch ratio of 1 is found to be efficient for power, dielectric heating [164], and separation control [163]. In this thesis, two different height to pitch ratios 1 and 2 for the serrated/saw tooth electrodes are considered.

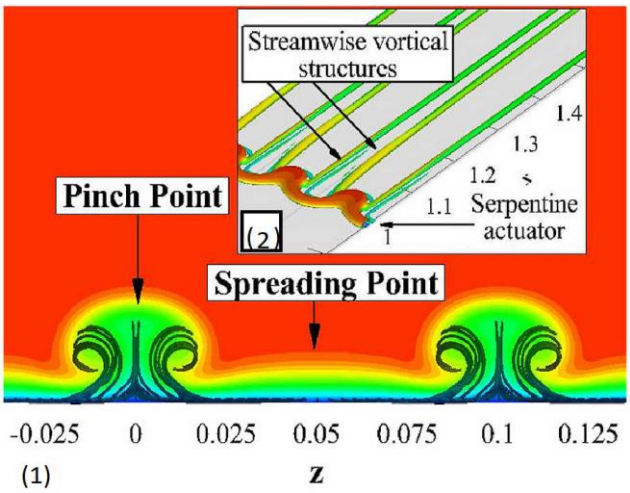

Figure 2.7. Streamlines and Q-criterion in the inset colored by velocity magnitude for a boundary layer flow with a serpentine electrode actuator [160].

2.3.4.2 Sliding discharge actuators

The practical applications of DBDs are restricted due to their limited discharge extension and small relative velocity. One of the promising methods to increase the discharge area and velocity is to add another exposed electrode to the DBD configuration, as shown in Figure 2.8, thus creating a three-electrode sliding discharge plasma actuator [165, 166]. Using a sliding discharge aims to extend the plasma discharge surface to increase the body force and scale the plasma actuation for large-scale applications. Depending on the polarity of the sliding electrode or third electrode, if it is negative, then the entire gap between the electrodes is occupied with the plasma. The performance increases with the increase in DC voltage, and then it drops due to the jet created in the opposite direction of DBD. The DC potential can be adjusted to change the resultant DBD jet angle [167, 168]. Thus, the sliding DBD actuator can generate strong aerodynamic effects in the three-dimensional space above the actuator. When the DC potential is positive, the discharge is similar to DBD [167]. The performance of the sliding DBD actuator increases with positive voltage compared to traditional DBD, without a noticeable power increase [165]. The increase in the

performance when a positive voltage is applied to the third electrode is due to the negative half-cycle space charge is accelerated due to the positive polarity on the sliding electrode. The velocity gain in the negative half cycle is higher than the velocity reduction in the positive half-cycle, resulting in a faster time-averaged velocity. However, the sliding DBD thrust increases up to a certain voltage on the third (sliding) electrode. It then sharply decreases [131] due to the formation of a reversed jet from the sliding electrode. This dissertation addresses this problem by designing a new plasma actuator.

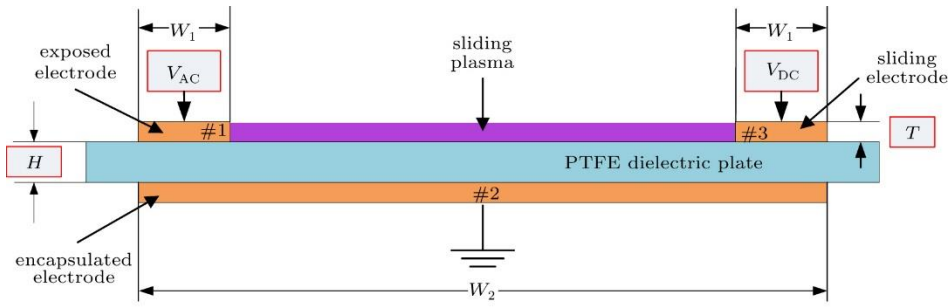

Figure 2.8. Schematic of the sliding dielectric barrier discharge plasma actuator [168].

2.4 Plasma Actuator for Propulsion and Control

2.4.1 *Propulsion*

The success of EHD technology has been limited due to the modest pressure achieved by the EHD thrusters; however, in applications where producing high pressure is not required, the EHD-driven flow can be of interest. Among the advantages of the EHD approach are operating at a small scale without moving parts, straightforward control of the system, and quiet operation. In propulsion applications, EHD converts electrical energy directly to kinetic energy, sidestepping manufacturing of small moving parts, e.g., wings of micro-flyers. The idea of using corona discharge for EHD thruster was proposed by Brown [169], who thought he has discovered an

unknown phenomenon producing force and provided some explanations on the Biefeld – Brown effect. Masuyama et al. investigated both a single and dual-stage EHD thruster and showed that thrust is proportional to the square of voltage beyond the corona inception [79]. Wilson et al. investigated the use of EHD thrust for aircraft propulsion and concluded that corona discharge is not very practical for that application [170]. More recently, Gilmore showed that EHD propulsion could be viable to drive small aircraft [171], which led to the demonstration of flying fixed-wing electro-aerodynamic (EAD) aircraft [17]. Similarly, the EHD thrusters have also been proposed as a propulsion method for small-scale ionocrafts [8, 16, 17, 172, 173].

2.4.2 *Control*

Flow control technology using pneumatic actuators to blow the boundary layers over the wing or boundary layer suction for drag reduction, and lift augmentation has been tested for several decades [2]. While these methods allow for reliable aircraft control in variable atmospheric conditions, each component generates significant turbulence when engaged, decreasing the aircraft's fuel efficiency. Additionally, the inherent size of these mechanical systems limits the control variability and imposes complex mechanical design constraints on the wing [101]. To improve on these mechanical systems and alleviate some of their inherent flaws, an avionic system is proposed in the form of an embedded plasma actuator. When integrated along the length of the wing and on various external components of the aircraft, plasma actuators offer the ability to directly control the flow with minimal power [100, 103, 174].

Plasma actuators installed on the airfoil surface can be used to modify the airflow in the boundary layer for drag reduction, lift augmentation, noise reduction, and separation control on airfoils. Velkoff et al. [18] have studied the effect of corona discharge on the laminar to turbulent

transition point on a flat plate. The transition point shifted by 43 mm for an external free stream velocity of 53 m/s. Several researchers studied drag reduction using corona discharge on a flat plate [175, 176]. Moreau and Léger [177, 178] studied corona discharge on an inclined flat plate at low velocity and have observed a reduction in drag. A maximum velocity of 2.75 m/s for 500 μA current and the effect of an external free stream on boundary layer profile and pressure distribution has been studied experimentally [177]. Previous research has shown that the effect of the discharge depends highly on the discharge regime and that strong effects of EHD actuators are not limited to small velocities [177, 179]. The DC discharge properties highly depend on external conditions. Roth et al. used two electrodes separated by a dielectric barrier to create a plasma sheet [19, 20]. The working principles and advantages of DBD over corona are already discussed in the previous sections.

Dielectric barrier discharge has been used to improve the aerodynamics of an airfoil for low and moderate Reynolds numbers up to $1.6 – 2.0 \times 10^6$ [22, 180]. Over the past couple of years, plasma flow control is focused on controlling the flow at high angles of attack where the flow separates from the leading edge. The maximum lift coefficient can be increased, and the stall can be delayed by some degrees, even though the control effect decreases with the free stream velocity. For instance, Tsubakino studied the effect of different actuator positions 5%, 10% and 20% from the leading edge in order to control the flow separation around NACA 0012 airfoil [181]. The actuators installed as close as possible to the leading edge, upstream of the separation point, effectively controlled the separation performance [43, 181, 182]. When actuated over an airfoil, a plasma device effectively reducing separation (see Figure 2.9). This phenomenon increases lift and decreases drag across the airfoil. There are different modes of control for plasma actuation (1). Steady mode and (2). Burst mode. In this thesis only steady actuation is considered. Plasma

actuators installed on different geometries like rounded trailing edge [39], a gurney flap [38, 40], or on a delta wing [183] have been shown to increase the lift and pitching moment on the airfoil. DBD actuators are tested on other geometries like a backward-facing step for turbulent flow [184, 185], vehicle model for drag reduction [186], cylinders for drag reduction, and noise reduction [187]. Most of the past work on the use of plasma actuator as a flow control device has focused on separation control and lift augmentation on two-dimensional geometries. This dissertation explores the feasibility of using plasma actuator for flow control at low angles of attack.

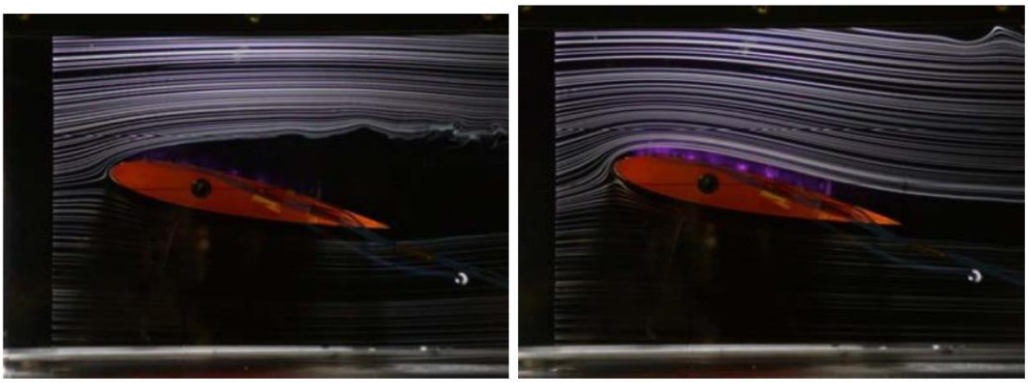

Figure 2.9. The effect of DBD over an airfoil and flow reattachment on a NACA 0015 airfoil when the plasma actuator is on [100].

2.5 CHAPTER SUMMARY

The field of electrohydrodynamic flow has been studied extensively for the past four decades for a wide variety of uses, with a small subset of those focused on EHD driven airflow. In that time, a fundamental understanding of the underlying physics has been developed. However, most of the efforts in analyzing the EHD driven flow still use guessed parameters for analytical and numerical models, rather than focused research efforts in developing analytical models from first principles and empirical models from experiments that can help build the EHD aircraft concept.

There are currently no analytical/empirical models that can predict the thrust, discharge characteristics of the plasma actuator.

The area of propulsion and control with plasma actuation received little attention or development before the last two decades, with most of the documented work occurring in the last decade. Most of the flow control with plasma actuators has focused on separation, lift augmentation, and drag reduction at high angles of attack, which will be helpful only in landing and take-off of aerial vehicles. A relatively little attention has been given to thrust generation and application of plasma at low angles of attack that can be used for cruise control for UAVs.

With no apparent methodology for model development and control of aerial vehicles at cruise conditions, there is an opportunity for novel solutions using plasma actuators.

Chapter 3. ELECTROHYDRODYNAMIC FLOW IN A POINT TO RING CORONA DISCHARGE

This work is published in Physics of Plasma [6] and Physical Review Fluids [7]. The CFD simulations and analytical model are developed by Dr. Yifei Guan [188], and the analytical model and CFD computation results are presented here for completeness.

In this chapter, an electrohydrodynamic (EHD) flow in an axisymmetric point-to-ring configuration is investigated experimentally. The electrical current associated with the corona discharge and the velocity induced by ions is studied over a range of input parameters as corona voltage and distance between anode and cathode. The corona current is measured on the anode, and the velocity profile is characterized using hotwire anemometry. The maximum flow velocity is at the centerline, and it decays rapidly with the radial distance due to the viscous and electric forces acting on the partially ionized gas. The electric to kinetic energy transfer efficiency is evaluated for the experiments.

3.1 Experimental Setup

The EHD flow is studied in a point-to-ring internal pipe geometry. Figure 3.1 shows the experimental setup. The apparatus consists of a high-voltage corona needle and a grounded ring electrode. The anode needle is a 0.5-mm-thick tungsten needle with a radius of curvature of 1 μm at the tip (measured using optical microscopy). The needle's sharpness is essential because it affects the corona discharge at lower voltages [189]. The tip of the needle is checked regularly for visible defects to ensure that it does not degrade over time. The ground electrode is a 1.58-mm-thick solid solder with an inner radius of 10 mm. The enclosure is fabricated using 3D printing in

a polylactic acid polymer. The distance between the anode and cathode (L) is set in the range of 3 to 7 mm using spacers. A variable high-voltage power supply (Bertan 205B-20R) is used to set the electric potential between the electrodes. The cathode current is measured on the cathode based on a voltage drop across a 1 MΩ resistor.

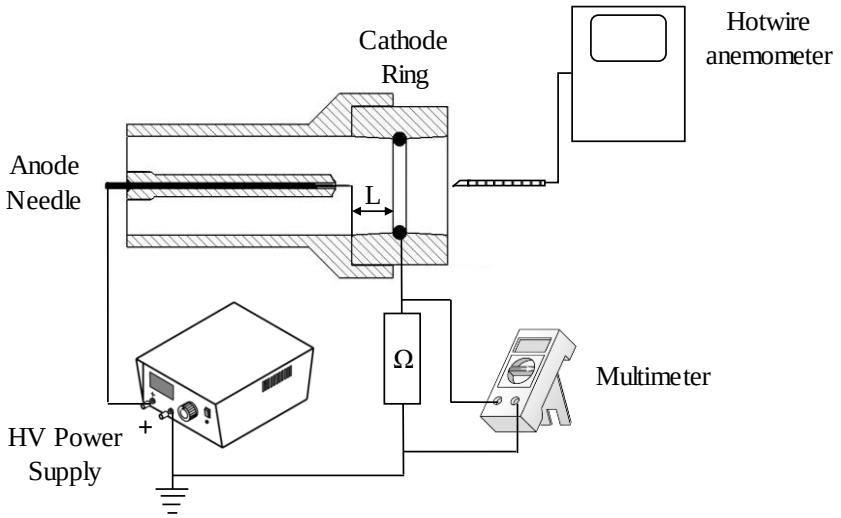

Figure 3.1. Schematic of the experimental setup – a high voltage is applied between the corona anode needle and the ion collecting cathode ring. The distance and voltage are varied.

The EHD experiment is operated in the positive corona mode in a temperature range of 22-25 ^{0}C, a relative humidity of 23-25%, and ambient pressure. For each anode-cathode distance, the voltage is increased from 4 kV (when the outlet velocity is measurable) to ~10 kV (when the arc discharge occurs). Constant current hot-wire anemometry is used to measure the flow velocity profile. A TSI 1213-20 probe connected to the anemometer (AA-1005) is positioned at the device's outlet. The anemometer is calibrated for a range of velocities from 0.2 to 8 m/s [190]. The entire experimental setup is mounted on an optical table; the anemometer probe is attached to a 3D translation stage to obtain space-resolved measurements. The anemometer data are collected at a frequency of 10 kHz using data acquisition hardware (myRIO-1900) over a sampling time of 30s.

The ion concentration at the device's exit is measured at a distance of 25.4 mm from the outlet using an air ion counter (Alpha Lab). The ion concentration measurements are not used in the analysis; instead, they provide an order of magnitude comparison between the experiments and simulations. Each experimental condition is tested at least five times to obtain independent statistical samples.

3.2 Results and Discussion

3.2.1 *Voltage – current characteristics*

The experimental data of the corona current for different voltages is shown in Figure 3.2. The corona current is compared with the analytical current expression as shown in Eq.(3.1)

$$I = \frac{3\pi\mu_b\varepsilon}{4r_c}\left(1 - \frac{L}{\sqrt{L^2 + R^2}}\right)(\varphi - \varphi_o)^2, \tag{3.1}$$

where I is the corona current, μ_b is the ion mobility, ε is the permittivity, r_c is the characteristic length scale of flow acceleration, L is the distance between the needle tip to the center of the cathode, R is the radius of the cathode ring, φ is the anode voltage and φ_o is the corona initiation voltage. The detailed formulation of the model is given in the following reference [6] and in Chapter 4. The I/φ vs. φ trends are different from the previously reported linear trends [191, 192] for the external flow in the point-to-ring corona configuration. The nonlinearity in the analytical model comes from the φ_o/φ term, as seen in Eq.(3.1). However, for the high values of φ where most previously reported data were collected, the linear curve fit may have been adequate. These trends can be used to evaluate boundary conditions for modeling of the acceleration region. One approach is to evaluate the critical properties of the acceleration zone at the onset of corona discharge, as the anode voltage approaches the critical voltage, i.e., $\varphi \to \varphi_o$, the φ_o= 2 kV based

on the x-axis. At this condition EHD flow velocity is negligible. As the corona voltage increases, the size of the acceleration zone r_c and the field intensity increase non-linearly. The current and velocity data in this non-linear region fluctuate, resulting in r_c variations. In the linear region, observed at the higher corona voltages and in previous reports [191, 192], both the current values and the EHD velocities were stable indicating well established ionization and acceleration regions. As in previous work, [50, 191, 192] the acceleration region dimensions are considered constant for a given electrode configuration, i.e., linearly dependent on L. The best fit for the data in the presented point-to-ring internal EHD flow is obtained when $r_c = 3 + 0.5(L - 3)$. This relationship is likely to change for a different electrode configuration.

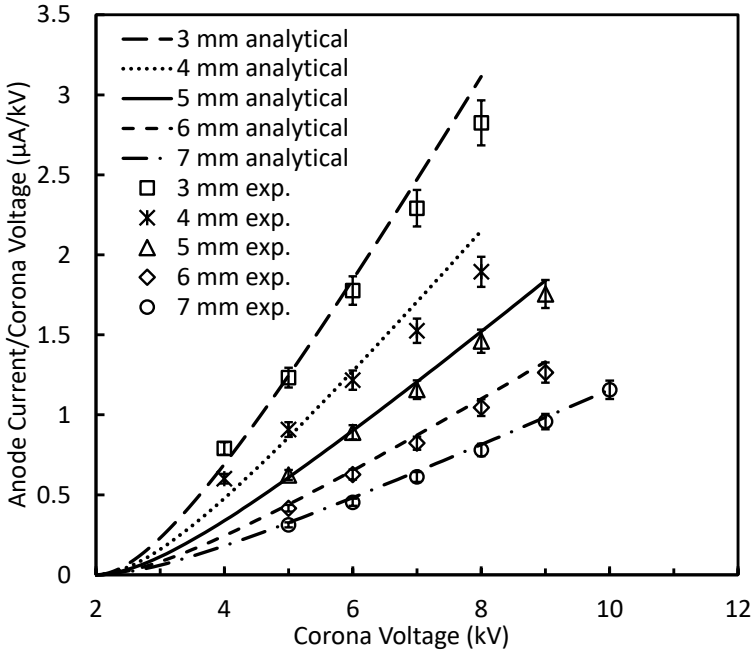

Figure 3.2. Current-voltage characteristics of point to ring corona discharge experimental data and analytical model [6].

3.2.2 *Voltage – velocity characteristics*

The EHD flow induced by point-to-ring discharge can be divided into three regions: ionization zone, acceleration region, and momentum conservation region. The ionization region does not have a significant effect on the momentum exchange between the charged species and neutral molecule as the momentum exerted by negative and positive species is assumed to be balanced, which is a well-accepted approximation for corona discharge driven EHD flows.[7, 26-28, 87, 90, 193-195]. Electro-kinetic phenomena such as plasma waves and streaming may have minor effects on the EHD flow development; however, in this study these second order effects are not considered. The momentum conservation region is the part of the domain where electric force is balanced or overcome by viscous forces near the walls. Figure 3.3 illustrates the relative positions of the ionization zone, EHD acceleration region, and EHD momentum dissipation region. The ion drift zone includes both the EHD acceleration region and the EHD momentum dissipation region [196-199], as shown in Figure 3.3. The ion drift zone is the region where the efficient charge density and the electric field are both non-zero. The size of the ion drift zone only depends on the geometry of the electrode configuration. The ion drift zone is the region where the efficient charge density and the electric field are both non-zero. The size of the ion drift zone only depends on the geometry of the electrode configuration. The steady state energy analysis for constant area as shown in Eq. (3.2) and the energy gained from the electric force as in Eq. (3.3) can be used to determine the maximum velocity induced by the corona discharge. The forcing is acting on the gas stream of the ionization zone and acceleration zone, thus integrating the energy within these limits yield maximum flow velocity as given as in Eq. (3.4).

$$SE_{inlet} = SE_{outlet} + SE_{e}, \tag{3.2}$$

$$SE_e = \frac{\int \rho_c E dr}{\rho}, \tag{3.3}$$

$$u_{max} = \sqrt{2SE_e}\left[\frac{3\varepsilon}{4\rho r_c}\int_b^{r_c} r^{-2} dr\right]^{1/2}(\varphi - \varphi_o), \tag{3.4}$$

where SE_e is the energy gained from the electric force, ρ_c is the charge density, E is the electric field, u_{max} is the maximum velocity induced by corona discharge, ρ is the air density and b is the ionization zone boundary.

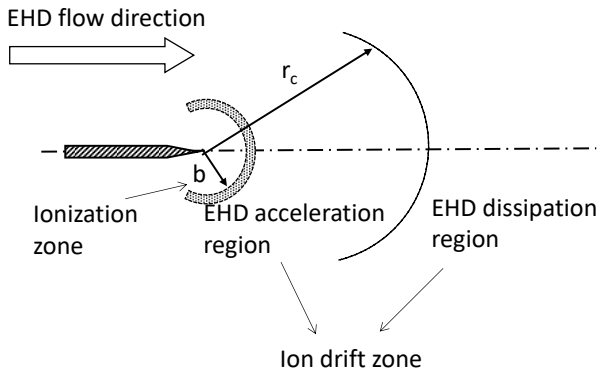

Figure 3.3. Diagram of the relations among the ionization zone, EHD acceleration region, and EHD dissipation region of a point-to-ring corona system.

Figure 3.4 shows the comparison of the voltage-velocity data against the analytical solution for a range of L = 3 – 7 mm and φ = 4 – 10 kV. The trends agree with the previously reported linear dependence between the maximum velocity and corona voltage observed for the point-to-ring corona configurations [192] and planar electric field ion generator [200]. The analytical solution uses $b = r_c/4$ as the ionization zone boundary for the integration of Eq. (3.4). Analytical solutions for corona current and maximum velocity are in very good agreement with the experimental data over the entire range of the entire range of geometrical and operational parameters of the EHD source.

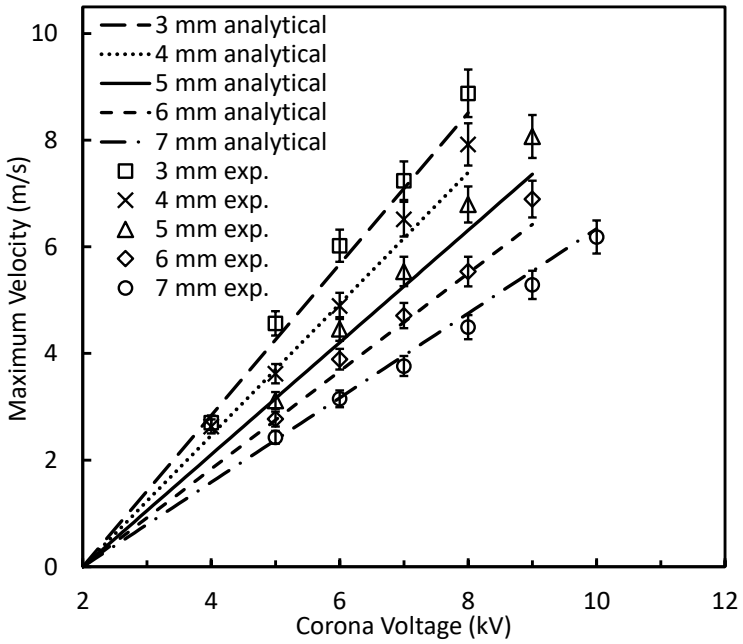

Figure 3.4. Maximum velocity as a function of corona voltage and electrode geometry for the experimental data and analytical model [6].

A novel numerical approach for EHD flow in a finite volume solver for axisymmetric point-to ring corona configurations is developed [7, 188]. CFD simulations are used to resolve the spatiotemporal characteristics of the flow. The detailed formulation of the numerical appraoach is discussed in [7, 188] and in section 11.3 when we have investigated the effect of particles in EHD systems. To study the spatial distribution of velocity, we compare the numerical and experimental velocity profiles at the outlet of the point-to-ring EHD flow generator. In Figure 3.5(a), the velocity profiles are plotted for two voltage values at a fixed electrode spacing (L = 3 mm). The higher voltage case produces higher velocities with very similar velocity profiles. Figure 3.5(b) shows that, at a fixed voltage, the velocity increases when L decreases. Both numerical and experimental results show a distinct peak at the axis. The velocity profiles then decay rapidly with radial distance. Numerical and experimental results agree within 5% error at the centerline, but the model

is less accurate at the edges of the domain. The discrepancy in this region may be due to flow instability in the shear flow region that modifies the radial location of the inflection points in the velocity profile.

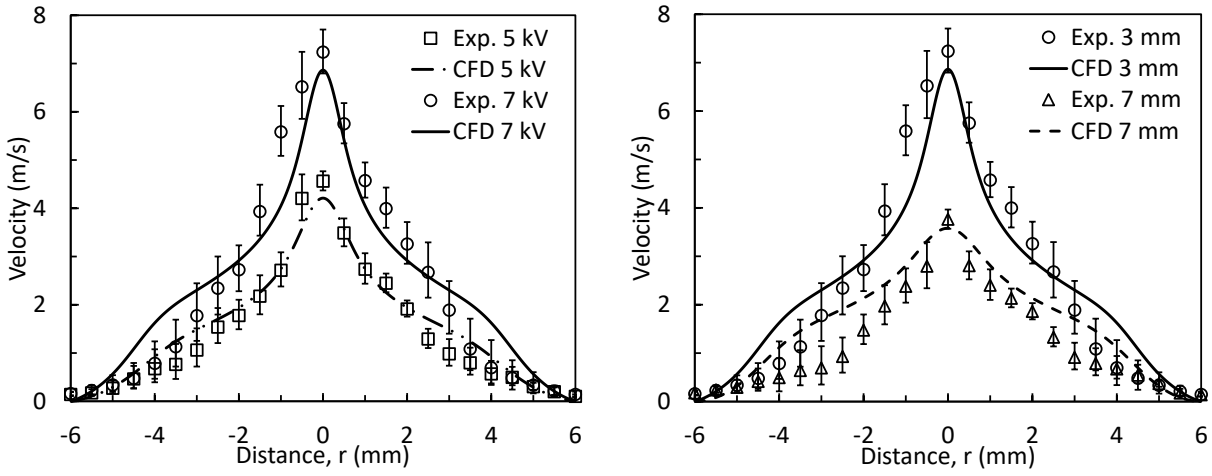

(a) (b)

Figure 3.5. Comparison between simulations and experiments for the velocity profiles at the outlet of the EHD generator; (a) varying corona voltages at a fixed distance, and (b) varying anode-cathode distance (L) at a fixed corona voltage.

The velocity profile shows that the EHD-induced airflow in a point-to-ring corona discharge has parallels to a submerged jet [201]. For submerged jets, the Reynolds number is determined based on the nozzle diameter and the mean velocity at the exit [202]. In the case of corona discharge flow, the nozzle is replaced by the EHD jet located at the centerline, immediately downstream of the corona electrode tip. The Reynolds number (Re) in the EHD flow is ~ 700-900, based on the diameter of the jet, for L = 3 mm, 7 kV, d_{jet}~ 2-3 mm, and mean velocity u ~ 4-5.5 m/s. Other cases have smaller Re due to lower jet velocities, except for the 3 mm, 8 kV case, where

Re is still < 1000 (~ 6.5 m/s in mean velocity and d_{jet} ~ 2-3 mm). Therefore, the EHD flow can be represented by a fully laminar jet (300<Re<1000) [202].

3.2.3 *Energy transfer efficiency*

The energy conversion efficiency can be calculated from the ratio of the kinetic energy flux in the flow at the exit of the EHD device to the electrical power produced by the corona discharge.

$$\eta = \frac{\frac{1}{2}\rho \int u^3 dA}{\varphi I} \tag{3.5}$$

The corona voltage and anode current are obtained from the experiments. The kinetic energy flux in the flow is calculated from both the experimental and numerical velocity profiles. Table 3.1 shows the values used in the calculation of energy transfer efficiency.

Table 3.1. Comparison of electrical and fluid power between the experiments and the CFD.

	3 mm, 5 kV	3 mm, 7 kV	7 mm, 7 kV
$W_{K,Exp}\ (mW)$	0.196 ± 16%	0.882 ± 19%	0.264 ± 23%
$W_{K,CFD}\ (mW)$	0.184	0.86	0.293
$I\ (\mu A)$	6.15	16.04	4.28
$W_E\ (mW)$	30.8	112.28	29.96

The numerical results agree well with the efficiency computed using the experimental data. Efficiency is higher in the 7 mm cases than in the 3 mm cases due to the smaller angle between the axial velocity and the electric field vectors. Energy transfer efficiency peaks at a certain corona voltage after which the efficiency decreases [7]. This nonlinear effect is likely due to the quadratic

relationship between the corona voltage and anode current. The increase in corona voltage results in a quadratic increase in the anode current and a cubic increase in the electric power $\varphi I \propto \varphi^3$. Maximum velocity at the centerline is linearly proportional to the corona voltage based on the Eq. Eq. (3.4) and previously reported experimental observations, but the kinetic power $\frac{1}{2}\rho \int u^3 dA$ is not proportional to φ^3 because u is not proportional to φ anywhere but on the centerline. At the high values of the corona voltage, the field lines also diverge due to the high space at the corona needle resulting in a negative work of the electric field.

3.3 CHAPTER SUMMARY

This work presents an experimental investigation of corona discharge-driven flow. The experimental data for flow in the point–to-ring internal geometry includes voltage, current, and velocity profile measurements. The experimental corona current is compared with the relationship found by analytical derivation. The model agrees within ~10% of the experimental measurements in the point-to-ring configuration. The conductance term I/φ has a nonlinear relationship with the corona voltage φ for low electric field values. The linear trends described in the literature hold for higher corona voltages. The analytical model captures the linearity of the EHD flow velocity with the corona voltage, as shown in the experimental data for the maximum velocity presented here and elsewhere. The maximum velocity is located at the centerline in this configuration. Unlike in canonical internal pipe flow, the velocity profile in the point-to-ring EHD flow is analogous to a submerged jet [201], for which the Re is determined by the dimension of the acceleration zone and mean velocity. Jet values of $\mathrm{Re} = 300 - 1000$ correspond to the laminar regime in the flow acceleration region [202]. The exit velocity profile is used to calculate the electric to kinetic energy transfer efficiency. The efficiency is highest when the point-to-ring distance is largest, due to a

smaller angle between the electric field gradient and the flow direction and to the lower viscous losses. The efficiency peaks at intermediate corona voltages, for a given electrode distance, due to the quadratic current-voltage relation and the nonlinear decrease of velocity away from the centerline, as well as the field line distortions caused by space charge effect near the ionization region.

Chapter 4. ANALYTICAL MODEL FOR ELECTROHYDRODYNAMIC THRUST

This analytical model is published in Proceedings of Royal Society A: Mathematical, Physical and Engineering Sciences [5].

In this chapter, we extend the analytical model for EHD flow [6] to formulate the expression for EHD thrust in 1-dimensional planar coordinates. The electric current density derived from the model is presented in the form of Mott-Gurney law. After the correction for the drag force, the EHD thrust model yields good agreement with the experimental data from three independent experimental studies, including our experiments and the previously published data [78, 79]. The EHD thrust expression derived from the first principles can be used in the design of propulsion systems and can be readily implemented in numerical simulations.

4.1 Analytical Model Development

Corona discharge generates a flow of charged species, and the assessment of the charge densities and the electric field is essential for the evaluation of the EHD force acting on the fluid. The charged species are generated in the region where the field strength exceeds the threshold for the breakdown of molecules in the fluid. For a wire-to-rod corona discharge, shown in Figure 4.1, ionization occurs near the wire. As the electric field strength decreases away from the emitter electrode, the ionization is hindered; however, the charged species moving in the inner electrode transfer their momentum to neutral molecules via elastic collisions. The charged species concentration in corona discharge can be calculated using the charge continuity equation, considering that three types of charged species are present positive ions, negative ions, and

electrons. The density N_k of the charged species k is described by the conservation equation [6, 196]

$$\frac{\partial N_k}{\partial t} + \nabla \cdot [(\mathbf{u} + \mu_b \mathbf{E}) N_k - D_e \nabla N_k] = \omega_k \,, \tag{4.1}$$

where $\mathbf{u}$ is the velocity vector of the bulk flow, $\mathbf{E}$ is the electric field, μ_k is the ion mobility of charged species k, and D_k is the ion diffusivity of the charged species and ω_k is the production rate of species k. The ionization can be conceptualized as a combination of two processes (1) ionization process of charged species generation and (2) recombination process where charges recombine. Transport of charged species in the field, their capture by the emitter electrode or ejection from the ionization region can aid or hinder the specific reaction in the plasma volume. One can avoid complex plasma chemistry considerations in the analysis of corona-induced EHD in air by making two key assumptions. (i) The ionization occurs only in the region when the electric field strength is greater than a threshold value $\sim 3E + 06\, V/m$ [55]. (ii) The total momentum transferred to the neutral gas molecules in the ionization region is negligible compared to the ion drift region as shown in Figure 4.1. In the ionization region, the momentum transfer is partially offset by the positive and negative species traveling in opposite directions and by a relatively small volume of the ionization region compared to the ion drift region. We assume that the momentum injection takes place in the ion drift region, where the net charge density is given by $\sum_k N_k = \rho_e$. With these two assumptions, the reduced charge continuity equation can be written as

$$\frac{\partial \rho_e}{\partial t} + \nabla \cdot [(\mathbf{u} + \mu_b \mathbf{E}) \rho_e - D_e \nabla \rho_e] = 0 \,, \tag{4.2}$$

where ρ_e is the charge density, μ_b is the ion mobility and is approximated as a constant $2.0 \times 10^{-4}\, m^2/V \cdot s$ [7, 90], and D_e is the ion diffusivity and can be determined using the electrical mobility equation.

$$D_e = \frac{\mu_b k_B T_e}{q}, \tag{4.3}$$

where k_B is the Boltzmann constant, T_e is the absolute temperature, and q is the elementary charge. The analytical expressions for $(\varphi - I)$ and $(\varphi - T)$ can be derived for steady-state conditions in planar coordinates from the simplified governing for charge density, Eq.(4.2).

Since the ion drift velocity is considerably higher than the EHD-induced bulk flow, the ion motion is assumed to be quasi-steady, and the Eq. (4.2) can be rewritten as

$$\nabla \cdot [(\mathbf{u} + \mu_b \mathbf{E})\rho_e - D_e \nabla \rho_e] = 0\,, \tag{4.4}$$

The forcing on the ions due to the electric field set up by potential between the electrodes is significantly greater, the space charge diffusion has not been typically considered [55]

$$\frac{\mathbf{u} + \mu_b \mathbf{E}}{D_e} \sim O(10^4). \tag{4.5}$$

The diffusion term can be neglected, and Eq (4.4) can be further reduced

$$\nabla \cdot [(\mathbf{u} + \mu_b \mathbf{E})\rho_e] = 0. \tag{4.6}$$

Guan et al. [7] have shown that space charge density influences the electric field lines (and thus the ion drift direction) in the vicinity of the ionization region for geometries with high angles (>45º) between the bulk flow direction and the line connecting anode and cathode in a point-to-ring geometry. In the geometry where the flow direction is aligned with electrode geometry, the space charge effect is significantly lower, and for the purpose of this derivation, is not considered. The electro-convective velocity due to external flow is negligible compared to the drift velocity $\left(\frac{|\mathbf{u}|}{|\mu_b \mathbf{E}|} = O(10^{-2})\right)$ in air discharge [55]. The continuity equation can be reduced to

$$\nabla \cdot [\mu_b \rho_e \mathbf{E}] = 0, \tag{4.7}$$

where $\mu_b \rho_e \mathbf{E} = \mathbf{J}$ is the current flux. The electric field satisfies Gauss's law

$$\nabla \cdot \mathbf{E} = \frac{\rho_e}{\varepsilon}, \tag{4.8}$$

where ε is the permittivity, and for air, it is close to the permittivity of the space. Combining with Eq.(4.8), the ion transport equation can be written as

$$\frac{\mu_b}{\varepsilon} \rho_e^2 - \mu_b \nabla \rho_e \nabla \varphi = 0. \tag{4.9}$$

Note that Eq.(4.9) is the same as in Sigmond [55]. Derivations for cartesian coordinates are similar to Guan [6]. Eq.(4.9) can be rearranged as

$$\nabla \varphi = \frac{\rho_e^2}{\varepsilon \nabla \rho_e}. \tag{4.10}$$

In one dimension (aligned with the flow acceleration), we have

$$\frac{d\varphi}{dx} = \frac{\rho_e^2}{\varepsilon \frac{d\rho_e}{dx}}. \tag{4.11}$$

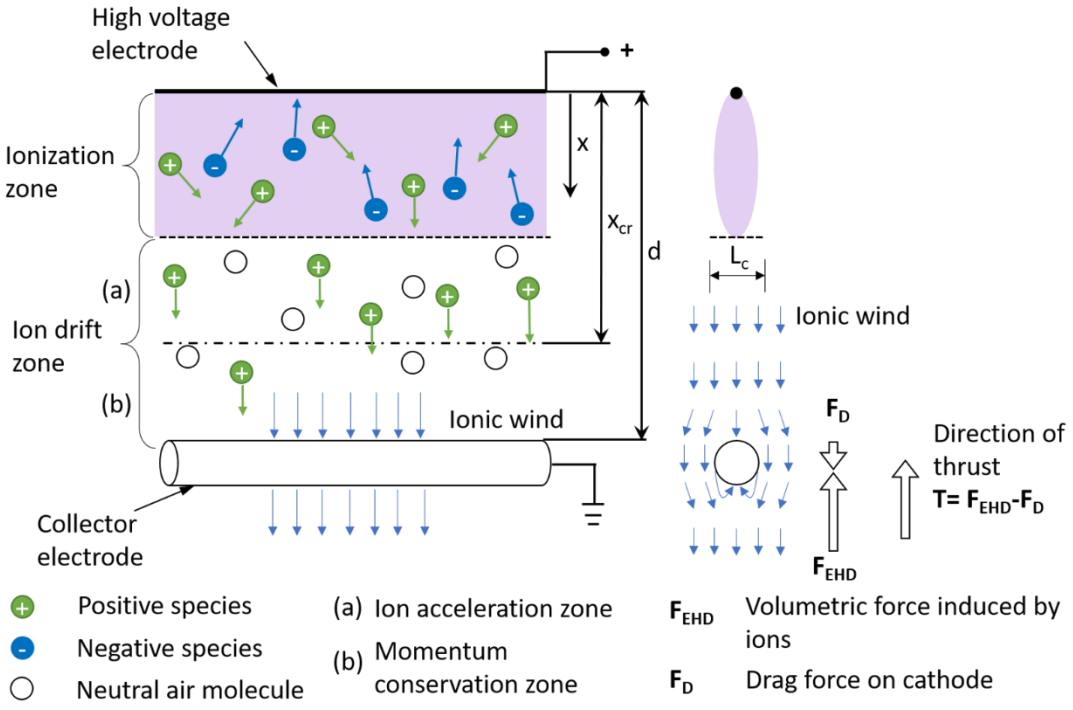

Figure 4.1. Diagram of a wire-to-cylinder EHD flow. In positive corona, the negative species produced in the ionization zone recombine with positive species or the emitter (anode). The super-equilibrium positive ions drift to the collector electrode (cathode), accelerating the bulk flow. Thrust force is the resultant of the Coulombic force induced by the ions and drag force on the cathode. The conceptual representation of the EHD system includes (i) ionization region, (ii) flow acceleration region where unipolar ion motion in the gas medium acts as a body force accelerating the flow, and (iii) momentum conservation region where the electric force is balanced or overcome by viscous effects.

Taking the *x*-derivative on both sides and substituting into Gauss's law, Eq. (4.8):

$$\frac{d^2\varphi}{dx^2} = -\frac{\rho_e}{\varepsilon} = \frac{2\rho_e \frac{d\rho_e}{dx}\left(\varepsilon \frac{d\rho_e}{dx}\right) - \rho_e^2\left(\varepsilon \frac{d^2\rho_e}{dx^2}\right)}{\left(\varepsilon \frac{d\rho_e}{dx}\right)^2}. \tag{4.12}$$

Rearranging

$$3\left(\frac{d\rho_e}{dx}\right)^2 = \rho_e\left(\varepsilon \frac{d^2\rho_e}{dx^2}\right) \tag{4.13}$$

and seeking the solution in the form

$$\rho_e = Kx^n\,, \tag{4.14}$$

then substituting into Eq.(4.13), the following expression is yielded

$$3n^2x^{2(n-1)} = n(n-1)x^{2n-2}. \tag{4.15}$$

From Eq. (4.15) $n = -1/2$ and $\rho_e = Kx^{-\frac{1}{2}}$, substitute to $E = -\frac{d}{dx}\varphi$

$$-\frac{d}{dx}\varphi = -\frac{\rho_e^2}{\left(\varepsilon \frac{d\rho_e}{dx}\right)} = \frac{2K}{\varepsilon}x^{1/2} \tag{4.16}$$

$$d\varphi = -\frac{2K}{\varepsilon}x^{1/2}dx. \tag{4.17}$$

Integrating on both sides gives

$$\varphi_c - \varphi = -\frac{4K}{3\varepsilon}x^{3/2}. \tag{4.18}$$

The coefficient K can be written as

$$K = \frac{3\varepsilon}{4x^{3/2}}(\varphi - \varphi_c), \tag{4.19}$$

where φ is the applied anode potential and φ_c is the constant potential in a corona discharge, which can be considered as potential at the *x*-location of the corona onset, or corona initiation voltage φ_o. The ion current flux between the anode and cathode is

$$J = \mu_b \rho_e E = \frac{9\mu_b \varepsilon(\varphi - \varphi_o)^2}{8x^3}. \tag{4.20}$$

The relationship in Eq.(4.20) shows that $J \propto x^{-3}$ and has a similar form to Mott-Gurney law [71, 78], i.e., $J = \frac{9\mu_b \varepsilon \varphi^2}{8d^3}$, which describes the space charge saturation limit, where d is the distance between the electrodes and φ is the applied potential. In corona discharge, the charged species are produced only after the onset potential is reached, so if φ is replaced by $\varphi - \varphi_o$ and $x = d$, the current flux relation becomes takes the form of Mott-Gurney law.

The EHD flow in planar wire-to-cylinder geometry can be divided into three regions: ionization zone, acceleration zone, and momentum conservation region. To define the conditions in the acceleration region, consider x_{cr}, which is the characteristic length scale of the flow acceleration. For wire-to-cylinder geometry, the ionization and drift regions can be approximated as an infinite plane (in the y-direction) where x_{cr} is the distance from the emitter to an examination position, as shown in Figure 4.1. The current flux at the location (x_{cr}) can be written as

$$J_{cr} = \mu_b \rho_e E = \frac{9\mu_b \varepsilon(\varphi - \varphi_o)^2}{8{x_{cr}}^3}, \tag{4.21}$$

$$I = \int J_{cr} dA = J_{cr} A, \tag{4.22}$$

where A is the cross-sectional area associated with ion interaction with the fluid at the location x_{cr}. For planar geometry (infinite length electrodes), the zone of ion interaction with the fluid can be normalized to a unit length $(L_c \times 1)$. Substituting cross-section area into Eq.(4.21) gives the current expression

$$I = \frac{9\mu_b \varepsilon(\varphi - \varphi_o)^2}{8L_c x_{cr}}. \tag{4.23}$$

To simplify, we introduce a characteristic dimension (Lc) that defines the ion-flow interaction region, then Eq.(4.23) can be reduced to

$$I = \frac{9\mu_b \varepsilon(\varphi - \varphi_o)^2}{8L_c^2}. \tag{4.24}$$

This current-voltage relationship is similar to Townsend's quadratic relationship for the coaxial cylinder electrode configuration $I = C\varphi(\varphi - \varphi_o)$, where C is a fitting coefficient, typically obtained from the experiments, and it is dependent on the geometry. The physical interpretation of the parameter C is proposed by Cooperman for duct-type electrostatic precipitator as $C \propto \mu_b / {L_c}^2$, where μ_b is the ion mobility and L_c is the characteristic length scale [53]. Our derivation also shows a similar physical interpretation of the Townsend constant:

$$C = \frac{9\mu_b \varepsilon}{8L_c^2}. \tag{4.25}$$

The derived $(\varphi - I)$ relationship Eq.(4.23) is more general than formulations given by Townsend [52], the values of φ_o and L_c must be determined for any specific geometry. Once the $(\varphi - I)$ the relationship is defined, force induced by EHD can be computed as the Coulomb force acting on the volume of fluid by the non-equilibrium concentration of ions between the anode and cathode

$$F_{EHD} = \int f dV = \int \rho_e E dV = \int_0^d \rho_e E A_L dx = \frac{Id}{\mu_b} = \frac{9\varepsilon(\varphi - \varphi_o)^2 d}{8L_c^2}, \tag{4.26}$$

where F_{EHD} is the volumetric force induced by the ions, and f is the force per unit volume.

Previous research [78, 79] shows the use of Townsend's current relation in Eq.(4.26) to determine the EHD force by fitting the constant C. However, the measured thrust does not always agree with the calculated EHD force, because the measured thrust is the result of the Coulombic and drag forces. Predicted thrust force from Townsend's current voltage relationship can be 70% greater than the measured one [78, 203], likely due to losses associated with drag and the 3D field effects. The determination of drag on the cathode in a wire-to-cylinder system requires the knowledge of the velocity profile. However, the velocity measurements can be challenging near the high voltage emitter and may not be available. It has been proposed that the mean ionic wind velocity associated with the corona discharge can be determined using the Bernoulli equation, see Moreau et al. [78] The mean velocity v and pressure P in the ionization zone as shown in Figure 4.1 can be approximated

$$P = \frac{1}{2}\rho v^2, \tag{4.27}$$

where ρ is the density of the fluid. The pressure gradient in the one-dimension coordinate system induced by the corona discharge can be written as

$$f = \frac{dP}{dx} \tag{4.28}$$

Combining Eq.(4.26) and Eq. (4.28), the expression for pressure can be written as

$$P = \int f\, dx = \frac{Id}{\mu_b A}. \tag{4.29}$$

The mean velocity of EHD flow can be determined from the eq (4.27)

$$v = \sqrt{\frac{2Id}{\mu_b \rho A}}. \tag{4.30}$$

The mean electric wind velocity can also be calculated using momentum balance over the entire domain by neglecting the pressure and viscous terms

$$\rho_e E = \rho v \frac{dv}{dx}, \tag{4.31}$$

$$\int \rho_e E dx = \int \rho v dv, \tag{4.32}$$

substituting Eq.(4.26) and integrating over the gap between anode and cathode gives

$$\frac{Id}{\mu_b A} = \frac{1}{2}\rho v^2. \tag{4.33}$$

After solving for v, the expression is identical to the equation (4.30).

The drag force due to the flow over the cathode can be calculated from the following expression

$$F_D = \frac{1}{2}\rho v^2 S C_{D,} \tag{4.34}$$

where F_D is the drag force, S is the cross-section area of the cathode and C_D is the drag coefficient of the cathode. Though in the case of corona discharge, the velocity profile is not uniform, Eq. (4.34) can be used as an approximation. Substituting Eq. (4.30) into Eq. (4.34) simplifies it further

$$F_D = \frac{Id}{\mu_b}\frac{SC_D}{A} = \theta F_{EHD}. \tag{4.35}$$

Here θ is a non-dimensionless quantity that is the ratio of the cross-section area of the cathode and corona discharge area multiplied by the drag coefficient of the cathode. The value of θ has to be less than unity and has to be determined for a specific cathode geometry. Thrust can be written as

$$T = (1 - \theta)F_{EHD}. \tag{4.36}$$

The derived $(\varphi - T)$ relationship is more general than particular formulations presented in ref [78]. This formulation can be used for determining the corona current and thrust forces in planar coordinates. Unlike the thrust force formulations that use Townsend relation with fitting parameter

C, our model captures the thrust force generated by ions including aerodynamic losses. Table 4.1 compares thrust characteristics derived from empirical [52, 72] data and our first-principles approach.

Table 4.1. Comparison of analytical expressions from state of the art and our work

	State of the art	Current work	Comparison
Current flux	$J = \frac{9\mu_b \varepsilon(\varphi)^2}{8d^3}$ Mott Gurney law [72]	$J = \frac{9\mu_b \varepsilon(\varphi - \varphi_o)^2}{8x^3}$	Current flux at any x; Model accounts for ionization onset – φ_0
Voltage – current characteristics	$I = C\varphi(\varphi - \varphi_o)$ Townsend relation [52]	$I = \frac{9\mu_b \varepsilon(\varphi - \varphi_o)^2}{8L_c^2}$	Length scale L_c provides a physical interpretation to fitting constant - C
Voltage – force characteristics	$F_{EHD} = \frac{C\varphi(\varphi - \varphi_o)d}{\mu_b}$	$F_{EHD} = \frac{9\varepsilon(\varphi - \varphi_o)^2 d}{8L_c^2}$	Coulombic force is computed from the first principles
Voltage – thrust characteristics	No expression	$T = (1 - \theta)F_{EHD}$	Model computes thrust and accounts for aerodynamic losses via parameter θ

4.2 Model Validation – Experimental Setup

Analytical model validation is performed by comparing to the EHD thrust measurement in a wire-to-airfoil geometry. In the experiments, we seek two primary correlations (i) voltage-current $(\varphi - I)$ based on the cathode current and (ii) voltage-thrust $(\varphi - T)$, where the thrust is measured directly. Figure 4.2 shows the schematic of the experimental setup. The emitter is a 100-micron

diameter tungsten wire, the cathode is a symmetrical airfoil (NACA 0024) fabricated of a 25-micron copper sheet and has a length of 25 mm. A thruster frame of 100 mm wide was built of a polylactic acid polymer. The frame was suspended from an analytical balance Metler Toledo (AE 240) with 40 g capacity and 0.01 g resolution. The distance between the electrodes (d) was varied in the range of 10 to 30 mm using spacers. The thruster mass is ~ 26 g in the 10 mm spacer configuration. A high voltage power supply (Glassman, model EH30P3) was used to set the electric potential between the electrodes. The cathode current was measured based on a voltage drop across a 0.5 MΩ resistor. The electrical connections of both electrodes were established by thin wire (100 μm in diameter) to minimize added weight. The thruster was hung from a hook on the underside of the balance using cotton strings to electrically isolate the balance and to avoid current leakage. The thrust was measured as a reduction in weight measure by the analytical balance. The experimental procedure is as follows: (i) the high voltage is switched off and the weight of the thruster is measured using the analytical balance (ii) the high voltage is switched on and the difference in the balance measurements is determined, the voltage value is increased in the increments of 1 kV. The experiment was operated in the positive corona mode in a room temperature range of 22-25 ºC, relative humidity of 24-26%, and ambient pressure. For each distance (d), the voltage was increased from 7 kV (when the thrust force becomes measurable) to ~ 29 kV (power supply limit or until a spark-over occurs). To verify the measurements, each experiment was repeated five times.

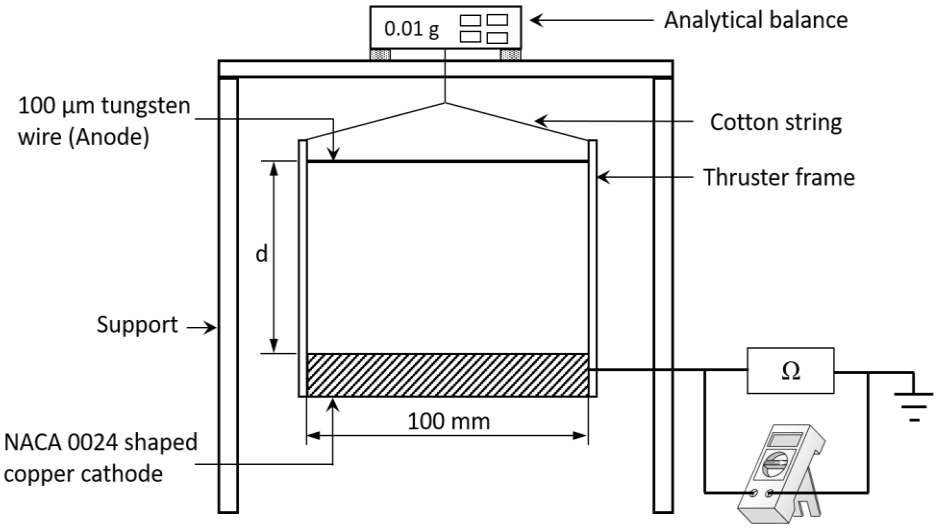

Figure 4.2. Schematic of the experimental setup. A high voltage is applied between the corona wire and the ion-collecting airfoil-shaped cathode. The distance and voltage are varied in the experiments.

4.3 Results and Discussion

4.3.1 *Voltage current characteristics*

The cathode current was obtained as a function of corona voltage and compared with the model in Figure 4.3. The I vs φ trends are similar to previously reported quadratic trends in the literature for different corona configurations [6, 52, 191], as shown in equation (4.24). The nonlinearity in the analytical model comes from the φ_o/φ term in equation (4.24). The trends can be used to evaluate legnth for the acceleration zone L_c . It is convenient to examine the condition $\varphi = \varphi_o$ where the EHD thrust is negligible. At higher corona voltages, the length of the acceleration zone and electric field intensity increases non-linearly. The previous work [6, 55] considers the characteristic dimension L_c as a constant for a given electrode configuration; it was used as a fitting parameter to determine the $(\varphi - I)$ curves, which are linearly dependent on d. By similar logic,

the best fit is obtained when $L_c = 10 + \beta(d - 10)$ and $\beta = 1$. This relationship is likely to change for a different electrode configuration.

The analytical model has excellent agreement with the experimental results at lower voltages and within ~10% at higher voltages. The discrepancy between the model predictions and the experimental results can be due to the current leakage, i.e., ions exiting the control volume and not participating in the momentum exchange. For greater corona voltages, the leakage increases leading to a larger difference between the model and experimental data. The discussion in the thrust data analysis presents several mechanisms contributing to the model underprediction of current and thrust as the voltage and electrode spacing increase.

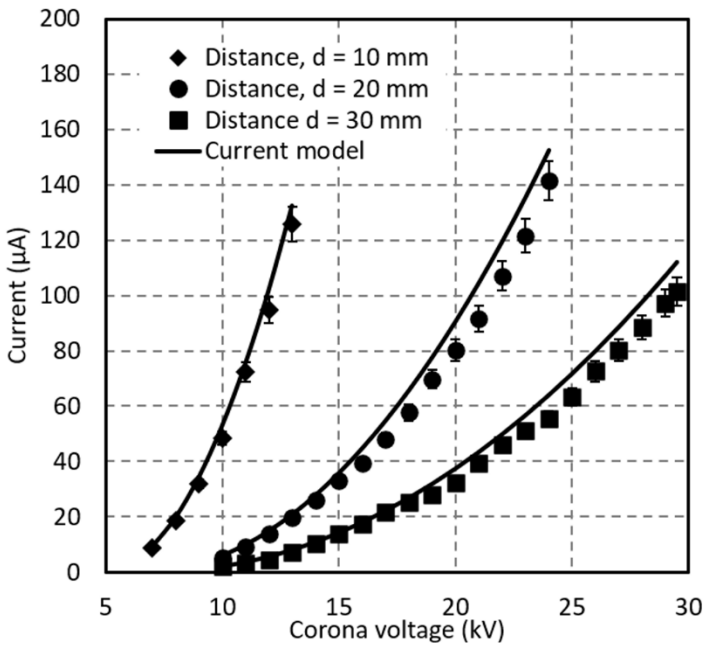

Figure 4.3. Voltage-current characteristics for the experimental data and the analytical solution.

4.3.2 *Electrode spacing effect*

The variation in distance between the electrodes has several effects (i) the strength of the E-field decreases with distance, (ii) the net thrust is proportional to the volume of the ion drift region (iii) greater electrode spacing results in higher viscous losses. Figure 4.4 compares the voltage-thrust data against and the analytical solution varying d = 10 – 30 mm and φ = 7 – 29.5 kV. The relationship between the thrust and voltage is quadratic, as predicted by equation (4.26), which agrees with the trends reported in the literature for a wire to cylinder corona configuration [78, 79]. These trends can be used to estimate corona onset voltage φ_o; at this condition, the thrust is negligible. The experimental data show that higher thrust is observed at smaller gap lengths for a given voltage as the electrical field strength is greater. However, smaller gap configurations are limited due to earlier electrical breakdown (sparkover leads to a loss of thrust). The experimental thrust data is compared with two different models, (i) model without the aerodynamic drag on the cathode, see Eq. (4.26) and (ii) model with aerodynamic drag losses Eq.(4.36). As the voltage increases, the model without drag correction over-predicts the experimental thrust as the aerodynamic drag correction is greater at higher flow velocities. The mean flow velocities generated by the EHD are determined using equation (4.30), and the cathode chord Reynold number varies from 1000 – 6000. The small dimensions of the cathode and the low velocities amplify the viscous effects and generate high drag [204]. At these low Reynolds number, the drag coefficient of the airfoil $C_d = 0.06$ is used based on previous work on dragonfly airfoil aerodynamics for Re < 8000 [205]. Here, the drag coefficient is kept constant for all cases. The calculated non-dimensional drag varies θ = 0.05 – 0.15 as given in Eq.(4.35) for different electrode gaps. The analytical model with drag force correction has better agreement with the experimental data at lower voltages. The model agrees within ~10% at higher voltages.

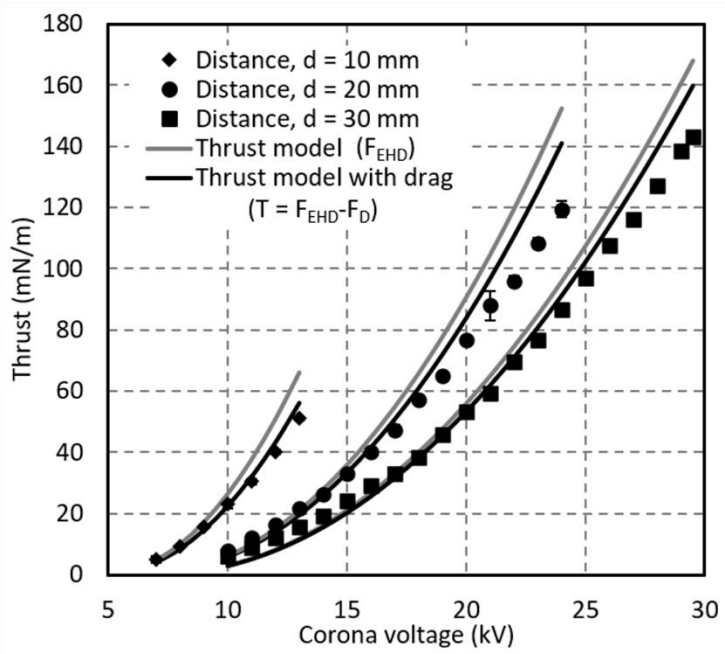

Figure 4.4. Voltage-thrust relationship for varying distances between the anode and cathode for positive corona discharge. The experimental data are compared with the analytical model with and without the aerodynamic drag on the cathode.

4.3.3 *EHD thrust model comparison with previous reports*

The model with drag correction is compared with the $(\varphi - T)$ data in wire-to-cylinder configurations from the literature [78, 79]. Figure 4.5 plots the comparison for two different electrode gaps: $d = 20$ mm [79], and $d = 30$ mm [78]. The fitting parameter $L_c = 17$ mm gives the best fit for both the studies, the model predicts the data within 10%, overpredicting the thrust at higher voltages. Table 4.2 summarizes the model parameters used for the comparison of analytical model and experimental data. The choice of Lc is dependent on the drag force calculations from Eq. (4.35). In modeling of our experimental data, we have experimentally determined φ_c based on onset current. In the previous data [78, 79], the value of φ_c is not known, thus we have chosen$\varphi_c = 6$kV (within the range of our experimental measurements). The

agreement can be improved if the values of onset voltage are known. Though it is not apparent in our data or from Moreau et al. [78], Masuyama and Barrett [79] have observed the flattening of the $(\varphi - T)$ trend at high voltages and the largest electrode gap conditions. The EHD thrust reaches saturation with the increase of potential. The presented 1-D model cannot account for this trend. At this time, we do not have an explanation for the discrepancy between the model and data at the highest voltage; however, we provide several hypotheses that may describe this behavior. (i) Nonlinear effects in the ionization region, where the increasing E-field does not produce ions at the same rate as in the lower conditions. (ii) The losses in the acceleration region due to the viscous dissipation are greater for the larger electrode gap. (iii) Space charge shielding effect, where a fraction of positive ions does not drift toward the cathode but rather are lost to surroundings (including surfaces around the experimental apparatus). This effect is likely to be enhanced as the distance between the electrodes increases. (iv) One-dimensional assumption cannot be used to describe flow, as the non-linear E-field leads to the formation of complex flow patterns. Additional investigations are required to test these hypotheses. 3D numerical modeling could be a good tool to study these effects.

Table 4.2. Model parameters used for state of the art and the current work.

	Modeling previous data	Modeling our data
φ_o	d = 20 mm, 6 kV [79] d = 30 mm, 6 kV [78]	d =10 mm, 4.8 kV d = 20 mm, 6.5 kV d = 30 mm, 7 kV
L_c	17 mm for both cases	$10 + \beta(d - 10)$ and $\beta = 1$

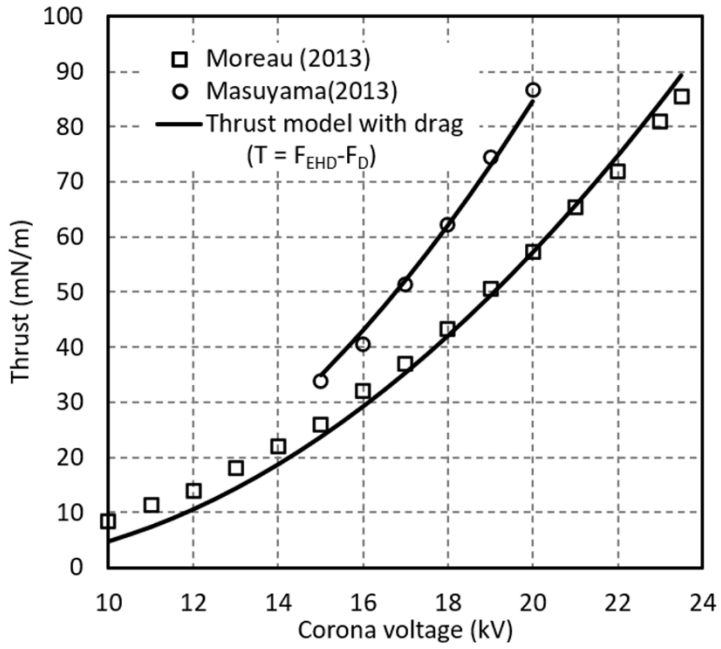

Figure 4.5. Comparison of the analytical model and existing thrust data from the literature. The model with drag losses accurately predicts the thrust data for two different cases: 20 mm separation from Masuyama [79] and 30 mm separation from Moreau [78].

4.4 CHAPTER SUMMARY

An analytical model describing the EHD thrust is developed in 1-D coordinates and compared with data for wire-to-airfoil and wire-to-cylinder configurations. The current density expression is analogous to Mott-Gurney law that provides the theoretical maximum of charge density between anode and cathode. The model includes a modified term to account for the corona onset voltage. The derived $(\varphi - I)$ relationship has a similar form as Townsend's equation with a modified constant proportional to $\mu_b/{L_c}^2$. The EHD thrust force is derived from $(\varphi - I)$ relationship accurately predicts the thrust at lower voltages. The aerodynamic drag correction improves the agreement at the higher voltages (greater velocities). The model agrees with the experimental data from three independent studies within 10%. The model's limitations of the model are in predicting

the thrust at the increasing voltages; these are likely the results of the simplified assumptions in the viscous losses, ionization region modeling including space charge effects, increased dimensionality of the electric field in large electrode gap geometries.

Chapter 5. PROPULSION OF INSECT SCALE ROBOT WITH EHD THRUSTERS

This work is published in PLOS One [8]. The fabrication and experiments are performed with the assistance of Hari Krishna Hari Prasad [206], and the fabrication methodology and experimental results are presented here for completeness.

In this chapter, we utilize laser machining fabrication to build EHD thrusters for centimeter-sized aerial robots. The process allows for a greater variety of electrode materials and eliminates the need for a clean room facility. For example, it allows fabricating a complete four-thruster device in a matter of minutes. Our four-thruster device measures 1.8 × 2.5 cm and is composed of steel emitters and a lightweight carbon fiber mesh. We measured the electrical current and thrust of each thruster of our four-thruster design, showing agreement with the Townsend relation. The peak thrust of our device, at 5.2 kV, was measured to be 3.03 times its 37 mg (363.0 μN) mass using a precision balance. In free flight, we demonstrated liftoff at 4.6 kV.

5.1 Fabrication and Assembly of EHD Thrusters

Our fabrication process emphasizes speed and simplicity by minimizing the number of components and fabrication time.

Previous work has used a silicon-on-insulator process for the fabrication of EHD thruster [16]. The emitter and collector electrodes were made from silicon patterned with a photolithographic mask. After a deep reactive ion etch (DRIE) process ablates through the wafer, the electrodes are once more etched with hydrofluoric acid (HF). In that work, insulating standoffs to separate the emitter from the collector were made from fused silica capillary tubing with an outer diameter of

400 μm. Connections between the tubing and electrodes were made with UV-curable epoxy. Power connections are made with the application of silver epoxy. An external jig was used to align the assembly. The device has 13 components (8 capillary tubes, four emitters, and one collector) in comparison to the most recently reported design for the "Ionocraft" that has 41 components (including sensor components) [207].

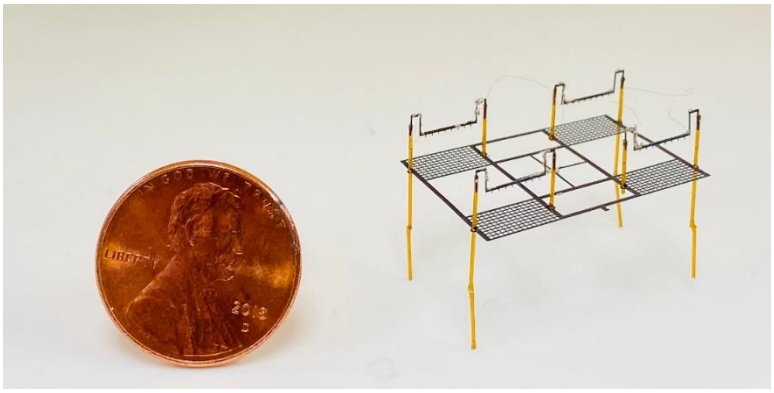

Figure 5.1. An assembled Quad-thruster robot next to a U.S.penny The 1.8 × 2.5 cm quad-thruster having a mass of 37 mg is shown. The robot components consist of a carbon fiber collector grid, four blue tempered steel emitters, and eight fiber optic glass tubes. All components are hand-assembled using external jigs.

Here, we use laser micro-machining instead of lithographically patterned silicon. Our laser is a diode-pumped solid-state (DPSS) frequency tripled Nd:Yag laser with 355 nm wavelength (PhotoMachining, Inc., Massachusetts). The DPSS laser output power is 2 W, its beam diameter is 20 μm, and position repeatability is about 3 μm. With this system, we can machine both the emitters and collectors in about ten minutes. The detailed fabrication and assembly procedure is described in this work [8, 206]. The fabricated and assembled quad-thruster device is shown in Figure 5.1.

5.2 Experimental Method and Results

The electrical characterization of each thruster in the quad thruster device was performed first. A high voltage positive DC power supply (Bertan 205B-20R) was used to create the potential difference between the emitter and the collector. The current associated with the discharge was determined from the power supply's built-in ammeter. Four measurements are taken for the corona current and the generated thrust at each actuation voltage. The sample mean and standard deviation are computed. The error bars used in Figure 5.2 and Figure 5.4 denote one standard deviation from the sample mean. Results are shown in Figure 5.2 for each of the four thrusters that comprise a single unit. The current and voltage trends are similar to previously reported quadratic trends [6, 51, 52]. We've fitted our data with Townsend's current model shown in Eq. (2.1) using a value of 2.2 and φ_o value of 3.6 kV, and the current-voltage relationship is plotted, showing that our data agree with the model. A peak force of 1.2 mN for the quad thruster is predicted from Eq. (2.4), which corresponds to a theoretical thrust-to-weight ratio of 3.5.

The thrust force calculated from the model is validated using experimental thrust measurement as shown in Figure 5.3; A similar setup has been used in previous studies [78]. The thruster was held directly above the balance with 0.1 mg resolution (Mettler Toledo) such that the collector grid was aligned parallel to the scale surface using a ceramic tweezer. This arrangement, with the thruster fixed, reduces the confounding effect of electrostatic forces acting on the aircraft through the tether wire. The distance between the collector grid and the weight scale is 21 mm. The scale reading was set to zero, and each thruster was energized to measure the thrust. A piece of Teflon was placed between the balance plateau and the collector to electrically isolate the balance and to avoid any leakage current. The measured thrust is the force exerted by the accelerated ionic wind

on the precision scale. It can be seen that the thrust increases with the voltage applied across the electrodes, as shown in Figure 5.4. The thrust trends follow the previously reported quadratic relationship with the applied voltage [5, 78, 79]. The maximum thrust generated occurs immediately before the sparkover is initiated, at which point thrust drops to zero and destroying the mesh. The peak force generated by each thruster was around 260 μN with a standard deviation of 20 μN. The model predictions were higher than the experimental results, but the results captured the trend. The difference between the model and experiments can be attributed to blockage and drag losses as shown in previous reports [5, 78]. The model described in Eq. (2.1) helped us to validate the thrust measurements and can form the basis for future constrained parametric optimization studies of the quad-thruster device.

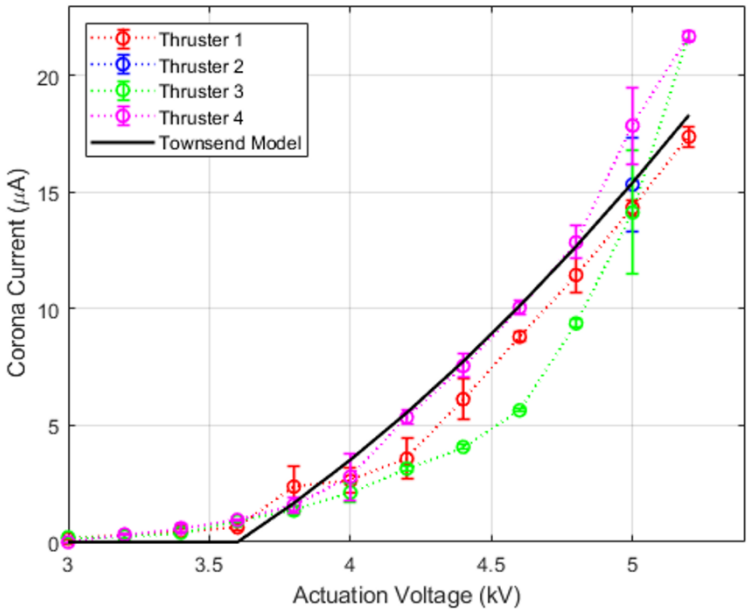

Figure 5.2. Corona current vs the applied voltage for each individual thruster. The measurements are fitted with a Townsend current model and accurately capture the theoretical trend. The calculated corona onset voltage is 3600 V with a standard deviation of 100 V.

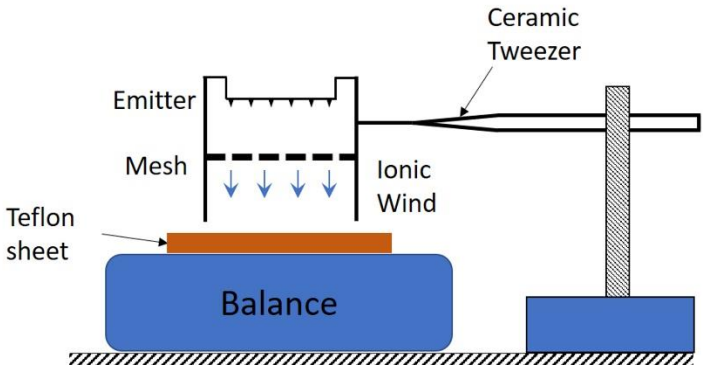

Figure 5.3. Schematic of thrust measurement apparatus. Thrust generated by the EHD thruster was measured by measuring the force produced by the ionic wind on the precision scale. Tethers are not shown for simplicity, and the thruster is not resting on the scale.

Thrust density and efficiency are important parameters in understanding the working and performance of EHD thruster compared to other designs. Thrust density is defined as the amount of thrust generated per unit area, whereas efficiency is defined as thrust per unit power. Thrust density for EHD thrusters is calculated from the effective area where EHD flow exists, i.e., the mesh area. Figure 5.5 shows how the thrust density varies with the corona input power of the EHD thruster. The electrical power was calculated from Eq. (2.2). A maximum thrust of 0.295 mN corresponds to 13.67 N/m^2 thrust density achieved at an input electrical power (aka corona power) of 90.4 mW. Therefore, the thrust density per unit power for the EHD thruster is 151.17 N/m^2W. The efficiency is about 3.265 mN/W. This data can be compared to a piezo-actuated flapping-wing such as the RoboFly [208], a measured efficiency of 12.2 mN/W. For a thrust of 0.736 mN, an input power of 60 mW, and a 308 mm^2 effective swept area of the wing, the thrust density is 2.39 N/m^2. Therefore, the thrust density per unit power is 39.8 N/m^2W. Therefore, while the efficiency of the EHD thruster is lower than a flapping-wing robot of comparable size (the efficiency of the flapping-wing robot is 3.74 times higher), the thrust density per unit power consumed is 3.8 times

higher for the EHD thruster. This is important because the thrust density correlates to the mass of the thruster, and therefore this metric represents a scale-independent (and propulsion-type-independent) measure of efficiency.

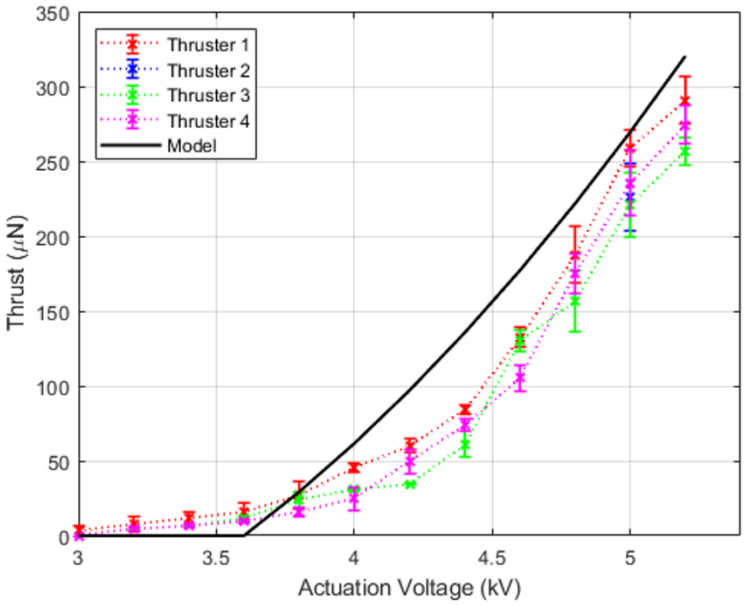

Figure 5.4. Thrust variation with applied voltage is depicted for each thruster of the quad-thruster device. The input voltages range from 3 kV to 5.2 kV. The Townsend current model shown in Figure 5.2 is used to compute the theoretical upper limit for the measured Coulomb force, and the data capture this trend.

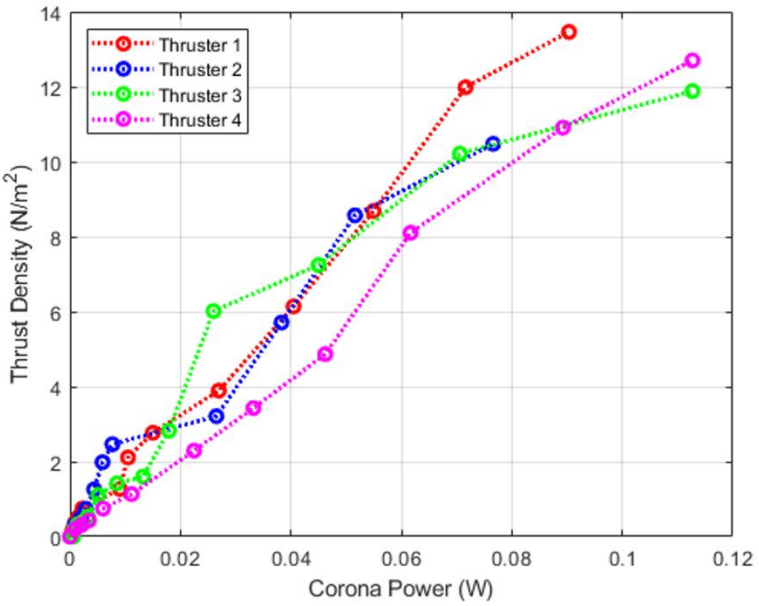

Figure 5.5. Efficiency in terms of thrust density versus the corona power for each thruster in the quad-thruster device. The data points shown displayed are mean values of thrust density and corona power.

For free flight experiments, the device was placed on a wooden table. The four emitters are interconnected with 51-gauge wires as mentioned above in the assembly section, and the quad thruster was actuated using two 58-gauge copper wires in front of a high-speed camera (Sony RX100). One 58-gauge connection is attached from the top to one of the inner ends of an emitter and the other connection is attached to the center of the collector grid. The power tethers were held using ceramic tweezers, and the strain was relieved. The inner legs were removed and attached to the outer legs of the thruster to increase the height and diminish the electrostatic interaction with the takeoff plane. With a voltage of 4.6 kV, lift off of quad thruster was achieved. Figure 5.6 provides an image sequence from the flight for the first 0.32 seconds before the wires touched each other, which ended the free flight. This conclusively shows that the device is able to lift its own weight, and in the future, a vertical liftoff can be achieved.

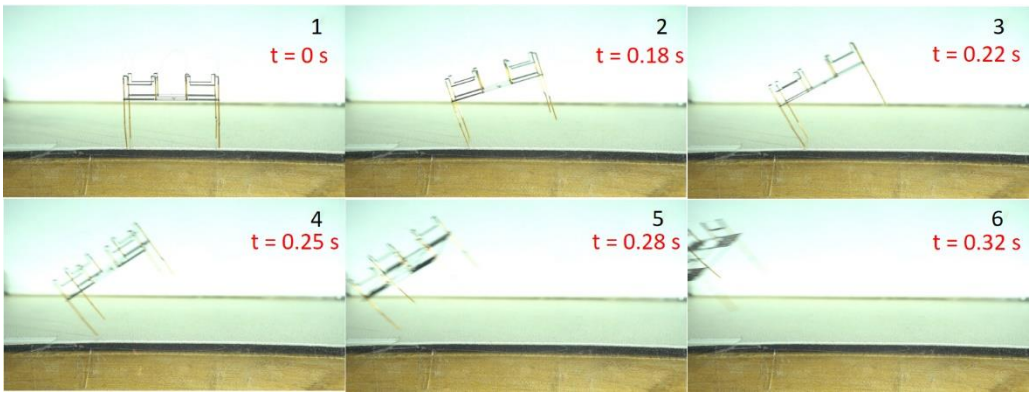

Figure 5.6. Frames captured at a frame rate of 240 fps from the quad-thruster in flight. The thruster is resting on the table with the collector connection dangling down and the emitter connection straight up.

5.3 Chapter Summary

A quad thruster was fabricated using UV laser micro-machining, and the performance of the quad thruster is characterized. Measured current and thrust values are in good agreement with the EHD theory. The variation across all the four thrusters in the device is minimal and the lift-off of the quad-thruster device is demonstrated. The device was able to lift its weight, as indicated by thrust measurements and free flight connected to a wire tether. The thrust-to-weight ratio of our device at takeoff voltage of 4.6 kV is 1.38, with a power consumption of 0.037 W. The peak thrust-to-weight ratio of our thruster at the maximum actuation voltage of 5.2 kV (with a typical operating range of 3.6 kV to 5.2 kV) is 3.03 with a power consumption of 0.104 W, which is slightly below the ratio of 4.5 reported previously [207]. We used fewer emitter rows than [207], and we expect that adding more rows will substantially increase lift with little added weight. We also believe there is ample opportunity to reduce the mass of our device by using thinner and lighter material. We plan to explore of different designs in finite element simulation to explore the configuration

space in greater detail. All of this work will contribute significantly to boosting the thrust-to-weight ratio of our quad thruster device which is fundamental for EHD propelled centimeter-scale aerial robots.

Chapter 6. CORONA DISCHARGE INDUCED FLOW ON A FLAT PLATE

In this chapter, electrohydrodynamic (EHD) flow induced by planar corona discharge in the wall boundary layer region is investigated experimentally and via a multiphysics computational model. The EHD has many potential engineering applications; its optimization requires a mechanistic understanding of ion and flow transport. The corona EHD actuator consisting of two electrodes located in the wall boundary layer creates an EHD driven wall jet. The applied voltage between the electrodes is varied, and the resulting effects in the charge density and flow field are measured. Constant current hotwire anemometry is used to measure velocity profile. The airflow near the wall acts as a jet and it reaches a maximum of 1.7 m/s with an energy conversion efficiency of ~2%. The velocity decreases sharply in the normal direction. Multiphysics numerical model couples ion transport equation and the Navier Stokes equations to solve for the spatiotemporal distribution of electric field, charge density and flow field. The numerical results match experimental data shedding new insights into mass, charge, and momentum transport phenomena. The EHD driven flow can be applied to flow control strategies and the design of novel particle collectors. This work is published in International Symposium on Electrohydrodynamics 2019, St. Petersburg, Russia [12].

6.1 EXPERIMENTAL SETUP

The EHD flow is studied on a conducting and non-conducting flat plate with a shallow rectangular cavity. Figure 6.1 shows the schematic representation of corona-discharge induced flow in the wall boundary layer region on a flat plate with a cavity. Its objective is to accelerate the flow near the wall to modify the boundary layer profile. The serrated edge copper electrode

with a thickness of 0.2 mm serves as the anode. The pitch of the sawtooth is 5 mm. The ground electrode is a 1.5 mm thick steel rod. The flat plate is fabricated using 3D printing in a polylactic acid polymer. A shallow rectangular cavity of 15 mm wide and 1.3 mm deep is built into the flat plate to aid ionization.

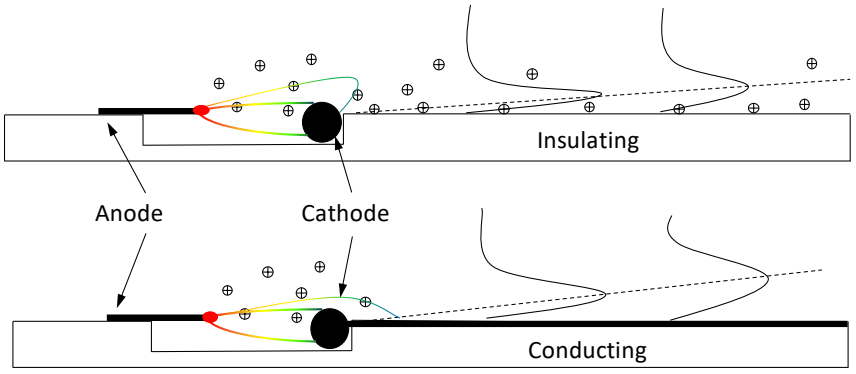

Figure 6.1. Schematic diagram of the corona driven EHD wall jet on conducting and non-conducting/insulating plate; colored lines show electrical field line, solid line – velocity profile.

The anode overhangs the backward-facing step of the cavity by 6 mm as shown in Figure 6.2 such that the distance between the anode tips and the cathode (L) is 9 mm. The width of the experimental setup is 100 mm. The cathode is flush mounted against the forward-facing step, see Figure 6.1. The top of the electrode protrudes 0.2 mm above the flat plate. The cathode protrusion results in the Stokes flow, not affecting the downstream velocity profile development. A variable voltage power supply (Bertan 205B-20R) is used to set the electrical potential between the electrodes. The cathode current is measured based on the voltage drop across a 1 MΩ resistor. The distance between the tip of the anemometer probe and the center of the cathode rod (D) is varied.

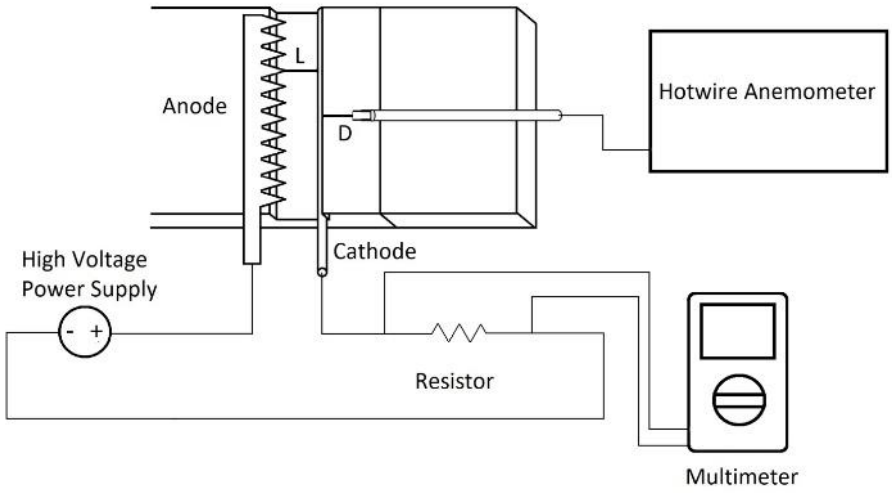

Figure 6.2. Schematic of the experimental setup. A DC high voltage is applied between the copper sawtooth anode and a steel rod cathode, the distance between the anode and cathode is 9 mm.

The anemometer was calibrated for a range of velocities 0.2 - 5 m/s. The data is collected at a frequency of 20 kHz using a data acquisition module (myRIO-1900, National Instruments Inc.), a sampling time of 15 s. The anemometer probe is mounted on an optical 3D stage; movement is controlled by micrometers with a range of 25 mm. The voltage between the anode and cathode is varied from 6 kV to 9 kV in 1 kV increments. The velocity signal from the data acquisition system is filtered using fast Fourier transform, and the frequencies higher than sampling frequency are removed.

6.2 MODELING

Commercial package ANSYS Fluent was used with custom subroutines model three-way coupling of ion motion, electric field, and fluid motion. Figure 6.3 shows the schematic of the modeled geometry; the 2D assumption is used in the numerical simulation. Detailed information on modeling is given in Chapter 11.3. The inlet and outlet of the domain are set to 0 Pa pressure inlet and outlet, and top wall is free wall and rest all are no-slip wall conditions.

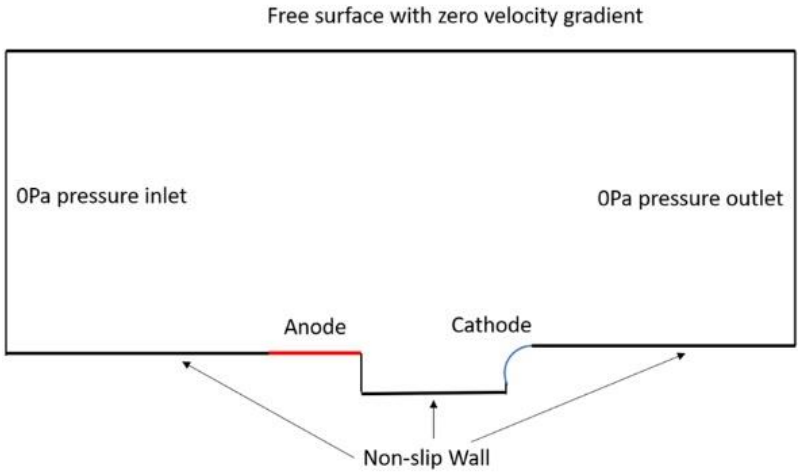

Figure 6.3. Computational domain for the numerical simulation.

6.3 RESULTS AND DISCUSSION

6.3.1 *Numerical results*

The CFD models the process by which the ion-molecule collisions accelerate the bulk flow. Figure 6.4 (a) shows the ion density contours for conducting and insulating plates. The ions are generated at the anode tip. Their motion is dominated by the electric field due to their high electric mobility, as the ion drift velocity is two orders of magnitude than the bulk flow [50]. The effect of space charge is observed as the charge density drifts upstream. The cathode recovers 85-90 % of the ion current that is generated, the other 10-15 % of charge species are recovered on the conducting plate reducing the parasitic effect of ions traveling upstream, as seen in the point to ring corona with insulating walls [7]. In the case of a non-conducting plate, the charged species are recovered by the cathode. The charge is more diffused in the conducting plate case, and it contributes to a change in maximum velocity position and increases the momentum injection compared to an insulating plate. To parameterize the effect of the electrostatic force on the flow, the ratio of electric to the inertial force is defined as a non-dimensional parameter $X = \rho_e \varphi / \rho \mathbf{u}^2$

[7]. Figure 6.4 (b) shows the velocity streamlines colored by the values of X, indicating the regions where the electric force is greater than the inertial force. The electric force is dominant between the cathode and anode, where both the ion concentration and electric field strength are high. In the region downstream of the cathode, the effect of the ion interaction with the flow is minimal. The electric force is more dominant in conducting plate cases compared to the insulating plate due to more charge injection and diffusion, as seen in Figure 6.4 (a) because of the additional ground.

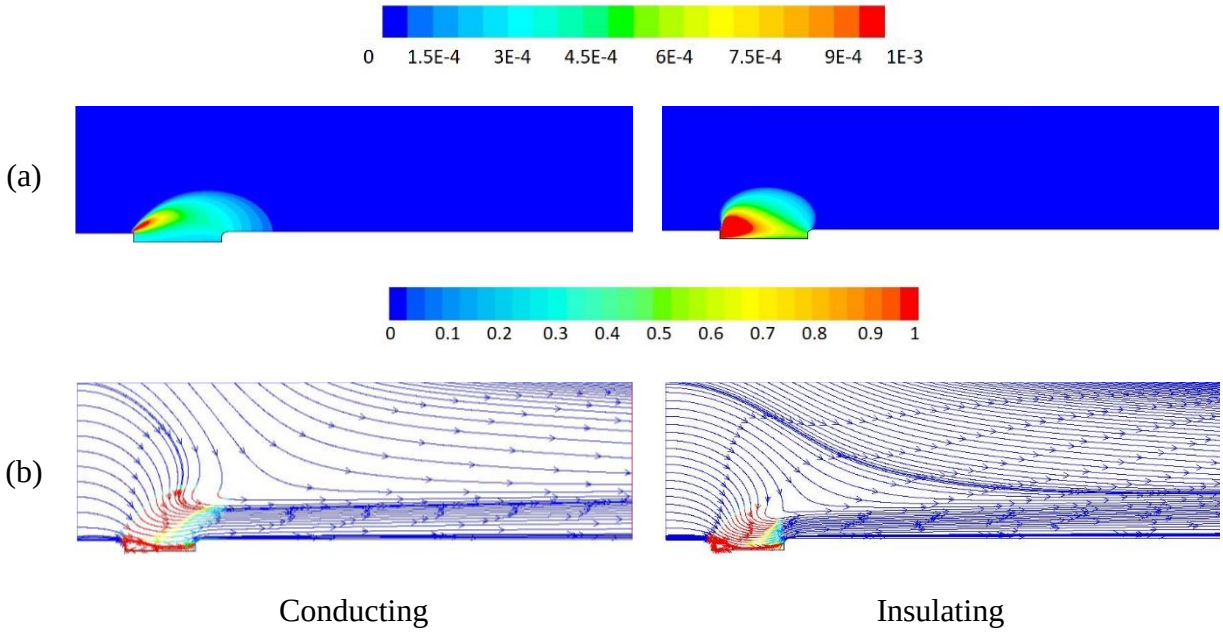

Figure 6.4. Contour plots of the (a) charge density (C/m^3) and (b) streamlines by local X (clipped to 1) for 8 kV case. Maximum – X = 100 for both conducting and insulating plates.

6.3.2 *Velocity – voltage characteristics*

The numerical results for φ = 8 kV case are compared with the experimental velocity profiles at D = 10 and 20 mm as shown in Figure 6.5. The corona-driven flow entrains gas in the vicinity; both streamwise and normal (impinging) components are present upstream of the cathode. Downstream of the cathode, the normal component diminishes. The experimental and numerical

velocity profile downstream of the cathode show similar trends exhibiting wall jet behavior [209-211]. The velocity reaches a maximum and then decays to near-zero away from the plate. Both CFD and experimental data show the maximum velocity is 2 mm from the surface. The maximum velocities in the numerical simulation are ~ 1.7 m/s at D = 20 mm and it is within the 10% of the experimental data. As we move away from the cathode, the maximum velocity decreases, and its location move away from the surface.

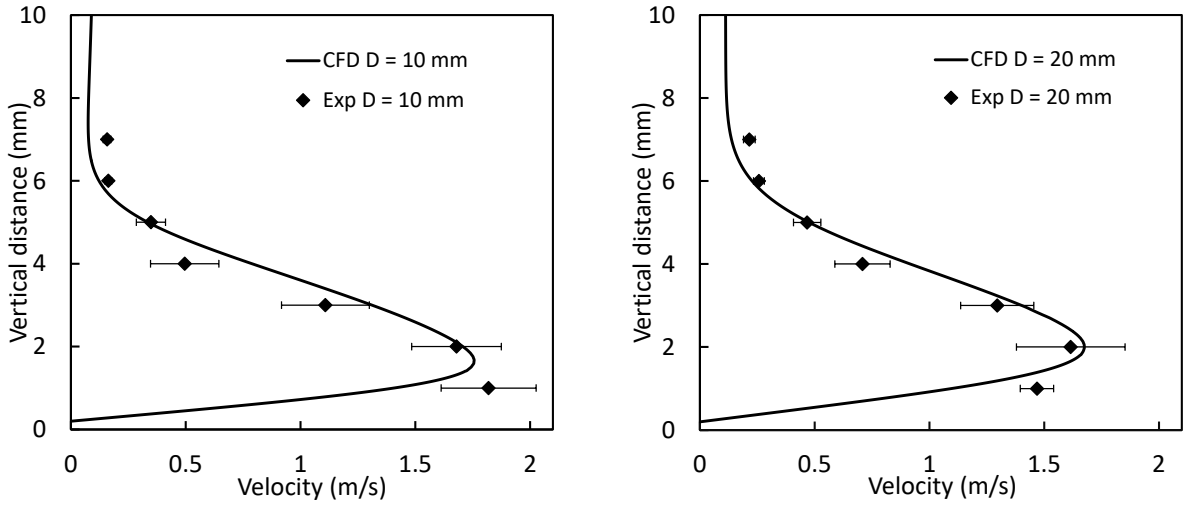

(a) (b)

Figure 6.5. Comparison of the velocity profiles between the experimental results and simulations at (a) D = 10 mm & (b) D = 20 mm of the EHD induced flow on a conducting flat plate.

The conducting surface of the wall has several effects (i) less parasitic losses associated with the upstream motion of the ions (ii) higher electric force to inertial force (iii) higher anode current. The velocity profiles for conducting and insulating plates at φ = 8 kV, D = 20 mm are compared in Figure 6.6. The jet is more spread out in y-direction for conducting plate compared to a non-conducting plate as charges diffuse more since the plate is at the ground. The maximum velocity position for conducting plate is 0.25 - 0.3 mm higher compared to an insulating plate. The region

in which $X > 1$ is big for conducting compared to insulating, and this contributes to more momentum injection. However, the insulating plate generates a wall jet with a higher maximum velocity compared to the conducting plate.

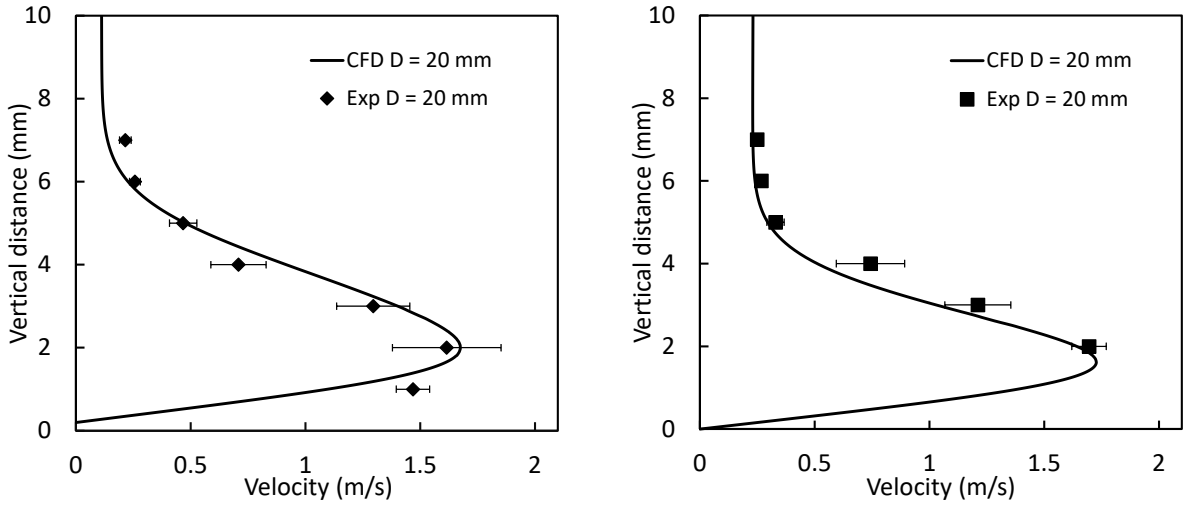

(a) (b)

Figure 6.6. Comparison of the velocity profiles for (a) conducting and (b) insulating plates at D = 20 mm.

6.4 Energy Transfer Efficiency

The energy conversion efficiency can be calculated from the ratio of the kinetic energy flux to the electrical power produced by the corona discharge using Eq. (3.5). The corona voltage and the anode current are obtained from the experiments. The kinetic energy flux is calculated for both experimental and numerical velocity profiles. Table 6.1 shows the values that are used for calculation. The energy transfer coefficient to the fluid is greater for external flow than internal flow due to the entrainment of the surrounding fluid. Parasitic losses associated with the upstream

motion of the ions and the formation of the flow recirculation zone due to adverse pressure gradient are avoided by introducing the conducting surface downstream of the cathode.

Table 6.1. Comparison of electrical and kinetic power between the experiments and CFD

	Conducting	Insulating
$W_{K,Exp}\ (mW)$	6.1 ± 15.2%	5.4 ± 19%
$W_{K,CFD}\ (mW)$	5.9	5.23
$I\ (\mu A)$	35	33.4
$W_E\ (mW)$	280	267

Energy transfer efficiency is 2.17 % ± 0.33% based on experimental and 2.1% based on CFD results for conducting plate and 2.02 % ± 0.38% and 1.95% for insulating plate. It was previously shown that the energy transfer efficiency is non-linear to corona voltage [7]. The energy transfer efficiency for external flows is higher than in the point-to-ring internal flow (~ 1%) [7]. Further improvement in the energy transfer efficiency can be achieved by optimization of electrode geometry configuration, operational condition. As discussed in this chapter, the surface corona discharge near the wall can be used to modify the airflow in the boundary layer, drag reduction, and separation control on airfoils. The effect of surface corona discharge on airfoils will be discussed in Appendix A.

6.5 CHAPTER SUMMARY

This work presents an experimental and numerical investigation of planar corona discharge in the wall boundary layer for conducting and insulating plate. The experimental data includes voltage, current, and velocity profile measurements. Multiphysics numerical simulation sheds

insights into the interaction of force exerted by the motion of the ions in the electrical field on the airflow. The addition of charge flux as a generation of ions allows for the direct computation of electric body force. The numerical simulations agree with experimental data within 10%. The velocity profile of the corona driven is similar to a wall jet downstream of the cathode. The conducting plate entrains more momentum than the insulating plate because of a bigger region where electric force $X > 1$ is dominant. Parametrization of the EHD wall jet and comparison with the traditional wall jet can be achieved using CFD modeling. The integrated velocity profile is used to calculate the electric to kinetic energy transfer efficiency. The efficiency is ~2%, which is greater than in the internal flow geometry due to higher flow entrainment. Energy transfer efficiency can be optimized by electrode geometry configuration, operational conditions.

Chapter 7. DBD PLASMA ACTUATOR: EMPIRICAL RELATIONS FOR DISCHARGE CURRENT AND MOMENTUM

This work is published in Journal of Physics D: Applied Physics [13]. The optical measurements and velocity measurements are performed by Anthony Tang [13], and the results are shown for completeness.

We present an experimental investigation of the DBD actuators, including electrical current associated with microdischarges, plasma volume, and the wall jet momentum over a range of alternating current (AC) frequencies (0.5 – 2 kHz) and peak-to-peak voltages up to 19.5 kV. This experimental work can serve as the foundation for improved DBD models. Discharge current is measured with a high temporal resolution, and plasma volume is characterized optically. The momentum induced by the DBD wall jet is computed based on the axial velocities measured downstream of the actuator using a custom-built pitot tube. Discharge current analysis demonstrated asymmetry between the positive and negative semi-cycle; both currents yielded a power-law relationship with empirical fitting coefficients. Plasma length varies linearly and volume quadratically with voltage. Although plasma length reached an asymptotic value at a higher frequency, the plasma volume grows due to the increasing height of the ionization region. In a simple 2D configuration, the DBD wall jet momentum shows near-linear dependency with discharge current in the range of voltages and frequencies considered in this chapter.

7.1 Experimental Setup and Diagnostics

7.1.1 *DBD actuator*

In the experimental setup, the electrodes are placed on opposite sides of the thin dielectric layer in the asymmetric configuration, as shown in Figure 7.1. Both electrodes have straight edges producing a uniform spanwise discharge, and thus, a 2D velocity profile. The dielectric material used in this study is Kapton (7700 VPM @ 25 °C). Each actuator has 1 layer of Kapton-FN (FEP layered Kapton) and 4 layers of Kapton-HN with a total thickness of ~330 μm (including the adhesive). The DBD actuator is installed on the 6″ by 8″ acrylic plastic sheet. The ground electrode (copper, 50 μm thick, 25 mm long, 110 mm wide) is flush-mounted on the acrylic plate. This encapsulation prevents plasma formation on the lower side of the dielectric material. The upper electrode (copper, 50 μm thick, 15 mm long, 110 mm wide) is glued onto the top of the Kapton dielectric layer. There is no overlap between the electrodes in the x-direction. The high-voltage (HV) electrode is exposed to atmospheric pressure air. The air-exposed HV electrode is connected to a Trek PM04014 power supply that provides up to 20 kV AC high voltage. The voltage and frequency were varied from 12 kV – 19.5 kV and 0.5 kHz – 2 kHz. This paper will use the coordinate system established in Figure 7.1.

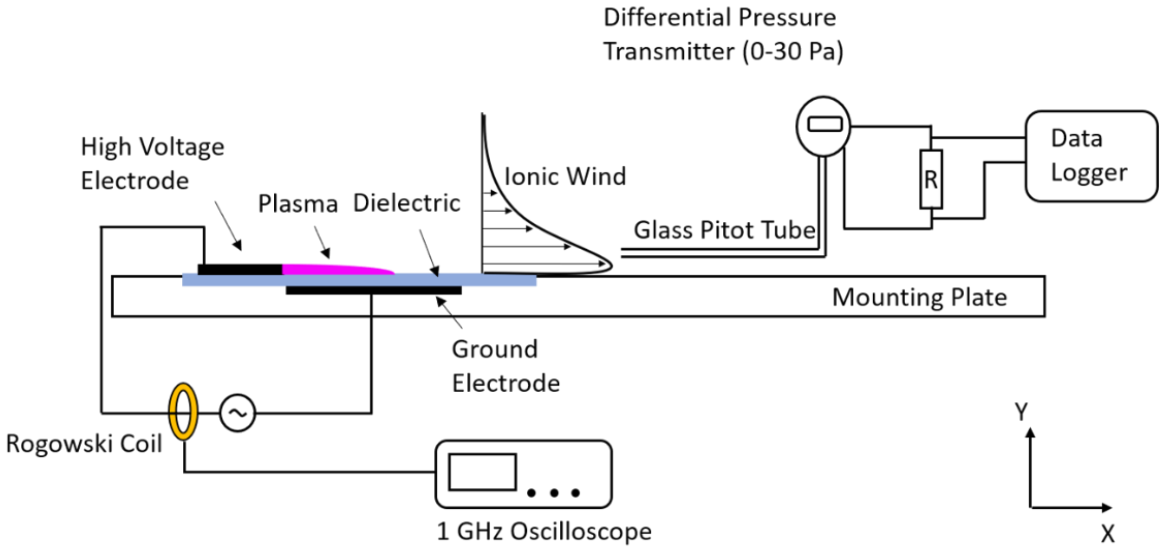

Figure 7.1. Schematic of the dielectric barrier discharge (DBD) plasma actuator. The plasma actuator is mounted on an acrylic glass plate, and the blue region is the dielectric layer separating the electrodes. The velocity is measured using a custom-built glass pitot tube, and the electrical characteristics are measured using a Rogowski coil.

7.1.2 *Plasma volume characterization*

Optical measurements can be employed to reveal the light emitted during the plasma actuation, and they can be used to characterize the plasma area or projected plasma volume region. Previous studies have explored the one-dimensional plasma length and the plasma length's temporal evolution [96, 99, 116]. The plasma region is captured using a camera, and thresholds are used to identify the plasma regions. Figure 7.2 below illustrates the plasma volume projection onto the x-y plane during the typical operation of the actuator. The threshold for this analysis is chosen to be 98% spectral intensity.

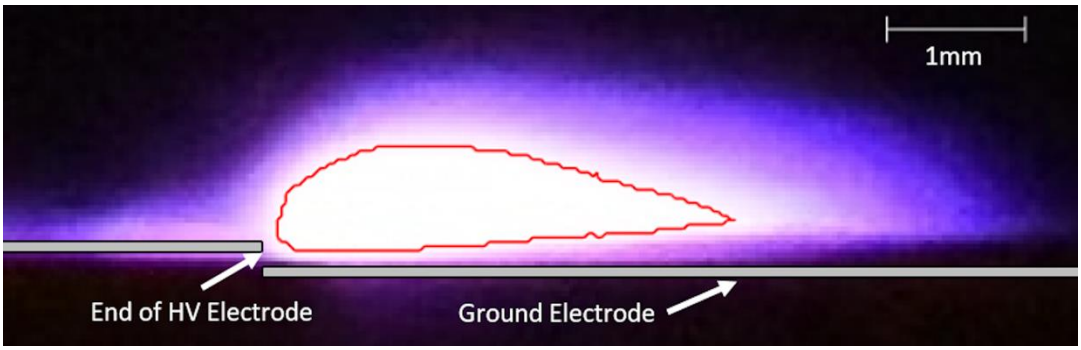

Figure 7.2. Plasma discharge region of DBD actuators at 12 kV and 2 kHz. A 98% threshold is outlined in red to calculate the plasma length and volume.

7.1.3 *Electrical measurements and signal processing*

In a DBD, the electric current flowing into the circuit can be viewed as the superposition of a low-frequency capacitive current and a discharge current. The discharge current is associated with plasma microdischarges, and they appear as a series of fast current pulses [212], as shown in Figure 7.3 (a). The current measurements are done using a 200 MHz bandwidth non-intrusive Pearson 2877 current monitor with a rise time of 2 ns. The current probe is placed around the wire driving the active electrode. The current monitor is connected to a Tektronix DPO 7054 oscilloscope that uses a bandwidth of 500 MHz to satisfy the Nyquist theorem by achieving a sampling rate of 1 GS/s. These conditions are essential for accurate capture of individual discharges that have been shown to occur on average over a 30 ns duration [121]. The high bandwidth and the sampling rate minimize the noise during the current measurements and can be used to compute the time-averaged electrical power [52]. A voltage from the power supply is also simultaneously displayed on the oscilloscope. Figure 7.3 (a) below shows a typical DBD current measurement with a voltage curve. Notation for positive discharge (PD) and negative discharge (ND) indicate the semi-cycles when voltage is rising or dropping, respectively.

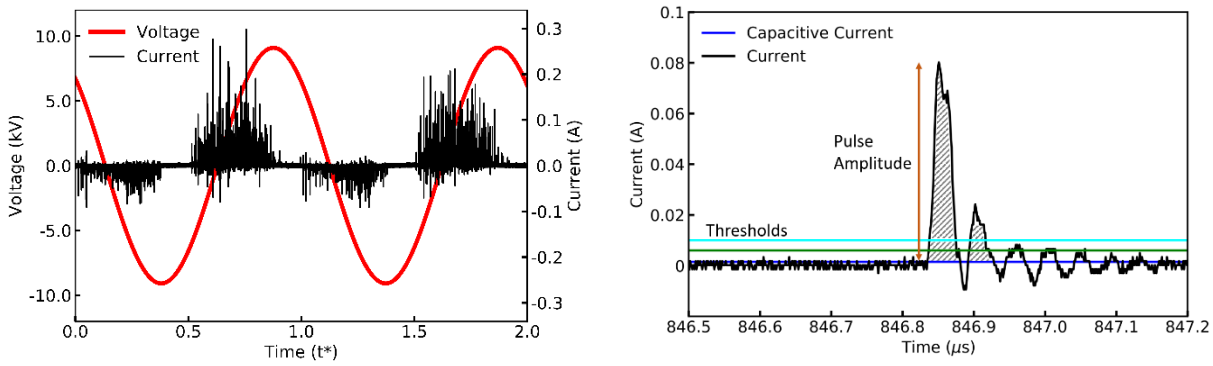

(a) (b)

Figure 7.3. (a) An example of DBD current at V=18 kV (p-p), f=1 kHz (b) Single microdischarge pulse in the positive phase with the underlying capacitive current (blue line) with two thresholds to characterize the microdischarge: (i) threshold of 6 mA (green line), (ii) the minimum pulse amplitude threshold of 10 mA (cyan line) for distinguishing a microdischarge. The brown arrow and the shaded region are examples of pulse amplitude and area respectively. The integration of the shaded area determines the charge associated with each discharge pulse.

To determine the current associated with the plasma microdischarges, we separate the capacitive current (displacement) from the raw signal. Several researchers have explored the capacitive current through analytical methods using a sinusoidal fit [113, 213]; others have removed the capacitive current through signal processing methods, including low-pass filters or Fast-Fourier Transform (FFT) [116, 121, 212]. In this study, we identify the capacitive current by considering the first 15 Fourier modes. The discharge current, the fast current events due to plasma microdischarges, appears as pulses emerging from a noisy baseline. Figure 7.3 (b) shows a current spike in the positive phase and the capacitive current and threshold to identify discharge current pulses. The capacitive current is used as a baseline to evaluate the intensity of the peaks. Two thresholds are introduced to reduce the effects of noise: (i) a threshold of 6 mA to evaluate the

intensity of peaks, shown as a green line, and (ii) the minimum pulse amplitude threshold of 10 mA represented by a cyan line. The thresholds are applied during the analysis of the raw data. The method allows to compute the charge generated by the current pulse and discharge current per unit time. The current data is analyzed for every 15 ns.

The DBD consists of positive and negative corona type discharges in the respective semi-cycles when the applied frequency is low [94]. In the first approximation, the discharge-flow interaction of an asymmetric DBD can be analogous to structure to corona discharge [132, 214], though the transient behavior, dielectric heating, and the alternating field add significant complexity to the problem. The conceptual representation of the EHD system includes (i) gas ionization region, (ii) flow acceleration region where unipolar ion motion in the gas medium acts as a body force accelerating the flow, and (iii) momentum conservation region dominated by the inertial and viscous terms of the NSE. These regions do not necessarily have clear boundaries; however, they can be characterized based on the field-ions-flow interaction dominant in each of them [6]. Previous analysis found that the thrust force induced from a DBD actuator is proportional to the energy consumption [123, 215]. The thrust force induced by ions is directly proportional to the discharge current or ion current in corona discharge [5]. For model development, an empirical relationship similar to Townsend's quadratic relationship can be used as a starting point to model discharge current [6, 52]. We can use the modified corona discharge energy consumption (W) equation to determine the discharge current of the actuator in Eq.(7.1)

$$W \sim f_{AC} C_{\mathrm{o}} (\varphi - \varphi_{\mathrm{o}})^2, \tag{7.1}$$

where C_o is the capacitance of the electric circuit, f_{AC} is the applied AC frequency, φ and φ_o are the applied and initiation voltage. We have assumed a power-law relation with frequency for the discharge current, as shown in Eq.(7.2)

$$I_{dis} \sim {f_{AC}}^{\alpha} C_o(\varphi - \varphi_o)^2, \tag{7.2}$$

where α is the AC frequency effect on the discharge current. The capacitance of the DBD actuator with charges temporally on the surface is hard to determine, so Eq. (7.2) is rewritten as

$$I_{dis} = {f_{AC}}^{\alpha} K(\varphi - \varphi_o)^2, \tag{7.3}$$

where K is the empirical constant similar to C_1 in Townsend current relationship $I_{dis} = C_1\varphi(\varphi - \varphi_o)$. The empirical relation in Eq. (7.3) can be used to determine the expressions for total discharge current, PD and ND currents, and we can evaluate the microdischarge properties in both cycles. The onset voltage of the corona discharge is determined using Peek's law [216]. The value of φ_o is determined from modified Peek's law [123] as shown in Eq.(7.4)

$$\begin{aligned} \varphi_0 &= m_v g_v \left(\frac{t_e}{2}\right) ln\left(\frac{2t_d + t_e/2}{t_e/2}\right), \\ m_v &= 1, g_v = 31\left(1 + \frac{0.308}{\sqrt{t_e/2}}\right), \end{aligned} \tag{7.4}$$

where t_e and t_d are the thickness of the electrode and dielectric layer, respectively. In this form, the equation can account for the effect of the variables contributing to the initiation voltage. The value of φ_0 is calculated to be 4.75 kV, and it agrees with previous experimental estimations of 5 kV, 7.5 kV and 10 kV and dielectric thicknesses of 0.15 mm, 3.18 mm and 6.35 mm, respectively

[135]. The φ_o value is used for developing different power-law relationships for the discharge current, the plasma volume, and the momentum induced by the wall jet.

7.1.4 *Wall jet characterization*

The flow field induced by ions characterizes the fluid mechanical properties of the plasma actuators. To measure the time-averaged ionic wind velocity, we employ a custom-made glass pitot tube with a 0.4 mm inner diameter and 0.5 mm outside diameter. Compared to traditional stainless steel pitot tubes, the glass tube minimizes electrical interaction with the discharge. This method has been previously used to characterize plasma actuators' performance [96, 212, 217]. The pitot tube mounted to an optical table and controlled in the x and y-axis, is connected to a Furness Controls FCO354 differential pressure transmitter (0 – 30 Pa) connected to a data logger. In this experiment, only x-velocity measurements are taken at varying x positions (10 mm, 15 mm, 40 mm, and 75 mm) downstream on the active electrode edge. At each x position, the y-velocity profile is obtained from the surface to 6 mm above the plate at increments of 0.25 mm or 0.5 mm (at a higher location). The DBD actuator's total momentum per meter spanwise can be found from the following expression

$$M = \rho \int_{y=0}^{y=\infty} U^2(y)dy. \tag{7.5}$$

7.2 Results and Discussion

7.2.1 *Effect of voltage and frequency on the plasma volume*

In this section, the impacts of voltage and frequency on the effective plasma region are discussed. Figure 7.4(a) presents the plasma length, measured from the edge of the plasma actuator to the furthest point downstream, as a function of voltage (12 kV – 19.5 kV) at varying frequencies

(0.5 kHz – 2 kHz). The plasma region measurements are time-averaged of at least four images for each condition. Recent studies have explored the discharge's temporal difference in the positive and negative cycles [218]. It is possible the plasma volume changes between the PD and ND, and the limitation of this work is that the photographs' exposure time (1/3 s) does not allow to capture of transient phenomena. For that reason, the individual contributions of PD and ND are not analyzed in this work, and only total discharge current is used in the empirical correlations. The results support previously reported results, both experimental and numerical, that plasma length increases linearly with applied voltage [99, 113]. However, increases in frequency appear to asymptotically increase plasma lengths until 2 kHz. This asymptotic limit may correspond to the asymptotic limit between the max velocity and frequency at similar voltages where max velocities did not increase after frequencies larger than approximately 2 kHz [94]. However, Orlov reported the plasma length asymptotically approaches a limit at approximately 6 kHz while at 5 kV [113]; thus there may be different asymptotic limits with varying dielectrics and electrode configuration. At our maximum conditions of 19.5 kV and 2 kHz, the dielectric layer breakdown occurred after 60 min of operation, which was not often sufficient to take the entire set of the velocity data; thus, we did not explore higher frequency conditions. It was possible to operate the actuator at lower voltages and higher frequencies and then develop universal power-law equations. However, as we attempted to maximize the momentum injection, this exploration is out of the paper's scope, and further experimentation at a broader range of frequencies is necessary.

While the physical mechanisms such as ion recombination may play a role in limiting the plasma length, the thickness of the dielectric material has been previously noted to play a significant role in plasma extension length. These results support previously reported lengths between 3 mm and 8 mm when the dielectric is less than 1 mm [96, 99, 153]. Thicker dielectrics

have seen plasma lengths up to 20 mm, and thus the asymptotic nature of Figure 7.4(a) may be due to the limiting length or thickness of the dielectric or the underlying ground electrode [96].

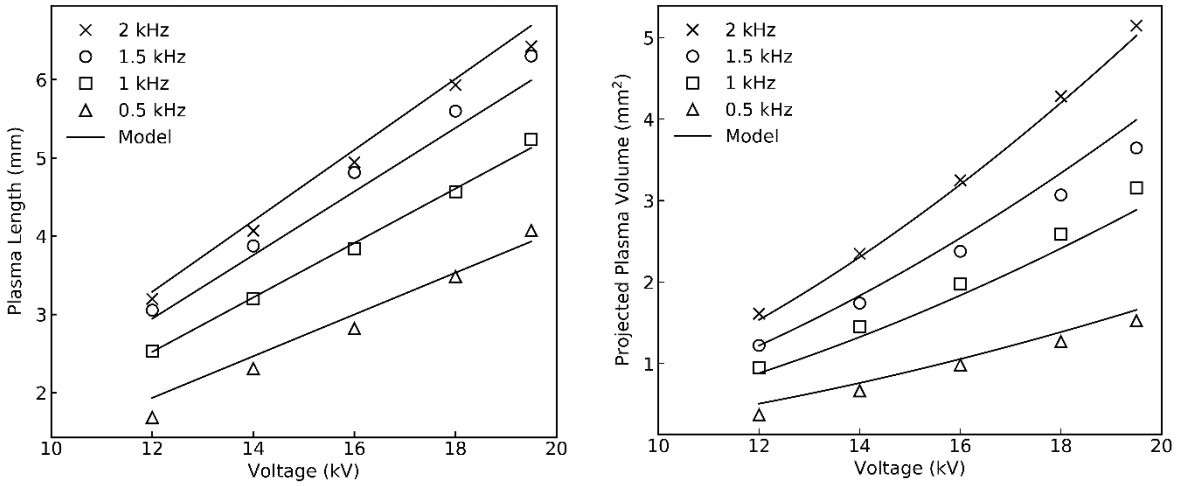

(a) (b)

Figure 7.4. Experimentally evaluated (a) plasma length and (b) projected plasma volume increase as a function voltage. Plasma length reaches an asymptotic value with frequency, but the plasma volume continues to increase.

Figure 7.4(b) presents the plasma volume, from the summation of pixels in the total effective plasma region, as a function of voltage (12 kV – 19.5 kV) at varying frequencies (0.5 kHz – 2 kHz). Our results suggest that the volume varies quadratically with the applied voltage. Interestingly, the plasma volume continues to grow with frequency up to 2 kHz, whereas the plasma length approaches a limit at 2 kHz at these operating conditions due to continued growth in plasma height. The results suggest that the plasma length to height ratio, L/H, remains approximately constant at 5.2 for the voltages and frequencies of this study. The results also agree with the half-Gaussian distribution reported in previous studies for other conditions [96, 150]. The Gaussian profile in the x and y directions is difficult to link to a physical mechanism outside of

time-averaged space charge interactions and electric field interactions with the dielectric. The L/H reduces to ~ 5.07 for the highest frequency, influencing the spatial distribution of body forces acting on the fluid and thus the resulting wall jet profile. Though the space charge distribution changes (shape of the ionization region), the preliminary analysis (See Figure 7.7) shows that average charge density does not change significantly between 1 and 2 kHz.

The empirical expressions for the plasma length and height can be determined through curve fitting. In this voltage range, plasma length (L_P) is found to vary linearly with voltage and by power-law with frequency as expressed in Eq. (7.6) and plasma volume (V_P) is found to exhibit a power-law relationship with both voltage and frequency as expressed in Eq.(7.7)

$$L_P = K_1 {f_{AC}}^{\alpha_1} (\varphi - \varphi_o), \tag{7.6}$$

$$V_P = K_2 {f_{AC}}^{\alpha} (\varphi - \varphi_o)^{\gamma}. \tag{7.7}$$

In numerical modeling for a source term, one needs to define the volume of charge injection. A gaussian ion-concentration distribution can then be applied to the empirical plasma length and height, and this relationship eliminates the dependency on a guessed Debye length. Subsequent coupling of body force and the Navier-Stokes equation allows for modeling the EHD force term.

7.2.2 *Discharge current characteristics*

Temporally resolved current measurements allow characterizing the microdischarges for both the positive and negative cycles. During the microdischarge, the charged species are transported towards the electrodes, thus generating an electrical signal in the form of a pulse superimposed on a slow-moving capacitive current. The latter can be subtracted, and the current associated with microdischarges can be analyzed. In the PD portion of the cycle, the electrons move towards the

exposed electrode, and in the ND, the electrons move towards the ground. We calculate the charge transported in each microdischarge and the total transported charge by adding up the contribution of each current microdischarge; the total discharge current is shown in Figure 7.3(b). The discharge current is normalized by a unit time. Previous work showed that a net charge of 40 nC is transported in a positive discharge cycle at 8.5 kV [116] and 10 nC is transported in a negative discharge cycle. As a comparison, we have observed a charge transport of 45 nC in PD and 15.3 nC in ND at 12 kV, 500 Hz. The discharge current is calculated for both PD and ND, and the net discharge current is calculated by adding both cycles. The experimental data is shown in Figure 7.5.

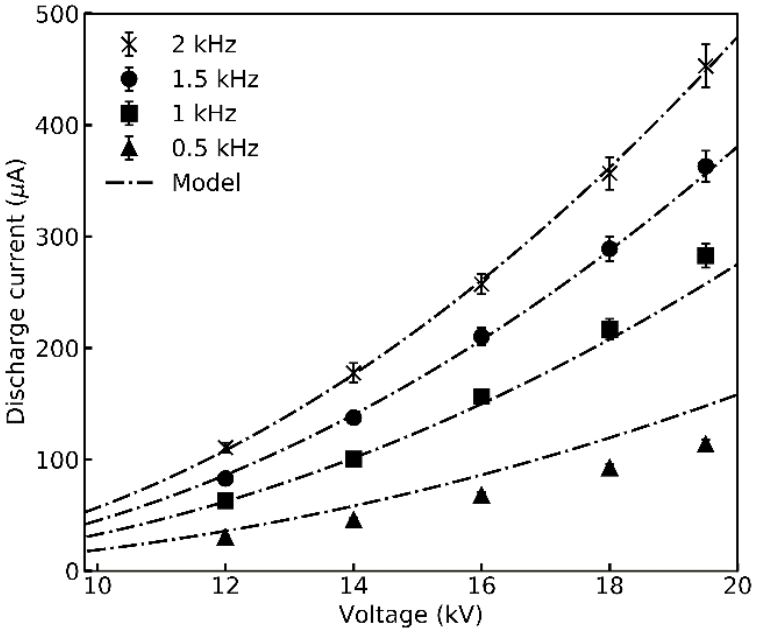

Figure 7.5. Discharge current as a function of applied voltage and frequency for the experimental data.

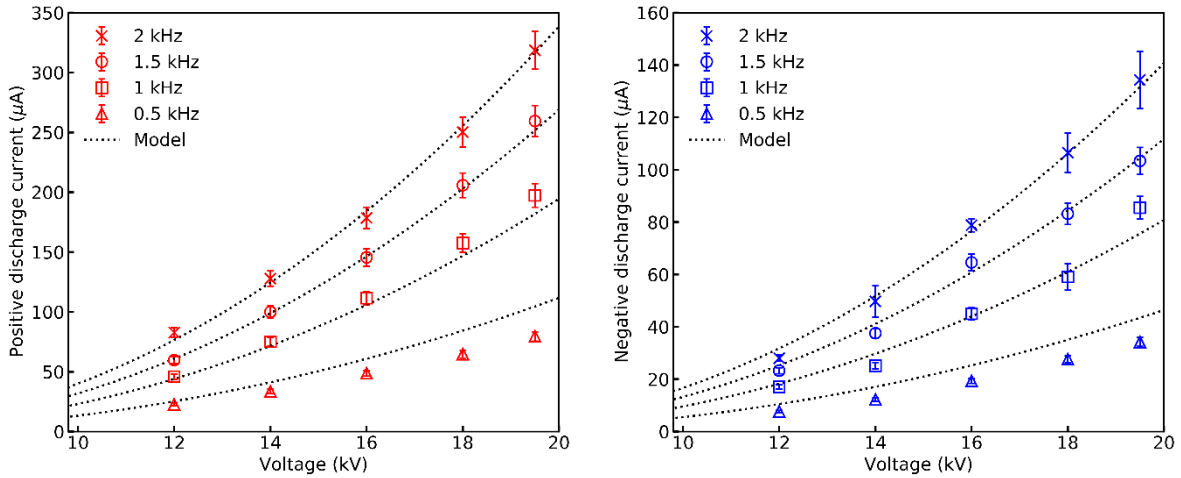

Figure 7.6. Discharge current as a function of applied voltage and frequency for the experimental data. The current varies quadratically with applied voltage, and the power-law relationships for positive and negative discharge current predict the values accurately.

The relationships for the discharge currents are obtained by comparing the experimental results and using the expression in Eq. (7.3). The I_{dis} versus φ trends are similar to previously reported quadratic trends in the literature [5, 115, 124]. As expected, the discharge current increases when the frequency increases since the number of cycles increase with the increase in frequency. However, the discharge current cannot continuously increase with the increase in frequency because the build-up of charges on the dielectric surface tends to dampen the charge transport. The model agrees with the experimental results at all voltages and frequencies within ~10% error. The large asymmetry is due to the number of current pulses in each cycle and the different mean charge transported by a single discharge [116]. The positive and negative discharge current models as shown in Eq.(7.8) and Eq. (7.9) are used to compare the empirical model and experimental data

$$I_{dis\_PD} = K_3 {f_{AC}}^{\alpha} (\varphi - \varphi_o)^2, \tag{7.8}$$

$$I_{dis\_ND} = K_4 {f_{AC}}^{\alpha} (\varphi - \varphi_o)^2, \tag{7.9}$$

where I_{dis_PD} and I_{dis_ND} are the discharge currents associated with positive and negative discharge, K_3 and K_4 are the empirical constants. In our experiments, the ratio of the K_3 and K_4 is 2.5, such as the positive discharge current is 2.5 times greater than the negative discharge current, as shown in Figure 7.6.

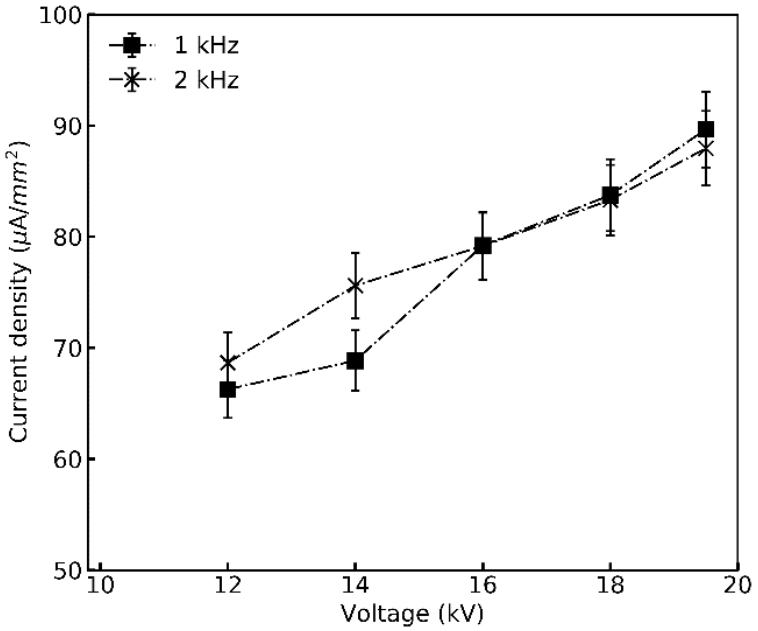

Figure 7.7. Current density for total discharge current and the current density remains the same for the two applied frequencies.

We calculate the current density from the discharge current and plasma volume. In Figure 7.7, the charge densities are plotted for 1 kHz and 2 kHz at varying voltages from 12 kV – 19.5 kV. The current density increases linearly with voltage in our experimental range. However, the current density is independent of frequency. The empirical relationships developed in the present study can be used to determine the charge density. In previous work, the simulation's charge density input is “tuned” to match the velocity profiles measured experimentally using an iterative approach

[219]. The discharge current and discharge volume computed in this manuscript can be used as input parameters for a numerical model, addressing time-resolved flow and detailed species transport modeling. The expressions in Eq. Eq.(7.8) and Eq. (7.9) can be used to gain insight into the momentum transfer process in positive and negative cycles.

7.2.3 *Relationship between discharge current and momentum*

Analysis of wall jet momentum arguably is more important for the characterization of the wall jet. It is also less susceptible to errors associated with probe positioning and geometry as multiple data points are taken at each x location. Figure 7.8(a) shows the DBD wall jet momentum calculated using equation (7.5) at x = 15 mm. The x = 10 mm location is not used; for the 19.5 kV condition, the 10mm case had lower velocities than 15 mm. This is likely due to (i) probe interaction with plasma volume (plasma length ~ 7 mm), (ii) the flow was still accelerating (X >1) where the ratio of Coulombic force and an inertial term in the Navier-Stokes equation is presented as a nondimensional parameter *X*. Excluding the 19.5 kV case, the momentum calculated at x = 10 mm is nearly identical to the momentum calculated at x = 15 mm. The momentum increases with the applied voltage and frequency for all studied conditions.

To understand the relationship between the fluid dynamic and plasma discharge, the induced wall jet momentum induced is plotted against the voltage and discharge current in Figure 7.8. As expected, the increase in voltage and frequency leads to higher momentum. We do not have sufficient data to quantify the trend. However, the comparison of momentum and total discharge current combines both frequency and voltage effects, reducing the data to a single line. In this analysis, only 8 data points are included over a relatively narrow range of frequencies. The least-square fit shows that the momentum increases linearly with the discharge current, as shown in

Figure 7.8(b), and it can be approximated by Eq. (7.10). From a mechanistic perspective, this is intuitive as the larger plasma volume, higher ion concentration, and stronger E-field lead to a greater number of ion-neutral molecule collisions accelerating the flow. The relationships linking frequency and voltage to discharge current are presented in Eq. (7.3). The obvious observation is that the planar DBD actuator can produce a higher momentum discharge current is maximized. The reduced-order model for DBD wall jet momentum is given by the following expression,

$$M = \beta K {f_{AC}}^{\alpha} (\varphi - \varphi_o)^2. \tag{7.10}$$

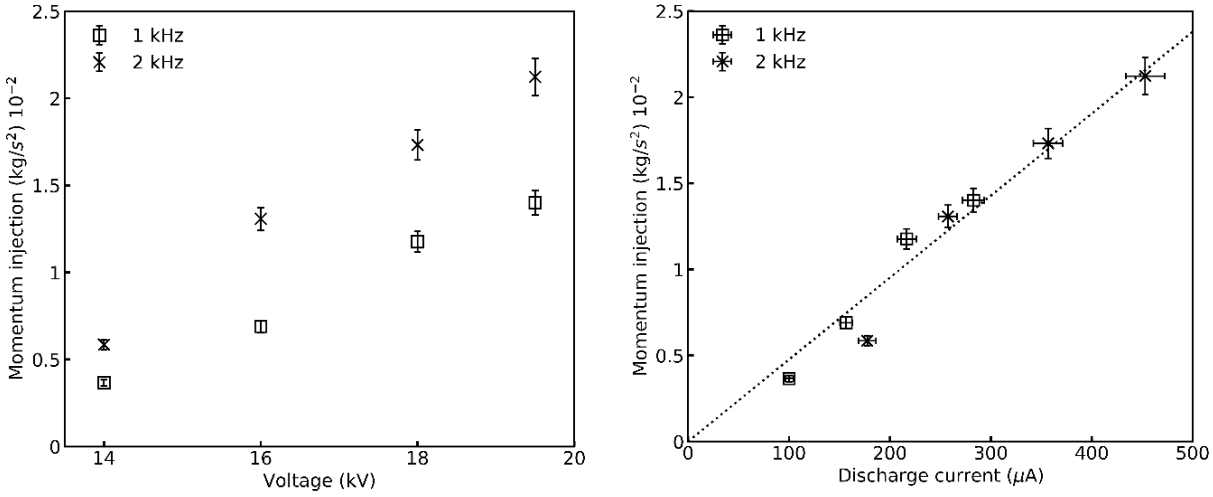

(a) (b)

Figure 7.8. Momentum of the wall jet vs. (a) voltage and (b) discharge current. The wall -jet momentum collapses onto a single line for both frequencies and is directly proportional to the discharge current.

The coefficients of this model are likely to depend on the electrode configuration and the properties of the dielectric media. It is also possible that the assumption of momentum being directly proportional to discharge current would break down at higher frequencies [123], and the exponents in the power-law relationship would change. At this time, we do not have sufficient data

to extrapolate the model to these conditions. Table 7.1 summarizes the formulation of the reduced-order model for asymmetric DBD actuator developed from the experimental measurements for the range φ = 12 – 19.5 kV, f_{AC} = 0.5 – 2 kHz. The data can be used for development and validation of reduced-order expressions and high-fidelity numerical models.

Table 7.1. Model parameters used for state of the art and the current work.

Property	Expression	Coefficients
Plasma length (L_P)	${K_1 f_{AC}}^{\alpha_1}(\varphi - \varphi_o)$	$K_1 = 2.35 \times 10^{-2}$ $\alpha_1 = 0.39$ $\varphi_o = 4.75$ kV
Plasma volume (V_P)	${K_2 f_{AC}}^{\alpha}(\varphi - \varphi_o)^{\gamma}$	$K_2 = 1.29 \times 10^{-4}$ $\alpha = 0.8$ $\gamma = 1.67$
Total discharge current (I_{dis})	${K f_{AC}}^{\alpha}(\varphi - \varphi_o)^2$	$K = 4.71 \times 10^{-3}$
Positive discharge current (I_{dis_PD})	${K_3 f_{AC}}^{\alpha}(\varphi - \varphi_o)^2$	$K_3 = 3.33 \times 10^{-3}$
Negative discharge current (I_{dis_ND})	${K_4 f_{AC}}^{\alpha}(\varphi - \varphi_o)^2$	$K_4 = 1.38 \times 10^{-3}$
Momentum (M)	${\beta K f_{AC}}^{\alpha}(\varphi - \varphi_o)^2$	$\beta = 4.76 \times 10^{-3}$

7.3 CHAPTER SUMMARY

We developed a reduced-order model for discharge current, current density, and momentum injection utilizing the data from the DBD actuator, i.e., plasma volume, electrical discharge current, and resulting momentum over a range of voltage (12 kV – 19.5 kV) and frequency (0.5 kHz – 2 kHz). The plasma length increases linearly with voltage, matching other previous studies, and the plasma volume is found to vary quadratically with voltage. The plasma volume continues to grow with a frequency up to 2 kHz, whereas the plasma length approaches a limit at 2 kHz at

these operating conditions. The increase in volume is due to continued growth in plasma height, suggesting that plasma volume can be a better input in CFD modeling.

The current associated with microdischarges was measured using a Rogowski coil with high temporal resolution. The charge transported in each microdischarge and the corresponding discharge current were calculated for both PD and ND semi-cycles. The discharge current analysis yielded a power law for the positive and negative discharge current associated with microdischarges in the form $I_{dis} = Kf^{\alpha}(\varphi - \varphi_o)^2$. Comparing the expressions, there is an asymmetry in the discharge currents between positive and negative cycles. The current density was calculated using discharge current and plasma volume. The discharge current density increases with voltage, and it is independent of frequency.

The discharge current expressions can be used for CFD calibration and assigning boundary conditions providing a more robust estimation of charge density and the discharge volume. The PD and ND semi-cycle current expressions can be used to understand each semi-cycle relative contribution to the momentum. In time-resolved modeling, these data can be used for model validation, providing insight into the nature of ion/field/flow interaction at each point of the AC cycle. The discharge current expressions and baseline velocity were used to develop a reduced-order model of DBD momentum injection, and the analysis of the plasma volume can be used in multiphysics modeling of the DBD. Empirical data for plasma volume correlates with EHD body force; it allows to improve the simplified DBD models. The simplified DBD model benefits from simulating plasma body force while eliminating the dependency on estimations based on the Debye length and charge density.

Chapter 8. DBD – DCA PLASMA ACTUATOR: EFFECT OF THIRD ELECTRODE

This chapter aims to demonstrate the advantage of a DC augmented dielectric barrier discharge (DBD – DCA) and to characterize its thrust and efficiency. Thrust force associated with the induced wall jet is measured in quiescent conditions over a range of input parameters, i.e., AC voltage, frequency, and DC voltage. The effects of positive and negative DC voltage on thrust augmentation are compared to the standard two-electrode DBD. The effectiveness of the actuator is evaluated for several operating conditions.

8.1 Experimental Methods and Diagnostics

8.1.1 *Plasma Actuator and Discharge Generation*

In this experimental study, two types of plasma actuators have been considered (a) DBD actuator and (b) DBD – DCA actuator. Both actuators have two 0.05 mm thick copper electrodes, one exposed electrode, and one encapsulated electrode separated by a dielectric material, as shown in Figure 8.1. All the electrodes have straight edges producing a uniform spanwise discharge. Each actuator has four layers of Kapton – HN and one layer of Kapton – CRC (corona resistant) with a total thickness of ~ 300 μm (including the adhesive). The plasma actuator is installed on the 0.15 m by 0.2 m flat polylactic acid polymer (PLA) plate. The exposed electrode of length 15 mm is glued onto the top of the Kapton dielectric layer. The ground electrode (encapsulated electrode) of length 25 mm is flush-mounted on the PLA flat plate. This encapsulation prevents plasma formation on the lower side of the dielectric material. There is no overlap between the exposed and encapsulated electrodes.

In DBD – DCA arrangement, the third electrode has a length of 25 mm; it is placed 25 mm downstream of the ground electrode, as shown in Figure 8.1(b). The spanwise width of all the electrodes is 100 mm. The actuator is installed at 10 mm from the leading edge of the flat plate.

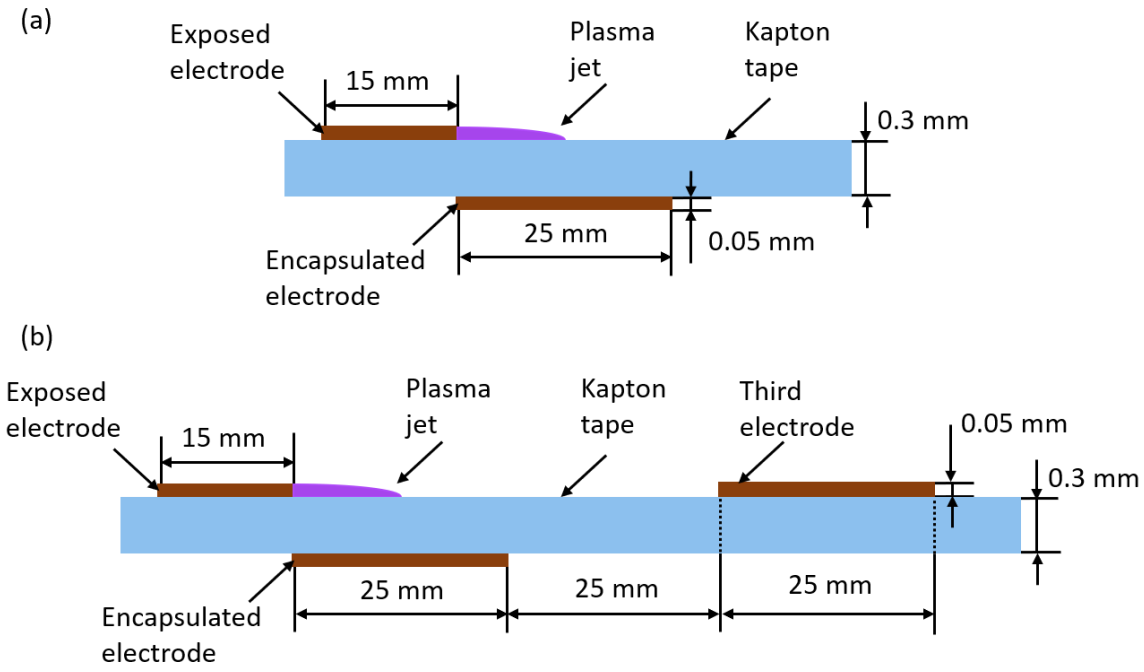

Figure 8.1. Schematic of (a) DBD and (b) DBD – DCA actuator. The plasma actuator is mounted on a 3D printed plate, and the blue region is the dielectric layer separating the electrodes.

The exposed HV electrode is connected to a Trek PM0414 power supply that provides up to 20 kV AC high voltage. The electrical current is measured using a 200 MHz bandwidth non – intrusive Pearson 2877 current monitor with a rise time of 2 ns. The current probe is placed around the energized wire driving the exposed electrode. The current monitor is connected to a Tektronix DPO 7054 oscilloscope; the data is acquired at a sampling rate of 1 G/s. The voltage from the power supply is also obtained simultaneously. The electrical power consumed by DBD is calculated by multiplying the voltage and current at each point in the time series and averaging

over a period. The time-averaged electrical power consumption by the actuator can be computed as

$$W_e = f_{AC} \int_0^t \varphi_{AC}(t) i(t) dt \tag{8.1}$$

where f_{AC} is the frequency of the applied voltage in Hz, and $\varphi_{AC}(t)$ and $i(t)$ are respectively the voltage and current at each point in the period. More details on current measurement can be found in Section 7.1.3. The voltage and frequency were varied from 12 kV – 19.5 kV and 1 kHz – 2 kHz. The third electrode is connected to HV DC power supply (Bertan 205B-20R) with variable DC voltage (0-18 kV); the DC current is measured directly from the power supply. The time averaged electrical power consumed by the DBD – DCA actuator can be computed by adding the power consumption from AC and DC as shown in Eq.(8.2)

$$W_{e\_DC} = W_e + \varphi_{DC} i_{DC} \tag{8.2}$$

where φ_{DC} and i_{DC} are DC voltage and current, respectively.

8.1.2 *Thrust Measurement Setup*

The thrust of the induced jet by the plasma actuator was measured as a reaction force. Figure 8.2 shows the schematic of the experimental setup for thrust force measurement. The actuator plate (~70 g) was suspended from an analytical balance Metler Toledo (AE 240) with 120 g capacity and 0.0001 g resolution. The electrical connections of the electrodes were established using a thin wire to minimize added weight. The flat plate was hung from a hook on the underside of the balance using cotton strings to electrically isolate the balance. The thrust was measured as a reduction in weight measured by the balance. To prevent ambient room air currents from

influencing the measurements, the entire setup was housed in a large quiescent chamber. A similar experimental setup was used to characterize the thrust generated by corona discharge [5] and dielectric barrier discharge [129]. The experimental procedure is as follows: (i) the high voltage is switched off and the mass of the plate is recorded (ii) the high voltage is switched on, and the difference in the mass measurements is determined, (iii) the experiment is repeated for the range of voltages and frequencies values at increments of 1 kV and 1 kHz respectively. The experiments were performed in a room with a temperature range of 22 ^{0}C – 25 ^{0}C, the relative humidity of 24% – 26% and ambient pressure. The frequency on the AC power supply is varied from 1 kHz – 2 kHz and for each frequency the peak-to-peak voltage φ_{AC} was increased from 12 kV (when the thrust force becomes measurable reliably) to 19 kV (power supply limit). For each input voltage, 5 measurements are recorded from the scale over a 60 s span once an initial stable reading was reached. The maximum error associated with the measurement is within 5%.

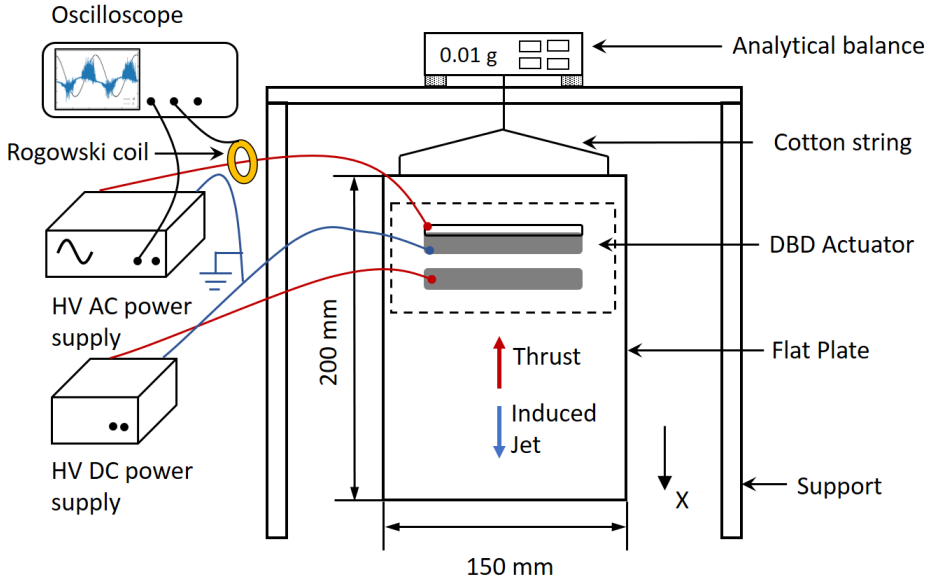

Figure 8.2. Experimental setup schematic for thrust force measurement.

8.2 RESULTS AND DISCUSSION

8.2.1 *Thrust characteristics of DBD*

The thrust force data is used to determine the momentum injection associated with the DBD wall jet. Figure 8.3 shows the thrust data for the range of φ_{AC} = 12 kV – 19 kV and f_{AC} = 0.5 kHz – 2 kHz. The thrust increases with φ_{AC} and f_{AC}, and follows a trend that is proportional to ${f_{AC}}^{\alpha}{\varphi_{AC}}^{2}$ as shown in Eq. (8.3), which agrees with the reported results in the literature [13, 137]

$$F_{EHD} = K_1 {f_{AC}}^{\alpha} (\varphi_{AC} - \varphi_o)^2 \tag{8.3}$$

where F_{EHD} is the force due to force induced by the ions, K_1 = 22.4 × 10^{-6} and α = 0.8 are experimental constants previously proposed in Ref [13], φ_o is the initiation voltage. At φ_{AC} = 18 kV and f_{AC} = 2 kHz, the thrust was at 12.46 mN/m for this experiment. Previous work reports a momentum injection of 17.3 mN/m based on the velocity measurements at X = 15 mm from the exposed electrode [13] (plate length ~ 40 mm). The measured thrust in this experiment (plate length = 200 mm) is the result of the momentum injection driven by EHD and viscous losses, so Eq. (8.3) is modified to account for viscous shear as shown in Eq. (8.4).

$$T = (1 - \theta)\, F_{EHD} \tag{8.4}$$

Here θ is a non-dimensionless quantity that accounts for the shear forces. The value of θ has to be less than unity and is dependent on plate length and other factors that are not studied here separately, such as electrode arrangement, plate roughness, etc. The experimental data can be used to determine θ in Eq. (8.4). Here, θ = 0.2 has the best correlation suggesting that in our experiment, the viscous drag on the 200 mm plate from the DBD wall jet is ~20%. Experiments by Durscher

and Roy also showed a 20% difference in the thrust measurements between 25 mm and 150 mm plate length [127].

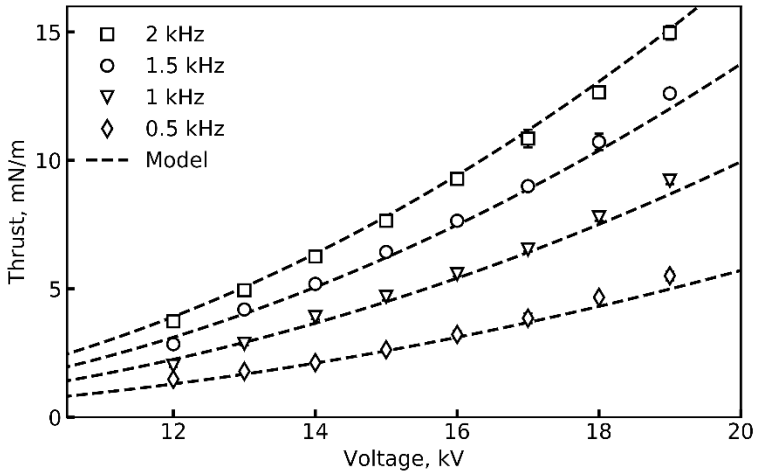

Figure 8.3. Thrust induced by the DBD wall jet as a function of input AC voltage and frequency. The data is compared with the empirical model with a correction factor (θ = 0.2) accounting for viscous shear.

8.2.2 *Thrust characteristics of DBD – DCA*

8.2.2.1 Grounded DCA electrode

The thrust of the DBD – DCA actuator with non-energized DC electrode (grounded) is compared with the two-electrode DBD actuator in Figure 8.4. The thrust results indicate a minimum difference (10%) at low input voltages with the addition of a third electrode. At the high voltages, an increase in thrust is more significant (~20 %). This increase is observed for both frequencies. At the maximum voltages tested, a difference of 1.96 mN/m and 3.45 mN/m was measured between DBD and DBD – DCA for 1 kHz and 2 kHz, respectively. This corresponds to a ~20 % increase in thrust for the DBD – DCA actuator. The mechanism for thrust increase

associated with the third ground electrode needs further investigation. Two complementary effects that are likely to play a role:

i. Surface charge redistribution: The third electrode acts as a sink for the charges accumulated on the dielectric surface during each half – cycle reducing the parasitic effect of ions traveling upstream in the other half cycle.

ii. Ion acceleration due to E – field modification: The addition of a ground downstream of the ionization region modifies instantaneous electrical field shape, accelerating flow in the X-direction more efficiently. This effect is significantly enhanced in the energized DBD – DCA discharge, as described later in the manuscript. This also can be viewed as a reduction of losses due to space charge, as has been previously in corona discharge EHD flows [6, 7].

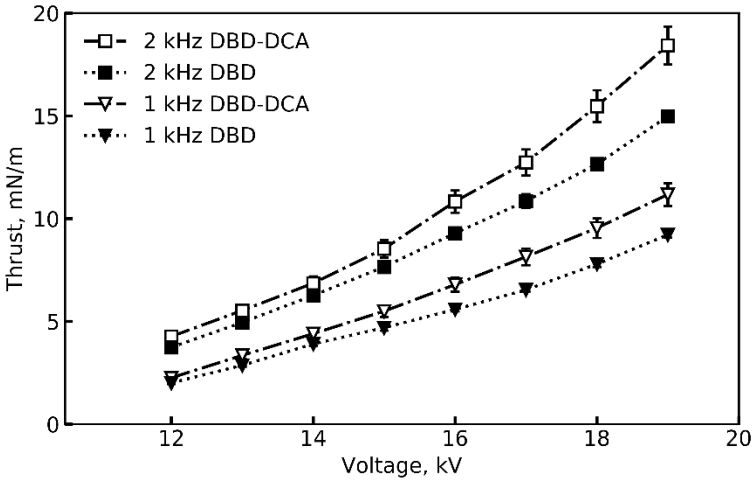

Figure 8.4. Thrust comparison between the DBD and the DBD – DCA with third electrode grounded as a function of applied voltage.

8.2.2.2 Effect of DC potential

Additional improvements in thrust can be obtained by accelerating the ions in the increasing E-field. Figure 8.5 shows the thrust force of the DBD – DCA plasma actuator at varied DC voltages and polarities. This plot shows that the thrust generated by the DBD – DCA depends on the applied DC voltage. Positive and negative DCA regimes can be identified. Similar to the grounded DBD – DCA discharge, the thrust increase can be attributed to several effects; however, we hypothesize that the primary mechanism stems from the greater acceleration of the opposite charge species during the corresponding half-cycle [165]. For example, species produced in the negative half cycle are more efficiently accelerated in the positive DCA configuration leading to an overall increase in thrust and vice versa.

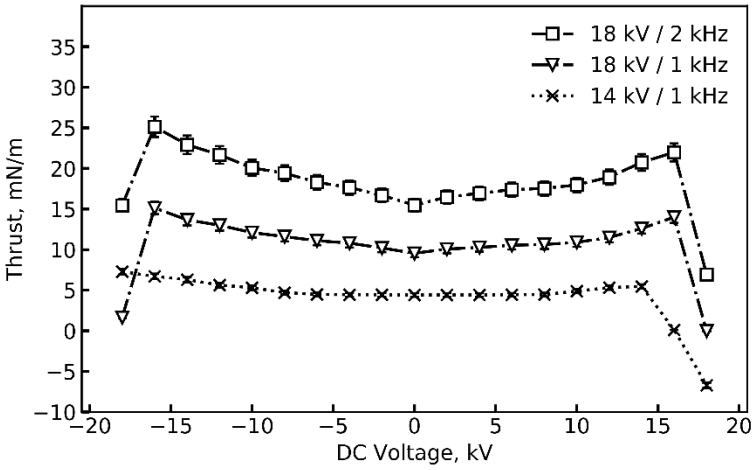

Figure 8.5. Thrust of the DBD – DCA plasma actuator as function of input DC voltage.

For positive DCA (i.e., $\varphi_{DC} > 0$), the thrust increases with the potential and reaches a maximum at $\varphi_{DC} = 14 \sim 16$ kV and drops to near zero or reverses direction in some cases. At φ_{AC} = 18 kV and f_{AC} = 2 kHz, the thrust reached ~22 mN/m at φ_{DC} = 16 kV, which is 1.73x higher than standard two-electrode DBD at the same conditions. In this case, only the transport of the negative discharge

is enhanced in the X-direction because of the electric field created between the exposed, the ground, and the positive DCA electrode. The thrust gained in the negative half-cycle is higher than the reduction in the positive half-cycle, resulting in an overall higher thrust. As the DC voltage increased further, the thrust is reversed. It is likely due to the onset positive discharge on the DCA electrode and subsequent generation of the EHD jet in the "− X" direction [131, 220].

In the negative DBD – DCA ($\varphi_{DC} < 0$) the thrust trends are similar as in positive DCA. The positive ions are accelerated towards the third electrode in the positive-going cycle. The thrust increases up to $\varphi_{DC} = -16$ kV, and sharply decreased when φ_{AC} = 18 kV, whereas it continues to increase when φ_{AC} = 14 kV case. The induced counter jet is formed later than in the positive DCA case. The mechanistic explanation for higher thrust achieved in the negative DCA is likely related to a greater abundance of positive species (i.e., higher discharge current) [13]. Secondary effects such as surface charge modification and lower recombination rates of charges may exist; however, these were not quantified in this work.

For both DC polarities, the thrust increase in the complementary half-cycle exceeds the reduction in another half cycle, increasing the overall thrust. Tang et al. has shown that the AC cycle is composed of positive and negative corona-type discharges, has a positive discharge current is 2.5x higher than that of negative discharge current [13]. The increase in the thrust is apparent in the negative DCA; however, it generates only 25% more thrust force than that of positive DCA. The likely explanation is that the negative semi-cycle generates a higher velocity than the positive one [94, 221].

The effect of frequency and AC voltage on thrust characteristics is also shown in Figure 8.5. The thrust is plotted for two voltages at a fixed frequency (1 kHz); not surprisingly, the higher

voltage case produces higher thrust due to a greater number of ionic species produced during discharge. The thrust increases with the DC voltage for φ_{AC} = 18 kV and peaks at 16 kV and −16 kV whereas for φ_{AC} = 14 kV case the thrust reaches a peak at 12 kV and it continuously increases with negative DC voltage. For a fixed voltage, the thrust increases with frequency, and the trends are almost similar for both frequencies. From these thrust characteristics, we can conclude that the major factors that could impact the thrust improvement are (1) E – field between the exposed and third electrodes and (2) change in discharge phenomena on the DCA electrode.

8.2.3 *Effectiveness of actuators*

The effectiveness of the actuators (ε) can be used as a metric for comparing the actuator performance. The effectiveness is defined as the ratio of the induced thrust to the consumed power as shown in Eq (8.5)

$$\varepsilon = \frac{T}{W_{elec}} \tag{8.5}$$

where T is the thrust force, W_{elec} is the electrical power consumption as calculated by Eq. (8.1) and (8.2). The effectiveness is an essential parameter in comparing which design configuration can achieve higher thrust while consuming less power [222]. The distinction between efficiency and effectiveness is described in refs [223, 224]. The effectiveness for DBD and DBD – DCA is compared in Table 8.1 at φ_{AC} = 18 kV for two different frequencies. The effectiveness is higher in the 1 kHz cases than in the 2 kHz cases due to the nonlinear effects with respect to frequency. The electrical power increases almost linearly with frequency [94, 115], but the thrust is proportional to ${f_{AC}}^{\alpha}$ as shown in Eq. (8.3), where coefficient α was experimentally shown to be less than unity. The electrical consumption of DBD at φ_{AC} = 18 kV for f_{AC} = 1 kHz and 2 kHz is equal to 58.5

W/m and 121.6 W/m respectively. From equation (8.5), the effectiveness of DBD is 0.133 mN/W at φ_{AC} = 18 kV and f_{AC} = 1 kHz. The calculated effectiveness agrees with the previous studies on DBDs [224]. The electrical power of DBD – DCA with ground DCA electrode is almost the same as DBD, while the effectiveness of DBD – DCA actuator is 20% more than the two-electrode DBD actuator. The addition of a ground DCA electrode leads to higher thrust for the same electrical power consumption. The power consumption for DBD – DCA at φ_{AC}= 18 kV and f_{AC} = 1 kHz with $\varphi_{DC} = 16$ kV and −16 kV is 60.7 W/m and 61.72 W/m respectively. The effectiveness for positive DBD – DCA at $\varphi_{DC} = 16$ kV increases by 73% and for negative DCA it increases by 84% at $\varphi_{DC} = -16$ kV compared to standard DBD. Based on this analysis, the DBD – DCA plasma actuator with negative DC voltage outperforms all the other cases.

Table 8.1. Comparison of effectiveness at different operating conditions for DBD and DBD – DCA at fixed AC voltage of 18 kV.

	1 kHz	2 kHz
DBD	0.133	0.104
DBD – DCA $\varphi_{DC} = 0$ kV	0.163	0.127
DBD – DCA $\varphi_{DC} = 16$ kV	0.230	0.176
DBD – DCA $\varphi_{DC} = -16$ kV	0.245	0.2

8.3 CHAPTER SUMMARY

The flow control performance of DC augmented dielectric barrier discharge (DBD – DCA) plasma actuator in quiescent air was studied over a range φ_{AC} = 12 – 19 kV for f_{AC} = 1 – 2 kHz. The body force generated by the actuator was determined by measuring the thrust of the EHD wall

jet in the X-direction. The DBD – DCA actuator has an additional exposed electrode, to which high DC voltage is applied. The DBD acts as an ionizer, and the third electrode is positioned downstream of the encapsulated electrode, thus creating a stronger E-field for accelerating the ions. The DBD – DCA with the grounded third electrode enhances the thrust by 20 % compared to standard DBD.

The effects of positive and negative DC voltage on thrust were parameterized. The thrust increases with the DC voltage reach a maximum; then, the thrust drops rapidly. For the same DC potential, the negative DCA produces 25% more thrust than the positive DCA. At φ_{AC} = 18 kV and f_{AC} = 2 kHz, a thrust force of 25.13 mN/m at φ_{DC} = − 16 kV, which was ~2x greater than the DBD actuator. The actuator's effectiveness (thrust to power ratio) was calculated for DBD and DBD – DCA over a range of operating conditions. The effectiveness of the DBD – DCA is 84% more than the two-electrode DBD plasma actuator.

Chapter 9. DBD – DCA PLASMA ACTUATOR: EFFECT OF ELECTRODE SHAPE

The advantage of the DBD – DCA plasma actuator compared to standard DBD is discussed in the previous Chapter 8. In this chapter, we introduce three different electrode shapes, and we compare the performance to the linear electrode. The electrical power consumption is evaluated based on the recorded electrical signals for all electrode shapes. The induced thrust is measured over a range of input parameters, i.e., AC voltage (φ_{AC}), frequency (f_{AC}), and DC voltage (φ_{DC}). The effects of positive and negative DC voltage on thrust augmentation for different electrode shapes are compared to the standard linear shape electrode DBD – DCA actuator.

9.1 EXPERIMENTAL METHODS AND DIAGNOSTICS

In this experimental study, a DBD – DCA plasma actuator with four different electrode shapes has been evaluated. The actuator consists of three 0.05 mm thick copper electrodes separated by a dielectric material, as shown in Figure 9.1. Each actuator has 4 layers of Kapton – HN and one layer of Kapton – CRC with a total thickness of ~300 μm. The plasma actuator is installed on the 0.15 m by 0.2 m flat polylactic acid polymer (PLA) plate. The exposed electrode of length L_1 mm is glued onto the top of the Kapton dielectric layer. Four types of electrode shapes are used: saw tooth – coarse & fine (Figure 9.2 (b) and (c)), fingers (Figure 9.2 (d)) and conventional linear shape (Figure 9.2 (a)). Figure 9.2 shows the plasma discharge of the actuators; the bright purple region shows the induced plasma. The contoured electrodes have greater plasma length compared to linear geometry. The plasma length for the linear, sawtooth – coarse, sawtooth – fine and finger-shaped electrodes are 100 mm, 220 mm, 412 mm, and 238 mm, respectively. The ground electrode of width (25+ L_2) mm is flush-mounted on the PLA flat plate, as shown in Figure 9.1. This

encapsulation prevents plasma formation on the lower side of the dielectric material. There is an overlap of L_2 mm between the exposed and encapsulated electrodes. The actuator design parameter variations are summarized in Table 9.1. The third electrode of length 25 mm is placed 25 mm downstream of the ground electrode. The spanwise width of all the electrodes is 100 mm. The actuator is installed at 10 mm from the leading edge of the flat plate.

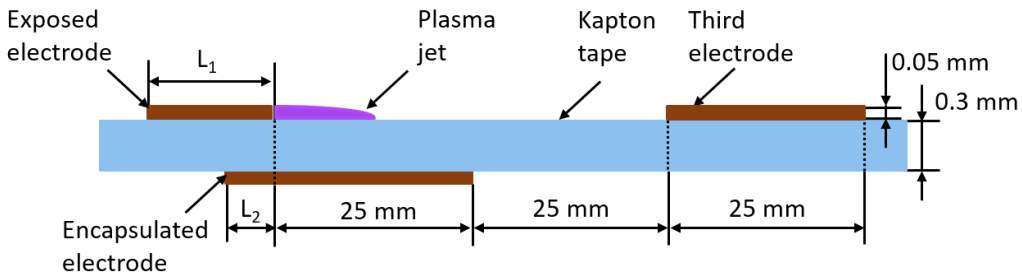

Figure 9.1. Schematic of DBD – DCA actuator. The length L_1 and L_2 are varied for different electrode shapes, and the plasma actuator is mounted on a 3D printed plate.

The exposed HV electrode is connected to a Trek PM0414 power supply that provides AC voltage and the encapsulated electrode is connected to the power supply ground line. The AC voltage (φ_{AC}) and frequency (f_{AC}) were varied from 12 kV – 19 kV and 1 kHz – 2 kHz. The third electrode is connected to the HV DC power supply (Bertan 205B – 20R) with a variable DC voltage (0 –18 kV) and polarity. The time-averaged electrical power consumed by the DBD – DCA actuator can be calculated using Eq. (8.2). More details on the electric measurements and power consumption can be found in 7.1.3 and 8.1.1. The thrust force is measured by an analytical balance Metler Toledo (AE 240) with 120 g capacity, 0.0001 g resolution and the flat plate was hung from a hook on the underside of the balance. The thrust was measured as a reduction in weight measured by the balance. Detailed experimental setup and procedure for thrust measurement is described in 8.1.2.

Table 9.1. Summary of geometric parameters of the plasma actuator in this study

Electrode shape	L_1 (mm)	L_2 (mm)	Plasma Length (mm)
Linear	15	0	100
Sawtooth - Coarse	15	10	220
Sawtooth - Fine	15	10	412
Fingers	20	15	238

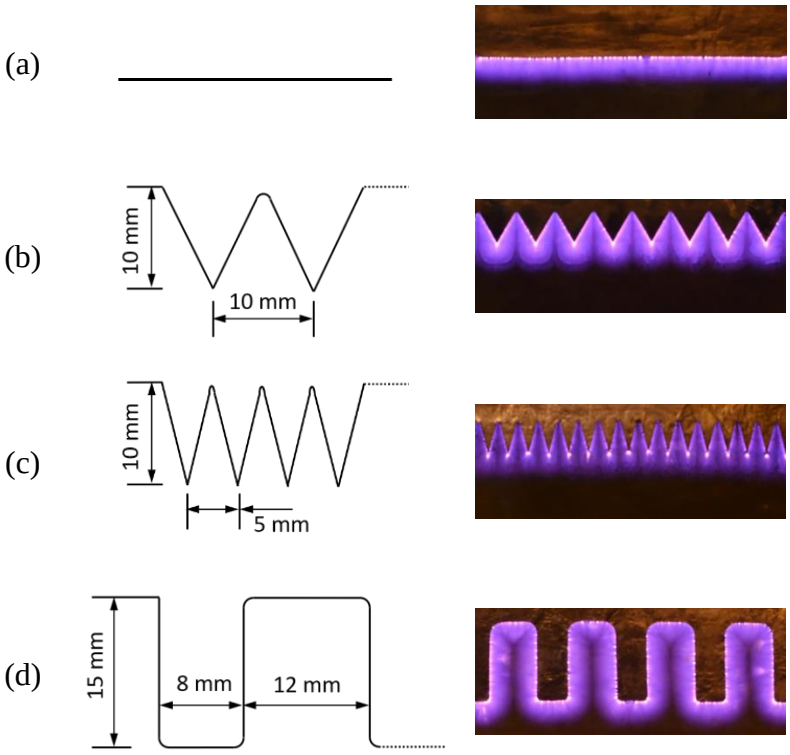

Figure 9.2. Schematics and discharge of shaped plasma actuators for (a) linear (b) sawtooth – coarse (c) sawtooth – fine and (d) finger designs.

9.2 RESULTS AND DISCUSSION

9.2.1 *Effect of electrode shape on power consumption*

To determine the effect of electrode shape on power consumption, the actuators are tested at a φ_{AC} = 18 kV and f_{AC} = 1 kHz & 2 kHz. The power consumption per unit width with different electrode shapes is presented in Figure 9.3 (a). The electrical power increases linearly with frequency for the linear electrode, whereas it has a power-law relation with frequency for other electrode shapes. The power per unit length for the sawtooth – coarse electrode is 10% and 28% higher than the linear electrode for 1 kHz and 2 kHz, respectively. The increase in the power consumption can be due to the greater plasma length. When the pitch of the sawtooth decreases, power consumption increases for both the frequency cases. The increment is 23% and 44% for 1 kHz and 2 kHz, respectively compared to the linear electrode and by 12.6% and 11.7% over coarse sawtooth. This confirms that when the pitch of the electrode decreases, the power consumption will increase due to the stronger electric field formed at the tip, as previously described by Gao et al [164]. The power consumption is the highest for the fingers electrode and is 57% and 96% more than the linear electrode for both frequencies. The entire contour of the electrode shape generates the plasma and the power consumption per plasma length is presented in Figure 9.3 (b). The maximum and minimum values are recorded for the linear electrode and fine sawtooth electrode with the shortest and longest plasma length compared to other electrode shapes. All contoured electrodes have lower power consumption per unit of plasma length than linear geometry suggesting some destructive E-field interferences in the electrode valleys, i.e., internal corners troths of the fingered electrode. These interferences are the highest at the fine shape sawtooth and lowest for the fingered electrode. The findings suggest a possibility for optimizing the shape and

pitch of the contoured electrode for maximum ion production per length surface coverage area of the actuator.

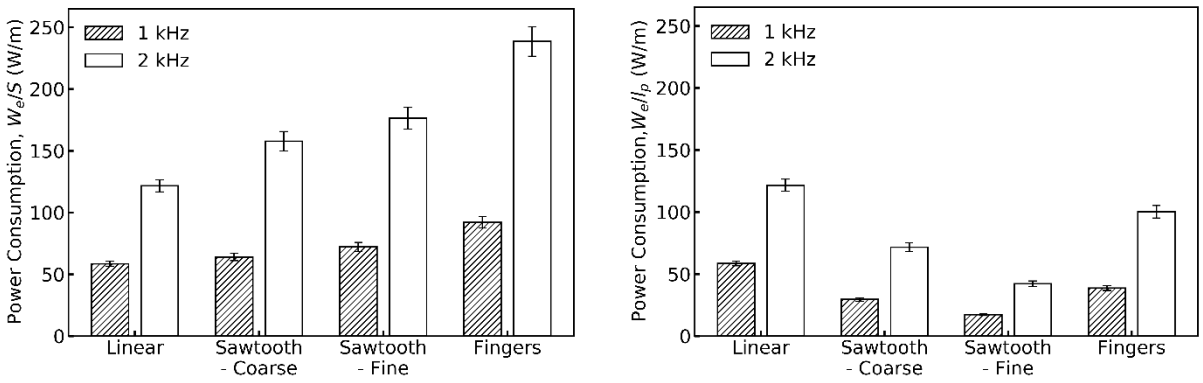

(a) (b)

Figure 9.3. Electrical power consumption with respect to (a) spanwise length and (b) plasma length for different electrode shapes at φ_{AC} = 18 kV for two different frequencies.

9.2.2 *Effect of electrode shape on thrust characteristics*

9.2.2.1 Grounded DCA electrode

The thrust of the DBD – DCA actuator non-energized (grounded) is compared for different electrode shapes as a function of applied voltage and frequency in Figure 9.4. The thrust forces of the DBD – DCA actuator with sawtooth and fingers electrode enhances the momentum injection. The coarse sawtooth electrode generates maximum thrust; at the maximum voltages tested, a thrust of 27.5 mN/m and 42.8 mNm was measured for 1 kHz and 2 kHz, respectively. This corresponds to a 2.5x increase over linear electrode DBD – DCA and 2.9x than the standard two-electrode DBD. The increase in thrust can be explained by two mechanisms: 1. Momentum injection: Increase in induced jet velocity due to greater plasma volume and plasma intensity at the sawtooth tips 2. Vorticity generation: As the momentum in DBD is injected perpendicular to the electrode's

edge; the contoured electrode creates vortex structures as the oblique (or opposing in case of fingers electrode) wall jets collide [160]. The vortices are propagated downstream, entraining into the boundary layer, thus increasing the thrust force. The thrust of the fine sawtooth actuator decreases by 20% (2x of linear electrode DBD – DCA) compared to the coarser sawtooth. It is likely due to narrow jet and less efficient vortex structure, as mentioned in a previous study [225]. The fingers electrodes, the power consumption is the highest due to the increased plasma volume (see Figure 9.2 (d)); however, the thrust improvement is only 2.3x over the linear electrode and is 10% lower than for the coarse sawtooth electrode at the same operating conditions. This is likely due to significant amount of power being used to create transverse (spanwise) opposing wall jets, whereas sawtooth electrode induces oblique wall jets that are efficient at injecting streamwise momentum and generating large vortex structures. The effect of frequency on thrust characteristics is also shown in Figure 9.4. The thrust is plotted for two frequencies for a range of applied voltages; not surprisingly, the higher frequency case produces higher thrust due to a greater number of ionic species produced during discharge.

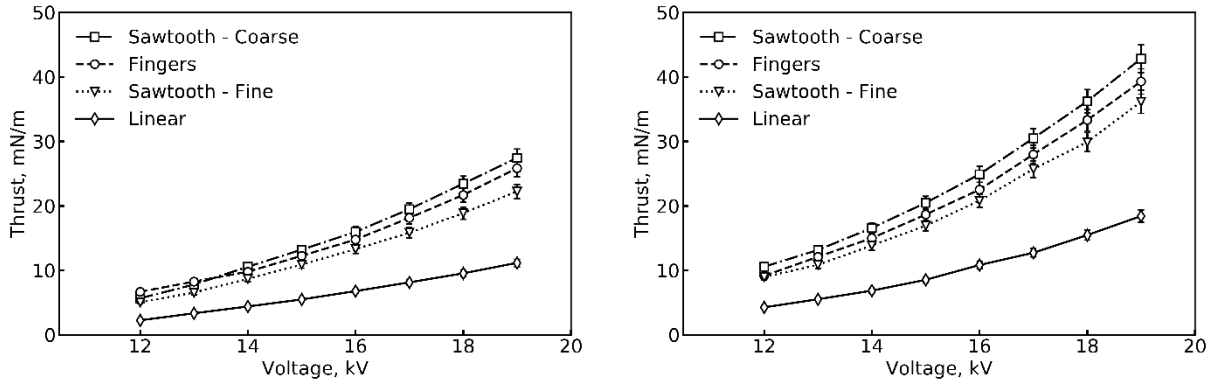

(a) (b)

Figure 9.4. Thrust comparison between different electrode shapes for DBD – DCA with third electrode grounded as a function of the applied voltage for (a) 1 kHz and (b) 2 kHz frequency.

In summary, the consideration for thrust optimization one should consider that: (1) the vortex structures increase momentum injection into the boundary layer, these are beneficial over the liner electrode (2) there is an optimum parameter for a pitch of the contoured electrode as the finer structure produce smaller vortices that less efficient for energizing the boundary layer (3) power used for vortex generation is competing with power used for X-momentum injected (thrust); thus the aspect ratio of the peaks or fingers play a role in optimization of X-momentum injection.

9.2.2.2 Effect of DCA potential

The thrust can be further increased by accelerating the ions when a streamwise E – field is applied. This effect is described in section 8.2.2.2 for the linear electrode. Figure 9.5 shows the thrust force of the contoured DBD – DCA plasma actuator at varied DCA voltages and polarities at φ_{AC} = 18 kV & f_{AC} = 2 kHz and compared with linear electrode shape. The thrust generated by the DBD – DCA actuator depends on the applied DC voltage.

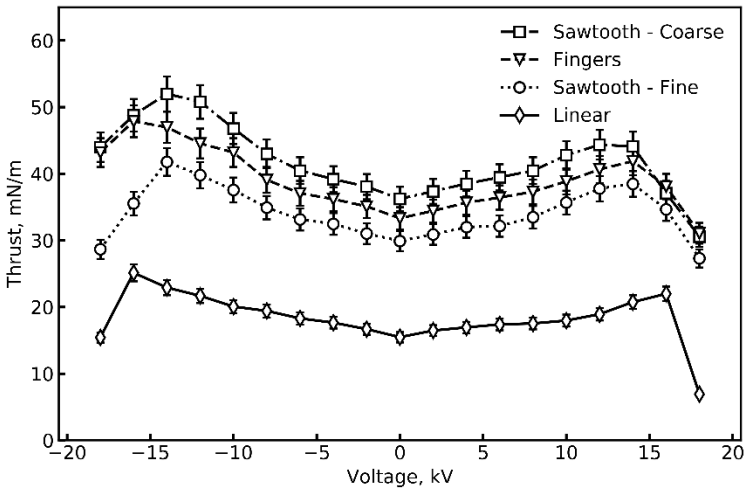

Figure 9.5. Thrust of the DBD – DCA plasma actuator as a function of input DC voltages for different electrode shapes.

For positive DCA (i.e., $\varphi_{DC} > 0$), the thrust increases with the potential and reaches a maximum at $\varphi_{DC} = 14 \sim 16$ kV and drops for high DC voltages. The sawtooth – coarse electrode reaches a maximum thrust of 44.34 mN/m at φ_{DC} = 12 kV, which is 2x times higher than linear electrode DBD – DCA at φ_{DC} = 16 kV. For sawtooth – fine and fingers electrodes, the thrust reached 38.4 mN/m and 41.8 mN/m at φ_{DC} = 14 kV, which is 1.75x and 1.9x times higher than the linear electrode. The charge transported in the negative discharge is enhanced in the X-direction because of the electric field created between the electrodes. As the DC voltage increased further, a jet in the "−X" direction is generated, leading to thrust reduction.

In the negative DCA ((i.e., $\varphi_{DC} < 0$), the thrust trends are similar as in the positive DCA. The positive ions are accelerated towards the third electrode in the positive-going cycle. The thrust increases up to φ_{DC} = −14 – −16 kV, and then sharply decreases. For both the polarities, the flow acceleration during the complementary half-cycle exceeds the reduction in the other half-cycle, thus increasing the overall thrust. The increase in the thrust is apparent in the negative DCA, as there is a greater abundance of positive species (~2x compared to negative species) in the DBD discharge, as quantified by the discharge current [13]. The linear electrode generates 25% more thrust force than the positive DCA. The coarse sawtooth electrode generates a maximum thrust of ~52 mN/m at φ_{DC} = 14 kV, which is 2x times higher than maximum thrust in linear electrode negative DCA case. For fine sawtooth and fingers electrodes, the thrust reached a maximum of 41.7 mN/m and 47.8 mN/m, which is 1.7x and 1.9x higher than linear electrode negative DCA case. The drop in the thrust as a function of DCA voltage (induced by counter jet) occurs earlier than in the linear electrode for all the electrode shapes case for both the polarities. This is likely due to the sharp tips on the electrodes changing the discharge characteristics. Secondary effects

such as surface charge modification, and vortex structure change due to the third electrode may exist; however, these effects are not quantified in the current work.

9.2.3 *Effectiveness of actuators*

The effectiveness of the actuator is an important parameter in comparing which design configurations can achieve higher thrust while consuming less power [222]. Note that for control purposes, the interaction with the free stream would play a significant role. The effectiveness is the ratio of the induced thrust to the consumed power, as shown in Eq. (8.5). The effectiveness for DBD – DCA with grounded electrode for different electrode shapes is shown in Figure 9.6 at a fixed frequency of 2 kHz for a range of voltages. The effectiveness is higher for coarse sawtooth electrode compared to all the electrode shapes. Coarse sawtooth DBD – DCA actuator has the best performance in terms of power conversion: its power consumption is 1.28x higher than the linear electrode, while the thrust generated is 2.5x larger than linear DBD – DCA. The effectiveness for the sawtooth – coarse DBD – DCA is 1.85x higher than the linear electrode. When the pitch of the electrode decreases, the effectiveness decreases by 21.4% as the thrust force decreases by 15% and the power consumption increase by 12%. The fingers electrode effectiveness is within 10% of the linear electrode since the power consumption is maximum among all the cases. Based on this, the DBD – DCA actuator with sawtooth – coarse electrode outperforms all the other cases.

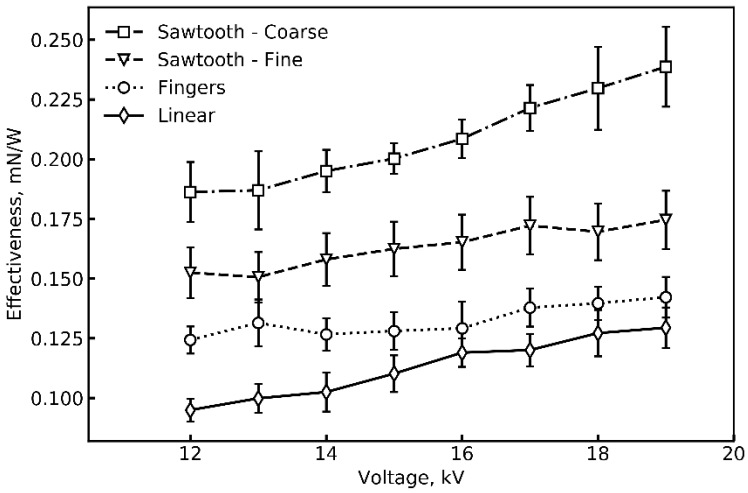

Figure 9.6. Effectiveness for different electrode shapes for grounded the third electrode at f_{AC} = 2 kHz for a range of voltages.

The effectiveness of the DBD – DCA actuator for different electrode shapes at maximum thrust conditions when the third electrode is powered is compared in Table 9.2. The effectiveness of the sawtooth – coarse electrode at maximum thrust conditions for DBD – DCA is 1.5x higher than the linear electrode DBD – DCA cases. The fingers electrode is less effective compared to the linear electrode when the third electrode is powered. The sawtooth – fine electrode is just 1.15x more effective than the linear electrode. The improvement in effectiveness with the third electrode is greater for linear electrode compared to other electrode shapes. This is likely due to (i) the sharp tips on the electrodes changing the discharge characteristics and the vortex structure change due to the third electrode; (ii) the one-dimensional (streamline) nature of the linear DBD momentum injection, which is aligned with the direction of DCA E-field. From this analysis, the DBD – DCA with a sawtooth – coarse electrode with negative DCA has the best performance; however additional optimization of the geometry is possible.

Table 9.2. Comparison of effectiveness for DBD – DCA at φ_{AC} = 18 kV, f_{AC} = 2 kHz at maximum thrust conditions for DCA voltages

Electrode shape	$\varphi_{DC} = 0$	$\varphi_{DC} > 0$	$\varphi_{DC} < 0$
Linear	0.127	0.176	0.2
Sawtooth – Coarse	0.23	0.274	0.318
Sawtooth – Fine	0.17	0.212	0.23
Fingers	0.14	0.172	0.196

9.3 CHAPTER SUMMARY

This chapter describes the improvement in the performance (DBD – DCA) plasma actuator by introducing different electrode shapes. The body force generated by the actuator was determined by measuring the thrust of the EHD wall – jet in the X-direction. The thrust is measured over a range of input parameters: AC voltage (φ_{AC}), frequency (f_{AC}), and DC voltage (φ_{DC}) for all the electrode shapes (sawtooth – coarse, sawtooth – fine, fingers) and compared them with the linear shape electrode. All contoured exposed electrodes generate significantly more thrust than the linear electrode. The thrust increase is due to large plasma volume and vorticity generation. Velocity is induced perpendicular to the electrode shapes, creating vortex structures as the wall jets collide and these vortices are propagated downstream entraining more fluid. The sawtooth – coarse, sawtooth – fine, and fingers electrode generates 2.5x, 2x, and 2.3x more than the linear electrode DBD – DCA respectively and 2.9x, 2.3x 2.5x more than standard two-electrode DBD.

The effects of positive and negative DC voltage on thrust were parameterized for all the electrode shapes at φ_{AC} = 18 kV & f_{AC} = 2 kHz. The thrust increases with the DC voltage reaches

a maximum value and drops when counter jet forms due to reverse discharge between DCA and exposed electrode. For the same potential, the negative DC voltage generates more thrust than positive DCA for all the electrode shapes. At 18 kV and 2 kHz, the sawtooth – coarse electrode generates a maximum thrust force of 52 mN/m, which was 2x times higher than maximum thrust induced by linear electrode negative DBD – DCA and 4x more than the standard two-electrode DBD. For sawtooth – fine and fingers electrode cases, the thrust reached a maximum of 41.7 mN/m and 47.8 mN/m, which is 1.7x and 1.9x higher than linear electrode negative DCA case and 3.3x and 3.8x more than standard two-electrode DBD. The actuator's effectiveness was calculated for the DBD – DCA actuator for different electrode shapes when the ground electrode is grounded over a range of operating conditions. The effectiveness of the sawtooth – coarse electrode is 1.85x more than the linear electrode. The effectiveness of the sawtooth – coarse electrode DBD – DCA, when the third electrode is powered, is 1.5x higher than the linear electrode DBD – DCA cases.

Chapter 10. FLOW CONTROL USING PLASMA ACTUATORS AT LOW ANGLES OF ATTACK

This study characterizes the effect of sawtooth DBD – DCA on the performance of NACA 0012 airfoil at low angles of attack in a subsonic wind tunnel. Force measurements were obtained to calculate the lift and drag coefficients and the pitching moment coefficient for $\alpha = 0^0 – 8^0$. The effect of the plasma actuator on the aerodynamic coefficients was determined for three Reynolds numbers. The effects of the DC voltage on the third electrode were also studied to estimate the control efficiency.

10.1 Wind Tunnel and Airfoil

The experiments were conducted in an open return subsonic wind tunnel at the University of Washington with a 0.7 m × 0.383 m rectangular cross-section and a 1.2 m long test section. The tunnel consists of a modular inlet with a series of 10 screens to condition the flow. Inlet is followed by a settling chamber and 10:1 contraction that attaches to the test section. The sidewalls of the test section are plexiglass, allowing for optical access. Downstream of the test section is a short diffuser section connected to a 40 hp, 3 – phase 460 VAC blower controlled by a variable frequency drive. The wind tunnel is shown in Figure 10.1.

The NACA 0012 airfoil was used in this study. This airfoil is chosen for its generic shape and well-known aerodynamic characteristics. The active control of the airfoil was also studied extensively, e.g., control of dynamic stall using plasma actuators [226-228], plasma slats, and flaps [38, 40, 229]. These studies provided data on loads and flow visualization. The airfoil has a 190.5 mm chord (c) and 381 mm span (b). The size of the airfoil was selected to minimize the blockage

effects and while maintaining a large chord Reynolds number. The airfoil was machined from polyurethane foam (Obomodulan) using traditional CNC machining. The endplates, made from the same material as an airfoil, are attached to the top and bottom of the airfoil, flush with walls of the test section, to minimize three-dimensional flow effects. The angle of attack α is set using an optical positioning system (Avago AS 38) with accuracy $\pm 0.02^0$. A stepper motor is used to control the angular position of the airfoil. The angle of attack was varied from $\alpha = 0^o - 8^o$ during the experiments. The free stream velocity is measured using a Pitot tube that was located at the entrance of the test section and is connected to an Ashcroft CXLdp 0 –10″ WC with an accuracy of 0.25%. This method was employed because it does not affect the flow in the test chamber since no probe is needed during the experiment. Three freestream velocities (U_∞) of 15 m/s (~ 35 mph), 20 m/s (~ 45 mph) and 25 m/s (~ 55 mph) were investigated. These velocities are comparable to those for a typical fixed-wing UAV. The corresponding chord Re numbers are 201k, 268k, and 335k. The Re is defined as

$$Re = \frac{U_\infty c}{\nu}, \tag{10.1}$$

where U_∞ is the freestream velocity, c is the chord of the airfoil and ν is the kinematic viscosity. In this study, the maximum angle of attack is 8^o, so the blockage ratio corrections are omitted from the Re calculation.

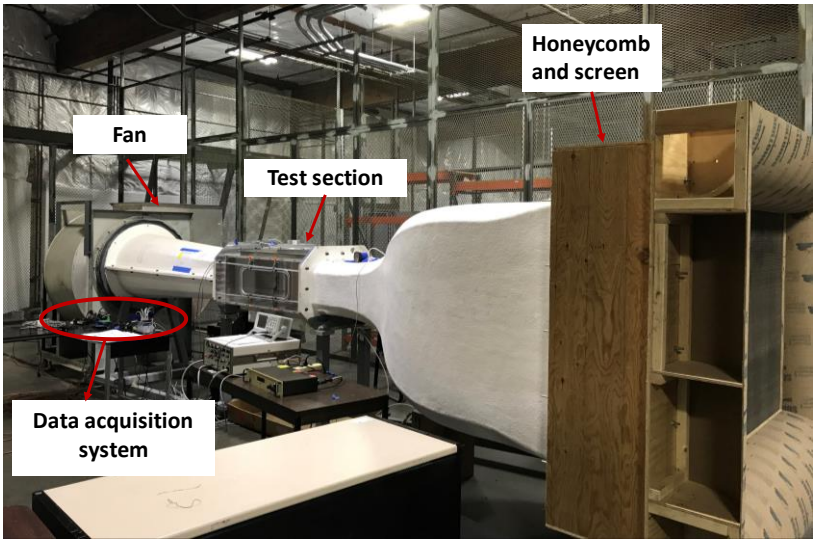

Figure 10.1. Wind tunnel at the Bowmen building of the University of Washington. From right to left: honeycomb and screen, converging section, test section, diffuser, fan section.

10.2 Force Measurements

The airfoil is mounted vertically, and the endplates are connected to the external force balance on the top and bottom of the test section, as shown in Figure 10.2. The entire assembly is rested on an air bearing and connected to the bottom load balance flexure. The top test section has an opening, through which the top endplate is attached to the load balance flexure. The force balance uses a strain gauge bridge providing voltage outputs proportional to lift and drag forces. Lift forces are measured by four strain gauges (two on each side), and drag forces are measured by two strain gauges (one per side). The output from the load cells is sampled for a minimum of 30 s at each flow condition at a rate of 1.6 kHz to obtain stable force data. The measured voltage signals are transferred to a data acquisition computer through a 24-bit strain gauge module (NI-9237) for post-processing. The measurements are repeated at least 10 times for each condition for statistical independence. The lift and drag coefficients are calculated as

$$C_L = \frac{L}{\frac{1}{2}\rho U_\infty^2 cb}, \tag{10.2}$$

$$C_D = \frac{D}{\frac{1}{2}\rho U_\infty^2 cb}, \tag{10.3}$$

where L and D are the time-averaged lift and drag, respectively, ρ is the air density c is the chord and b is the span of the airfoil model. The measurement range is 711 N for the lift force and 106 N for the drag force, with an accuracy of 0.04% and 0.03% of the full range, respectively. The resulting uncertainties in the force coefficients are less than 3%. The pitching moment coefficient is calculated using Eq.(10.4) about quarter chord location based on the measured lift force at the leading and trailing edges of the airfoil.

$$C_M = \frac{M}{\frac{1}{2}\rho U_\infty^2 cb}, \tag{10.4}$$

where M is the pitching moment calculated at quarter chord.

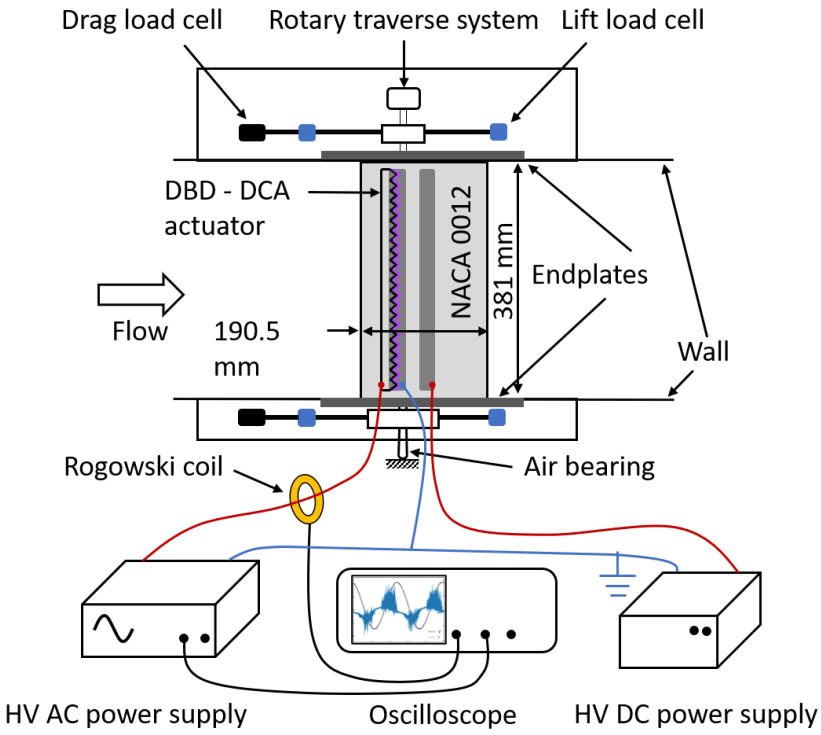

Figure 10.2. Schematic of the experimental setup for the lift, drag and pitching moment measurements on the airfoil with sawtooth DBD – DCA actuator.

10.3 Plasma Actuator

The plasma actuator consists of three 0.05 mm thick copper electrodes separated by four layers of Kapton film (7700 VPM @ 25 ◦C) of thickness 0.088 mm as shown in Figure 10.3(a). The exposed high voltage electrode is fabricated using electro-discharge machining to produce a sawtooth pattern, as shown in Figure 10.3(b). The sawtooth pattern was selected based on a preliminary optimization study [230]. Gao et al. also reported that sawtooth a pitch-to-height ratio of 1 is favorable for power consumption, dielectric heating, and velocity induced by plasma [164]. The trough of the sawtooth is rounded to eliminate the high electric field concentration. The exposed and encapsulated electrodes are overlapped such that the ground electrode edge is aligned with the troughs of the sawtooth pattern. The width of the ground electrode is 25 mm and is long

enough to allow for the development of the plasma sheet. The third electrode with a width of 25 mm, is placed 20 mm from the downstream edge of the ground electrode. The spanwise length of the electrodes is 350 mm. The actuator is installed at the 18% chord from the leading edge (x/c = 0.18) as shown in Figure 10.3(c). The location is selected based on the reported position of separation bubble for NACA 0012 airfoil: 0.1 c – 0.6 c for $\alpha = 2^0 - 8^0$ at $Re = 3 \times 10^5$ [231].

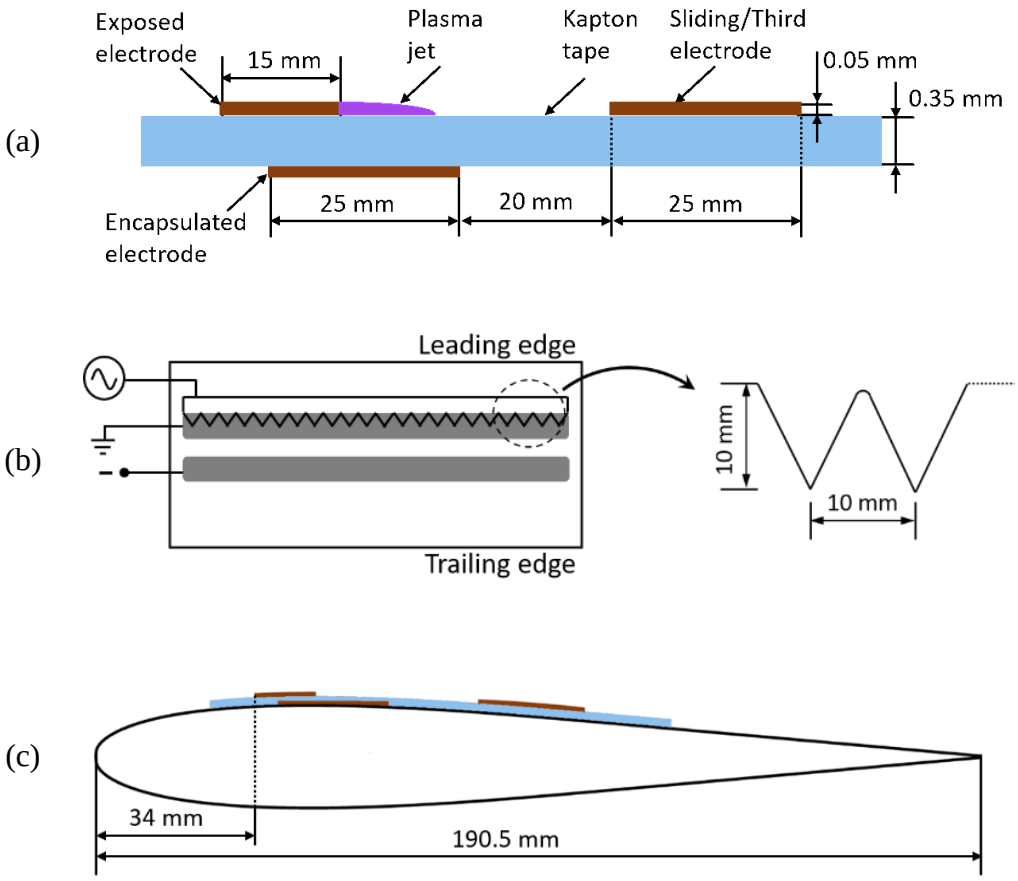

Figure 10.3. Sawtooth DBD – DCA actuator installed on NACA 0012 airfoil (a) dimensions of the plasma actuator (b) geometry of the sawtooth electrode pattern, and (c) actuator installation position on the airfoil.

10.4 Power Supply and Electrical Measurements

The exposed electrode is connected to the HV AC power amplifier Trek 615-10. The input signal is the sinusoidal wave with the peak-to-peak voltage φ_{p-p} = 18 kV with a 1.25 kV DC bias voltage and frequency f = 2 kHz. The current is measured using Pearson model 8590C current probe positioned around the wire driving the exposed electrode. The current monitor is connected to a Tektronix DPO2024 oscilloscope that uses a bandwidth of 200 MHz to satisfy the Nyquist condition for achieving a sampling rate of 400 MS/s required for the accurate capture of individual discharges with a typical duration of ~ 30 ns [13]. The high bandwidth and the sampling rate minimize the noise during the current measurements and can be used to compute the time-averaged electrical power [1]. The voltage from the power supply is also measured simultaneously. Figure 10.4 shows the voltage and current traces with time. The third electrode is connected HV DC power supply (Bertan 205B-20R) with variable negative DC voltage $\varphi_{DC} = -$ (0 – 15) kV to the third electrode, and the current is measured directly from the power supply.

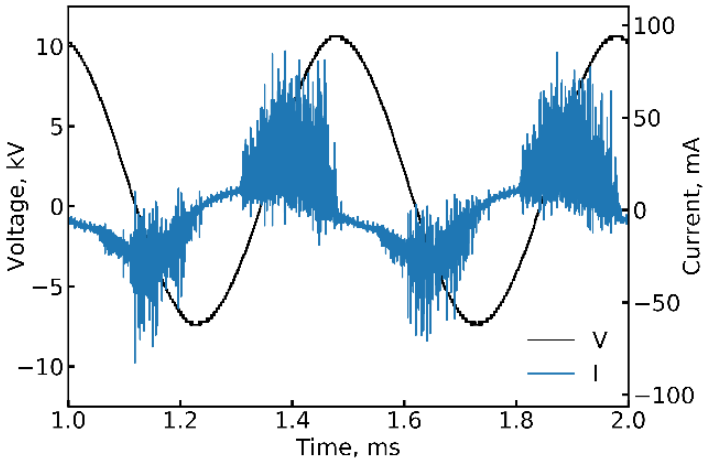

Figure 10.4. DBD current with voltage signals at 18 kV(p-p) and 2 kHz applied frequency.

10.5 Results and Discussion

10.5.1 *Baseline performance*

The thin plasma actuator installed on the airfoil may affect the boundary layer development similar to a thin trip [232]; thus, the effect of a passive actuator (Plasma OFF) on the aerodynamic characteristics is explored first. These tests also provide validation of force measurements. The lift and drag coefficients vs. the angle of attack are plotted in Figure 10.5. The data is compared with the previous reports for 2D NACA0012 airfoil, e.g., data for Re = 160k – 200k [233, 234] and numerical simulations (XFOIL) for Re = 200k [235]. The lift coefficient at Re = 201k shown in Figure 10.5(a) agrees well with the previous literature. The actuator in its OFF state does not change the aerodynamic characteristics of the airfoil. Other studies reported that thin strips [232] and low profile vortex generators [236] with a similar thickness to our actuator reported separation delay. Since we limit $\alpha < 8^o$ the separation delay at higher angles has not been evaluated. The drag measurements in Figure 10.5(b) agree well with previous reports literature except for Ladson, which likely due to the difference in chord lengths. The chord length in Ladson data is 914 mm, while in our experiment, it is 190.5 mm. Our data, however, agrees well with the shorter chord length (150 mm) data of Sheldahl & Klimas.

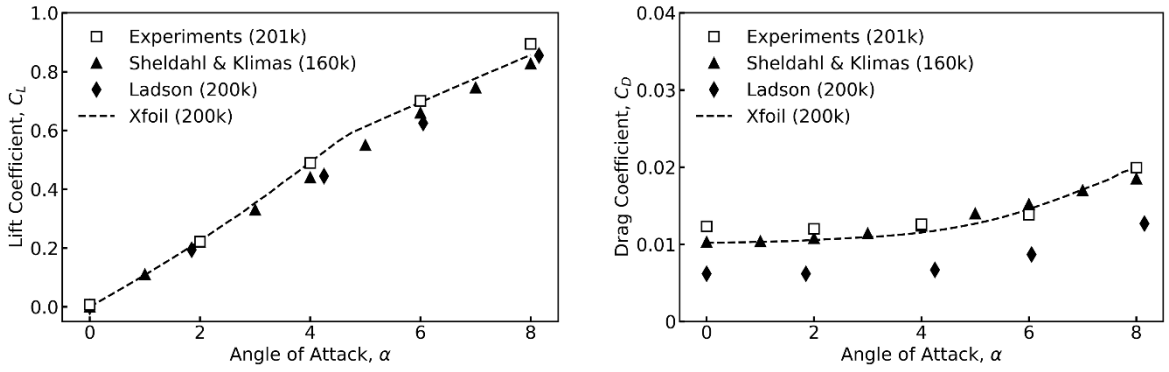

(a) (b)

Figure 10.5. Comparison of measured aerodynamic coefficients for NACA 0012 airfoil, with XFOIL calculations [235] and data from the literature [233, 234].

10.5.2 *Effect of DCA voltage*

Vaddi et al. demonstrated the sawtooth DBD – DCA actuator mounted on a flat plate generates 4x more thrust than DBD by accelerating the ions in the negative DC field [230]. Greater momentum injected can be utilized in the airfoil case. Figure 10.6 shows the effect of the flow acceleration by DC field on aerodynamic coefficients for two different angles of attack at a free stream speed of 15 m/s. The voltage on the third electrode is varied from 0 kV to −15 kV. A plasma OFF case is given for reference. DBD is operated at φ_{p-p} = 18 kV, φ_{bias} = 1.25 kV and f = 2 kHz. The bias voltage is applied to increase the amount of time with positive voltage during the AC cycle. All data is reported based on the instantaneous force measurement, i.e., within 3 seconds after the actuator is energized.

In all the cases, the lift coefficient increases with the DC field. Compared to the plasma-OFF condition, the sawtooth DBD – DCA with φ_{DC}= 0 kV (the third electrode grounded) case does not result in a significant lift, drag, or pitching moment change. As the magnitude of DCA voltage

increases, significant changes are observed. The lift coefficient increases by ~ 0.03 for both angles of attack at $\varphi_{DC} = -15$ kV. The highest tested voltage case (−15 kV) corresponds to ~7% increase in the lift at α = 4º. Two mechanisms can explain lift augmentation. (1) Momentum Injection: Stronger DC field accelerate the flow, similar to a corona discharge EHD flow [5, 6]. The resulting jet propagates towards the trailing edge creating higher velocity flow on the suction side of the airfoil. (2) Vorticity Generation: Velocity is induced perpendicular to the sawtooth edge creates vortex structures as the oblique wall jets collide [160]. The induced vortices trigger a rapid transition to the turbulent boundary and hinder the development of the laminar separation bubble. Vorticity and the momentum entertainment into the boundary layer locally accelerate the flow on the succession side of the airfoil, creating additional lift.

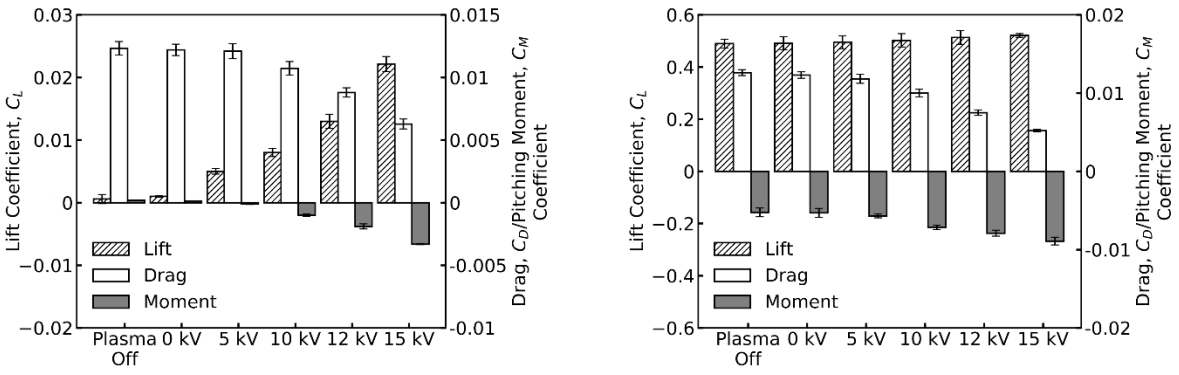

(a) (b)

Figure 10.6. Aerodynamic performance at different φ_{DC} potentials for two different angles of attack (a) 0º and (b) 4º (U_∞= 15 m/s), DBD - DCA is operated at φ_{p-p} = 18 kV, φ_{bias} = 1.25 kV and f = 2 kHz.

The drag reduction on the airfoil, as seen in Figure 10.6 can be attributed to the momentum injection (i.e., thrust) and the vorticity generation by the sawtooth DBD - DCA actuator.

Experiments with the straight edge electrode can potentially elucidate the individual contributions of each mechanism. For α = 0º case, the first significant change in C_D (12% drop) is at $\varphi_{DC} = -10$ kV. However, C_D drops by 50% at $\varphi_{DC} = -15$ kV. The total change from plasma OFF to maximum DBD – DCA input is $\delta C_D \sim 0.006$. For α = 4º case, this difference is greater $\delta C_D \sim 0.0074$, suggesting that DBD – DCA actuator alters the flow field on the suction side of the airfoil, such as removing the separation bubble leading to additional drag reduction.

One of the major findings is the effectiveness of the sawtooth DBD – DCA to alter the pitching moment. The momentum injection and vorticity generation at the trailing edge creates a greater pitching moment, which increases at the higher φ_{DC} voltage as expected. The pitching moment changes by ~0.0035 for both angles of attack with no plasma actuation and plasma actuation with $\varphi_{DC} = -15$ kV. The results show that the control efficiency has a strong dependence on DCA electrode potential. The position of the actuator will also affect the pitching moment; however, this topic is outside the current scope.

10.5.3 *DBD – DCA: function of angle of attack*

To maximize the effect of the actuator on the airfoil performance, for the next set of experiments, the DCA voltage is held at −15 kV. The performance is assessed based on the relative difference between plasma ON and plasma OFF conditions. The results from the plasma actuation as a function of α are presented in Figure 10.7, with U_∞= 15 m/s. The experiments are conducted at φ_{p-p} = 18 kV, φ_{bias} = 1.25 kV and f = 2 kHz. As a function of the angle of attack, the lift increase is nearly constant, see Figure 10.7(a). At α = 0° with actuator ON, the improvement in lift coefficient is ~ 0.03. Similar lift trends have been reported with plasma gurney flaps [38, 40]. However, the drag force increases when plasma gurney flaps are introduced. The sawtooth DBD

– DCA actuator generates both significant lift and reduction in drag at low angles of attack. The lift increase δC_L = 0.03 – 0.04 while reducing drag coefficient δC_D ~ (0.006 – 0.008) over the range of $\alpha = 0^o – 8^o$, see Figure 10.7(b).

The quarter chord pitching moment is shown in Figure 10.7(c). With the lift enhancement, the pitching moment has a negative value for all angles of attack tested. The pitching moment changes by 0.003 – 0.005 when the actuator is energized. The plasma ON condition for the DBD-DCA actuator mounted on the suction side of the airfoil leads to a greater negative pitching moment (nose-up) for all angles of attack.

(a)

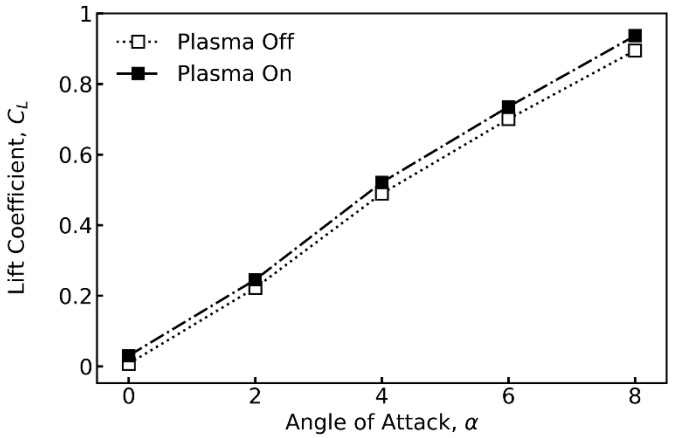

(b)

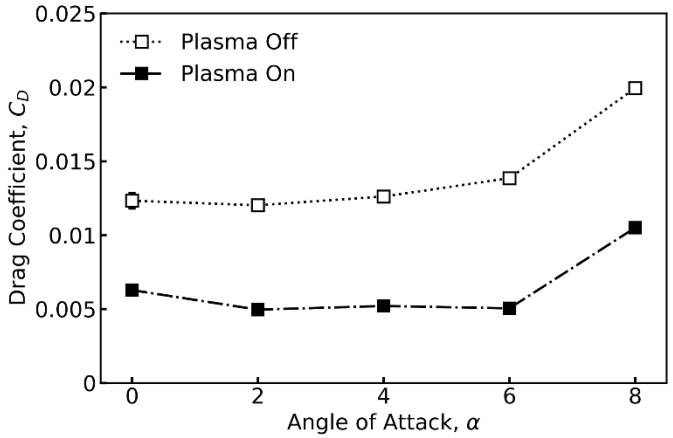

(c)

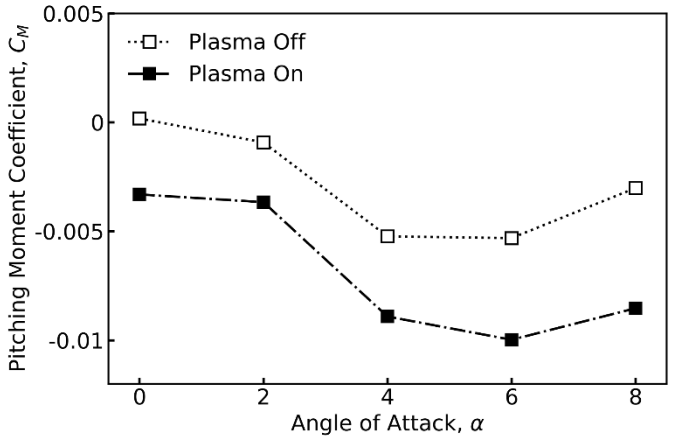

Figure 10.7. Aerodynamic characteristics (a) Lift (b) Drag (c) Pitching moment with/without plasma actuation at U_∞= 15 m/s. DBD - DCA is operated at φ_{p-p} = 18 kV, φ_{bias} = 1.25 kV, φ_{DC} = −15 kV and f = 2 kHz.

10.5.4 *Effect of Reynolds number*

The freestream velocities were varied from 15 m/s to 25 m/s, corresponding to the chord *Re* = 201k – 335k. Figure 10.8 shows the effect of the Reynolds number on airfoil performance with sawtooth DBD – DCA actuator. Figure 10.8 (a) shows that the change in the lift (δC_L) for the lowest wind speed increases with α. However, DBD-DCA actuation at higher velocities δC_L has only a slight increase with the angle of attack at a given Reynolds number. The effect of plasma actuation decreases with an increase with free stream velocity, which agrees with previous reports of maximum lift scaling as $\delta C_{L,max} \propto U_\infty^2$ [237]. The change in drag coefficient as a function of *Re* is shown in Figure 10.8 (b). As the free stream velocity increases, the drag reduction (δC_D) decreases. At U_∞ = 25 m/s, plasma ON condition results in a drag reduction of about 20%, compared to 50% at U_∞ = 15 m/s. The δC_D is also slightly decreases as a function of angle of attack for all wind speeds.

The pitching moment change (δC_M) is shown in Figure 10.8(c), for the actuator location considered in this work, with the Reynolds number is similar to δC_D. The δC_M slightly decreases with the angle of attack for all wind speeds. The effectiveness of the actuator for control purposes diminishes at higher velocities; however, the optimization of actuator location can lead to additional improvement in δC_M. With proper aircraft design, this metric could provide sufficient control authority for smaller UAVs.

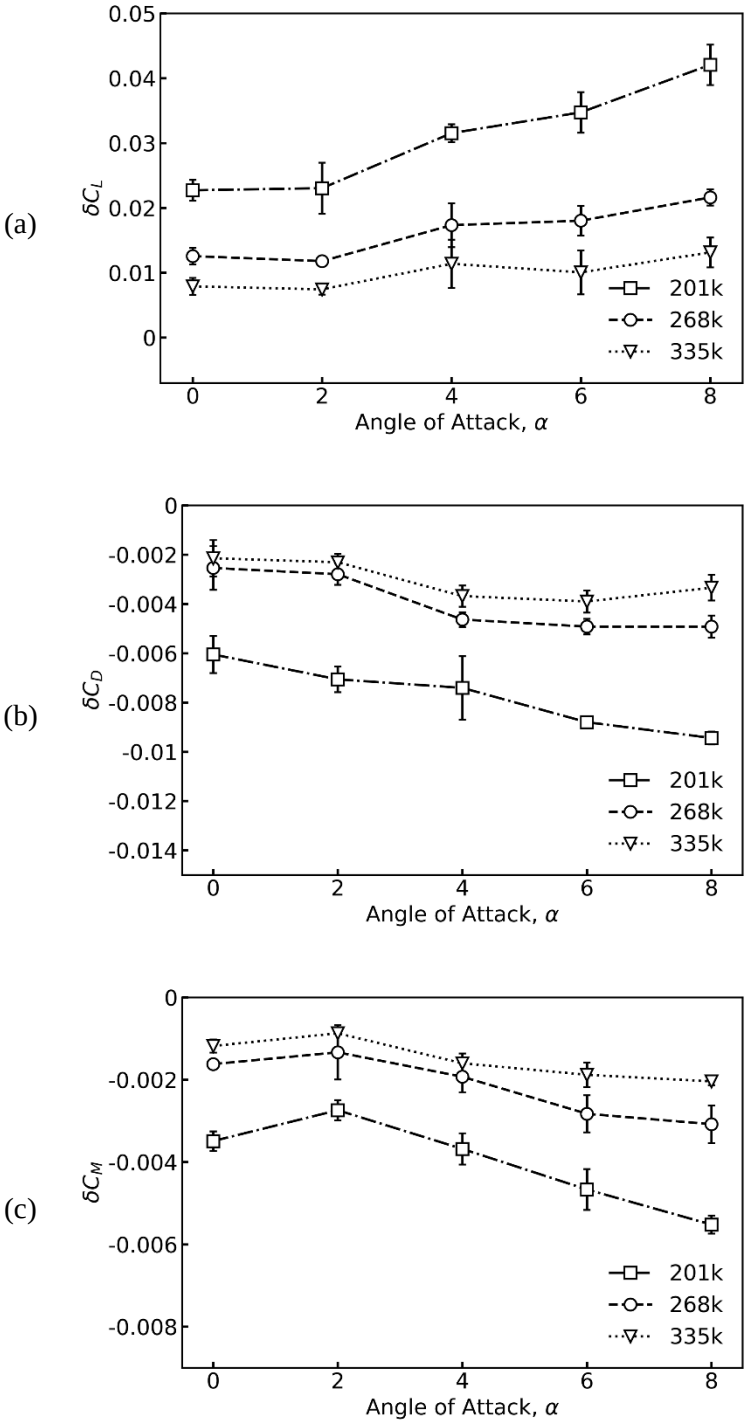

Figure 10.8. Effect of Reynolds number on (a) Lift (b) Drag (c) Pitching Moment for sawtooth DBD – DCA actuator.

10.5.5 *Energy Transfer Efficiencies*

The actuator's performance on the aerodynamic coefficients is assessed in the previous section; another important metric is the effectiveness of the actuator performance. The effectiveness is the ratio of the actuator thrust to the consumed electrical power [125, 238]. Recently the term effectiveness has been used to evaluate the maximum lift due to plasma actuation and the consumed power [43]. The lift and drag effectiveness are defined as given in Eq. (10.5) and (10.6)

$$\varepsilon_l = \frac{\Delta L}{W_{elec}} \tag{10.5}$$

$$\varepsilon_d = \frac{\Delta D}{W_{elec}} \tag{10.6}$$

where ε_l and ε_d are the lift and drag effectiveness, ΔL and ΔD are the average change in lift and drag forces with and without plasma. The change in lift and drag forces is almost constant for a given Reynolds number, so the ΔL and ΔD are calculated as follows,

$$\Delta L = \frac{1}{\alpha}\int_0^{\alpha} (L_{ON} - L_{OFF})\, d\alpha, \tag{10.7}$$

$$\Delta D = \frac{1}{\alpha}\int_0^{\alpha} (D_{ON} - D_{OFF})\, d\alpha. \tag{10.8}$$

The time-averaged electrical power consumed by the actuator can be computed as

$$W_{elec} = f\int_0^{t} \varphi(t) i(t) + \varphi_{DC} i_{DC} \tag{10.9}$$

where $i(t)$ and i_{DC} are AC and DC current respectively and t is the time period. The power is computed for at least five independent measurements for each condition. The electrical power

consumption does not change with the free stream velocity, at least in the range of 0 – 30 m/s, which agrees with previous work [239, 240]. Here it is computed for φ_{p-p} = 18 kV, φ_{bias} = 1.25 kV, $\varphi_{DC} = -15$ kV and f = 2 kHz.

The lift and drag effectiveness for different free stream velocities is shown in Table 10.1. The effectiveness values decrease with the freestream velocities as the control authority decreases with free stream velocity as shown in Figure 10.8. An analysis by Ferry [224] on the feasibility of plasma actuator for aerodynamic control concluded that with straight electrode plasma actuator effectiveness of 0.11 mN/W concludes that a 0.5 kg aircraft with 0.76 m^2 wing area requires 0.47 – 2.22 kW of power for trim. In the current study, the lift effectiveness of 4.53 – 5.03 mN/W and drag effectiveness of 1.03 – 1.26 mN/W is achieved for sawtooth DBD – DCA plasma actuator and would require a much lesser power. This indicates that the technology level is appropriate for practical applications.

Table 10.1. Sawtooth DBD – DCA effectiveness at different Reynolds number.

Reynolds number	Lift effectiveness (mN/W)	Drag effectiveness (mN/W)
201k	5.03 ± 8%	1.26 ± 19%
268k	4.71 ± 5%	1.14 ± 15%
335k	4.53 ± 7%	1.03 ± 21%

10.6 CHAPTER SUMMARY

This study provides a proof-of-concept demonstration of a novel DBD – DCA actuator for active flow control utilizing NACA 0012 airfoil at subsonic flow speeds with Re = 201k – 335k and low angles of attack. The actuator was mounted in co-flow orientation on the suction side of

the airfoil: the active AC electrode was positioned at 18% chord and the DCA electrode at 48% chord. Effects of DCA potential, angle of attack, wind speeds on airfoil performance were investigated. The DCA potential increases the lift coefficient, reduced drag, and significantly affects the pitching moment of the airfoil. These effects can be explained by two mechanisms (1) increase of momentum injection due to DCA effect, (2) Vorticity generation due to a sawtooth-shaped electrode.

The lift curve with plasma actuation is almost parallel to no actuation for all angles of attack $\alpha = 0^0 - 8^0$ and the change in C_L~0.03 – 0.04. The δC_L with and without plasma actuation decreases with free stream velocity, and the scaling factor agrees with the literature. The drag coefficient decreases with the φ_{DC} and a drag reduction of 50% is measured when $\varphi_{DC} = -15$ kV at $U_\infty = 15$ m/s. Consistent δC_M shows DBD – DCA can be used for active flow at low angles of attack for low-velocity UAVs. One of the limitations of plasma actuators is their ineffectiveness at high velocities; future research should address the performance of DBD-DCA actuators at higher wind speeds. To improve control authority, the research should explore different positions and orientations of the actuator. Another topic of interest is gain insight into the interaction between the free flow and the momentum injection into the flow boundary layer for sawtooth DBD – DCA either by flow visualization or surface pressure measurements.

Chapter 11. INVESTIGATION OF PARTICLES IN EHD SYSTEMS

Previous chapters Chapter 5 & Chapter 10 discussed the successful integration of the EHD system for propulsion and control of aerial vehicles. It demonstrated the benefits of EHD wind on thrust and aerodynamic forces and discussed key results from wind tunnel testing. In this chapter, we focus on a concern related to environmental pollution and how we can use the EHD technology to build sensors to detect pollutants. The fundamental mechanisms of particle collection within an EHD system are discussed, and a new particle charging method in EHD and a novel particle sensor based on the EHD particle charging method are presented. This work is published in Journal of Aerosol Science [9] and International Symposium on Electrohydrodynamics 2019 [11].

11.1 Behavior of Ultrafine Particles in EHD Flow

Gas-phase collisions between the particles and ion medium play an important role in governing the behavior of aerosols [241-244] and dusty plasmas [245, 246]. The presence of the electric field and the ion medium plays a major role in particle trapping since particles acquire a charge from ion collisions [247]. The electrostatic force on a charged particle in the electric field can be greater than gravitational, inertial, and thermal forces. Electrostatic precipitator (ESP) devices can collect fine and ultrafine particles and are widely used in sampling and filtration applications. Conventional ESPs employ a point-plate, point-cylinder, wire-plate, point-ring configuration. In a typical electrostatic particle collector, the flow is induced by an external source; the corona discharge-induced flow is typically not considered. However, the ionic interaction used to collect the particles can be used to generate the flow and enhance particle charging in corona discharge-driven flow. It is challenging to gain insight into the particle charging mechanism in the high ion

concentration and electric field environment due to the complexity of the physical phenomena and a lack of experimental data.

Corona discharge is an electrical breakdown of air in which ions are generated in the high electric field region near the high energy anode; these ions drift towards the grounded cathode. The collisions of ions with the neutral air molecules result in a macroscopic wind, which is also known as electro-hydrodynamic (EHD) flow or ionic wind. The EHD effect has been used for plasma-assisted combustion [23, 24], convective cooling [26-29] and control of the aircraft [2, 78]. The application of EHD technology has been limited due to the modest pressure values achieved by the EHD blowers. However, in the applications with the low-pressure drop, the EHD driven flow can provide novel solutions [7, 172, 248]. Among the benefits of the EHD approach are the ability to operate at a small scale without moving parts and quiet operation [8, 16, 78]. The current-voltage relationship describes the ion transport between the electrodes. The classical voltage to the current relationship was derived by Townsend for a coaxial corona configuration [249]. This quadratic relationship has been observed for other configurations, i.e., point to plate [50] and point to ring corona [7]. A generalized analytical model for voltage to current and voltage to velocity relationship for EHD driven flow has been recently developed [6]. The maximum velocity for point-to-ring electrode configuration was recorded at ~9 m/s; the analytical model provides a good comparison with the experimental data.

Particle charging mechanisms have been an active research area, field and diffusion charging expressions [250-253] were developed for large particles (0.3 μm – 10 μm). Fuchs [254] and Marlow and Brock [242] developed diffusion charging expression for smaller particles, a combined field and diffusion charging expression was proposed by Liu and Kapadia [255]. Most

particle charging expressions were developed for spherical particles; however, recent experimental results for square particles demonstrated enhanced particle charging due to corners and edges [256]. Experimental and numerical studies have demonstrated a good agreement in the size range of 0.3 μm – 10 μm [257-259]. Multiple experimental studies for the PM in the size range of 30 nm – 400 nm [260-263] agree with the theoretical models. Nanoparticle generation and behavior in low-temperature plasma produced by DBD discharge were studied [264], and particles smaller than 20 nm are generated [265, 266]. Several researchers have also shown that for particles smaller than 30 nm, a fraction of particles was not charged and not collected [244, 267-272]. This phenomenon is called partial charging. Experimental and theoretical studies conducted by Dey et al. [262], Pui et al. [267], Li et al. [268], Liu and Pui [273] showed that Fuchs theory successfully predicted the charging probability of ultrafine particles. However, the scientific literature does not provide experimental data or numerical modeling related to the collection of nanoparticles in EHD dominated flow associated with high ion concentration and strong electric field.

In this chapter, we analyze particle transmission in the primary needle-to-tube EHD flow. The flow is studied experimentally and by numerical simulations to obtain the spatiotemporal characteristics of ion concentration, velocity, and electric field. Particles are aspirated by the corona discharge-driven flow, charged due to their collision with ions, and are collected onto the ground electrode. Nanoparticle transmission efficiency is determined experimentally at various corona voltages for ambient and NaCl particles showing low transmission (high collection) efficiency for particles below 20 nm. The experimental data suggest that the particles smaller than 20 nm can attain and hold a unit charge in the vicinity of the ionization region of the corona-induced EHD flow, leading to their increased collection. A novel particle collector based on the

EHD particle charging method is studied, and particles are collected on an optically transparent coated surface. The sample is extracted into PDMS and analyzed for fluorescence.

11.2 Experimental Methods

11.2.1 *Design and working principle of EHD particle collector*

The EHD particle collector aspirates the particle into the corona induced flow, rapidly charges the particles in the charging region, and collects the charged particles on the ground electrode; no moving parts are required for operation as the flow is aspirated by the EHD phenomenon. The high ion concentration and the strong electric field between the corona and ground electrodes result in efficient charging and high collection efficiencies of particles. Figure 11.1 shows the principle of operation of the EHD particle collector. The device consists of a high-voltage needle electrode positioned on the axis of symmetry and a grounded conductive tube serving as a collection electrode. When a high voltage is applied, the neutral air molecules are ionized by the strong electric field at the tip of the corona electrode [50, 51]. In positive corona discharge, electrons are attracted to the high voltage corona electrode, positive ions such as O_2^+ and O^+ drift towards the cathode. As the high-velocity ions repelled from the corona electrode, they collide with the neutral air molecules driving the EHD flow. Particles aspirated by the EHD flow travel through the high electric field, high ion concentration (ion drift) region where high-velocity ions bombard the particle imparting a charge via two mechanisms: (1) diffusion charging which is due to random collisions, and (2) field charging which is when the ions travel along the electric field. It is typically assumed that diffusion charging is predominant for smaller diameter particles, i.e., d_p< 200 nm [267, 274]. However, in ion-driven flow, the ion/molecule and ion/particle collisions are more frequent and more energetic than in the diffusion charging scenario. The Coulomb force caused

by the electric field between the corona electrode and grounded collection substrate forces particles towards the collection electrode.

The EHD device used in this study consists of a corona needle and a ground collection electrode, as shown in Figure 11.1. The high voltage needle is a 0.5 mm thick tungsten wire with a tip curvature of 1 μm (measured using optical microscopy); the sharp tip yields high electric field strength and results in consistent EHD flow velocity data. As shown in the previous studies [275], needle sharpness affects the generation of the corona at lower voltages. The corona needle is regularly inspected for pitting using optical microscopy to ensure the consistent performance of the device. The ground electrode is an aluminum tube ID 7 mm with a rounded edge, the radius of curvature is 3 mm, and the tube length is 25 mm. The ground electrode has a rounded edge (radius of curvature 3 mm) to reduce the local E-field leading to spark-over, thus allowing the operation over a wider voltage range. The electrode holder is fabricated using 3D printing from Polylactic Acid material (PLA). The needle is located on the axis of symmetry at a 3 mm distance from the edge of the ground electrode, see Figure 11.5.

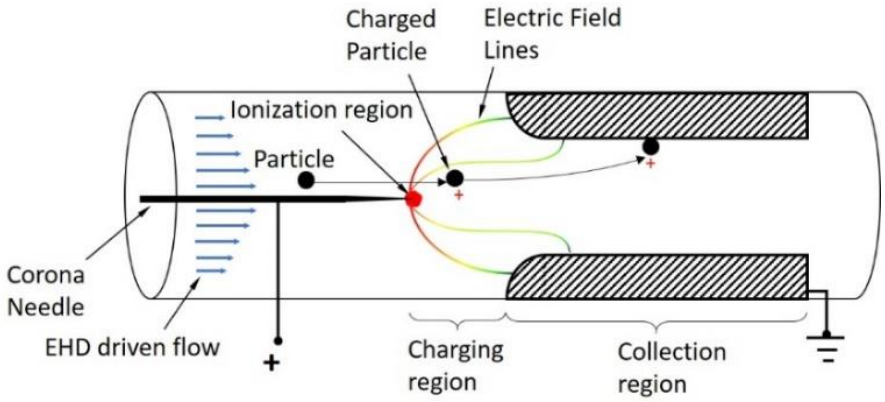

Figure 11.1. Schematic of EHD particle collector in point to tube configuration.

11.2.2 *Flow field measurements*

The flow velocity is important in particle transmission study as it affects the particle residence time in the charging and the collection regions. Previous reports used an external pump to aspirate the particles through the corona region, the flow rate can be controlled to achieve maximum collection efficiency [276, 277]. In the current work, particles are aspirated without the aid of an external pump and it is important to characterize the velocity generated by the corona discharge induced flow. A hot-wire anemometer (AN-1005) is used to measure the velocity profile at the device's outlet. These velocity measurements are also used for calculations of the flow sampling rate. TSI 1213-20 hot wire probe connected to anemometer is positioned at the outlet of the device. The anemometer is calibrated for the range of 0.2 m/s – 5 m/s using the standard calibration procedure. The data from the anemometer is collected at a frequency of 10 kHz with a data acquisition module (National Instruments, myRIO-1900) for a sampling time of 10 seconds. A variable high voltage positive power supply (Bertan 205B-20R) is used to create the potential difference between the needle and the grounded tube. The corona current is measured on the cathode using a voltage drop across a 1 MΩ resistor, as shown in Figure 11.2(a). The onset of corona generation was observed at 2 kV; however, the current measurements in the experiments below 3 kV were not consistent in the day-to-day operations. In this work, the voltage on the needle is varied from 3 kV to 5 kV. For corona voltage above ~6 kV, spark over events occurred. All experiments were performed in ambient air at temperatures of 22 C – 25 C, relative humidity range of 30% – 35%, and pressure of 1 atm.

11.2.3 *Test particles and their preparation*

The transmission efficiency of the device is determined for two particle types (i) ambient particles from a typical laboratory environment, the particle chemical composition or their origin are not known, and (ii) NaCl particles generated in the well-mixed aerosol chamber [278, 279]. Both particle types have been previously used in electrostatic particle studies as test particles [11, 25, 260, 261].We estimated that the particles exceed their saturation charge due to the high charge density environment as they travel through the charging region (as shown in Figure 11.7), and a charge neutralizer is not used. A particle sizer (TSI SMPS 3910) is used to monitor the particle concentration. For ambient particles, their number concentration upstream was typically 3×10^3 count/cc with a median diameter of 45 nm. Previous reports have indicated that non-equilibrium low-temperature plasma generates small particles with a diameter less than 20 nm [265, 266]. . We have performed a series of experiments to determine the particles that are generated from corona discharge. The particle concentration spikes 10% and 5% for 10 nm and 20 nm particles, respectively. The concentration has dropped to the baseline level after 10 seconds, indicating that only a short burst of particles was produced at the onset of corona discharge, as shown in Figure 11.3. The background particles would not change the transmission efficiency results as the particle concentration reaches saturation.

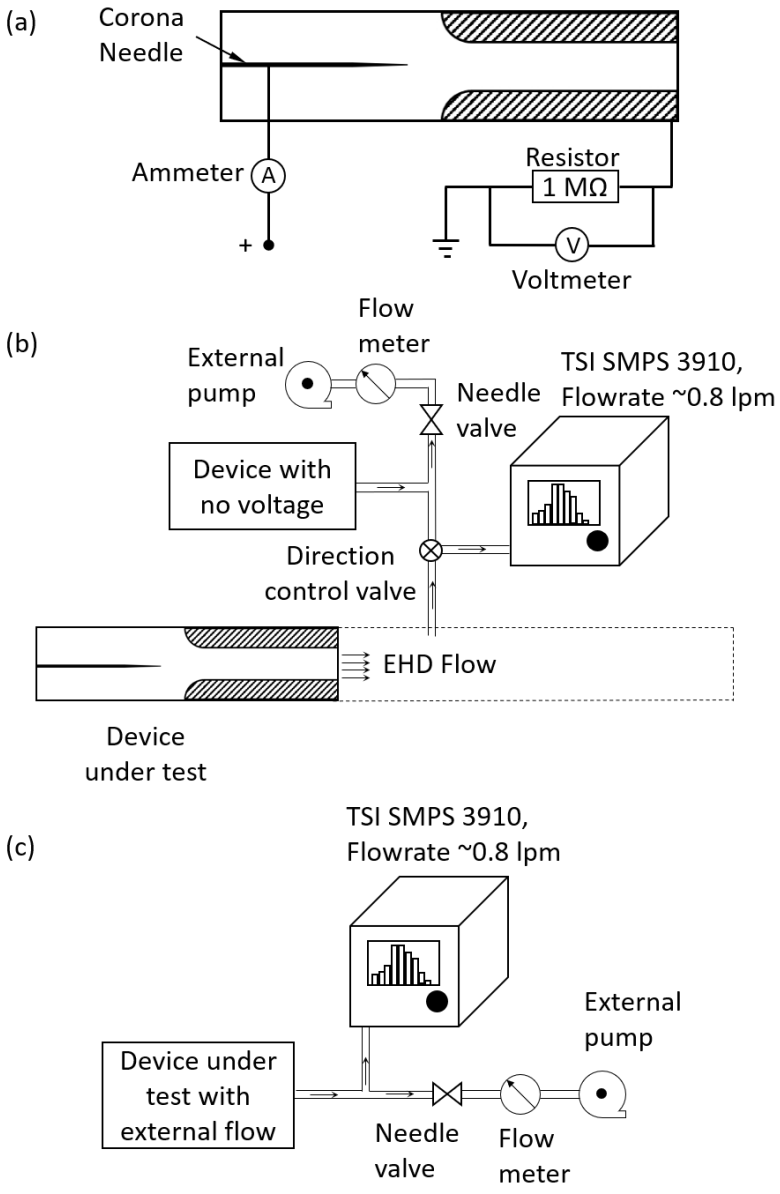

Figure 11.2. Experimental setup for (a) corona current measurement and particle transmission study (b) EHD driven flow; the flow rate through the particle collector can be controlled with an external pump and (c) non-EHD experiment with active corona discharge.

In addition to the ambient particle experiments where the morphology and electrical properties of the particle may vary, the device's performance is characterized using lab-generated NaCl particles. The particles were generated with Up-Mist Medication nebulizer (MADA Products,

Carlstadt, NJ, USA), using dilute solutions of NaCl in distilled water. The nebulizer is connected to HEPA-filtered air to provide the flow required for the generation of NaCl particles. The NaCl particles are generated in a custom 0.3 m^3 stainless steel, well-mixed aerosol chamber. The large volume of the chamber and the mixing fans provide well-mixed conditions, the aerosol concentration in the chamber was spatially uniformed [279]. The particle size distribution depends on the solution concentration, which was prepared to provide particles in size range of 10 nm – 150 nm range. The sodium chloride particle concentration (~ 10^6 #/cc) is two orders of magnitude higher than the background concentration observed in the distilled water nebulization experiment (~1500 #/cc). During NaCl solution nebulization, the particle distribution is dominated by the NaCl particles, the size distributions for distilled water and NaCl solution are given in Figure 11.4 (a) and (b).

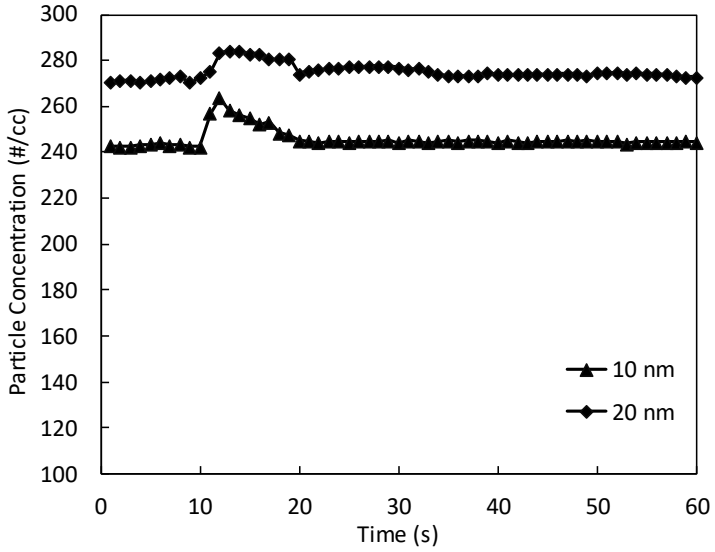

Figure 11.3. Time fluctuations of particle background concentration for corona discharge.

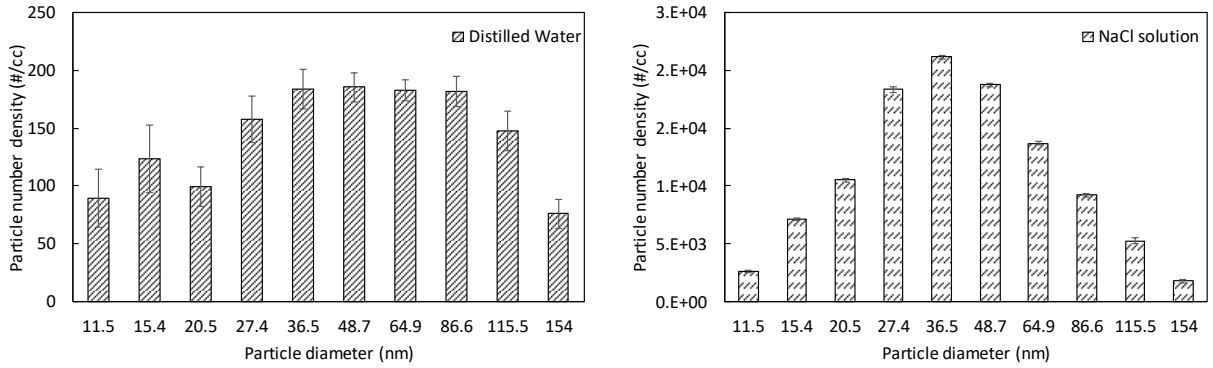

(a) (b)

Figure 11.4. (a) Particle number density (#/cc) distribution for distilled water. Majority of the particles are in the size range of 36- 86 nm (b) Particle number density distribution (#/cc) in sodium chloride experiments.

11.2.4 *Experimental setup for transmission efficiency*

The experimental study characterizing the device's performance consists of two parts: (i) determining the transmission efficiency for EHD flow as a function of corona voltage (ii) examining the effect of particle residence on the transmission efficiency where the flow rate was adjusted keeping the corona voltage constant. The measurements are carried out with the experimental setup as shown in Figure 11.2 (b) and (c). In the EHD flow scenario, see Figure 11.2 (b), two identical EHD devices are connected to the particle sizer in parallel. A selection valve allows for sampling from the EHD collector isokinetically or to switch to the parallel device and sample at the flowrates of the EHD collector. The flowrate of the EHD collector is determined from the velocity measurements. The reference particle concentration $C(no\_Voltage, d_p)$ was determined at the flowrate for each of the experimental conditions which were set by the sampling flow rate of particle sizer (0.8slpm) and an external pump connected in parallel and controlled by

a needle valve. The flow rate of the reference flow is measured using a flowmeter (4140 D, TSI, Shoreview, MN). The flowmeter is calibrated aginst Gilibrator.

To investigate the effect of particle residence on the transmission efficiency, additional flow control was added to increase or reduce the particle residence time in the ionization and the collection regions while maintaining an active corona discharge. The device was connected by a T connector to the ultrafine particle sizer (TSI SMPS 3910) and an external pump with adjustable flow rate, see Figure 11.2(c). Electrostatic dissipative tubing is used for fluidic connections to minimize particle losses. Both reference (no electric field) and EHD collector devices have identical geometries and fluidic connections, see Figure 11.2 (b). A particle sizer (TSI SMPS 3910) in the single size bin mode is used to measure the particle concentrations. The comparison of particle number concentration from the experiments with and without corona provides the transmission efficiency of the device. Similar methodology has been used in previous studies, e.g., [247, 280] and it can be described by the expression:

$$\eta = \frac{C(Voltage, d_p)}{C(no\_Voltage, d_p)}, \tag{11.1}$$

where η is the transmission efficiency, d_p is the particle diameter indicating a specific particle size range, and C is the particle concentration in the prescribed size bin. The transmission efficiency expression is similar to the uncharged ratio as described in previous literature [281, 282]. In the current study, the data is recorded based on the measurement for individual size bin, instead the entire size spectrum scan to address temporal fluctuation in the particle concentration and size distribution in the environment. The sampling time was 60 seconds, and each experiment was repeated at least three times to obtain statistically relevant particle size data. The ozone

concentration was measured using an ozone analyzer (Model 450, Teledyne Instruments) downstream (25 mm) of the tube over the range of corona voltages. Ozone concentration varies from 14 ppb – 24 ppb at the exit of the device for an applied voltage range of 3 kV – 5 kV.

11.3 MODELING

Computational fluid dynamics (CFD) modeling is performed to gain insight into the flow properties in the EHD device as the velocity, ion concentration, and electric field are essential for studying the conditions that effect particle behavior. Note that particle trajectories are not modeled in this work due to ambiguity in the particle charging model. Additional work is required to validate the particle charging and transport models. ANSYS Fluent software was used with custom subroutines for the two-way coupling of ion motion and fluid flow. Figure 11.5 shows the schematic of the modeled geometry. The model is taking advantage of axial symmetry, and 2D axisymmetric model is used. The 3D simulation requires a high computational cost considering high-resolution mesh requirements for the volumetric flux ionization model. The 2D assumption for modeling the corona region showed sufficient accuracy in previous work [7, 86] and the EHD flow general [283-287].

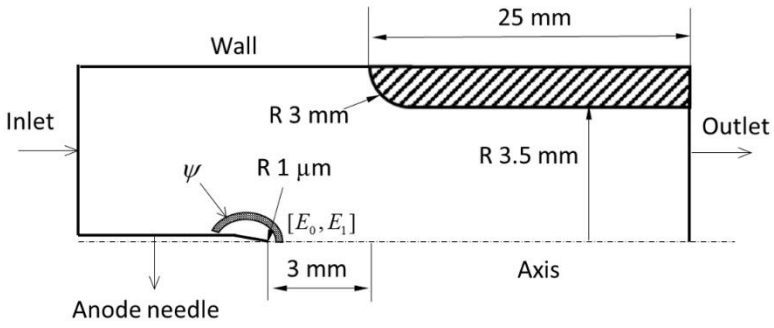

Figure 11.5. Schematic of the computational domain; the model includes the ion generation region defined by the thresholds of the electric field.

The flow field is solved using a finite volume laminar solver; the ion motion effects are incorporated by adding user-defined scalars to represent the electric potential φ and charge density ρ_e. The electric force's effect on the flow is solved by introducing a body force $F_e = -\rho_e \nabla\varphi$ into the momentum equations, thus the governing equations for the flow are:

$$\nabla \cdot \mathbf{u} = 0 \tag{11.2}$$

$$\rho \frac{D\mathbf{u}}{Dt} = -\nabla P + \mu \nabla^2 \mathbf{u} - \rho_e \nabla\varphi \tag{11.3}$$

μ is the dynamic viscosity of the air, ρ is the density of the air, $\mathbf{u}$ is the velocity vector and P is the static pressure. The equations for charge transport are:

$$\frac{\partial \rho_e}{\partial t} + \nabla \cdot [(\mathbf{u} + \mu_b \mathbf{E})\rho_e - D_e \nabla \rho_e] = S_e \tag{11.4}$$

$$\nabla^2 \varphi = -\frac{\rho_e}{\varepsilon} \tag{11.5}$$

where μ_b is the ion mobility, which is approximated as a constant [*2.0E-4 m^2/(Vs)*] [6, 7] and ε is the electric permittivity of free space. D_e is the ion diffusivity described by the electrical mobility equation as in Eq. (4.3) [6, 7]. S_e is the source term of charge density which has a unit of $C/m^3 \cdot s$, it is calculated from the corona current measured at the anode. In the simulation, the charges are introduced into the computational domain within the ionization zone boundary region at the rate calculated from the anode current. Instead of defining a thin surface within the computational

domain to mark as the ionization zone boundary, a region with finite volume is determined by the electric field strength magnitude and constrained within 1 mm of the needle tip.

$$S_e = \begin{cases} \frac{I}{\psi}, for\ |E| \in [E_0, E_1]\ \&\ x_{tip} - x < 1mm \\ 0, otherwise \end{cases} \tag{11.6}$$

where ψ is the volume of the region satisfying $[E_0, E_1]\ \&\ x_{tip} - x < 1mm$ and I is the corona current. The $x_{tip} - x$ term limits the ion production along the needle; in the experiments, the needle tip extends only 1 mm from the needle holder. E_0 is the critical field below which the number of ions recombination is larger than production per drift length, and it is for air. E_1 is the breakdown electric field strength for air (*3.23* MV/m). In fact, both E_0 and E_1 can be used as the criteria for ionization boundary. Since the charge density is balanced inside the ionization region, the corona current equals the ionization boundary's charge density flux. Therefore, by introducing a volumetric flux of charges coming into the domain, the two ionization boundary conditions are used to mark the numerical "ionization region" where the charges (ions) are generated. More details on the treatment can be found in [7].

Table 11.1. Numerical schemes

Model Parameter	Spatial Discretization
P-V Coupling	SIMPLE
Pressure	2nd order upwind
Momentum	2nd order upwind
Electrical potential	2nd order upwind
Charge density	1st order upwind

Table 11.2. Boundary conditions for the numerical simulations

Boundary	The value given at the boundary
Inlet pressure	Atmospheric pressure
Outlet pressure	Atmospheric pressure
Anode needle	3~5 kV & Zero diffusion flux for charge
Cathode tube	0 kV & Zero diffusion flux for charge
Wall boundaries	Zero diffusion flux for electric potential & charge density

Table 11.1 shows the numerical schemes used in the CFD calculations. The second order upwind scheme is used to reduce numerical diffusion. The transient laminar solution is computed, the convergence criteria and the simulation time are set to achieve a time steady velocity profile at the outlet. Since the ion's drift velocity is orders of magnitude greater than the convective flow velocity, the solution for charge transport and electric field converge significantly faster (in convective time) than the flow equations. The boundary conditions are shown in Table 11.2. The total pressure difference between the inlet and outlet is zero as the flow is accelerated only by the ionic drag.

11.4 Results and Discussion

11.4.1 *Voltage-current characteristics*

The corona current and ion concentration at the exit are measured to determine the ion production and ion transport. Table 11.3 shows the corona current (anode current) vs. anode voltage. The current increases with the applied voltage quadratically, which agrees with other results in the literature for different corona configurations [50, 51, 191, 249, 288]. The current

values from the experiments were used in the numerical model as the ionization zone boundary condition. In the CFD, the cathode (grounded electrode) current is determined by integrating the charge flux on the cathode surface.

The cathode current in the simulation agrees within 5% with the experimental measurements. Based on the simulations, the cathode recovers 85-90% of the ion current generated by corona; the other 10-15% are associated with ions exiting the geometry. These computed values of cathode current are in good agreement with the experimental data providing confidence in the numerical approach with respect to ion concentration field in the ionization and collection regions of the EHD collector.

$$I_{cathode} = \int -\mu_b \rho_e \nabla\varphi \mathbf{dA}_{\mathbf{cathode}} \tag{11.7}$$

where $I_{cathode}$ is the cathode current and $\mathbf{A}_{\mathbf{cathode}}$ is the area vector of the cathode.

Table 11.3. Comparison of cathode current between the experiments and CFD

Voltage (kV)	Anode current (μA)	The experimental cathode current (μA)	CFD cathode current (μA)
3	0.7	0.62	0.59
4	3.8	3.34	3.23
5	7.5	6.68	6.64

11.4.2 *Numerical results*

The numerical approach models the process by which the ion-molecule collisions accelerate the bulk flow. Figure 11.6 (a) shows the computed electric field lines. The maximum electric field strength is near the tip of the corona needle, where a small radius of curvature concentrates the

electric field lines, and the field intensity reaches the threshold for ion generation. The effect of the space charge on the electric field is apparent by field line distortions in the region of high ion concentration. These distortions are significantly smaller away from the electrode tip where the charge density is reduced.

(a)

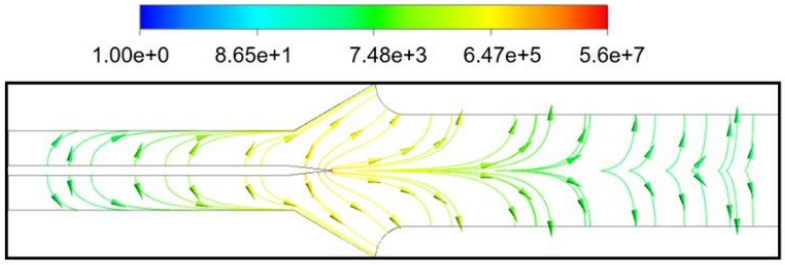

(b)

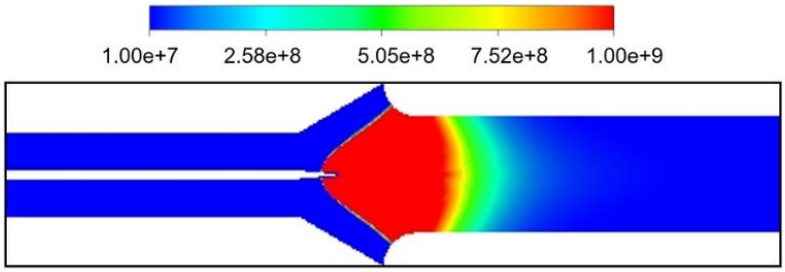

(c)

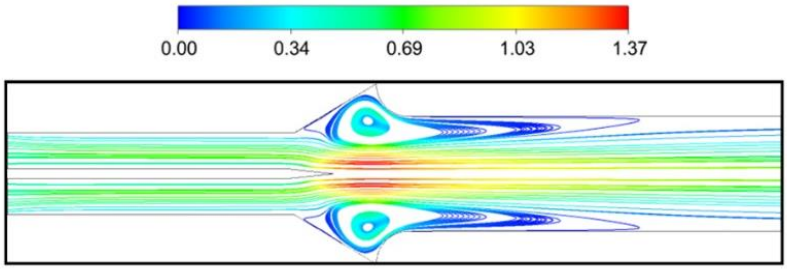

Figure 11.6. Contour plots of the (a) electric field (V/m), (b) ion concentration (#/cc), the contours are clipped to 1e+9#/cc, the maximum value is 5.93+9 #/cc (c) velocity (m/s) and for 3 kV corona voltage between the needle and the ground tube.

Figure 11.6 (b) shows the ion density contours. The ions are generated at the needle tip, and their motion is dominated by the electric field due to their high electrical mobility, as the ion drift velocity is two orders of magnitude greater than the bulk flow [7, 50, 192]. Downstream of the charging region, the electric field is weak, especially near the centerline, the ions exit the domain due to high flow velocities. A recirculation zone is formed upstream of the cathode tube near the rounded edge, as shown in Figure 11.6 (c). This is due to the flow expansion, which creates an adverse pressure gradient in the near-wall region.

11.4.3 *Velocity voltage characteristics*

To validate the EHD modeling approach, the numerical results for corona voltages of φ = 3 kV - 5 kV are compared with the experimental exit velocities. Figure 11.7 shows the velocity profiles plotted for three voltage values. The experiments and numerical results show the maximum velocity is located at the centerline; the profile decays with radial distance. The maximum velocity of the point-to-cylinder corona discharge device is ~4 m/s for both experiments and simulations at 5 kV corona voltage. At higher voltages, arc discharge occurs, the flow velocity drops to zero. The maximum velocities in the numerical simulation are within 10% of the experimental data; the predictions are less accurate at the edges of the domain. The maximum outlet velocity increases linearly with corona voltage. The linear trend of centerline velocity is observed previously in experiments [7, 192]. As the corona voltage increases, the discrepancy between the experiments and CFD increases, and this may be due to averaging of velocity measurements across the hotwire element.

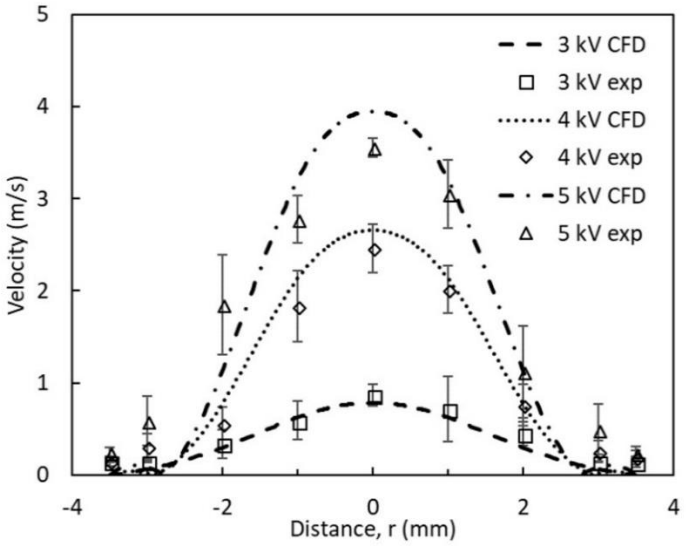

Figure 11.7. Comparison of velocity profile between the experimental results and simulations at the outlet of the EHD induced flow device as shown in Figure 11.6(c).

The velocity profile shows that EHD induced flow in a point-to-tube corona discharge resembles Poiseuille flow near the axis and is significantly different from the pressure-driven flow profile near the walls. The point EHD source generates the flow similar to the submerged laminar jet flow [289]. Laminar flow characteristics are apparent from the experimental data. The Reynolds number (*Re)* is determined based on the tube diameter and the mean velocity at the exit; *Re*~160 for corona voltage of 3 kV and *Re*~400 for corona voltage of 5 kV. Since the 6 kV cases result in the arc, it appears that the corona-induced flow without additional contribution from the pressure term remains laminar for the considered internal flow geometry. If flow instabilities are present in the jet at its source, these temporal fluctuations decay when the flow reaches the outlet.

11.4.4 *Particle transmission*

Particle behavior in the EHD flow was studied experimentally. Figure 11.8 shows the particle transmission efficiency of sodium chloride and ambient particles at different corona voltages. The

lab-generated NaCl particles have higher particle concentrations compared to ambient particles. The transmission efficiency data is similar for both particle types. The transmission efficiency plot can be divided into three distinct regions (i) 10 nm – 20 nm, (i) 20 nm – 85 nm, and (1) 85 nm – 150 nm.

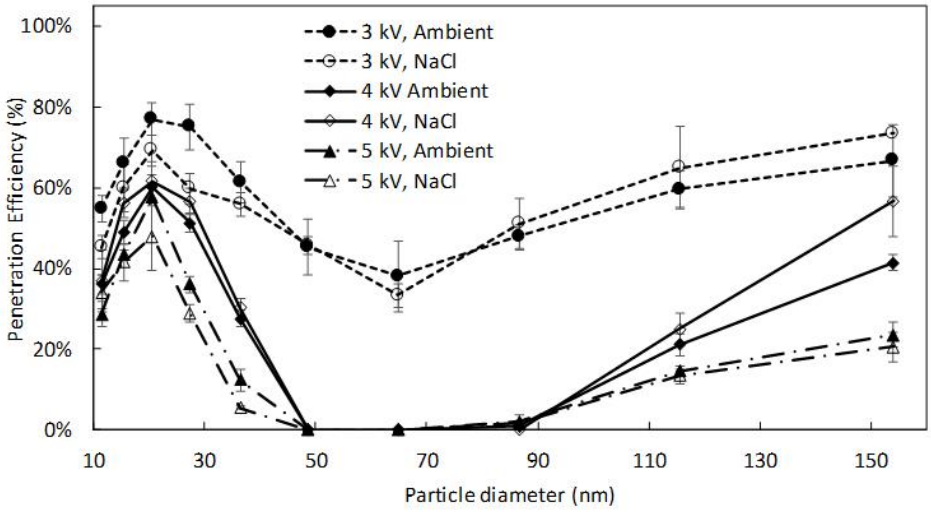

Figure 11.8. Particle transmission efficiency as a function of their size; results for NaCl (unfilled symbols) and ambient particles (filled symbols) at different corona voltages.

For all corona voltages, the transmission efficiency of particles smaller than 20 nm increases with the increase of particle size, i.e., the lowest transmission efficiency for the 10 nm – 20 nm range is observed for 10 nm particles. This behavior has not been previously investigated in the literature. The transmission efficiency of 10 nm particles decreases from 55% at 3 kV corona voltage to 30% for 5 kV corona voltage. These low transmission efficiencies indicate that in EHD flow, 10 nm particle acquire charge with a higher probability that has been reported. Previous research [241, 244, 254, 268, 272, 290] suggests that only a small fraction of particles is charged when the particle diameter is less than 30 nm. For example, according to classical diffusion charging models [254, 267, 268], 12% - 37% of 10 nm particle would acquire charges by the

thermal ions, and the contribution of the field charging is negligible for this particle size. In our experiments, 45% - 70% of 10 nm particles were collected thus acquired at least one charge when passed through the charging region of the EHD driven flow. As the corona voltage increases, the ion concentration and the ion mobility (ion velocity) increases, leading to more frequent and more energetic collisions with the particles. With respect to the increasing transmission efficiency in the 10 nm – 20 nm size range, the previous studies show that it is unlikely for these smaller particles to receive and hold multiple charges [242, 267, 272] independent of particle type. As the particle size increases from 10 nm – 20 nm, their electrical mobility decreases resulting in higher transmission efficiency. Similar trends have been observed in our experiments from 10 nm – 20 nm between NaCl and ambient particles for the range of applied voltages.

The particle size range of 20 nm – 85 nm exhibits a more traditional behavior; as the particle size increases, the transmission efficiency decreases, due to the ability of the particles to carry multiple charges [244, 267, 268, 281, 282] resulting in the higher electrical mobility thus, the lower transmission efficiency. Here the electrical mobility increases faster than the inertial and the drag forces governing the particle motion. For particles greater than 85 nm, the transmission efficiency increases with the increase of their diameter. The drag and inertial forces on the particle increase resulting in the decrease in the migration velocity even though particles attain multiple charges. This trend is consistent with the previous research showing that for polydisperse particles, the transmission efficiency reaches a minimum and then increases for larger particles [244, 262, 268, 272]. However, one of the key findings presented in the current work is the different the ratio of charged to uncharged particle in 10 nm – 20 nm region. We demonstrate that for 10 nm – 20 nm particles, the ratio is approaching unity, as all particles are collected in the presence of repelling electrode; thus, all particles must possess one or more charges. At this time, we do not have a way

to quantify the number of charges as a function of particle size, particle morphology or chemical composition.

The particle-laden flow passes through the charging region where both ion concentration and electrical field are high resulting in the high collision frequency between the ions and the particle in the flow. The collisions with high-energy ions result in high particle charging efficiency and lower particle transmission. The highest charging rate is at the tip of the electrode as the ion concentration (2.44E+11 #/cc), and electric field strength (7.49E+07 V/m) are the highest. The maximum ion concentration and electric field strength for different corona voltages are given in Table 11.4. The ion concentration reduces away from the tip due to radial ion motion caused by the ion drift towards the ground electrode and the space charge effect.

Table 11.4. Maximum computed ion concentration and electric field strength in the ionization zone a function of corona voltages

Voltage (kV)	Ion concentration (#/cc)	Electric field strength (V/m)
3	5.93 E+09	5.6E+07
4	8.62E+10	6.78E+07
5	2.44E+11	7.49E+07

To summarize, the trends of particle transmission in EHD driven flow is similar to the previously reported results for particle greater than 20 nm. However, the significantly lower transmission of 10 nm particles is observed likely due to the efficient charging in the region of high ion concentration / high electrical field within the corona discharge. Here, we also do not quantify the exact number of charges on the particle as a function of ion concentration or electrical field strength; the detailed analytical or empirical model for the dynamic particle charging process

in the corona region is not available. The charges acquired on the particle surface may be stripped from the particle by collision with neutral molecules as the particle travels through the domain into the region with a less intense E-field with lower charge density.

To gain insight into the particle charging and capture dynamics, a series of experiments and numerical simulations were performed (i) by varying the particle residence time in the charging zone and (ii) by varying the particle mobility in the collection zone. The flow rates (thus the residence times) are controlled by the external pump, as shown in Figure 11.2(a). Though the flow in these experiments is not driven by EHD, all particles travel through the ion drift region. The residence time is a function of the bulk flow rate as well as the local flow field effect that is affected by the addition to the body force generated by the corona discharge. Figure 11.9 shows the results of the numerical simulations. The baseline case is the EHD driven flow at 5 kV and flow rate of ~2 slpm (U = 0.9 m/s, *Re*~400) as determined by both CFD and by integrating the experimental velocity profile. Two additional cases are examined where the flow rates were set to 1 slpm (U=0.45 m/s, *Re*~200) and 5 slpm (U=2.25 m/s, *Re*~ 1000) to investigate the effect of the residence time. The corona induced flow has a significant effect on the velocity profile. Figure 11.9 (right) shows flow streamlines colored by the non-dimensional parameter X defined as the ratio of electrostatic force to the inertial force $X = \rho_e \varphi / \rho \mathbf{u}^2$[7]. As the flow rate increases, the inertial term contribution acting on the flow and the particles increases as shown by the smaller region of $X > 1$. For the 5 slpm case, this EHD dominated region exists only near the needle tip while for the lower flowrates all streamlines (thus the particle entering the device) experience $X > 1$ condition.

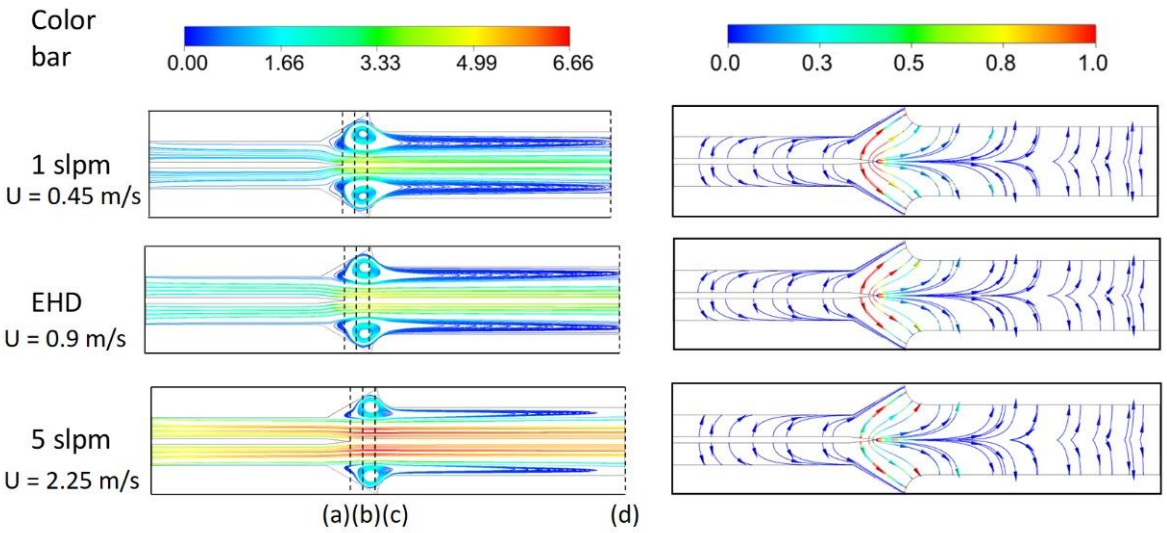

Figure 11.9. Velocity streamlines (left) and non-dimensional parameter X (right) plotted on electric field lines for 1 slpm, EHD (~2 slpm), and 5 slpm flowrates. The dash lines on the streamline plot indicate the location at which velocity profiles are compared.

The velocity profiles at the cross-sections in the charging zone and at the exit are studied to elucidate the residence time effect on particle collection. Figure 11.10(a) shows the velocity profiles at the anode for three different flow rates at a fixed voltage of 5 kV. The higher flow rate reduces the time for the particles to acquire charges as well as the charged particles residence time in the high-intensity electrical field (once the particle sufficiently enters grounded tube the electrical field drops significantly. Both of these conditions yield higher penetration efficiency. Figure 11.10 (b) and (c) shows the velocity profile at the cathode and in between the electrode pair. The velocity profiles have a recirculation region near the wall, the length of the recirculation increases for low flow rates indicating the greater influence of the EHD effect. The corona driven flow produces an adverse pressure gradient at the wall due to local flow acceleration at the axis. For the low flow rate cases, particles entering the device may get trapped in the recirculation regions which increases their residence time in the charging region decreasing their penetration

efficiency. However, in the laminar flow, cross-stream transport is slow (governed by molecular diffusion), and the fraction of total flow entering the recirculation cannot be very high.

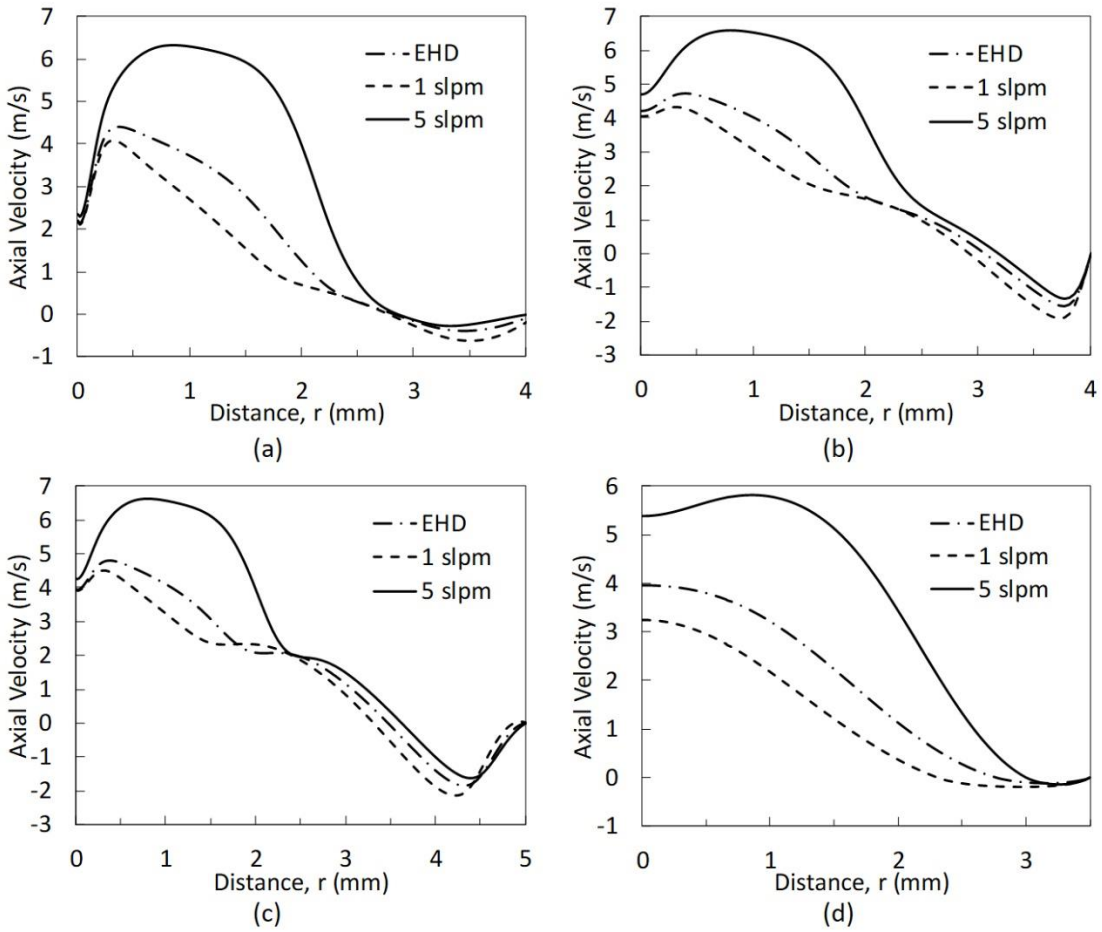

Figure 11.10. Computed velocity profiles in the EHD collector at various axial cross-sections for 5 kV potential difference between the electrodes: a) at the anode electrode (tip of the needle), b) at the cathode electrode (plane aligned with edge of the tube), c) halfway distance between anode and cathode, d) at the exit.

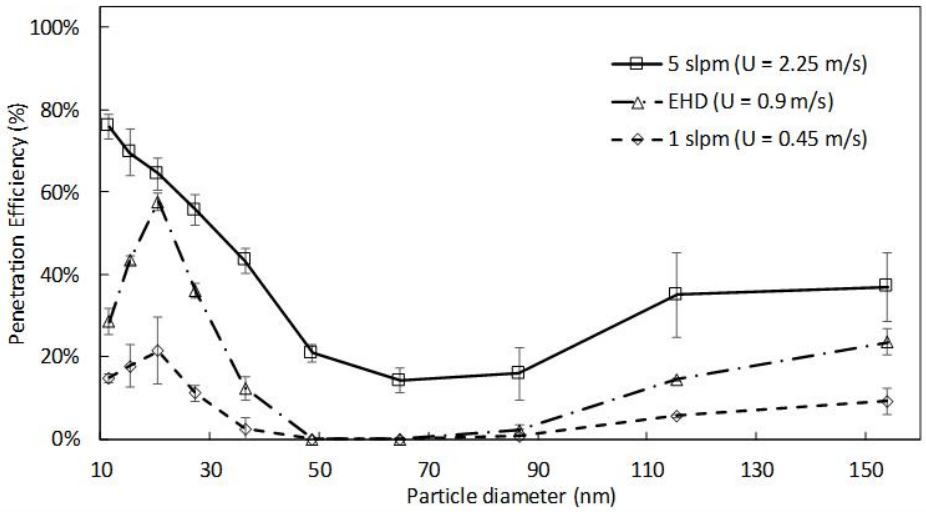

Figure 11.11. Particle transmission efficiency as a function of particle size and flow rate for corona voltage of 5 kV.

Figure 11.11 shows the transmission efficiency of ambient particles for 1 slpm (U = 0.45 m/s), EHD (U = 0.9 m/s), and 5 slpm (2.25 m/s) cases, the corona voltage for all cases is 5 kV. The transmission efficiency trend for particle greater than 20 nm is similar to the data as shown for EHD cases (see Figure 11.8). For the 10 nm – 20 nm size range, the trends change as a function of the flow rate. As expected, the low flow rate (high residence time) results in lower transmission for all particles. The trends similar to EHD flow is observed for particles in 10 nm – 20 nm range suggesting the high fraction of the particles are charged, and these particles have sufficient time in the electric field to be collected onto the ground electrode. The transmission efficiency for 10 nm decreased from 29% to 15%. Another important data trend is the decrease in transmission of 20 nm particle from ~60% in the EHD case to ~20% in the 1 slpm case. If it is assumed that 20 nm particle can carry only a single charge, the most likely explanation for this drop the transmission efficiency is the increase of particle residence time in the high E-field region. The estimation of the particle residence time distribution is challenging as the flow profile is non-uniform, strong

recirculation patterns exist in the particle charging region due to the local momentum source. The higher flow rate case is dominated by the pressure-driven flow as indicated by the parameter X. As the residence time decreases, the transmission efficiency of 10 nm particle increases from 29% to 75% and decreases for the sizes up to 85 nm and then increases, which similar to previously reported results [244, 262, 268, 272, 290].

In the EHD driven case, the flow residence time in the region dominated by EHD ($X > 1$) is ~8 ms – 10 ms. As the flow rate increases to 5 slpm, the residence time drops to ~ 2 ms – 3 ms, and it increases to ~ 17 ms – 20 ms for 1 slpm. The residence time of particle aspirated by the flow is not calculated due to challenges related to the particle charging models in the EHD driven flow. However, based on the experimental results, the fraction of 10 nm - 20 nm particles acquiring charge is as high as 80% for the case with the largest EHD dominated region. The EHD dominated region is also varying in size, thus, a greater portion of the flow (and the particles) passes through it at the lower velocity cases.

The particle forcing in the collection region is varied by introducing a repelling electrode along the axis of symmetry. A voltage of 100 V is applied to the repelling electrode, to increase the Coulombic force acting on the particle in the region between the repelling electrode and the collection tube. The applied voltage on the repelling voltage has no effect on the ionization current (i.e., ion concentration in the charging did not change). Figure 11.12 shows the penetration efficiency of particles with and without repelling voltage. For all the particles, the penetration efficiency decreases with the addition of repelling voltage. The transmission efficiency of 10 nm particles decreases from 28 % to 3 % and for 20 nm particles decreases from 58 % to 3.5 %. Similar results have been observed in previous reports [11, 247, 277]. These low transmission efficiencies

indicate that all the particles receive and retained positive charge(s) in the high ion concentration region. As shown in Figure 11.9, due to mass conservation in the flow acceleration zone, the majority of streamlines are forces to pass through the high ion concentration region. The ion concentration in the ionization region exceeds values of 10E+9 #/cc, which are higher than reported in literature (Table 11.4). Though additional studies to separate the effects charging and residence time in the high-intensity E-field are needed, one can conclude that the charging and collection of the ultrafine particles can be enhanced by their exposure to high charge density-high electric field region. The detailed charging mechanism is not considered in this work, however, the information presented here can aid the development of modified particle charging and transport models that can account for the effect of high ion concentration and strong E-field on particle transport.

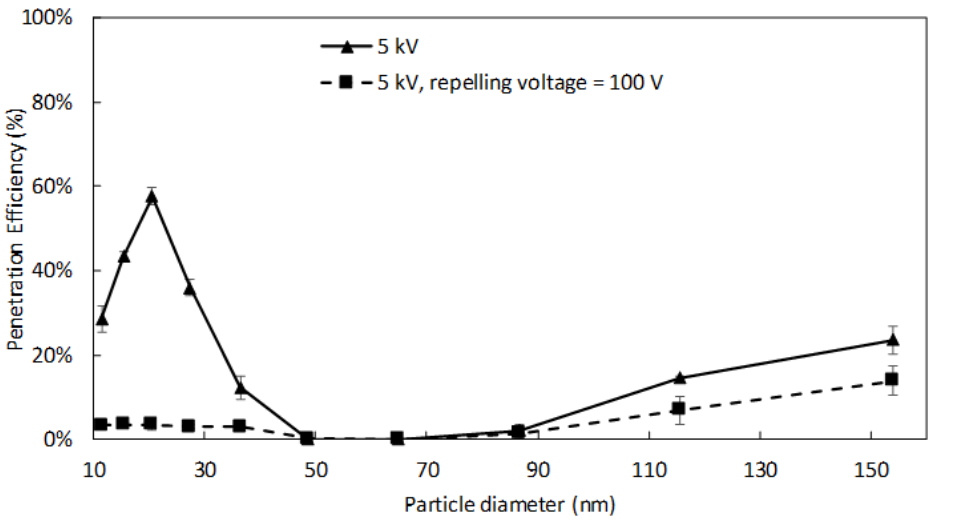

Figure 11.12. Particle transmission efficiency as a function of particle size and repelling voltage for corona voltage of 5 kV.

11.5 Exposure Monitor and In-Situ Analysis

Exposure to airborne particulates, such as particulate emissions from combustion and other manufacturing processes, engineered nanomaterials (ENMs) or endotoxins contained in bacterial cell walls can trigger or exacerbate asthma or cardiovascular diseases. Several studies [291, 292] have compared the relative toxicity of size-fractioned particulates from different sources or locations. Several researchers have reported efforts to develop wearable PM monitors and collectors [278, 279, 293-295]. The use of filters in the wearable sampler is limited due to high pump power consumption, large form factors, and cumbersome setup. Electrostatic collectors can be used to overcome some of these limitations [296]. However, determination of the chemical composition of particles involves liquid extraction as pre-processing steps, which makes offline laboratory analysis cumbersome.

Combustion-generated ultrafine particles (UFP) consist of elemental carbon (EC) and organic carbon (OC). Brown carbon (BrC), characterized by a significant fraction of OC, is a major air pollution component with known health risks [297] and adverse environmental impacts [298]. Though the severity and mortality of many diseases have been linked to UFP exposure, there is uncertainty about specific causative agents' influence. Size distributions, particle morphologies, optical properties, and chemical compositions of these aerosols vary significantly [299, 300]. The UFP chemical composition determines the potential for biochemical reactions with tissue and cells. BrC forms from the incomplete combustion of fossil, biomass, and other carbonaceous fuels. More than 100 polycyclic aromatic hydrocarbons (PAHs) cluster together to form liquid-like particles [301]. The planar nature and inherent stability of aromatic compounds are linked to the formation of soot particles [302, 303]. The size of PAHs in young soot has been approximated by molecular dynamics simulations to be between four rings (Pyrene) and 19 rings (circumcoronene) [304, 305].

The PAHs participating in PM formation or components condensed on PM during the secondary growth [306, 307] can be oxidized in the flame [308, 309]; however, a significant organic fraction is retained by the particle, especially in the low temperature (incomplete) combustion [310].

Total organic carbon (TOC) is an established method for estimating the PM samples' organic fraction [311, 312]. Though the organic fraction in BrC contains a variety of complex hydrocarbon compounds [308, 313], PAHs have been reported to be a major cause of oxidative damage [314-316]. The United States Environmental Protection Agency (EPA) has established a panel of 16 PAH compounds as priority pollutants representing a range of molecular structures with MW=128 to 278 g/mol. More recent reports [317] suggest that larger PAH molecules have a greater carcinogenic impact [318]. PAHs are good candidates for analysis by spectroscopic techniques as they have high absorption coefficients and quantum yields [319]. While fluorescence spectroscopy is very sensitive (~1 ng/mL) for PAH detection [314-316], by itself, it is not specific.

EEM introduces an orthogonal dimension to the standard fluorescence analysis by scanning over a range of single-wavelength-excitations and stacking fluorescence emissions at each excitation wavelength, which provides a three-dimensional (3D) spectral fingerprint. In this 3D matrix, fluorescence red-shifts for higher molecular weights of OC compounds. This variation allows to further differentiate the types of compounds in a complex mixture with overlapping individual spectra. EEM has been previously used for the analysis of combustion PM [320-323]. The challenges of deconvolving the overlapping peaks can be addressed by data-driven techniques [310, 324]. However, similar to the standard laboratory methods, EEM analysis of aerosol samples suffers labor-intensive steps involving sample collection on filters, solvent extraction, filtration, and serial dilutions, which is not amenable for miniaturized sensors. Solid-phase (SP) extraction

into transparent media suitable for spectroscopic interrogation can eliminate these steps enabling in-situ analysis required to develop miniaturized sensors. PDMS provides an attractive option among solid-phase solvents as it is inert, non-toxic, non-flammable, and optically transparent. As PDMS has a relatively low fluorescent background, it is well suited for EEM analysis. For example, liquid phase (LP) -EEM, combined with machine learning for spectra deconvolution, has been used for source identification [324] and source apportionment of environmental samples [325].

Collection of particles on an optically clear substrate is advantageous and can use fluorescence analysis without the extraction of particles. EEM analysis presents an attractive technique among fluorescence-based methods as the multiple single-wavelength-excitations allow simultaneous determination of multiple fluorescent components. EEM analysis has been used previously to analyze fluorophore solutions and for qualitative analysis of organic compound composition in soot [326-328]. Collection of airborne particles on a filter, their extraction into a solvent like cyclohexane and fluorescence analysis is time-consuming. Collection on a transparent substrate followed by solid-phase extraction into the PDMS layer enables in-situ analysis. This section demonstrates a novel electrostatic precipitator (ESP) to collect particles on an optically transparent coated surface and is driven by corona discharge-induced flow. The sample is extracted into PDMS and analyzed for fluorescence. The approach is tested using a laboratory-generated PM, i.e., cigarette smoke, the solid phase EEM [329] is compared to the liquid extraction into cyclohexane[310, 324, 330, 331].

11.5.1 *Design of exposure monitor*

The principle of operation of the ESP is to aspirate the sample by corona discharge induced flow, rapidly charge the particles in the charging zone and collect the particles onto the collection substrate. The high ion concertation and the strong electric field between the corona and ground electrodes result in efficient charging and high collection efficiencies of particulate matter. Figure 11.13 shows the cross-section schematic of the EHD particle collector. The device consists of a high-voltage wire and a grounded rod. When a positive high voltage is applied, the neutral air molecules are ionized. The high voltage ions transfer their momentum to neutral molecules driving the EHD flow. Particles that enter the device aspirated by EHD driven flow are charged and propelled into the collection region. The Coulomb force caused by the electric field between the repelling and ground electrode forces particles onto the glass slide.

The EHD collector used in this study consists of a 0.1 mm diameter tungsten wire and a ground rod of 1.6 mm diameter, as shown in Figure 11.13. The cross-section of the outlet is 25 mm by 10 mm. The horizontal distance between the corona and the ground electrode is 10 mm. The particles are collected onto a microscope glass slide with dimensions of 75 mm by 25 mm. A repelling electrode of negative potential is added on the top surface of the rectangular duct to increase the collection efficiency of the device, and it is 50 mm by 25 mm. The enclosure is fabricated by 3D printing from Polylactic acid (PLA) material. The operating voltage on the corona electrode is varied from 10 kV – 12 kV, and on the repelling electrode is varied from 0 kV – 2 kV. For corona voltage beyond ~13 kV, spark-over occurs.

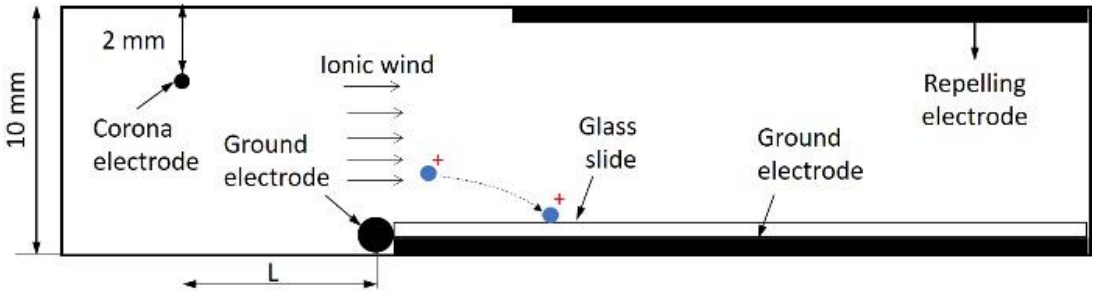

Figure 11.13. Schematic of the electrostatic precipitator

11.5.2 *Particle studies*

Two sets of experiments are conducted in this study (i) to determine PM collection efficiency, ambient particle collection in a typical laboratory environment where the composition of particles is not known, (ii) to demonstrate in-situ fluorescent measurement lab generated cigarette smoke PM were used. For collection efficiency measurements, two identical EHD collectors are connected to a particle sizer in parallel. A selection valve allows for sampling from the EHD collector isokinetically or to switch to the parallel device and sample at the flow rates of the EHD collector. The latter measurements are used as the reference for collection efficiency calculations [261]. Electrostatic dissipative tubing is used for fluidic connections. Both reference (no E-field) and EHD collector devices have identical geometries and fluidic connections. Real-time particle sizers (TSI SMPS 3910) are used to measure the ultrafine PM concentrations. The comparison of particle number concentration from the reference and the EHD collector provides the collection efficiency of the device, as discussed in Eq (11.1).

In addition to the ambient particle measurements, the device's performance is characterized using lab combustion-generated aerosols. The experiments are conducted in a custom-built 0.1 m^3 aerosol chamber [278, 279]. The lab-generated PM was collected onto a glass slide of the EHD collector and PTFE filters. The flow rate of the PTFE filters is the same as that of the EHD particle

collector. Sylgard 184 components were mixed in an appropriate weight ratio to obtain Polydimethylsiloxane (PDMS) solution. After collection, the glass slide was removed from the device and coated with the PDMS solution. We cured the coating for 24 hours at room temperature. Extraction of organic compounds into PDMS was allowed for 24 hours. The glass slide was placed in the custom holder at an angle of 60 degrees to the line of excitation. Collection optics was placed perpendicular to the excitation light.

EEM data was recorded using a spectrofluorometer (Aqualog-880-C, HORIBA Instruments Inc. Edison, NJ). Spectra were recorded for excitation wavelength between 200 nm to 600 nm with 2nm increments. For each excitation wavelength, emission was recorded. To account for Rayleigh scattering, the EEM of blank glass was subtracted. The remaining Rayleigh and Raman scattering peaks were removed using in-house software. The filter sample was extracted into cyclohexane to provide reference measurement. A comparison of liquid-phase extraction EEM (LP-EEM) and solid-phase EEM (SP-EEM) is presented.

11.5.3 *Results and discussion*

Particle behavior in the EHD flow was studied experimentally at 12 kV potential applied between the electrodes. The flow rate induced by corona discharge at these voltage conditions is 16.01 ± 0.37 slpm. Figure 11.14 shows the collection efficiency of ambient particles at a fixed corona voltage and different repelling voltages. The collection efficiency plot can be divided into two regions i) 10 nm – 50 nm, ii) 50 nm – 150 nm. The collection efficiency increases from 10 nm – 50 nm and stays relatively constant up to 150 nm for operation without repelling voltage. As the particle size increases, the particles can carry multiple charges [262, 268], resulting in higher electrical mobility. For all the repelling voltages, the collection efficiency increases from 10 nm –

50 nm. This behavior has been previously reported in the literature [247]. For example, the collection efficiency of 10 nm increases from 30% (no repelling voltage) to 90% for 2 kV repelling voltage. These high collection efficiencies indicate that high ion concentration and high E-field intensity lead to high charging efficiency for a wide range of particle sizes.

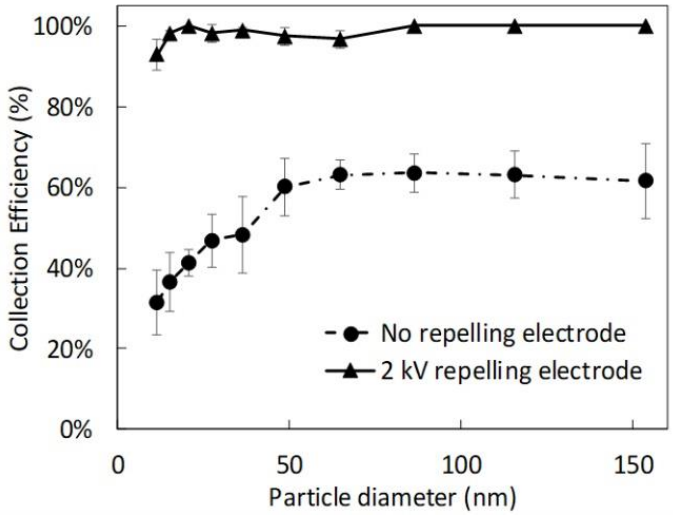

Figure 11.14. Size wise collection efficiency for ambient particles for different repelling voltages.

Lab generated particulate matter (Cigarette smoke) is collected onto the glass slide in the EHD collector at the optimum operating conditions (12 kV corona voltage and 2 kV repelling voltage) and PTFE filters. EEM analysis shows that SP-EEM of cigarette smoke is similar to its LP-EEM, see Figure 11.15. Hence, the fluorescence of combustion-generated PM can be analyzed using solid-phase extraction. The fluorescence intensity of SP-EEM was greater than in LP-EEM which likely due to sample dilution in the liquid analysis. The scattering in SP-EEM was greater compared to LP-EEM for the same concentration, which required additional post-processing using a custom MatLab algorithm. Also, the PAH extraction efficiency of PDMS is possibly lower compared to cyclohexane. To address these two issues and increase the sensitivity of SP-EEMs, further research is needed.

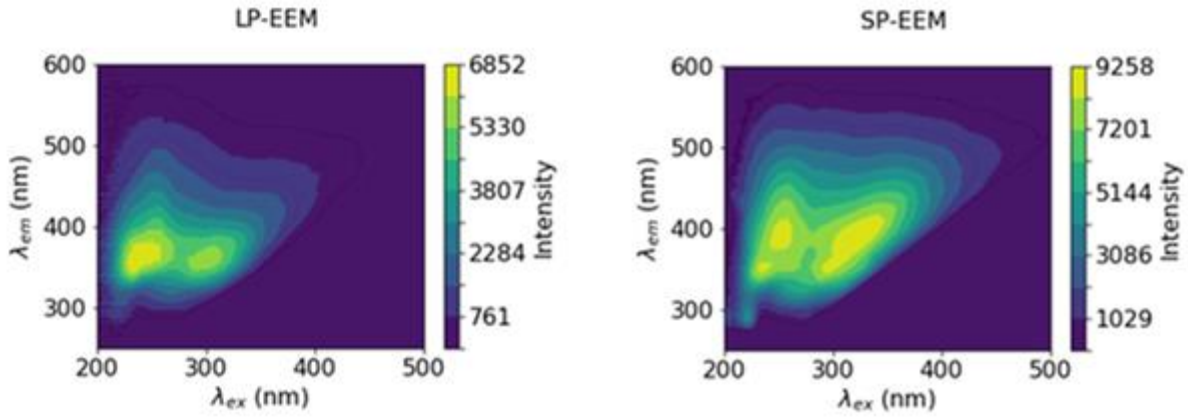

Figure 11.15. EEM of liquid extraction and solid-state fluorescence of cigarette smoke. All features in LP-EEM are retained in the SP-EEM Schematic of the electrostatic precipitator.

11.6 Chapter Summary

This chapter provides an experimental and numerical investigation of particle behavior in the EHD flow. An EHD needle-to-tube device aspirates the flow and collects the particle sample onto the collection electrode without using external pumps or moving parts. The experimental data includes voltage, current, exit velocity profile measurements. Multiphysics numerical simulations show the interaction of the Coulombic force exerted by the ions on the airflow. The addition of charge flux as a model for the gas ionization zone allows for the direct computation of EHD flow, adding the body force to the modified NSE. The numerical simulations agree with experimental data within 10%. The corona-induced flow for the investigated internal flow scenarios remains laminar, the *Re* = 100-400 for the range of operating corona voltages.

Ambient PM and NaCl nanoparticles were used to study the particle behavior in EHD-driven flow; the transmission efficiency is independent of particle type. Measured transmission efficiencies in EHD device are in good agreement with the traditional theories except for the

particles in the 10 nm – 20 nm range. The particle transmission for flow for EHD driven flow is significantly lower. The transmission efficiency for smaller particles is lower than reported by previous research, likely due to the high fraction of 10 nm - 20 nm particles acquiring a unit charge in the EHD dominated region ($X>1$). As the particle size increases from 10 nm to 20 nm, their electrical mobility reduces due to increased particle mass while still possessing only a single charge. This hypothesis is further tested by varying the particle residence time and particle mobility in the EHD dominated region. The transmission efficiency drops to 15% – 20% indicating that the fraction of 10 nm – 20 nm particles with at least one charge is greater than 80% – 85% when the particle residence time increases. The charging to uncharged particle ratio is approaching unity in the particle mobility experiments as all the particles are collected in the presence of repelling electrode; thus, all particles must possess one or more charges. These results suggest the charging of nanoparticles can be enhanced by their prolonged exposure to ion bombardment in the high charge density, high electric field region.

An exposure monitor was developed based on corona-driven EHD flow collection for PM. The collection efficiency of the device is around ~95% for the corona voltage of 12 kV, and repelling voltage of 2 kV over a broad range of particle sizes indicates that high ion concentration and high E-field intensity lead to high charging for ultrafine PM. Cigarette smoke is collected onto the glass slide using the optimized conditions and onto a reference PTFE filter. The fluorescence excitation-emission matrix is compared between the liquid extract and solid-state fluorescence. SP-EEM is similar to LP-EEM, enabling sensor development for in-situ analysis of combustion-generated PM.

Chapter 12. CONCLUSIONS AND FUTURE WORK

12.1 CONCLUSIONS

This dissertation has furthered the development of plasma actuation for propulsion and control of aerial vehicles by developing a deeper understanding of the momentum injection by the plasma actuator. This work also presents methods to improve the momentum and change in aerodynamic forces due to plasma actuation on NACA 0012 at low angles of attack that can be feasible for realistic applications.

Initially, an analytical model that couples space charge, electric field, and momentum transfer is developed in 1D planar coordinates from first principles. The electric current density is analogous to Mott – Gurney law. The derived $(\varphi - I)$ relationship has a similar form as Townsend's relation and is in good agreement with the experimental data. The electrohydrodynamic thrust force is derived from $(\varphi - I)$ relationship and a correction factor for the drag force is introduced for accurate predictions. The model is validated for three independent experiments and agrees within 10%. This thrust model allows for the prediction of thrust force and provides a mathematical framework for the interaction between charged species and fluid.

The second accomplishment is a reduced-order model development for discharge current, current density, and momentum injection utilizing the data from the DBD actuator, i.e., plasma volume, electrical discharge current, and resulting velocity profile. The discharge current analysis yielded an expression similar to the derived $(\varphi - I)$ relationship. The discharge current is directly proportional to the momentum injection and power law in the form of $M = \beta K f_{AC}^{\alpha}(\varphi - \varphi_0)^2$ is obtained. As with DBD actuators, this empirical model can be used to determine the momentum

injected by the actuators and the discharge current expression can be used for accurate boundary conditions in multiphysics modeling of the DBD.

Along with the empirical model for DBD, a new DC augmented dielectric barrier discharge (DBD – DCA) plasma actuator with increased performance was developed. The thrust force of the DBD – DCA plasma actuator with negative DCA generates ~2x greater force than standard DBD. The thrust of the DBD – DCA actuator was increased by introducing various electrode shapes. The maximum thrust generated by the coarse saw tooth electrode DBD – DCA was 52 mN/m and was 4x more than the standard DBD, 2x more than the linear electrode DBD – DCA. By conducting a parametric study on DBD – DCA actuator, we gain an understanding of the conditions required for thrust augmentation.

Finally, the aerodynamic forces on NACA 0012 with the best performing coarse sawtooth electrode DBD – DCA were calculated at low angles of attack. The plasma actuation has increased the lift coefficient by 15% and decreased the drag by 50%. These aerodynamic force measurements allow for calculating forces on aircraft that are crucial for understanding flight control performance.

The presented thesis provides insight into the plasma actuation for aerial vehicles. The results assisted in developing new plasma actuators and can be applied for controlling an aerial vehicle without any moving parts.

12.2 PATH FORWARD

This section proposes future efforts required to bring the plasma actuation technology to a successful airplane integration; it focuses on both scientific and engineering development.

12.2.1 *Momentum characterization with free stream*

Most of the research conducted in this dissertation has focused on the thrust characterization of the actuators in quiescent environments. Future research should extend the study in determining the interaction between the free flow and DBD momentum injection, vortex structures, and the effect of the third electrode with the free stream velocity.

12.2.2 *Improved plasma actuator model*

The analytical and semi-empirical models presented in this dissertation provide a step forward in the plasma actuators modeling and performance characterization. The analytical/semi-empirical expressions can be incorporated into a commercial CFD package to simulate the plasma actuator characteristics. The semi-empirical/analytical expressions coupled with CFD can be used to optimize geometry for improved performance.

12.2.3 *Ozone mitigation*

Plasma actuators often create ozone as a by-product of the ion generation process in the atmospheric air. Ozone can be corrosive to some materials, toxic in high concentrations, and therefore ozone must be mitigated before it leaves the system. Recently ozone mitigation catalysis methods are proposed, and similar methods can be implemented for plasma actuators.

12.2.4 *Acoustic noise characterization*

Adaptation of a concept that utilizes the principles of EHD to produce thrust, in conjunction with low noise electrical power generators for UAV applications, can lead to a substantial reduction in overall noise. An EHD-propelled UAV offers an attractive alternative to conventional aircraft propulsion, and the noise reduction should be quantified.

12.2.5 *Concept plane - plasma actuation*

This dissertation has shown the effect of plasma actuators on the aerodynamic coefficients over a range of wind speeds and AOA for a 2D airfoil section. Based on the 2D tests from the wind tunnel, a concept plane based on plasma actuation can be developed. Control performance of plasma actuation has to be determined.

BIBLIOGRAPHY

[1] E. Moreau, "Airflow control by non-thermal plasma actuators," *Journal of physics D: applied physics*, vol. 40, no. 3, p. 605, 2007.

[2] G. Touchard, "Plasma actuators for aeronautics applications-State of art review," *IJ PEST*, vol. 2, no. 1, pp. 1-25, 2008.

[3] T. C. Corke, C. L. Enloe, and S. P. Wilkinson, "Dielectric Barrier Discharge Plasma Actuators for Flow Control *," *Annu. Rev. Fluid Mech.*, vol. 42, no. 1, pp. 505-529, 2010, doi: 10.1146/annurev-fluid-121108-145550.

[4] I. Adamovich *et al.*, "The 2017 Plasma Roadmap: Low temperature plasma science and technology," *Journal of Physics D: Applied Physics*, vol. 50, no. 32, p. 323001, 2017.

[5] R. S. Vaddi, Y. Guan, A. Mamishev, and I. Novosselov, "Analytical model for electrohydrodynamic thrust," *Proceedings A: Mathematical, Physical and Engineering Sciences*, vol. 476, no. 2241, 2020.

[6] Y. Guan, R. S. Vaddi, A. Aliseda, and I. Novosselov, "Analytical model of electro-hydrodynamic flow in corona discharge," *Physics of Plasmas*, vol. 25, no. 8, 2018, doi: 10.1063/1.5029403.

[7] Y. Guan, R. S. Vaddi, A. Aliseda, and I. Novosselov, "Experimental and numerical investigation of electrohydrodynamic flow in a point-to-ring corona discharge," *Physical Review Fluids*, vol. 3, no. 4, p. 043701, 2018.

[8] H. K. Hari Prasad, R. S. Vaddi, Y. M. Chukewad, E. Dedic, I. Novosselov, and S. B. Fuller, "A laser-microfabricated electrohydrodynamic thruster for centimeter-scale aerial robots," *PloS one*, vol. 15, no. 4, pp. e0231362-e0231362, 2020, doi: 10.1371/journal.pone.0231362.

[9] R. S. Vaddi, Y. Guan, and I. Novosselov, "Behavior of ultrafine particles in electro-hydrodynamic flow induced by corona discharge," *Journal of aerosol science*, vol. 148, 2020, doi: 10.1016/j.jaerosci.2020.105587.

[10] P. Fillingham, R. S. Vaddi, A. Bruning, G. Israel, and I. V. Novosselov, "Drag, lift, and torque on a prolate spheroid resting on a smooth surface in a linear shear flow," *Powder technology*, vol. 377, pp. 958-965, 2021, doi: 10.1016/j.powtec.2020.09.042.

[11] R. S. Vaddi, G. Mahamuni, and I. Novosselov, "Development of an EHD induced wind driven personal exposure monitor and in-situ analysis of characterization of exposure," presented at the International Symposium on Electrohydrodynamics, ISEHD'19, St. Petersburg, Russia, 2019.

[12] R. S. Vaddi, Y. Guan, Z. Y. Chen, A. Mamishev, and I. Novosselov, "Experimental and Numerical Investigation of Corona Discharge Induced Flow on a Flat Plate," presented at the International Symposium on Electrohydrodynamics, ISEHD'19, St. Petersburg, Russia, 2019.

[13] A. C. B. Tang, R. S. Vaddi, A. Mamishev, and I. V. Novosselov, "Empirical Relations for Discharge Current and Momentum Injection in DBD Plasma Actuator," *Journal of physics. D, Applied physics*, 2021, doi: 10.1088/1361-6463/abec0b.

[14] R. S. Vaddi, C. Sota, A. Mamishev, and I. Novosselov, "Active Flow Control of NACA 0012 Airfoil using Sawtooth Direct Current Augmented Dielectric Barrier Discharge Plasma Actuator," *arXiv preprint arXiv:2106.11453*, 2021.

[15] Y. Guan, R. S. Vaddi, A. Aliseda, and I. Novosselov, "Comparison of Analytical and Numerical Models for Point to Ring Electro-Hydrodynamic Flow," presented at the International Symposium on Electrohydrodynamics, ISEHD'19, St. Petersburg, Russia, 2019.

[16] D. S. Drew and K. S. J. Pister, "First takeoff of a flying microrobot with no moving parts," ed, 2017, pp. 1-5.

[17] H. Xu *et al.*, "Flight of an aeroplane with solid-state propulsion," *Nature*, vol. 563, no. 7732, p. 532, 2018, doi: 10.1038/s41586-018-0707-9.

[18] J. Ketcham and H. R. Velkoff, "Effect of an electrostatic field on boundary- layer transition," *AIAA Journal*, vol. 6, no. 7, pp. 1381-1383, 1968, doi: 10.2514/3.4756.

[19] D. M. S. J. Reece Roth, "Electrohydrodynamic Flow Control with a Glow-Discharge Surface Plasma," *AIAA Journal*, vol. 38, no. 7, p. 7, 2000.

[20] S. P. Wilkinson, D. M. Sherman, and J. R. Roth, "Boundary Layer Flow Control with a One Atmosphere Uniform Glow Discharge Surface Plasma - NASA/CR-1998-207309," ed: Sponsoring Organization: NASA Langley Research Center, 1998.

[21] K.-S. Choi, T. Jukes, and R. Whalley, "Turbulent boundary-layer control with plasma actuators," *Philosophical Transactions of the Royal Society of London A: Mathematical, Physical and Engineering Sciences*, vol. 369, no. 1940, pp. 1443-1458, 2011.

[22] X. Zhang, Y. Huang, X. Wang, W. Wang, K. Tang, and H. Li, "Turbulent boundary layer separation control using plasma actuator at Reynolds number 2000000," *Chinese Journal of Aeronautics*, vol. 29, no. 5, pp. 1237-1246, 2016, doi: 10.1016/j.cja.2016.08.006.

[23] Y. Ju and W. Sun, "Plasma assisted combustion: Progress, challenges, and opportunities," *Combustion and Flame*, vol. 162, no. 3, pp. 529-532, 2015, doi: 10.1016/j.combustflame.2015.01.017.

[24] A. Y. Starikovskii, N. B. Anikin, I. N. Kosarev, E. I. Mintoussov, S. M. Starikovskaia, and V. P. Zhukov, "Plasma-assisted combustion," vol. 78, ed, 2006, pp. 1265-1298.

[25] I. A. Krichtafovitch, V. L. Gorobets, S. V. Karpov, and A. V. Mamishev, "Electrostatic Fluid Accelerator and Air Purifier - the Second Wind," presented at the Annual Meeting of the Electrostatics Society of America, Edmonton, Canada, 2005.

[26] D. B. Go, S. V. Garimella, and T. S. Fisher, "Numerical Simulation of Microscale Ionic Wind for Local Cooling Enhancement," ed. USA, 2006, pp. 45-53.

[27] D. B. Go, S. V. Garimella, T. S. Fisher, and R. K. Mongia, "Ionic winds for locally enhanced cooling," *Journal of Applied Physics*, vol. 102, no. 5, 2007, doi: 10.1063/1.2776164.

[28] D. B. Go, R. A. Maturana, T. S. Fisher, and S. V. Garimella, "Enhancement of external forced convection by ionic wind," *International Journal of Heat and Mass Transfer*, vol. 51, no. 25, pp. 6047-6053, 2008, doi: 10.1016/j.ijheatmasstransfer.2008.05.012.

[29] N. E. Jewell-Larsen, C. P. Hsu, I. Krichtafovitch, S. Montgomery, J. Dibene, and A. Mamishev, "CFD analysis of electrostatic fluid accelerators for forced convection cooling," *Dielectrics and Electrical Insulation, IEEE Transactions on*, vol. 15, no. 6, 2008, doi: 10.1109/TDEI.2008.4712680.

[30] C.-C. Wang and S. Roy, "Electrodynamic enhancement of film cooling of turbine blades," *Journal of Applied Physics*, vol. 104, no. 7, pp. 073305-073305-10, 2008, doi: 10.1063/1.2990074.

[31] P. Zhao, S. Portugal, and S. Roy, "Efficient needle plasma actuators for flow control and surface cooling," *Applied physics letters*, vol. 107, no. 3, p. 33501, 2015, doi: 10.1063/1.4927051.

[32] P. C. Dörr and M. J. Kloker, "Crossflow transition control by upstream flow deformation using plasma actuators," *Journal of applied physics*, vol. 121, no. 6, p. 063303, 2017, doi: 10.1063/1.4975791.

[33] N. Szulga, O. Vermeersch, M. Forte, and G. Casalis, "Experimental and Numerical Study of Boundary Layer Transition Control Over an Airfoil Using a DBD Plasma Actuator," *Procedia IUTAM*, vol. 14, pp. 403-412, 2015, doi: 10.1016/j.piutam.2015.03.067.

[34] D. Li Yong Wang Xunnian Zhang, "Control strategies for aircraft airframe noise reduction," *Chinese journal of aeronautics*, vol. 26, no. 2, pp. 249-260, 2013, doi: 10.1016/j.cja.2013.02.001.

[35] L. Al-Sadawi, T. P. Chong, and J.-H. Kim, "Aerodynamic noise reduction by plasma actuators for a flat plate with blunt trailing edge," *Journal of Sound and Vibration*, vol. 439, pp. 173-193, 2019, doi: 10.1016/j.jsv.2018.08.029.

[36] G. P. G. da Silva, J. P. Eguea, J. A. G. Croce, and F. M. Catalano, "Slat aerodynamic noise reduction using dielectric barrier discharge plasma actuators," *Aerospace Science and Technology*, vol. 97, p. 105642, 2020.

[37] J. Cai, Y. Tian, X. Meng, X. Han, D. Zhang, and H. Hu, "An experimental study of icing control using DBD plasma actuator," *Experiments in fluids*, vol. 58, no. 8, pp. 1-8, 2017, doi: 10.1007/s00348-017-2378-y.

[38] P. F. Zhang, A. B. Liu, and J. J. Wang, "Aerodynamic Modification of NACA 0012 Airfoil by Trailing-Edge Plasma Gurney Flap," *AIAA Journal*, vol. 47, no. 10, pp. 2467-2474, 2009, doi: 10.2514/1.43379.

[39] M. Kotsonis, R. Pul, and L. Veldhuis, "Influence of circulation on a rounded-trailing-edge airfoil using plasma actuators," *Experiments in fluids*, vol. 55, no. 7, pp. 1-14, 2014, doi: 10.1007/s00348-014-1772-y.

[40] L.-H. Feng, T.-Y. Shi, and Y.-G. Liu, "Lift Enhancement of an Airfoil and an Unmanned Aerial Vehicle by Plasma Gurney Flaps," *AIAA Journal*, vol. 55, no. 5, pp. 1622-1632, 2017, doi: 10.2514/1.J055426.

[41] K. Kato, C. Breitsamter, and S. Obi, "Flow separation control over a Gö 387 airfoil by nanosecond pulse-periodic discharge," *Experiments in fluids*, vol. 55, no. 8, pp. 1-19, 2014, doi: 10.1007/s00348-014-1795-4.

[42] L. Wang, C. W. Wong, Z. Lu, Z. Wu, and Y. Zhou, "Novel Sawtooth Dielectric Barrier Discharge Plasma Actuator for Flow Separation Control," *AIAA Journal*, vol. 55, no. 4, pp. 1405-1416, 2017, doi: 10.2514/1.J055507.

[43] F. Messanelli, E. Frigerio, E. Tescaroli, and M. Belan, "Separation Control by Plasma Actuators: Effects of Direct Momentum Injection and Vortex Generation," *Flow, turbulence and combustion*, vol. 104, no. 4, pp. 895-926, 2019, doi: 10.1007/s10494-019-00092-2.

[44] B.-G. Cho, S.-H. Hwang, M. Park, J. K. Park, Y.-B. Park, and H. G. Chae, "The effects of plasma surface treatment on the mechanical properties of polycarbonate/carbon nanotube/carbon fiber composites," *Composites. Part B, Engineering*, vol. 160, pp. 436-445, 2019, doi: 10.1016/j.compositesb.2018.12.062.

[45] Y. Hong *et al.*, "Air-plasma surface modification of epoxy resin substrate to improve electroless copper plating of printed circuit board," *Vacuum*, vol. 170, p. 108967, 2019, doi: 10.1016/j.vacuum.2019.108967.

[46] M. Raguse *et al.*, "Understanding of the importance of the spore coat structure and pigmentation in theBacillus subtilisspore resistance to low-pressure plasma sterilization," *Journal of physics. D, Applied physics*, vol. 49, no. 28, p. 285401, 2016, doi: 10.1088/0022-3727/49/28/285401.

[47] A. Sakudo, Y. Yagyu, and T. Onodera, "Disinfection and Sterilization Using Plasma Technology: Fundamentals and Future Perspectives for Biological Applications," *International journal of molecular sciences*, vol. 20, no. 20, p. 5216, 2019, doi: 10.3390/ijms20205216.

[48] K. Ananthakumar, D. Rajamani, E. Balasubramanian, and J. Paulo Davim, "Measurement and optimization of multi-response characteristics in plasma arc cutting of Monel 400™ using RSM and TOPSIS," *Measurement : journal of the International Measurement Confederation*, vol. 135, pp. 725-737, 2019, doi: 10.1016/j.measurement.2018.12.010.

[49] A. Parthiban, J. P. Prasath, P. Vivek, and R. Pugazhenthi, "Experimental Investigation of Plasma ARC Cutting for Stainless Steel Sheet," *International Journal of Mechanical and Production Engineering Research and Development*, vol. 8, no. 1, pp. 907-914, 2018, doi: 10.24247/ijmperdfeb2018110.

[50] R. S. Sigmond, "Simple approximate treatment of unipolar space-charge-dominated coronas: The Warburg law and the saturation current," *Journal of Applied Physics*, vol. 53, no. 2, pp. 891-898, 1982, doi: 10.1063/1.330557.

[51] J. S. Townsend, *Electricity in gases*. Oxford: Clarendon Press, 1915.

[52] J. S. Townsend, "XI. The potentials required to maintain currents between coaxial cylinders," *The London, Edinburgh, and Dublin Philosophical Magazine and Journal of Science*, vol. 28, no. 163, pp. 83-90, 1914.

[53] P. Cooperman, "A theory for space-charge-limited currents with application to electrical precipitation," *Transactions of the American Institute of Electrical Engineers, Part I: Communication and Electronics*, vol. 79, no. 1, pp. 47-50, 1960.

[54] R. Sigmond and M. Goldman, "Electrical Breakdown and Discharges in Gases-Part B, Macroscopic Processes and Discharges," *Eds. EE Kunhardt and LH Luessen, Plenum, NY*, 1981.

[55] R. Sigmond, "Simple approximate treatment of unipolar space-charge-dominated coronas: The Warburg law and the saturation current," *Journal of Applied Physics*, vol. 53, no. 2, pp. 891-898, 1982.

[56] P. Giubbilini, "The current-voltage characteristics of point-to-ring corona," *Journal of applied physics*, vol. 64, no. 7, pp. 3730-3732, 1988.

[57] X. Meng, H. Zhang, and J. Zhu, "A general empirical formula of current–voltage characteristics for point-to-plane geometry corona discharges," *Journal of Physics D: Applied Physics*, vol. 41, no. 6, p. 065209, 2008.

[58] K. Yamada, "An empirical formula for negative corona discharge current in point-grid electrode geometry," *Journal of applied physics*, vol. 96, no. 5, pp. 2472-2475, 2004.

[59] S. I. Wais and D. D. Giliyana, "Sphere-to-plane electrodes configuration of positive and negative plasma corona discharge," *Am J Mod Phys*, vol. 2, no. 2, pp. 46-52, 2013.

[60] P. Mikropoulos and V. Zagkanas, "A computational method for positive corona inception in the coaxial cylindrical electrode arrangement in air under variable atmospheric conditions," in *Proceeding of the 16 th International Symposium on High Voltage Engineering. Paper B-10*, 2009.

[61] Y. Zheng, B. Zhang, and J. He, "Current-voltage characteristics of dc corona discharges in air between coaxial cylinders," *Physics of Plasmas*, vol. 22, no. 2, p. 023501, 2015.

[62] A. A. Martins, "Simulation of a wire-cylinder-plate positive corona discharge in nitrogen gas at atmospheric pressure," *Physics of Plasmas*, vol. 19, no. 6, p. 063502, 2012.

[63] P. Giubbilini, "Mobility measurement of large ions in air from a point-to-ring corona source," *Journal of applied physics*, vol. 81, no. 5, pp. 2101-2104, 1997.

[64] Y. Zhang, L. Liu, Y. Chen, and J. Ouyang, "Characteristics of ionic wind in needle-to-ring corona discharge," *Journal of Electrostatics*, vol. 74, pp. 15-20, 2015.

[65] V. T. Dau, T. X. Dinh, T. T. Bui, C.-D. Tran, H. T. Phan, and T. Terebessy, "Corona based air-flow using parallel discharge electrodes," *Experimental Thermal and Fluid Science*, vol. 79, pp. 52-56, 2016.

[66] M. J. Johnson, R. Tirumala, and D. B. Go, "Analysis of geometric scaling of miniature, multi-electrode assisted corona discharges for ionic wind generation," *Journal of Electrostatics*, vol. 74, pp. 8-14, 2015.

[67] R. Tirumala and D. B. Go, "Comparative study of corona discharge simulation techniques for electrode configurations inducing non-uniform electric fields," *Journal of Electrostatics*, vol. 72, no. 2, pp. 99-106, 2014.

[68] M. Robinson, "Movement of air in the electric wind of the corona discharge," *Transactions of the American Institute of Electrical Engineers, Part I : Communication and Electronics*, vol. 80, no. 2, p. 8, 1961.

[69] S.-I. Cheng, "Glow discharge as an advanced propulsion device," *ARS Journal*, vol. 32, no. 12, pp. 1910-1916, 1962.

[70] E. A. Christenson and P. S. Moller, "Ion-neutral propulsion in atmospheric media," *AIAA Journal*, vol. 5, no. 10, pp. 1768-1773, 1967.

[71] L. Pekker and M. Young, "Model of ideal electrohydrodynamic thruster," *Journal of Propulsion and Power*, vol. 27, no. 4, pp. 786-792, 2011.

[72] N. F. Mott, *Electronic processes in ionic crystals*, 2d ed. ed. (Ionic crystals). Oxford: Oxford, Clarendon Press, 1948.

[73] P. A. Durbin, "Asymptotic analysis of corona discharge from thin electrodes," 1986.

[74] S. Mukkavilli, C. Lee, K. Varghese, and L. Tavlarides, "Modeling of the electrostatic corona discharge reactor," *IEEE transactions on plasma science*, vol. 16, no. 6, pp. 652-660, 1988.

[75] J.-S. Chang, P. A. Lawless, and T. Yamamoto, "Corona discharge processes," *IEEE Transactions on plasma science*, vol. 19, no. 6, pp. 1152-1166, 1991.

[76] F. Yang *et al.*, "Corona driven air propulsion for cooling of electronics," in *XIIIth International Symposium on High Voltage Engineering*, 2003, vol. 1, no. 4.

[77] L. Li, S. J. Lee, W. Kim, and D. Kim, "An empirical model for ionic wind generation by a needle-to-cylinder dc corona discharge," *Journal of Electrostatics*, vol. 73, pp. 125-130, 2015.

[78] E. Moreau, N. Benard, J.-D. Lan-Sun-Luk, and J.-P. Chabriat, "Electrohydrodynamic force produced by a wire-to-cylinder dc corona discharge in air at atmospheric pressure," *Journal of Physics D: Applied Physics*, vol. 46, no. 47, p. 475204, 2013.

[79] K. Masuyama and S. R. Barrett, "On the performance of electrohydrodynamic propulsion," *Proceedings of the Royal Society A: Mathematical, Physical and Engineering Sciences*, vol. 469, no. 2154, p. 20120623, 2013.

[80] K. Adamiak and P. Atten, "Simulation of corona discharge in point–plane configuration," *Journal of electrostatics*, vol. 61, no. 2, pp. 85-98, 2004.

[81] L. Zhao and K. Adamiak, "EHD flow in air produced by electric corona discharge in pin–plate configuration," *Journal of electrostatics*, vol. 63, no. 3, pp. 337-350, 2005.

[82] L. Zhao and K. Adamiak, "Numerical simulation of the effect of EHD flow on corona discharge in compressed air," *IEEE Transactions on Industry Applications*, vol. 49, no. 1, pp. 298-304, 2013.

[83] P. Lawless and L. Sparks, "Interactive computer model for calculating VI curves in ESPs (electrostatic precipitators): Version 1. 0. Report for July 1984-July 1986," Research Triangle Inst., Durham, NC (USA), 1986.

[84] S. Cristina, G. Dinelli, and M. Feliziani, "Numerical computation of corona space charge and VI characteristic in DC electrostatic precipitators," *IEEE Transactions on industry applications*, vol. 27, no. 1, pp. 147-153, 1991.

[85] T. Yamamoto, M. Okuda, and M. Okubo, "Three-dimensional ionic wind and electrohydrodynamics of tuft/point corona electrostatic precipitator," *IEEE Transactions on Industry Applications*, vol. 39, no. 6, pp. 1602-1607, 2003.

[86] K. Adamiak, "Numerical models in simulating wire-plate electrostatic precipitators: a review," *Journal of Electrostatics*, vol. 71, no. 4, pp. 673-680, 2013.

[87] N. Jewell-Larsen, P. Zhang, C.-P. Hsu, I. Krichtafovitch, and A. Mamishev, "Coupled-physics modeling of electrostatic fluid accelerators for forced convection cooling," in *9th AIAA/ASME Joint Thermophysics and Heat Transfer Conference*, 2006, p. 3607.

[88] D. B. Go, S. V. Garimella, and T. S. Fisher, "Numerical simulation of microscale ionic wind for local cooling enhancement," in *Thermal and Thermomechanical Phenomena in Electronics Systems, 2006. ITHERM'06. The Tenth Intersociety Conference on*, 2006: IEEE, pp. 45-53.

[89] D. B. Go, S. V. Garimella, T. S. Fisher, and R. K. Mongia, "Ionic winds for locally enhanced cooling," *Journal of Applied Physics*, vol. 102, no. 5, p. 053302, 2007.

[90] N. Jewell-Larsen, C. Hsu, I. Krichtafovitch, S. Montgomery, J. Dibene, and A. V. Mamishev, "CFD analysis of electrostatic fluid accelerators for forced convection cooling," *IEEE Transactions on Dielectrics and Electrical Insulation*, vol. 15, no. 6, 2008.

[91] N. A. Kaptsov, "Electrical phenomena in gases and vacuum," ed. Gostehizdat, Moscow, 1950.

[92] F. Peek, "The law of corona and the dielectric strength of air," *Proceedings of the American Institute of Electrical Engineers*, vol. 30, no. 7, pp. 1485-1561, 1911.

[93] J. Kriegseis, C. Schwarz, A. Duchmann, S. Grundmann, and C. Tropea, "PIV-based estimation of DBD plasma-actuator force terms," in *50th AIAA aerospace sciences meeting including the new horizons forum and aerospace exposition*, 2012, p. 411.

[94] M. Forte, J. Jolibois, J. Pons, E. Moreau, G. Touchard, and M. Cazalens, "Optimization of a dielectric barrier discharge actuator by stationary and non-stationary measurements of the induced flow velocity: application to airflow control," *Experiments in Fluids*, vol. 43, no. 6, pp. 917-928, 2007, doi: 10.1007/s00348-007-0362-7.

[95] E. Moreau, J. Cazour, and N. Benard, "Influence of the air-exposed active electrode shape on the electrical, optical and mechanical characteristics of a surface dielectric barrier discharge plasma actuator," *Journal of Electrostatics*, vol. 93, pp. 146-153, 2018.

[96] N. Benard and E. Moreau, "Electrical and mechanical characteristics of surface AC dielectric barrier discharge plasma actuators applied to airflow control," *Experiments in Fluids*, vol. 55, no. 11, p. 1846, 2014.

[97] G. Neretti, P. Seri, M. Taglioli, A. Shaw, F. Iza, and C. A. Borghi, "Geometry optimization of linear and annular plasma synthetic jet actuators," *Journal of Physics D: Applied Physics*, vol. 50, no. 1, p. 015210, 2016.

[98] E. Defoort, R. Bellanger, C. Batiot-Dupeyrat, and E. Moreau, "Ionic wind produced by a DC needle-to-plate corona discharge with a gap of 15 mm," *Journal of Physics D: Applied Physics*, vol. 53, no. 17, p. 175202, 2020.

[99] C. L. Enloe, T. E. McLaughlin, R. D. VanDyken, K. D. Kachner, E. J. Jumper, and T. C. Corke, "Mechanisms and responses of a single dielectric barrier plasma actuator: plasma morphology," *AIAA Journal*, vol. 42, no. 3, p. 589, 2004, doi: 10.2514/1.2305.

[100] J. Reece Roth and X. Dai, "Optimization of the aerodynamic plasma actuator as an electrohydrodynamic (EHD) electrical device," vol. 19, ed, 2006, pp. 14604-14631.

[101] T. Matsuno, H. Kawazoe, and R. C. Nelson, "Aerodynamic control of high performance aircraft using pulsed plasma actuators," ed, 2009.

[102] M. Han, J. Li, Z. Niu, H. Liang, G. Zhao, and W. Hua, "Aerodynamic performance enhancement of a flying wing using nanosecond pulsed DBD plasma actuator," *Chinese Journal of Aeronautics*, vol. 28, no. 2, pp. 377-384, 2015, doi: 10.1016/j.cja.2015.02.006.

[103] S. Grundmann, M. Frey, and C. Tropea, "Unmanned aerial vehicle (UAV) with plasma actuators for separation control," in *47th AIAA Aerospace Sciences Meeting including The New Horizons Forum and Aerospace Exposition*, 2009, p. 698.

[104] A. R. Hoskinson and N. Hershkowitz, "Differences between dielectric barrier discharge plasma actuators with cylindrical and rectangular exposed electrodes," *Journal of Physics D: Applied Physics*, vol. 43, no. 6, p. 065205, 2010, doi: 10.1088/0022-3727/43/6/065205.

[105] J. Omidi and K. Mazaheri, "Micro-plasma actuator mechanisms in interaction with fluid flow for wind energy applications: Physical parameters," *Physics of Fluids*, vol. 32, no. 7, p. 077107, 2020.

[106] F. Rodrigues, J. Pascoa, and M. Trancossi, "Analysis of innovative plasma actuator geometries for boundary layer control," in *ASME 2016 International Mechanical Engineering Congress and Exposition*, 2016: American Society of Mechanical Engineers Digital Collection.

[107] E. Moreau, K. Bayoda, and N. Benard, "Streamer propagation and pressure waves produced by a nanosecond pulsed surface sliding discharge: effect of the high voltage electrode shape," *Journal of Physics D: Applied Physics*, 2020.

[108] R. J. Durscher and S. Roy, "Three-dimensional flow measurements induced from serpentine plasma actuators in quiescent air," *Journal of physics. D, Applied physics*, vol. 45, no. 3, p. 035202, 2012, doi: 10.1088/0022-3727/45/3/035202.

[109] R. Joussot, A. Leroy, R. Weber, H. Rabat, S. Loyer, and D. Hong, "Plasma morphology and induced airflow characterization of a DBD actuator with serrated electrode," *Journal of physics. D, Applied physics*, vol. 46, no. 12, p. 125204, 2013, doi: 10.1088/0022-3727/46/12/125204.

[110] F. Rodrigues, A. Mushyam, J. Pascoa, and M. Trancossi, "A new plasma actuator configuration for improved efficiency: The stair-shaped dielectric barrier discharge actuator," *Journal of Physics D: Applied Physics*, vol. 52, no. 38, p. 385201, 2019.

[111] G. I. Font, "Boundary Layer Control with Atmospheric Plasma Discharges," *AIAA Journal*, vol. 44, no. 7, pp. 1572-1578, 2006, doi: 10.2514/1.18542.

[112] G. Font and W. Morgan, "Plasma discharges in atmospheric pressure oxygen for boundary layer separation control," in *35th AIAA Fluid Dynamics Conference and Exhibit*, 2005, p. 4632.

[113] D. M. Orlov, *Modelling and simulation of single dielectric barrier discharge plasma actuators*. Thesis (Ph.D.), University of Notre Dame, 2006.

[114] G. R. Tathiri, E. Esmaeilzadeh, S. M. Mirsajedi, and H. M. Moghaddam, "Experimental Investigation of "Why an AC Dielectric Barrier Discharge Plasma Actuator is Preferred to DC Corona Wind Actuator in Boundary Layer Flow Control?," *Journal of Applied Fluid Mechanics*, vol. 7, no. 3, pp. 525-534, 2014.

[115] J. Pons, E. Moreau, and G. Touchard, "Asymmetric surface dielectric barrier discharge in air at atmospheric pressure: electrical properties and induced airflow characteristics," *Journal of physics. D, Applied physics*, vol. 38, no. 19, pp. 3635-3642, 2005, doi: 10.1088/0022-3727/38/19/012.

[116] I. Biganzoli, R. Barni, and C. Riccardi, "Temporal evolution of a surface dielectric barrier discharge for different groups of plasma microdischarges," *Journal of physics. D, Applied physics*, vol. 46, no. 2, p. 025201, 2013, doi: 10.1088/0022-3727/46/2/025201.

[117] I. Biganzoli, R. Barni, C. Riccardi, A. Gurioli, and R. Pertile, "Optical and electrical characterization of a surface dielectric barrier discharge plasma actuator," *Plasma sources science & technology*, vol. 22, no. 2, p. 25009, 2013, doi: 10.1088/0963-0252/22/2/025009.

[118] I. Biganzoli, R. Barni, and C. Riccardi, "Note: On the use of Rogowski coils as current probes for atmospheric pressure dielectric barrier discharges," *Review of scientific instruments*, vol. 84, no. 1, pp. 016101-016101, 2013, doi: 10.1063/1.4773233.

[119] C. Louste, G. Artana, E. Moreau, and G. Touchard, "Sliding discharge in air at atmospheric pressure: electrical properties," *Journal of Electrostatics*, vol. 63, no. 6-10, pp. 615-620, 2005.

[120] C. A. Borghi, A. Cristofolini, G. Grandi, G. Neretti, and P. Seri, "A plasma aerodynamic actuator supplied by a multilevel generator operating with different voltage waveforms," *Plasma sources science & technology*, vol. 24, no. 4, p. 45018, 2015, doi: 10.1088/0963-0252/24/4/045018.

[121] J.-C. Laurentie, J. Jolibois, and E. Moreau, "Surface dielectric barrier discharge: Effect of encapsulation of the grounded electrode on the electromechanical characteristics of the plasma actuator," *Journal of Electrostatics*, vol. 67, no. 2-3, pp. 93-98, 2009.

[122] J. Kriegseis, B. Möller, S. Grundmann, and C. Tropea, "Capacitance and power consumption quantification of dielectric barrier discharge (DBD) plasma actuators," *Journal of electrostatics*, vol. 69, no. 4, pp. 302-312, 2011, doi: 10.1016/j.elstat.2011.04.007.

[123] J.-S. Yoon and J.-H. Han, "One-equation modeling and validation of dielectric barrier discharge plasma actuator thrust," *Journal of Physics D: Applied Physics*, vol. 47, no. 40, p. 405202, 2014.

[124] B. Dong, J. M. Bauchire, J. M. Pouvesle, P. Magnier, and D. Hong, "Experimental study of a DBD surface discharge for the active control of subsonic airflow," *Journal of physics. D, Applied physics*, vol. 41, no. 15, p. 155201, 2008, doi: 10.1088/0022-3727/41/15/155201.

[125] J. Kriegseis, A. Duchmann, C. Tropea, and S. Grundmann, "On the classification of dielectric barrier discharge plasma actuators: A comprehensive performance evaluation study," *Journal of Applied Physics*, vol. 114, no. 5, 2013, doi: 10.1063/1.4817366.

[126] C. L. Enloe *et al.*, "Mechanisms and responses of a dielectric barrier plasma actuator: Geometric effects," *AIAA journal*, vol. 42, no. 3, pp. 595-604, 2004.

[127] R. Durscher and S. Roy, "Evaluation of thrust measurement techniques for dielectric barrier discharge actuators," *Experiments in fluids*, vol. 53, no. 4, pp. 1165-1176, 2012, doi: 10.1007/s00348-012-1349-6.

[128] D. E. Ashpis and M. C. Laun, "Characterization of DBD Plasma Actuators Performance without External Flow-Part I: Thrust-Voltage Quadratic Relationship in Logarithmic Space for Sinusoidal Excitation," in *47th AIAA Plasmadynamics and Lasers Conference*, 2016, p. 4013.

[129] D. E. Ashpis and M. C. Laun, "Dielectric Barrier Discharge Plasma Actuator Thrust Measurement Methodology Incorporating Antithrust Hypothesis," *AIAA journal. American Institute of Aeronautics and Astronautics*, vol. 55, no. 12, p. 4181, 2017, doi: 10.2514/1.J055856.

[130] D. E. Ashpis, M. C. Laun, and E. L. Griebeler, "Progress Toward Accurate Measurement of Dielectric Barrier Discharge Plasma Actuator Power," *AIAA Journal*, vol. 55, no. 7, pp. 2254-2268, 2017, doi: 10.2514/1.J055816.

[131] T. Matsuno, M. Sugahara, H. Kawazoe, and H. Nishida, "Development of serrated multi-electrode plasma actuators for enhanced force production," in *54th AIAA Aerospace Sciences Meeting*, 2016, p. 1691.

[132] A. R. Hoskinson, N. Hershkowitz, and D. E. Ashpis, "Force measurements of single and double barrier DBD plasma actuators in quiescent air," *Journal of Physics D: Applied Physics*, vol. 41, no. 24, p. 245209, 2008, doi: 10.1088/0022-3727/41/24/245209.

[133] M. Kotsonis, S. Ghaemi, L. Veldhuis, and F. Scarano, "Measurement of the body force field of plasma actuators," *Journal of physics. D, Applied physics*, vol. 44, no. 4, p. 045204, 2011, doi: 10.1088/0022-3727/44/4/045204.

[134] S. P. Wilkinson, E. Siochi, G. Sauti, T.-B. Xu, M. Meador, and H. Guo, "Evaluation of dielectric-barrier-discharge actuator substrate materials," in *45th AIAA Plasmadynamics and Lasers Conference*, 2014, p. 2810.

[135] F. O. Thomas, T. C. Corke, M. Iqbal, A. Kozlov, and D. Schatzman, "Optimization of Dielectric Barrier Discharge Plasma Actuators for Active Aerodynamic Flow Control," *AIAA Journal*, vol. 47, no. 9, pp. 2169-2178, 2009, doi: 10.2514/1.41588.

[136] J. Zito, D. Arnold, T. Houba, J. Soni, R. Durscher, and S. Roy, "Microscale dielectric barrier discharge plasma actuators: Performance characterization and numerical comparison," in *43rd AIAA Plasmadynamics and Lasers Conference*, 2012, p. 3091.

[137] J.-S. Yoon and J.-H. Han, "Semiempirical Thrust Model of Dielectric Barrier Plasma Actuator for Flow Control," *Journal of Aerospace Engineering*, vol. 28, no. 1, p. 4014041, 2015, doi: 10.1061/(ASCE)AS.1943-5525.0000353.

[138] N. Benard, N. Balcon, and E. Moreau, "Electric wind produced by a surface dielectric barrier discharge operating over a wide range of relative humidity," in *47th AIAA Aerospace Sciences Meeting including The New Horizons Forum and Aerospace Exposition*, 2009, p. 488.

[139] M. Wicks and F. O. Thomas, "Effect of Relative Humidity on Dielectric Barrier Discharge Plasma Actuator Body Force," *AIAA Journal*, vol. 53, no. 9, pp. 2801-2805, 2015, doi: 10.2514/1.J053810.

[140] X. Che *et al.*, "Study of flow fields induced by surface dielectric barrier discharge actuator in low-pressure air," *Physics of plasmas*, vol. 21, no. 4, p. 43508, 2014, doi: 10.1063/1.4871722.

[141] J. Kriegseis, K. Barckmann, J. Frey, S. Grundmann, and C. Tropea, "Simultaneous investigation of pressure effects and airflow influence on DBD plasma actuators," in *51st AIAA Aerospace Sciences Meeting including the New Horizons Forum and Aerospace Exposition*, 2013, p. 756.

[142] N. Benard, N. Balcon, and E. Moreau, "Electric wind produced by a surface dielectric barrier discharge operating in air at different pressures: aeronautical control insights," *Journal of physics. D, Applied physics*, vol. 41, no. 4, p. 042002, 2008, doi: 10.1088/0022-3727/41/4/042002.

[143] Y. Wu, Y. Li, M. Jia, H. Song, and H. Liang, "Effect of pressure on the emission characteristics of surface dielectric barrier discharge plasma," *Sensors and actuators. A. Physical.*, vol. 203, pp. 1-5, 2013, doi: 10.1016/j.sna.2013.07.023.

[144] J. Soni and S. Roy, "Low pressure characterization of dielectric barrier discharge actuators," *Applied physics letters*, vol. 102, no. 11, p. 112908, 2013, doi: 10.1063/1.4796176.

[145] Z. Wu, J. Xu, P. Chen, K. Xie, and N. Wang, "Maximum Thrust of Single Dielectric Barrier Discharge Thruster at Low Pressure," *AIAA Journal*, vol. 56, no. 6, pp. 2235-2241, 2018, doi: 10.2514/1.J056641.

[146] P. Versailles, V. Gingras-Gosselin, and H. D. Vo, "Impact of Pressure and Temperature on the Performance of Plasma Actuators," *AIAA Journal*, vol. 48, no. 4, pp. 859-863, 2010, doi: 10.2514/1.43852.

[147] B. Jayaraman, Y.-C. Cho, and W. Shyy, "Modeling of dielectric barrier discharge plasma actuator," *Journal of Applied physics*, vol. 103, no. 5, p. 053304, 2008.

[148] Y. Suzen and G. Huang, "Simulations of flow separation control using plasma actuators," in *44th AIAA Aerospace Sciences Meeting and Exhibit*, 2006, p. 877.

[149] J. Huang, T. C. Corke, and F. O. Thomas, "Plasma actuators for separation control of low-pressure turbine blades," *AIAA journal*, vol. 44, no. 1, pp. 51-57, 2006.

[150] T. Brauner, S. Laizet, N. Benard, and E. Moreau, "Modelling of dielectric barrier discharge plasma actuators for direct numerical simulations," in *8th AIAA Flow Control Conference*, 2016, p. 3774.

[151] A. R. Hoskinson, "Measurements and simulations of surface dielectric barrier discharges used as plasma actuators," ed: ProQuest Dissertations Publishing, 2009.

[152] C. L. Enloe, T. E. McLaughlin, G. I. Font, and J. W. Baughn, "Parameterization of Temporal Structure in the Single-Dielectric-Barrier Aerodynamic Plasma Actuator," *AIAA Journal*, vol. 44, no. 6, pp. 1127-1136, 2006, doi: 10.2514/1.16297.

[153] C. Enloe, T. McLaughlin, R. Van Dyken, and J. Fischer, "Plasma structure in the aerodynamic plasma actuator," in *42nd AIAA Aerospace Sciences Meeting and Exhibit*, 2004, p. 844.

[154] U. Seth, P. Traoré, F. Duran-Olivencia, E. Moreau, and P. Vazquez, "Parametric study of a DBD plasma actuation based on the Suzen-Huang model," *Journal of Electrostatics*, vol. 93, pp. 1-9, 2018.

[155] T. Brauner, S. Laizet, N. Benard, and E. Moreau, "Modelling of dielectric barrier discharge plasma actuators for direct numerical simulations," ed: AAAI, 2016.

[156] T. C. Corke and D. Orlov, "Modelling and simulation of single dielectric barrier discharge plasma actuators," T. C. Corke, Ed., ed: ProQuest Dissertations Publishing, 2006.

[157] C. L. Enloe, G. I. Font, T. E. McLaughlin, and D. M. Orlov, "Surface Potential and Longitudinal Electric Field Measurements in the Aerodynamic Plasma Actuator," *AIAA Journal*, vol. 46, no. 11, pp. 2730-2740, 2008, doi: 10.2514/1.33973.

[158] Z. Li, B. Hu, S. Lan, J. Zhang, and J. Huang, "Control of turbulent channel flow using a plasma-based body force," *Computers & fluids*, vol. 119, pp. 26-36, 2015, doi: 10.1016/j.compfluid.2015.07.001.

[159] K. Mazaheri, J. Omidi, and K. Kiani, "Simulation of DBD plasma actuator effect on aerodynamic performance improvement using a modified phenomenological model," *Computers & Fluids*, vol. 140, pp. 371-384, 2016.

[160] M. Riherd and S. Roy, "Serpentine geometry plasma actuators for flow control," *Journal of Applied Physics*, vol. 114, no. 8, 2013, doi: 10.1063/1.4818622.

[161] C. W. Wong, L. Wang, W. Ma, and Y. Zhou, "New Sawtooth Plasma Actuator Configuration and Mechanism Behind Improved Control Performance," *AIAA Journal*, vol. 58, no. 4, pp. 1881-1886, 2020, doi: 10.2514/1.J058814.

[162] Z. Liu, M. Zhang, and L. Wang, "Investigation on 3D flow field induced by a plasma actuator with serrated electrode," *Science bulletin (Beijing)*, vol. 61, no. 6, pp. 481-487, 2016, doi: 10.1007/s11434-016-1030-1.

[163] F. Messanelli and M. Belan, "A Comparison Between DBD and Corona Actuators with Non-Straight Electrodes," in *Progress in Turbulence VI*: Springer, 2016, pp. 197-201.

[164] K. P. Guoqiang Gao, Lei Dong, Wenfu Wei, Guangning Wu, "Parametric study on the characteristics of a SDBD actuator with a serrated electrode," *Plasma science & technology*, vol. 19, no. 6, pp. 66-73, 2017, doi: 10.1088/2058-6272/aa5b39.

[165] R. Sosa, H. Kelly, D. Grondona, A. Márquez, V. Lago, and G. Artana, "Electrical and plasma characteristics of a quasi-steady sliding discharge," *Journal of physics. D, Applied physics*, vol. 41, no. 3, p. 035202, 2008, doi: 10.1088/0022-3727/41/3/035202.

[166] R. Sosa, E. Arnaud, E. Memin, and G. Artana, "Study of the flow induced by a sliding discharge," *IEEE transactions on dielectrics and electrical insulation*, vol. 16, no. 2, pp. 305-311, 2009, doi: 10.1109/TDEI.2009.4815157.

[167] B. Zheng, J. Chen, C. Ge, X. Ke, and H. Liang, "Flow visualization and mechanisms of three-electrode sliding discharge plasma actuator," *Proceedings of the Institution of Mechanical Engineers. Part G, Journal of aerospace engineering*, vol. 233, no. 13, pp. 4788-4799, 2019, doi: 10.1177/0954410019830266.

[168] B.-R. Zheng, M. Xue, and C. Ge, "Dynamic evolution of vortex structures induced by tri-electrode plasma actuator," *Chinese physics B*, vol. 29, no. 2, p. 24704, 2020, doi: 10.1088/1674-1056/ab671f.

[169] B. T. Townsend, "Electrokinetic apparatus," ed: Google Patents, 1960.

[170] J. Wilson, H. D. Perkins, and W. K. Thompson, "An investigation of ionic wind propulsion," 2009.

[171] C. K. Gilmore and S. R. Barrett, "Electrohydrodynamic thrust density using positive corona-induced ionic winds for in-atmosphere propulsion," *Proceedings of the Royal Society A: Mathematical, Physical and Engineering Sciences*, vol. 471, no. 2175, p. 20140912, 2015.

[172] D. Drew, D. S. Contreras, and K. S. J. Pister, "First thrust from a microfabricated atmospheric ion engine," ed, 2017, pp. 346-349.

[173] V. Y. Khomich and I. E. Rebrov, "In-atmosphere electrohydrodynamic propulsion aircraft with wireless supply onboard," *Journal of Electrostatics*, vol. 95, pp. 1-12, 2018, doi: 10.1016/j.elstat.2018.07.005.

[174] D. F. Opaits, *Dielectric barrier discharge plasma actuator for flow control, final report*. Cleveland, Ohio: Thesis (Ph.D)--Princeton University, 2012.

[175] F. Soetomo, G. M. Colver, and K. Forouraghi, "Micro-force measurement of drag on a small flat plate in the presence of a corona discharge," *Journal of Electrostatics*, vol. 64, no. 7, pp. 525-530, 2006, doi: 10.1016/j.elstat.2005.10.006.

[176] M. Malik, L. Weinstein, and M. Hussaini, "Ion wind drag reduction," in *21st Aerospace Sciences Meeting*, 1983, p. 231.

[177] L. Léger, E. Moreau, G. Artana, and G. Touchard, "Influence of a DC corona discharge on the airflow along an inclined flat plate," *Journal of Electrostatics*, vol. 51, no. 1-4, pp. 300-306, 2001, doi: 10.1016/S0304-3886(01)00089-4.

[178] L. Leger, E. Moreau, and G. Touchard, "Electrohydrodynamic airflow control along a flat plate by a DC surface corona discharge-Velocity profile and wall pressure measurements," in *1st Flow Control Conference*, 2002, p. 2833.

[179] G. Artana, J. D'Adamo, L. Leger, E. Moreau, and G. Touchard, "Flow control with electrohydrodynamic actuators," *AIAA Journal*, vol. 40, pp. 1773-1779, 2002, doi: 10.2514/3.15259.

[180] M. Sato, K. Asada, T. Nonomura, H. Aono, A. Yakeno, and K. Fujii, "Mechanisms for turbulent separation control using plasma actuator at Reynolds number of 1.6× 106," *Physics of Fluids*, vol. 31, no. 9, p. 095107, 2019.

[181] D. Tsubakino, Y. Tanaka, and K. Fujii, "Effective layout of plasma actuators for a flow separation control on a wing," in *45th AIAA Aerospace Sciences Meeting and Exhibit*, 2007, p. 474.

[182] J.-J. Wang, K.-S. Choi, L.-H. Feng, T. N. Jukes, and R. D. Whalley, "Recent developments in DBD plasma flow control," *Progress in aerospace sciences*, vol. 62, pp. 52-78, 2013, doi: 10.1016/j.paerosci.2013.05.003.

[183] M. P. Patel, T. T. Ng, S. Vasudevan, T. C. Corke, and C. He, "Plasma Actuators for Hingeless Aerodynamic Control of an Unmanned Air Vehicle," *Journal of Aircraft*, vol. 44, no. 4, pp. 1264-1274, 2007, doi: 10.2514/1.25368.

[184] P. Sujar-Garrido, N. Benard, E. Moreau, and J. P. Bonnet, "Dielectric barrier discharge plasma actuator to control turbulent flow downstream of a backward-facing step," *Experiments in fluids*, vol. 56, no. 4, pp. 1-16, 2015, doi: 10.1007/s00348-015-1939-1.

[185] N. Benard *et al.*, "Turbulent separated shear flow control by surface plasma actuator: experimental optimization by genetic algorithm approach," *Experiments in fluids*, vol. 57, no. 2, pp. 1-17, 2016, doi: 10.1007/s00348-015-2107-3.

[186] D. Kim, H. Do, and H. Choi, "Drag reduction on a three-dimensional model vehicle using a wire-to-plate DBD plasma actuator," *Experiments in fluids*, vol. 61, no. 6, 2020, doi: 10.1007/s00348-020-02961-3.

[187] X. Zhang, K.-S. Choi, Y. Huang, and H.-x. Li, "Flow control over a circular cylinder using virtual moving surface boundary layer control," *Experiments in fluids*, vol. 60, no. 6, pp. 1-15, 2019, doi: 10.1007/s00348-019-2745-y.

[188] Y. Guan, *Study of laminar electrohydrodynamic flows*. Thesis (Ph. D.)-University of Washington, 2019.

[189] Y.-s. Cheng, H.-C. Yeh, and G. M. Kanapilly, "Collection efficiencies of a point-to-plane electrostatic precipitator," *The American Industrial Hygiene Association Journal*, vol. 42, no. 8, pp. 605-610, 1981.

[190] P. Stainback and K. Nagabushana, "Review of hot-wire anemometry techniques and the range of their applicability for various flows," *Electronic Journal of Fluids Engineering*, vol. 1, p. 4, 1993.

[191] P. Giubbilini, "The current-voltage characteristics of point-to-ring corona," *Journal of Applied Physics*, vol. 64, 1988.

[192] L. L. Yu Zhang, Yang Chen, Jiting Ouyang, "Characteristics of ionic wind in needle-to-ring corona discharge," *Journal of Electrostatics*, vol. 74, p. 6, 2015.

[193] B. L. Owsenek and J. Seyed-Yagoobi, "Theoretical and experimental study of electrohydrodynamic heat transfer enhancement through wire-plate corona discharge," *Journal of heat transfer*, vol. 119, no. 3, p. 7, 1997.

[194] F. A. Davide Cagnoni, Thomas Christen, Nicola Parolini, Ivica Stevanovic, Carlo de Falco, "Multiphysics simulation of corona discharge induced ionic wind," *Journal of Applied Physics*, vol. 114, no. 233301, p. 10, 2013.

[195] H. Yala and Y. Zebboudj, "Finite-element solution of monopolar corona in a coaxial system," *European physical journal. Applied physics*, vol. 19, no. 2, pp. 123-129, 2002, doi: 10.1051/epjap:2002058.

[196] M. R. Bouazza, K. Yanallah, F. Pontiga, and J. H. Chen, "A simplified formulation of wire-plate corona discharge in air: Application to the ion wind simulation," *Journal of Electrostatics*, vol. 92, pp. 54-65, 2018, doi: 10.1016/j.elstat.2018.02.001.

[197] K. Yanallah and F. Pontiga, "A semi-analytical stationary model of a point-to-plane corona discharge," *Plasma sources science & technology*, vol. 21, no. 4, p. 045007, 2012, doi: 10.1088/0963-0252/21/4/045007.

[198] S. Chen, J. C. P. Y. Nobelen, and S. Nijdam, "A self-consistent model of ionic wind generation by negative corona discharges in air with experimental validation," *Plasma sources science & technology*, vol. 26, no. 9, p. 95005, 2017, doi: 10.1088/1361-6595/aa86b8.

[199] P. Seimandi, G. Dufour, and F. Rogier, "An asymptotic model for steady wire-to-wire corona discharges," *Mathematical and computer modelling*, vol. 50, no. 3, pp. 574-583, 2009, doi: 10.1016/j.mcm.2009.03.005.

[200] C. Kim, D. Park, K. C. Noh, and J. Hwang, "Velocity and energy conversion efficiency characteristics of ionic wind generator in a multistage configuration," *Journal of electrostatics*, vol. 68, no. 1, pp. 36-41, 2010, doi: 10.1016/j.elstat.2009.09.001.

[201] L. D. Landau, E. M. Lifshitz, J. B. Sykes, and W. H. Reid, *Fluid Mechanics* (Course of theoretical physics, no. 6). Pergamon press inc, 1959.

[202] K. McNaughton and C. Sinclair, "Submerged jets in short cylindrical flow vessels," *Journal of Fluid Mechanics*, vol. 25, no. 2, pp. 367-375, 1966.

[203] N. Monrolin, F. Plouraboue, and O. Praud, "Electrohydrodynamic Thrust for In-Atmosphere Propulsion," *AIAA J.*, vol. 55, no. 12, pp. 4296-4305, 2017, doi: 10.2514/1.J055928.

[204] H. Schlichting and K. Gersten, *Boundary-Layer Theory*, 9th ed. 2017 ed. Berlin, Heidelberg: Berlin, Heidelberg: Springer Berlin Heidelberg, 2017.

[205] D.-E. Levy and A. Seifert, "Simplified dragonfly airfoil aerodynamics at Reynolds numbers below 8000," *Physics of Fluids*, vol. 21, no. 7, 2009, doi: 10.1063/1.3166867.

[206] H. K. Hari Prasad, *Development and control of micro-ionic thrusters for centimeter-scale aerial robots*. Thesis (M.S.)-University of Washington, 2020.

[207] D. S. Drew, N. O. Lambert, C. B. Schindler, and K. S. J. Pister, "Toward Controlled Flight of the Ionocraft: A Flying Microrobot Using Electrohydrodynamic Thrust With Onboard Sensing and No Moving Parts," *IEEE robotics and automation letters*, vol. 3, no. 4, pp. 2807-2813, 2018, doi: 10.1109/LRA.2018.2844461.

[208] Y. M. Chukewad, A. T. Singh, J. M. James, and S. B. Fuller, "A new robot fly design that is easier to fabricate and capable of flight and ground locomotion," in *2018 IEEE/RSJ International Conference on Intelligent Robots and Systems (IROS)*, 2018: IEEE, pp. 4875-4882.

[209] M. Glauert, "The wall jet," *Journal of Fluid Mechanics*, vol. 1, no. 6, pp. 625-643, 1956.

[210] W. K. George, H. Abrahamsson, J. Eriksson, R. I. Karlsson, L. Löfdahl, and M. Wosnik, "A similarity theory for the turbulent plane wall jet without external stream," *Journal of Fluid Mechanics*, vol. 425, pp. 367-411, 2000.

[211] P. Fillingham and I. V. Novosselov, "Wall jet similarity of impinging planar underexpanded jets," *International Journal of Heat and Fluid Flow*, vol. 81, p. 108516, 2020/02/01/ 2020, doi: https://doi.org/10.1016/j.ijheatfluidflow.2019.108516.

[212] A. Debien, N. Benard, and E. Moreau, "Streamer inhibition for improving force and electric wind produced by DBD actuators," *Journal of Physics D: Applied Physics*, vol. 45, no. 21, p. 215201, 2012.

[213] T. C. Corke, M. L. Post, and D. M. Orlov, "Single dielectric barrier discharge plasma enhanced aerodynamics: physics, modeling and applications," *Experiments in Fluids*, vol. 46, no. 1, pp. 1-26, 2009.

[214] A. R. Hoskinson and N. Hershkowitz, "Modelling of dielectric barrier discharge plasma actuators with thick electrodes," *Journal of physics. D, Applied physics*, vol. 44, no. 8, p. 085202, 2011, doi: 10.1088/0022-3727/44/8/085202.

[215] J. R. Roth, "Aerodynamic flow acceleration using paraelectric and peristaltic electrohydrodynamic effects of a one atmosphere uniform glow discharge plasma," *Physics of plasmas*, vol. 10, no. 5, pp. 2117-2126, 2003.

[216] M. N. Lyulyukin, A. S. Besov, and A. V. Vorontsov, "The Influence of Corona Electrodes Thickness on the Efficiency of Plasmachemical Oxidation of Acetone," *Plasma chemistry and plasma processing*, vol. 31, no. 1, pp. 23-39, 2011, doi: 10.1007/s11090-010-9265-0.

[217] J. Pons, E. Moreau, and G. Touchard, "Electrical and aerodynamic characteristics of atmospheric pressure barrier discharges in ambient air," 2004.

[218] K. Kourtzanidis, G. Dufour, and F. Rogier, "Self-consistent modeling of a surface AC dielectric barrier discharge actuator: In-depth analysis of positive and negative phases," *Journal of Physics D: Applied Physics*, vol. 54, no. 4, p. 045203, 2020.

[219] P. G. Huang, D. E. Ashpis, J. D. Jacob, and Y. B. Suzen, "Numerical Simulations of Plasma Based Flow Control Applications," ed, 2005.

[220] T. Matsuno, M. Kawaguchi, N. Fujita, G. Yamada, and H. Kawazoe, "Jet vectoring and enhancement of flow control performance of trielectrode plasma actuator utilizing sliding discharge," in *6th AIAA Flow Control Conference*, 2012, p. 3238.

[221] J. Boeuf, Y. Lagmich, and L. Pitchford, "Contribution of positive and negative ions to the electrohydrodynamic force in a dielectric barrier discharge plasma actuator operating in air," *Journal of applied physics*, vol. 106, no. 2, p. 023115, 2009.

[222] C. Porter, J. Baughn, T. McLaughlin, L. Enloe, and G. Font, "Temporal force measurements on an aerodynamic plasma actuator," in *44th AIAA Aerospace Sciences Meeting and Exhibit*, 2006, p. 104.

[223] R. Durscher and S. Roy, "Novel multi-barrier plasma actuators for increased thrust," in *48th AIAA Aerospace Sciences Meeting including the New Horizons Forum and Aerospace Exposition*, 2010, p. 965.

[224] J. Ferry and J. Rovey, "Thrust measurement of dielectric barrier discharge plasma actuators and power requirements for aerodynamic control," in *5th Flow Control Conference*, 2010, p. 4982.

[225] M. Belan and F. Messanelli, "Compared ionic wind measurements on multi-tip corona and DBD plasma actuators," *Journal of electrostatics*, vol. 76, pp. 278-287, 2015, doi: 10.1016/j.elstat.2015.06.008.

[226] N. L. Whiting, D. Castaneda, N. J. Webb, and M. Samimy, "Control of Dynamic Stall over a NACA 0012 Airfoil Using NS-DBD Plasma Actuators," in *AIAA Scitech 2020 Forum*, 2020, p. 1568.

[227] H. Abdelraouf, A. M. N. Elmekawy, and S. Z. Kassab, "Simulations of flow separation control numerically using different plasma actuator models," *Alexandria engineering journal*, vol. 59, no. 5, pp. 3881-3896, 2020, doi: 10.1016/j.aej.2020.06.044.

[228] M. Abdollahzadeh, J. C. Pascoa, and P. J. Oliveira, "Comparison of DBD plasma actuators flow control authority in different modes of actuation," *Aerospace science and technology*, vol. 78, pp. 183-196, 2018, doi: 10.1016/j.ast.2018.04.013.

[229] L.-H. Feng, T. N. Jukes, K.-S. Choi, and J.-J. Wang, "Flow control over a NACA 0012 airfoil using dielectric-barrier-discharge plasma actuator with a Gurney flap," *Experiments in fluids*, vol. 52, no. 6, pp. 1533-1546, 2012, doi: 10.1007/s00348-012-1263-y.

[230] R. S. Vaddi, A. Mamishev, and I. Novosselov, "Direct Current Augmented Dielectric Barrier Discharge Plasma Actuator: Effect of Electrode Shape," *AIAA Journal (submitted)*, 2021.

[231] J. Winslow, H. Otsuka, B. Govindarajan, and I. Chopra, "Basic Understanding of Airfoil Characteristics at Low Reynolds Numbers," *Journal of Aircraft*, vol. 55, no. 3, pp. 1050-1061, 2018, doi: 10.2514/1.C034415.

[232] L. W. Traub, "Experimental Investigation of the Effect of Trip Strips at Low Reynolds Number," *Journal of Aircraft*, vol. 48, no. 5, pp. 1776-1784, 2011, doi: 10.2514/1.C031375.

[233] R. E. Sheldahl and P. C. Klimas, "Aerodynamic characteristics of seven symmetrical airfoil sections through 180-degree angle of attack for use in aerodynamic analysis of vertical axis wind turbines," Sandia National Labs., Albuquerque, NM (USA), 1981.

[234] C. L. Ladson, *Effects of independent variation of Mach and Reynolds numbers on the low-speed aerodynamic characteristics of the NACA 0012 airfoil section*. National Aeronautics and Space Administration, Scientific and Technical Information Division, 1988.

[235] M. Drela, "XFOIL: An analysis and design system for low Reynolds number airfoils," in *Low Reynolds number aerodynamics*: Springer, 1989, pp. 1-12.

[236] J. C. Lin, "Review of research on low-profile vortex generators to control boundary-layer separation," *Progress in aerospace sciences*, vol. 38, no. 4, pp. 389-420, 2002, doi: 10.1016/S0376-0421(02)00010-6.

[237] T. Corke, B. Mertz, and M. Patel, "Plasma flow control optimized airfoil," in *44th AIAA Aerospace Sciences Meeting and Exhibit*, 2006, p. 1208.

[238] K. Masuyama and S. R. H. Barrett, "On the performance of electrohydrodynamic propulsion," *Proceedings: Mathematical, Physical and Engineering Sciences*, vol. 469, no. 2154, pp. 1-16, 2013, doi: 10.1098/rspa.2012.0623.

[239] N. Benard, P. Noté, M. Caron, and E. Moreau, "Highly time-resolved investigation of the electric wind caused by surface DBD at various ac frequencies," *Journal of electrostatics*, vol. 88, pp. 41-48, 2017, doi: 10.1016/j.elstat.2017.01.018.

[240] R. Pereira, D. Ragni, and M. Kotsonis, "Effect of external flow velocity on momentum transfer of dielectric barrier discharge plasma actuators," *Journal of applied physics*, vol. 116, no. 10, p. 103301, 2014, doi: 10.1063/1.4894518.

[241] N. A. Fuchs, "On the stationary charge distribution on aerosol particles in a bipolar ionic atmosphere," *Geofisica pura e applicata*, journal article vol. 56, no. 1, pp. 185-193, September 01 1963, doi: 10.1007/bf01993343.

[242] W. H. Marlow and J. R. Brock, "Unipolar charging of small aerosol particles," *Journal of Colloid And Interface Science*, vol. 50, no. 1, pp. 32-38, 1975, doi: 10.1016/0021-9797(75)90250-7.

[243] M. H. Lee *et al.*, "Enhanced collection efficiency of nanoparticles by electrostatic precipitator with needle-cylinder configuration," *Journal of Nanoscience and Nanotechnology*, vol. 16, no. 7, pp. 6884-6888, 2016, doi: 10.1166/jnn.2016.11322.

[244] Y. Zhuang, Y. Jin Kim, T. Gyu Lee, and P. Biswas, "Experimental and theoretical studies of ultra-fine particle behavior in electrostatic precipitators," *Journal of Electrostatics*, vol. 48, no. 3, pp. 245-260, 2000, doi: 10.1016/S0304-3886(99)00072-8.

[245] L. Ravi and S. L. Girshick, "Coagulation of nanoparticles in a plasma," *Physical review. E, Statistical, nonlinear, and soft matter physics*, vol. 79, no. 2 Pt 2, p. 026408, 2009, doi: 10.1103/PhysRevE.79.026408.

[246] J. Pelletier, "Dusty plasmas: physics, chemistry and technological impacts in plasma processing," *Plasma Physics and Controlled Fusion*, vol. 42, no. 2, pp. 227-227, 2000, doi: 10.1088/0741-3335/42/2/701.

[247] S.-H. Huang and C.-C. Chen, "Ultrafine aerosol penetration through electrostatic precipitators," *Environmental Science & Technology*, vol. 36, no. 21, pp. 4625-4632, 2002, doi: 10.1021/es011157+.

[248] N. E. Jewell-Larsen, D. A. Parker, I. A. Krichtafovitch, and A. V. Mamishev, "Numerical simulation and optimization of electrostatic air pumps," ed, 2004, pp. 106-109.

[249] J. S. Townsend, "The potentials requires to maintain currents between coaxial cylinders," *The London, Edinburgh and Dublin philosophical magazine and journal of science*, vol. 28, no. 163, p. 8, 1914.

[250] M. Pauthenier and M. Moreau-Hanot, "La charge des particules sphériques dans un champ ionisé," *Journal de Physique et le Radium*, vol. 3, no. 12, pp. 590-613, 1932.

[251] H. Rohmann, "Methode zur Messung der Größe von Schwebeteilchen," *Zeitschrift für Physik*, vol. 17, no. 1, p. 13, 1923.

[252] H. J. White, "Particle Charging in Electrostatic Precipitation," *American Institute of Electrical Engineers, Transactions of the*, vol. 70, no. 2, pp. 1186-1191, 1951, doi: 10.1109/T-AIEE.1951.5060545.

[253] H. J. White, *Industrial electrostatic precipitation*. Reading, Mass.: Reading, Mass., Addison-Wesley Pub. Co., 1963.

[254] N. Fuchs, "The charges on the particles of aerocolloids," *Izv. Akad. Nauk. SSSR, Ser. Geogr. Geofiz*, vol. 11, pp. 341-348, 1947.

[255] B. Y. H. Liu and A. Kapadia, "Combined field and diffusion charging of aerosol particles in the continuum regime," *Journal of Aerosol Science*, vol. 9, no. 3, pp. 227-242, 1978, doi: 10.1016/0021-8502(78)90045-9.

[256] L. Unger, D. Boulaud, and J. P. Borra, "Unipolar field charging of particles by electrical discharge: effect of particle shape," *Journal of Aerosol Science*, vol. 35, no. 8, pp. 965-979, 2004, doi: 10.1016/j.jaerosci.2004.01.006.

[257] S. J. Park and S. S. Kim, "Electrohydrodynamic flow and particle transport mechanism in electrostatic precipitators with cavity walls," *Aerosol Sci. Technol.*, vol. 33, no. 3, pp. 205-221, 2000.

[258] J. H. Goo and J. W. Lee, "Stochastic simulation of particle charging and collection characteristics for a wire-plate electrostatic precipitator of short length," *Journal of Aerosol Science*, vol. 28, no. 5, pp. 875-893, 1997, doi: 10.1016/S0021-8502(96)00475-2.

[259] V. T. Dau, T. X. Dinh, C.-D. Tran, T. Terebessy, T. C. Duc, and T. T. Bui, "Particle precipitation by bipolar corona discharge ion winds," *Journal of Aerosol Science*, vol. 124, pp. 83-94, 2018, doi: 10.1016/j.jaerosci.2018.07.007.

[260] A. Miller, G. Frey, G. King, and C. Sunderman, "A handheld electrostatic precipitator for sampling airborne particles and nanoparticles," *Aerosol Science and Technology*, vol. 44, no. 6, pp. 417-427, 2010.

[261] J. Roux, R. Sarda-Estève, G. Delapierre, M. Nadal, C. Bossuet, and L. Olmedo, "Development of a new portable air sampler based on electrostatic precipitation," *Environmental Science and Pollution Research*, vol. 23, no. 9, pp. 8175-8183, 2016, doi: 10.1007/s11356-015-5522-3.

[262] L. Dey and C. Venkataraman, "A Wet Electrostatic Precipitator (WESP) for Soft Nanoparticle Collection," *Aerosol Science and Technology*, vol. 46, no. 7, pp. 750-759, 2012, doi: 10.1080/02786826.2012.664295.

[263] K. H. Yoo, J. S. Lee, and M. D. Oh, "Charging and Collection of Submicron Particles in Two-Stage Parallel-Plate Electrostatic Precipitators," *Aerosol Science and Technology*, vol. 27, no. 3, pp. 308-323, 1997, doi: 10.1080/02786829708965476.

[264] N. Jidenko and J. P. Borra, "Kinematics of charged nanometric particles in silent discharges," *Journal of Physics D: Applied Physics*, vol. 38, no. 4, pp. 617-620, 2005, doi: 10.1088/0022-3727/38/4/014.

[265] J. P. Borra, N. Jidenko, J. Hou, and A. Weber, "Vaporization of bulk metals into single-digit nanoparticles by non-thermal plasma filaments in atmospheric pressure dielectric barrier discharges," *Journal of Aerosol Science*, vol. 79, pp. 109-125, 2015, doi: 10.1016/j.jaerosci.2014.09.002.

[266] N. Jidenko, C. Jimenez, F. Massines, and J. P. Borra, "Nano-particle size-dependent charging and electro-deposition in dielectric barrier discharges at atmospheric pressure for thin sio x film deposition," *Journal of Physics D: Applied Physics*, vol. 40, no. 14, pp. 4155-4163, 2007, doi: 10.1088/0022-3727/40/14/009.

[267] D. Y. H. Pui, S. Fruin, and P. H. McMurry, "Unipolar Diffusion Charging of Ultrafine Aerosols," *Aerosol Science and Technology*, vol. 8, no. 2, pp. 173-187, 1988, doi: 10.1080/02786828808959180.

[268] M. Li and P. D. Christofides, "Collection efficiency of nanosize particles in a two-stage electrostatic precipitator," *Industrial & engineering chemistry research*, vol. 45, no. 25, pp. 8484-8491, 2006.

[269] P. Intra and N. Tippayawong, "An Overview of Unipolar Charger Developments for Nanoparticle Charging," *Aerosol Air Qual. Res.*, vol. 11, no. 2, pp. 187-209, 2011, doi: 10.4209/aaqr.2010.10.0082.

[270] C. Qi, D.-R. Chen, and P. Greenberg, "Performance study of a unipolar aerosol mini-charger for a personal nanoparticle sizer," *Journal of Aerosol Science*, vol. 39, no. 5, pp. 450-459, 2008, doi: 10.1016/j.jaerosci.2008.01.003.

[271] R. C. Flagan and J. H. Seinfeld, *Fundamentals of air pollution engineering*. Courier Corporation, 2012.

[272] G.-Y. Lin and C.-J. Tsai, "Numerical Modeling of Nanoparticle Collection Efficiency of Single-Stage Wire-in-Plate Electrostatic Precipitators," *Aerosol Science and Technology*, vol. 44, no. 12, pp. 1122-1130, 2010, doi: 10.1080/02786826.2010.512320.

[273] B. Y. H. Liu and D. Y. H. Pui, "On unipolar diffusion charging of aerosols in the continuum regime," *Journal of Colloid And Interface Science*, vol. 58, no. 1, pp. 142-149, 1977, doi: 10.1016/0021-9797(77)90377-0.

[274] W. C. Hinds, *Aerosol technology : properties, behavior, and measurement of airborne particles*, 2nd ed. New York: Wiley, 1999, pp. xx, 483 pages.

[275] Y.-S. Cheng, H.-C. Yeh, and G. M. Kanapilly, "Collection efficiencies of a point-to- plane electrostatic precipitator," *American Industrial Hygiene Association Journal*, vol. 42, no. 8, pp. 605-610, 1981, doi: 10.1080/15298668191420350.

[276] J. Dixkens and H. Fissan, "Development of an electrostatic precipitator for off- line particle analysis," *Aerosol Science and Technology*, vol. 30, no. 5, pp. 438-453, 1999, doi: 10.1080/027868299304480.

[277] G. Mahamuni, B. Ockerman, and I. Novosselov, "Electrostatic Capillary Collector for In-Situ Spectroscopic Analysis of Aerosols," *Aerosol Science and Technology*, pp. 1-40, 2019, doi: 10.1080/02786826.2019.1600653.

[278] J. He *et al.*, "Evaluation of micro-well collector for capture and analysis of aerosolized Bacillus subtilis spores," *PloS one*, vol. 13, no. 5, p. e0197783, 2018.

[279] J. He and I. V. Novosselov, "Design and evaluation of an aerodynamic focusing micro-well aerosol collector," *Aerosol Science and Technology*, vol. 51, no. 9, pp. 1016-1026, 2017, doi: 10.1080/02786826.2017.1329515.

[280] M. Yao and G. Mainelis, "Investigation of Cut-Off Sizes and Collection Efficiencies of Portable Microbial Samplers," *Aerosol Science and Technology*, vol. 40, no. 8, pp. 595-606, 2006, doi: 10.1080/02786820600729146.

[281] M. Adachi, Y. Kousaka, and K. Okuyama, "Unipolar and bipolar diffusion charging of ultrafine aerosol particles," *Journal of Aerosol Science*, vol. 16, no. 2, pp. 109-123, 1985, doi: 10.1016/0021-8502(85)90079-5.

[282] F. J. Romay and D. Y. H. Pui, "On the Combination Coefficient of Positive Ions with Ultrafine Neutral Particles in the Transition and Free-Molecule Regimes," *Aerosol Science and Technology*, vol. 17, no. 2, pp. 134-147, 1992, doi: 10.1080/02786829208959566.

[283] C. Druzgalski, M. Andersen, and A. Mani, "Direct numerical simulation of electroconvective instability and hydrodynamic chaos near an ion-selective surface," *Physics of Fluids*, vol. 25, no. 11, p. 110804, 2013.

[284] Y. Guan and I. Novosselov, "Two Relaxation Time Lattice Boltzmann Method Coupled to Fast Fourier Transform Poisson Solver: Application to Electroconvective Flow," *Journal of Computational Physics (accepted for publication)*, 2019, doi: 10.1016/j.jcp.2019.07.029.

[285] Y. Guan, J. Riley, and I. Novosselov, "Three-dimensional electroconvective vortices in cross flow," *Physical Review E*, vol. 101, no. 3, p. 033103, 03/03/ 2020, doi: 10.1103/PhysRevE.101.033103.

[286] Y. Guan and I. Novosselov, "Numerical analysis of electroconvection in cross-flow with unipolar charge injection," *Physical Review Fluids*, vol. 4, no. 10, p. 103701, 10/01/ 2019, doi: 10.1103/PhysRevFluids.4.103701.

[287] Y. Guan, S. L. Brunton, and I. Novosselov, "Sparse nonlinear models of chaotic electroconvection," *arXiv preprint arXiv:2009.11862*, 2020.

[288] Y. Kimio, "An empirical formula for negative corona discharge current in point-grid electrode geometry," *Journal of Applied Physics*, vol. 96, no. 5, pp. 2472-2475, 2004.

[289] L. D. Landau, *Fluid mechanics*. London : Reading, Mass.: London : Pergamon Press ; Reading, Mass. : Addison-Wesley Pub. Co., 1959.

[290] G. M. Alonso, A. Hernandez-Sierra, and E. Alguacil, "Electrical charging of aerosol nanoparticles and sonne practical applications," *Rev. Metal*, vol. 39, pp. 41-57, 2003.

[291] J. Schwartz, A. Zanobetti, and T. Bateson, "Morbidity and Mortality Among Elderly Residents of Cities with Daily PM Measurements," *Revised Analyses of Time-Series Studies of Air Pollution and Health*, vol. Special Report, pp. 25-72

[292] E. Samoli *et al.*, "Estimating the exposure- response relationships between particulate matter and mortality within the APHEA multicity project.(Research)," *Environmental Health Perspectives*, vol. 113, no. 1, p. 88, 2005, doi: 10.1289/ehp.7387.

[293] X. Lin, K. Willeke, V. Ulevicius, and S. Grinshpun, "Effect of Sampling Time on the Collection Efficiency of All-Glass Impingers," *American Industrial Hygiene Association Journal*, vol. 58, no. 7, pp. 480-488, 1997, doi: 10.1080/15428119791012577.

[294] D. Schmechel *et al.*, "A Two- stage Personal Cyclone Sampler for the Collection of Fungal Aerosols and Direct ELISA and PCR Sample Analysis," vol. 119, ed, 2007, pp. S188-S188.

[295] Glen E Duncan *et al.*, "Using the design-feedback iterative cycle to improve the usability of a personal air pollution monitor," *Submitted to Environmental Health ENHE-D-18-00238*, July 2018.

[296] T.-Y. Wen, I. Krichtafovitch, and A. V. Mamishev, "The key energy performance of novel electrostatic precipitators," *Journal of Building Engineering*, vol. 2, pp. 77-84, 2015, doi: 10.1016/j.jobe.2015.04.006.

[297] A. Peters *et al.*, "Translocation and potential neurological effects of fine and ultrafine particles a critical update," *Particle and fibre toxicology*, vol. 3, no. 1, p. 13, 2006.

[298] S. Fuzzi *et al.*, "Particulate matter, air quality and climate: lessons learned and future needs," *Atmospheric chemistry and physics*, vol. 15, no. 14, pp. 8217-8299, 2015.

[299] M. Elbayoumi, N. A. Ramli, and N. F. F. Md Yusof, "Spatial and temporal variations in particulate matter concentrations in twelve schools environment in urban and overpopulated camps landscape," *Building and Environment*, vol. 90, pp. 157-167, 8// 2015, doi: http://dx.doi.org/10.1016/j.buildenv.2015.03.036.

[300] M. M. Patel *et al.*, "Spatial and Temporal Variations in Traffic-related Particulate Matter at New York City High Schools," *Atmospheric environment (Oxford, England : 1994)*, vol. 43, no. 32, pp. 4975-4981, 2009, doi: 10.1016/j.atmosenv.2009.07.004.

[301] R. A. Dobbins, "Soot inception temperature and the carbonization rate of precursor particles," *Combustion and Flame*, vol. 130, no. 3, pp. 204-214, 2002.

[302] S. E. Stein and A. Fahr, "High-temperature stabilities of hydrocarbons," *The Journal of Physical Chemistry*, vol. 89, no. 17, pp. 3714-3725, 1985.

[303] M. Commodo *et al.*, "On the early stages of soot formation: Molecular structure elucidation by high-resolution atomic force microscopy," *Combustion and Flame*, vol. 205, pp. 154-164, 2019.

[304] D. Chen, J. Akroyd, S. Mosbach, D. Opalka, and M. Kraft, "Solid–liquid transitions in homogenous ovalene, hexabenzocoronene and circumcoronene clusters: A molecular dynamics study," *Combustion and Flame*, vol. 162, no. 2, pp. 486-495, 2015.

[305] D. Aubagnac-Karkar, A. El Bakali, and P. Desgroux, "Soot particles inception and PAH condensation modelling applied in a soot model utilizing a sectional method," *COMBUSTION AND FLAME*, vol. 189, pp. 190-206, 2018.

[306] J. Davis, K. Tiwari, and I. Novosselov, "Soot morphology and nanostructure in complex flame flow patterns via secondary particle surface growth," *Fuel*, vol. 245, pp. 447-457, 2019/06/01/ 2019, doi: https://doi.org/10.1016/j.fuel.2019.02.058.

[307] J. Davis, "Characterization of combustion generated particulates produced in an inverted gravity flame reactor " Ph.D., University of Washington, Seattle, 2019.

[308] C. P. West *et al.*, "Molecular Composition and the Optical Properties of Brown Carbon Generated by the Ethane Flame," *ACS Earth and Space Chemistry*, vol. 4, no. 7, pp. 1090-1103, 2020/07/16 2020, doi: 10.1021/acsearthspacechem.0c00095.

[309] J. Davis, E. Molnar, and I. Novosselov, "Nanostructure transition of young soot aggregates to mature soot aggregates in diluted diffusion flames," *Carbon*, vol. 159, pp. 255-265, 2020/04/15/ 2020, doi: https://doi.org/10.1016/j.carbon.2019.12.043.

[310] G. Mahamuni *et al.*, "Excitation–Emission Matrix Spectroscopy for Analysis of Chemical Composition of Combustion Generated Particulate Matter," *Environmental Science & Technology*, vol. 54, no. 13, pp. 8198-8209, 2020/07/07 2020, doi: 10.1021/acs.est.0c01110.

[311] J. J. Cao *et al.*, "Spatial and seasonal variations of atmospheric organic carbon and elemental carbon in Pearl River Delta Region, China," *Atmospheric Environment*, vol. 38, no. 27, pp. 4447-4456, 2004/09/01/ 2004, doi: 10.1016/j.atmosenv.2004.05.016.

[312] J. C. Chow, J. G. Watson, L. W. A. Chen, J. Rice, and N. H. Frank, "Quantification of PM2.5 organic carbon sampling artifacts in US networks," (in English), *Atmospheric Chemistry and Physics*, vol. 10, no. 12, pp. 5223-5239, 2010/06/15/ 2010, doi: https://doi.org/10.5194/acp-10-5223-2010.

[313] P. Lin, L. T. Fleming, S. A. Nizkorodov, J. Laskin, and A. Laskin, "Comprehensive Molecular Characterization of Atmospheric Brown Carbon by High Resolution Mass Spectrometry with Electrospray and Atmospheric Pressure Photoionization," *Analytical Chemistry*, vol. 90, no. 21, pp. 12493-12502, 2018/11/06/ 2018, doi: 10.1021/acs.analchem.8b02177.

[314] Y. Wei, I.-K. Han, M. Hu, M. Shao, J. Zhang, and X. Tang, "Personal exposure to particulate PAHs and anthraquinone and oxidative DNA damages in humans," *Chemosphere*, vol. 81, no. 10, pp. 1280-1285, 2010/11/01/ 2010, doi: 10.1016/j.chemosphere.2010.08.055.

[315] S. Bonetta *et al.*, "DNA damage in A549 cells exposed to different extracts of PM2.5 from industrial, urban and highway sites," *Chemosphere*, vol. 77, no. 7, pp. 1030-1034, 2009/11/01/ 2009, doi: 10.1016/j.chemosphere.2009.07.076.

[316] Y. Wei, I.-K. Han, M. Shao, M. Hu, J. Zhang, and X. Tang, "PM2.5 Constituents and Oxidative DNA Damage in Humans," *Environ. Sci. Technol.*, vol. 43, no. 13, pp. 4757-4762, 2009/07/01/ 2009, doi: 10.1021/es803337c.

[317] V. Samburova, B. Zielinska, and A. Khlystov, "Do 16 Polycyclic Aromatic Hydrocarbons Represent PAH Air Toxicity?," *Toxics*, vol. 5, no. 3, 2017/08/15/ 2017, doi: 10.3390/toxics5030017.

[318] IARC, *Some non-heterocyclic polycyclic aromatic hydrocarbons and some related exposures* (International Agency for Research on Cancer monographs on the evaluation of carcinogenic risks to humans). Lyon, France: Geneva: IARC Press, International Agency for Research on Cancer, 2010.

[319] I. Berlman, *Handbook of florescence spectra of Aromatic Molecules*. Elsevier (in en), 2012, p. 488.

[320] H. J. Lee, A. Laskin, J. Laskin, and S. A. Nizkorodov, "Excitation–emission spectra and fluorescence quantum yields for fresh and aged biogenic secondary organic aerosols," *Environmental science & technology*, vol. 47, no. 11, pp. 5763-5770, 2013.

[321] S. M. Phillips and G. D. Smith, "Further evidence for charge transfer complexes in brown carbon aerosols from excitation–emission matrix fluorescence spectroscopy," *The Journal of Physical Chemistry A*, vol. 119, no. 19, pp. 4545-4551, 2015.

[322] Q. Chen, F. Ikemori, and M. Mochida, "Light absorption and excitation–emission fluorescence of urban organic aerosol components and their relationship to chemical structure," *Environmental Science & Technology*, vol. 50, no. 20, pp. 10859-10868, 2016.

[323] J. T. Matos, S. M. Freire, R. M. Duarte, and A. C. Duarte, "Natural organic matter in urban aerosols: Comparison between water and alkaline soluble components using excitation–emission matrix fluorescence spectroscopy and multiway data analysis," *Atmospheric Environment*, vol. 102, pp. 1-10, 2015.

[324] J. W. Rutherford *et al.*, "Excitation emission matrix fluorescence spectroscopy for combustion generated particulate matter source identification," *Atmospheric Environment*, vol. 220, p. 117065, 2020/01/01/ 2020, doi: https://doi.org/10.1016/j.atmosenv.2019.117065.

[325] J. W. Rutherford, "Source Apportionment of Combustion Generated Particulate Matter Air Pollution using Excitation Emission Matrix Fluorescence Spectroscopy and Machine Learning," 2019.

[326] T. Aizawa and H. Kosaka, "Investigation of early soot formation process in a diesel spray flame via excitation—emission matrix using a multi-wavelength laser source," *International Journal of Engine Research*, vol. 9, no. 1, pp. 79-97, 2008, doi: 10.1243/14680874JER01407.

[327] K. Booksh, A. Muroski, and M. Myrick, "Single-measurement excitation/emission matrix spectrofluorometer for determination of hydrocarbons in ocean water. 2. Calibration and quantitation of naphthalene and styrene," *Analytical Chemistry*, vol. 68, no. 20, pp. 3539-3544, 1996, doi: 10.1021/ac9602534.

[328] R. D. Jiji, G. A. Cooper, and K. S. Booksh, "Excitation-emission matrix fluorescence based determination of carbamate pesticides and polycyclic aromatic hydrocarbons," *Analytica Chimica Acta*, vol. 397, no. 1, pp. 61-72, 1999, doi: 10.1016/S0003-2670(99)00392-X.

[329] G. Mahamuni *et al.*, "Solid-phase excitation-emission matrix spectroscopy for chemical analysis of combustion aerosols," *PLOS ONE*, vol. 16, no. 5, p. e0251664, 2021, doi: 10.1371/journal.pone.0251664.

[330] G. Mahamuni, "Excitation Emission Matrix Fluorescence Spectroscopy based Sensing of Combustion Generated Particulate Matter," Ph.D., Mechanical Engineering, University of Washington, 2020.

[331] J. W. Rutherford, T. V. Larson, T. Gould, E. Seto, I. V. Novosselov, and J. D. Posner, "Source apportionment of environmental combustion sources using excitation emission matrix fluorescence spectroscopy and machine learning," *Atmospheric Environment*, vol. 259, p. 118501, 2021/08/15/ 2021, doi: https://doi.org/10.1016/j.atmosenv.2021.118501.

[332] S. Peronaci and M. Baselli, *Aerodynamics of an airfoil with plasma actuators of different kinds and geometries*. Thesis (M.S.) - Politecnico di Milano, 2015.

[333] P. Fillingham, K. Kottapalli, X. Zhan, and I. V. Novosselov, "Characterization of adhesion force in aerodynamic particle resuspension," *Journal of aerosol science*, vol. 128, pp. 89-98, 2019, doi: 10.1016/j.jaerosci.2018.11.006.

[334] Z. Lanying, F. Najjar, S. Balachandar, and P. Fischer, "Forces on a finite-sized particle located close to a wall in a linear shear flow," *Physics of fluids (1994)*, vol. 21, no. 3, p. 33302, 2009, doi: 10.1063/1.3082232.

[335] A. Richter and P. A. Nikrityuk, "Drag forces and heat transfer coefficients for spherical, cuboidal and ellipsoidal particles in cross flow at sub-critical Reynolds numbers," *International journal of heat and mass transfer*, vol. 55, no. 4, pp. 1343-1354, 2012, doi: 10.1016/j.ijheatmasstransfer.2011.09.005.

[336] L. W. Rong, Z. Y. Zhou, and A. B. Yu, "Lattice–Boltzmann simulation of fluid flow through packed beds of uniform ellipsoids," *Powder technology*, vol. 285, pp. 146-156, 2015, doi: 10.1016/j.powtec.2015.06.047.

[337] C. Ke, S. Shu, H. Zhang, H. Yuan, and D. Yang, "On the drag coefficient and averaged Nusselt number of an ellipsoidal particle in a fluid," *Powder technology*, vol. 325, pp. 134-144, 2018, doi: 10.1016/j.powtec.2017.10.049.

APPENDIX A. SEPARATION CONTROL USING CORONA AND DBD ACTUATOR

In this chapter, we study the effect of plasma actuators on aerodynamic forces on a NACA 0012 airfoil. The force measurements in the wind tunnel are done for two different kinds of plasma actuators 1. Corona actuator 2. DBD actuator. These quantitative results are followed by qualitative analysis like aerodynamic force coefficient augmentation, and electro-mechanical efficiencies.

A.1. PLASMA ACTUATORS

In this thesis, we have considered two different tip angles 30^0 & 60^0 for the serrated/saw tooth electrodes as shown in Figure A.1. The plasma actuators consist of copper electrodes made from 0.05 mm thick foil. All the electrodes have a 350 mm working span to have enough tips. The sawtooth electrodes are fabricated using electro-discharge machining. All the cathode electrodes were made of 25 mm wide, 0.05 mm thick copper tape exception of the cathode of the corona, which was a copper rod with a diameter of 1.6 mm.

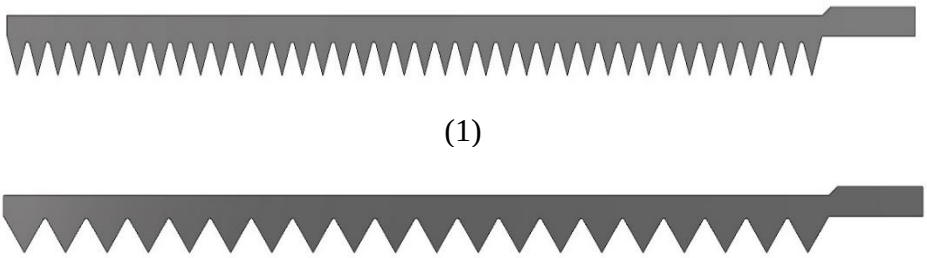

(1)

(2)

Figure A.1. Electrodes under test, 1 is the multi-tip electrode with a fine pitch of 5 mm and 2 is the multi-tip electrode with a coarse pitch of 10 mm.

A representative multi-tip corona actuator is shown in Figure A.2, the representation is planar while in the experiment they are mounted on a curved surface. We tested the fine pitch electrode, while the cathode is a rod with a diameter of 1.6 mm. The tip to cathode gap is 25 mm. The cathode is mounted in a rectangular cavity and the tips are protruded out from the cavity. The tips are aligned with the leading edge at the positive angles of attack; the anode and cathode are always on the suction side of the airfoil. With this configuration, the tips induce a velocity parallel to the surface of the airfoil over the suction surface.

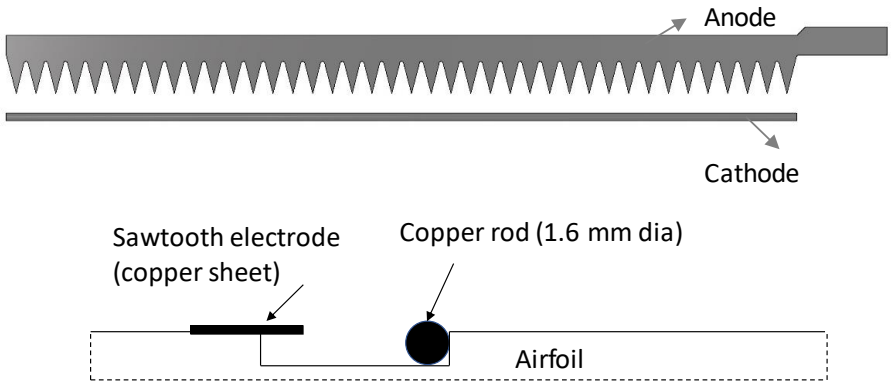

Figure A.2. Electrodes under test, 1 is the multi-tip electrode with a fine pitch of 5 mm and 2 is the multi-tip electrode with a coarse pitch of 10 mm.

DBD actuators are assembled in the way as shown in Figure A.3 to ensure uniform discharge in the spanwise direction. They are mounted on the curved surface of the airfoil similar to corona actuators. The two copper electrodes are aligned in the spanwise direction. The ground electrode is always aligned with the troughs of the saw tooth electrode. The ground electrode is a rectangle with a length of 25 mm. Its length of 25 mm is long enough to allow the complete development of the plasma sheet for all the actuators. The electrodes are separated by 4 layers of Kapton film of thickness 0.088 mm. The ground electrode is sprayed with cyanoacrylate to eliminate the formation of plasma under the dielectric layer.

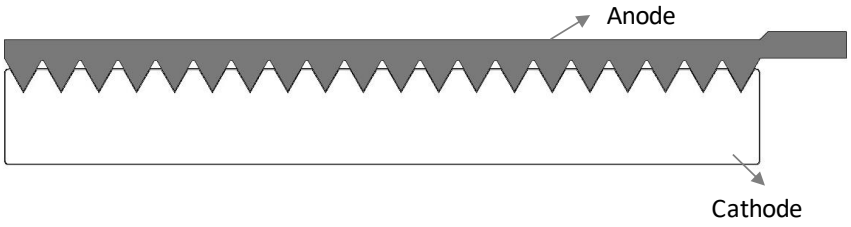

Figure A.3. Schematic of a dielectric barrier discharge actuator. The roots of the saw tooth are aligned with the ground electrode.

A.2. Results and Discussion

This section presents the experimental results obtained during wind tunnel testing. These quantitative results are accompanied by a qualitative interpretation of the physical phenomena. The purpose of the corona and DBD actuators is the same i.e., to energize the boundary layer, to increase the lift coefficient, and to ensure a change in the pitching moment. The effectiveness is different for both the actuators. This is mainly due to the different type of discharge.

In corona actuators, the tip is the preferential location of the discharge, whereas in DBD the choice of saw tooth geometry has different reasons. This particular geometry allows for the generation of the transverse component of velocity. In this way, counter-rotating vortices originate in the regions between the tips. Vortices drive high-velocity fluid towards the boundary layer. The multi-tip DBD generates a strong ionic wind, starting from the tips that energize the boundary layer and allows for desired flow control. The operating principle of vortex structures is similar to a vortex generator. The size of the generated vortices is dependent on the distance between the tips. In order to obtain this, the distance between tips must be sufficient enough to create vortices of adequate size. Multi-tip geometry increases the production of thrust because of the intense

electric field near the tips. This can be seen in Figure A.4 where it is more luminous at the tips compared to the other regions.

Figure A.4. DBD operating on an airfoil.

We need to characterize the aerodynamic curves for a NACA 0012 airfoil without plasma actuators in our wind tunnel. Therefore, we need to study its clean aerodynamic characteristics. This allowed us to have a common ground and to obtain a basis for comparison. In order to study the aerodynamic parameters, a bare airfoil with trip dots and without electrodes has been assembled in the testing section. As mentioned before, we have analyzed four different freestream velocities (5 m/s, 10 m/s & 15 m/s; Q = 0.3 psf, 1.3 psf & 2.9 psf respectively). The aerodynamic curves for the airfoil are shown in Figure A.5.

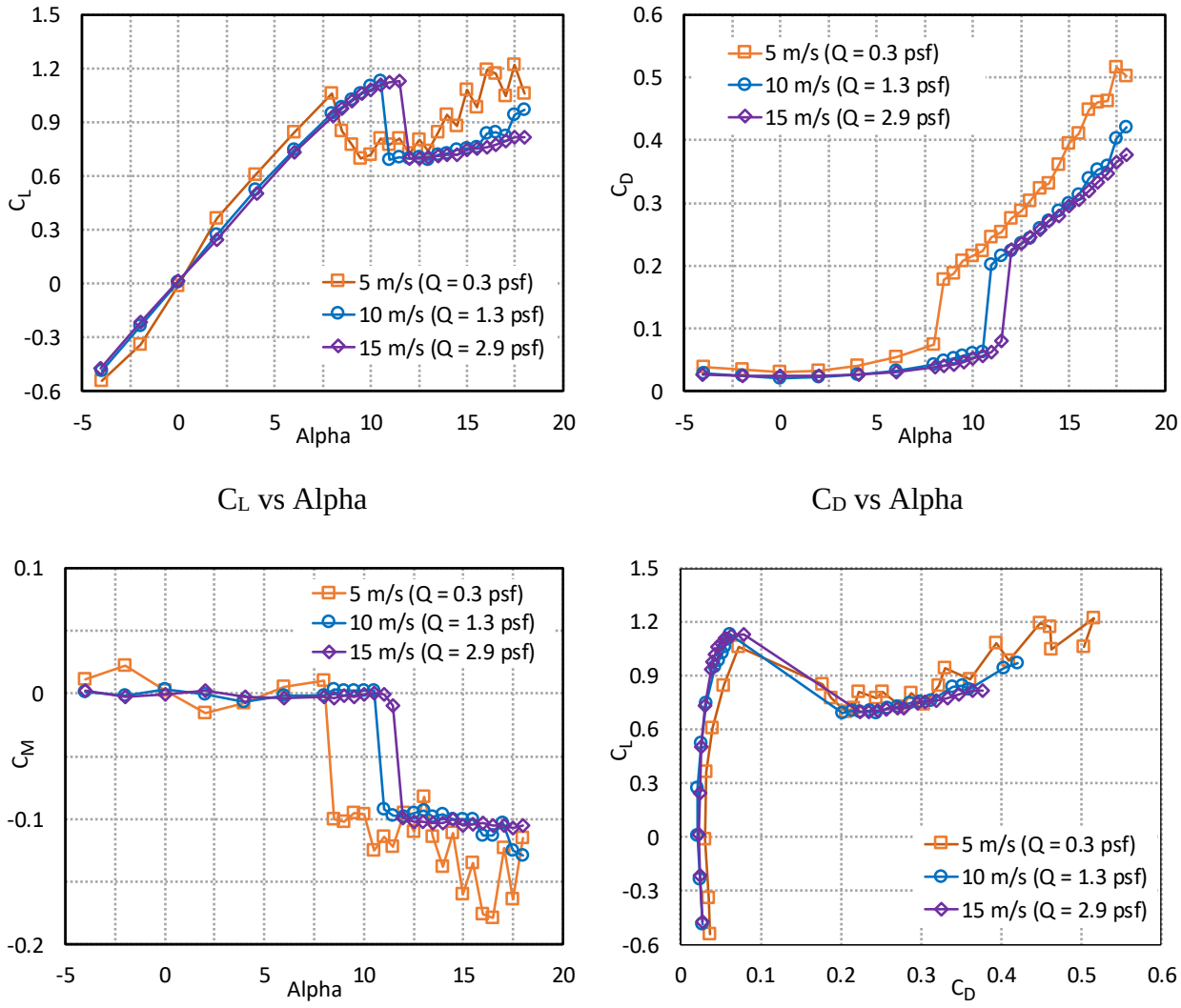

Figure A.5. Aerodynamic curves of NACA 0012 airfoil from wind tunnel testing.

As it should be, when the speed increases, the maximum achievable lift coefficient increases, and the stall angle increases. The lift coefficient for free stream velocity of 5 m/s after the stall angle oscillates. This can be attributed to the low Reynolds effects on the airfoil and the flow separates and reattaches [231]. A similar pattern can be observed in the pitching moment data as well.

In Figure A.6, the wind tunnel data has been compared with the aerodynamic curves available in the literature (XFOIL predictions). They are roughly at the same Reynolds numbers of our experiments at 15 m/s and with a NACA 0012 airfoil. The modified NACA 0012 airfoil changes the slope of lift coefficient and the maximum lift coefficient compared to a traditional one. However, the modified and traditional airfoil behave the same and the $C_{L,\,MAX}$ is approximately the same. Instead, in our test, the stall happened 0.5^0 earlier and the behavior after the stall is quite different. The aerodynamic forces acting on the airfoil at low Reynolds numbers are strongly linked to the characteristics of the separated flow region on the airfoil that is very sensitive to the free stream environment.

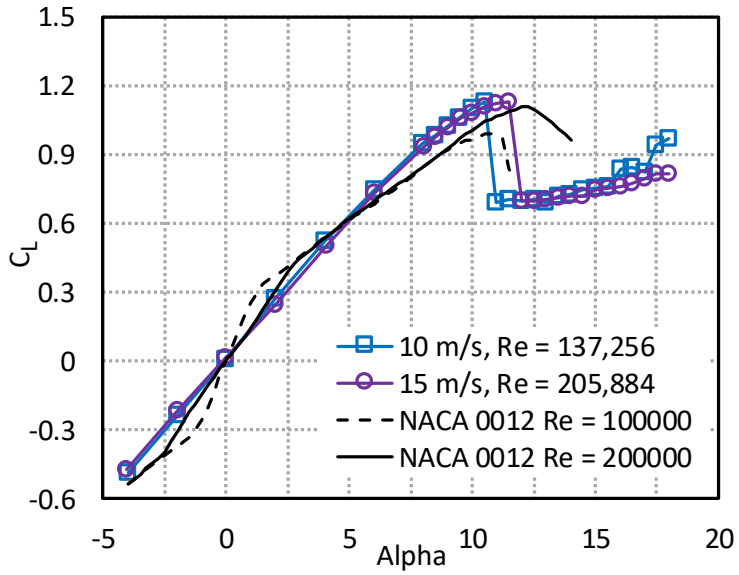

Figure A.6. Comparison of NACA 0012 test data with XFOIL predictions.

A.2.1. Plasma Actuators on Aerodynamic Performance

In this section, all the aerodynamic performance parameters are reported. We will focus on the maximum lift coefficient increase and stall angle delay. Before showing the results, we will use the following terminology from here onwards:

- % $C_{L, MAX}$ – Change in the maximum lift coefficient with and without EHD flow
- α_{Delay} – Change in the separation angle
- EHD OFF – Actuator is installed on the wing but turned off
- EHD ON – Actuator is tuned on and the operating conditions are mentioned

The percentage values are calculated between the actuator turned off and turned-on performances and they do not include clean aerodynamics of the wing.

A.2.2. Corona Actuator on Aerodynamic Performance

In Figure A.7, aerodynamic curves are shown in order to introduce the concepts of lift increase, drag reduction, and stall delay. Aerodynamic characteristics of actuator turned on and off are shown to demonstrate the actual effectiveness of the plasma actuators. The data is obtained over an average of multiple tests and it has proved excellent repeatability. The corona actuator is installed at 18% chord position on the airfoil. The distance between the anode and cathode is 30 mm. The corona actuator is operated at a DC voltage of 28 kV and it induces a wall jet along the surface the airfoil. Due to the curvature of the airfoil, the pressure gradient appears. When the pressure gradient becomes positive, separation takes place and this is the point of separation. This zone creates a decrease in lift and increase in drag. The EHD actuator induces a wall jet and, because of the wall jet phenomena, the flow reattaches. When the actuator is turned on, the maximum lift coefficient increases and its position is moved to a higher angle of attack so that stall is postponed. We have presented the data for 10 m/s and we have seen an increase of 10.6 % in $C_{L, MAX}$ and α_{Delay} is increased by 1.5^0. In the drag coefficient plots, there is a reduction of drag

coefficient for all the angles of attack and we can see a reduction of drag at 11^0 and the increase in lift force. The drag coefficient is decreased by ~70% until 11^0

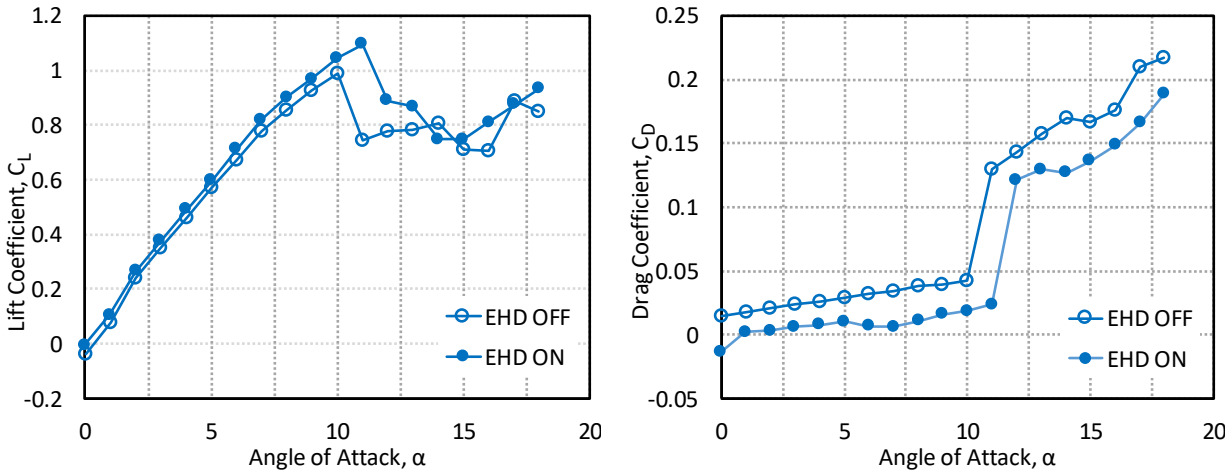

(a) (b)

Figure A.7. Corona actuator performance on (a) lift and (b) drag coefficients for free stream velocity of 10 m/s (Re = 134,089).

A.2.3. DBD Actuator on Aerodynamic Performance

Aerodynamic performance of the airfoil by DBD actuators is discussed in this section. DBD actuators are usually two metal sheets flush mounted between a dielectric layer and an alternating voltage is applied between the electrodes. We have installed the electrodes on two different positions on the airfoil 18% and 25% of the chord. Lift, drag and pitching moment characteristics of the airfoil with and without EHD flow generated by DBD are given in Figure A.8 and Figure A.9. We have determined the aerodynamic parameters for two different free stream velocities (5 m/s & 10 m/s). For the free stream velocity of 5 m/s, EHD phenomenon is noticeable at a lower angle of attacks, whereas with the increase of free stream velocity EHD phenomenon is not as significant as it is at 5m/s free stream velocity. Due to the entrainment of the flow by the EHD, the

surface pressure distribution changes, which leads to the increase in lift coefficient. The maximum lift coefficient and the stall angle in all the cases have increased. The $C_{L,MAX}$ has increased by 28.8% and 5% when the actuator is at 18% chord and 26.22% and 8.9% when the actuator is at 25% chord for free stream velocities of 5 m/s and 10 m/s respectively. Similar results are reported in the literature as well [332]. As the lift force has increased due to EHD, which in turn creates a moment and this additional moment created on the airfoil can be used to control the aircraft. The actuators are operated at 13.5 kV p-p, 2 kHz sinusoidal wave.

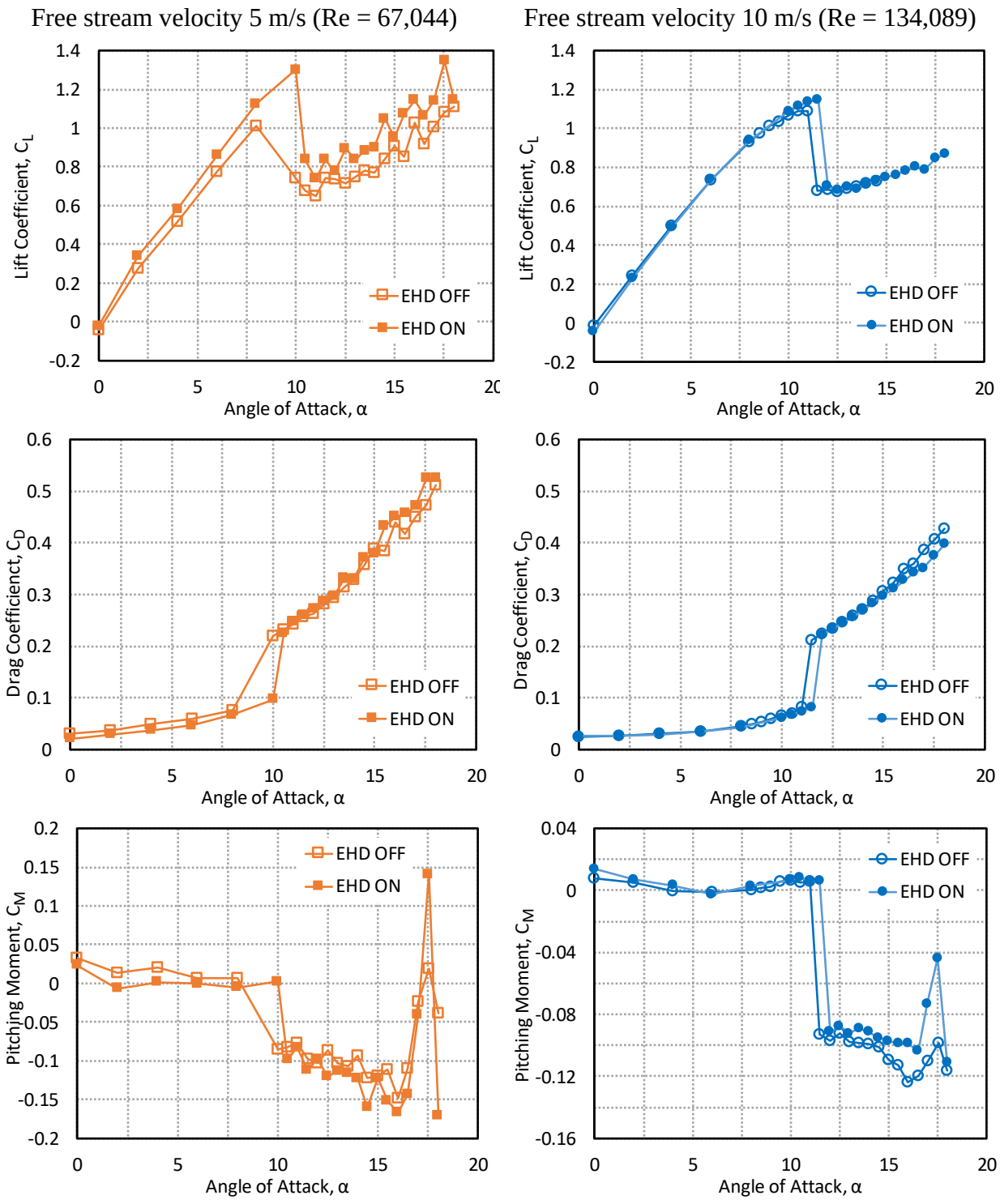

Figure A.8. DBD performance on aerodynamic coefficients for two different free stream velocities, the actuator is placed at 18% chord position.

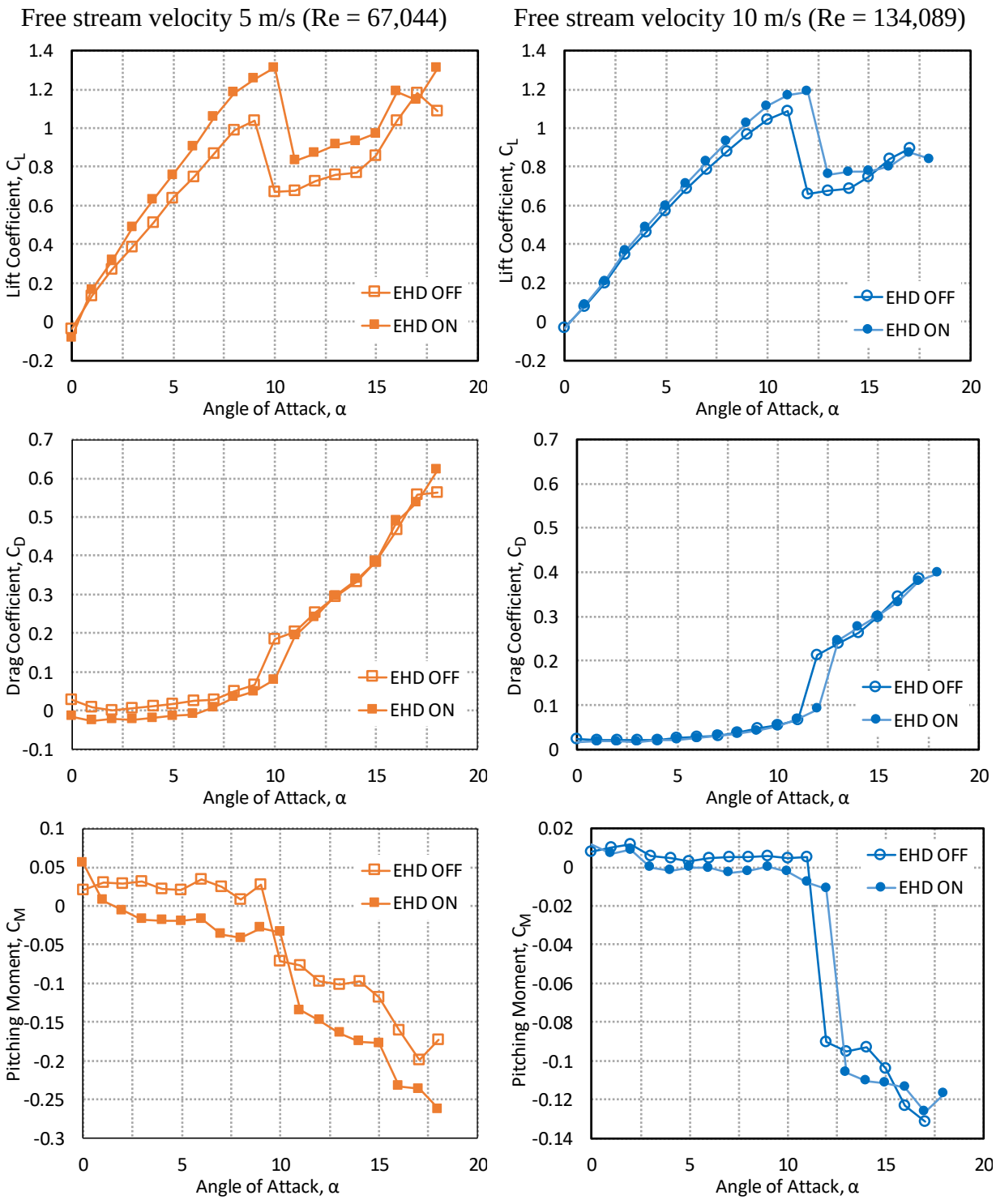

Figure A.9. DBD performance on aerodynamic coefficients for two different free stream velocities; the actuator is placed at 25% chord position.

A.2.4. Lift Coefficient Augmentation

This section shows the results in terms of the percentage increase in the maximum lift coefficient for all the actuators. The increase of the maximum lift coefficient, reported for all the tests performed for coronas and for DBDs is calculated as shown in Eq.(A.1).

$$\Delta C_{L,Max} = \frac{C_{L,Max,ON} - C_{L,Max,OFF}}{C_{L,Max,OFF}} \quad \text{(A.1)}$$

All the results related to the lift coefficient increase are mentioned in Table

Table A.1. Lift coefficient increase for corona and DBDs.

Corona	10 m/s	DBD	5 m/s	10 m/s
C – 18%	10.6 %	D – 18%	28.8 %	5 %
		D – 25%	26.2%	8.9 %

Performances rapidly decrease when the freestream velocity increases. For both sets of actuators the performance of corona actuators is higher than DBD at the same free stream velocity.

APPENDIX B. AERODYNAMIC FORCES ON PROLATE SPHEROIDS

The aerodynamic forces acting on a spherical particle are well studied and there are currently no established relations for forces on non-spherical particles. We developed new relations for drag coefficient on prolate-spheroidal particles attached to a surface in a linear shear flow and in uniform flow using direct numerical simulations. Some of the work is published in Powder Technology [10].

B.1. METHODOLOGY

B.1.1. Problem Description

Typical particles of interest for aerodynamic resampling will be on the order of microns in height, and therefore under any aerodynamic removal scenario will be resting in the linear viscous sublayer [333]. Particles lie with their long axis parallel to the surface. In this chapter, rigid prolate spheroids resting on the surface parallel to their long axis in a linear shear flow. The x-,y- and z-coordinates represent the streamwise, wall-normal and spanwise directions respectively. The incidence angle θ is defined as the rotation of the spheroid about the y-axis, as shown in Figure B.1.

The aspect ratio (AR), η, of the particles as the ratio of the major axis to the minor axis

$$\eta = \frac{b}{a}, \tag{B.1}$$

Such that an aspect ratio of 1 represents a sphere. In this work for particle in linear shear flow, aspect ratios of 1.5, 2,3 and 5 each at angles of 0^0, 30^0, 45^0, 60^0 and 90^0. For particle study in

uniform flow, aspect ratio of 5 and angle of 90^0 are considered. The characteristic diameter for the prolate spheroids is used to determine the Reynolds number

$$Re = \frac{U_\infty (a^2 b)^{\frac{1}{3}}}{\upsilon}. \tag{B.2}$$

The Reynolds number in this study are varied from 0.1 -10, since the maximum Reynolds number when the ellipsoid resting on a smooth surface is 12 and higher Reynolds number is out of scope in this work. The drag coefficients on the particle is calculated using equivalent diameter

$$C_D = \frac{F_d}{\frac{1}{2}\rho U_\infty^2 \frac{\pi (a^2 b)^{\frac{1}{3}}}{4}} \tag{B.3}$$

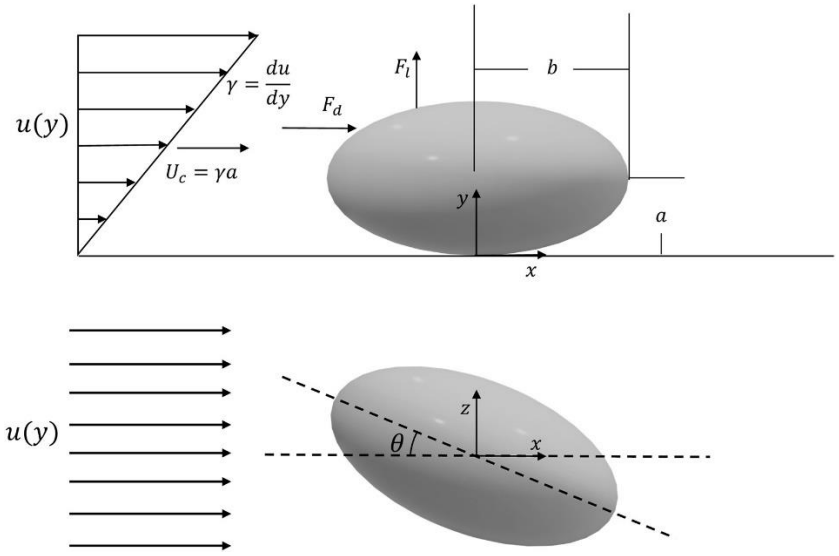

Figure B.1. Schematic diagram of a prolate spheroid resting on the surface in a shear flow with a side-view (top) and top-view (bottom).

B.1.2. Computational Approach

The commercial finite volume solver Ansys Fluent 18.2 was used to solve the three-dimensional, steady, incompressible Navier Stokes equations. For the particle in uniform flow case, the computational domain is considered as a large box with dimensions $40\ d_p \times 15\ d_p \times 20\ d_p$. The ellipsoid particle is placed in the centre of the computational domain and an incident angle of 90^0. For particle in the linear shear flow case, the computational domain with dimensions $40\ d_p \times 10\ d_p \times 20\ d_p$ is considered. To avoid the singularity at the contact point between the particle and the surface, particles were modelled with a small gap of $0.01\ d_p$ away from the surface. The width of the domain is only considered as $20\ d_p$, as we have determined that by increasing the size of the computational domain, the drag and lift coefficient changes are minimal. Velocity inlet and pressure outlet are applied in this simulation to determine the effects of Reynolds number on drag coefficient.

B.2. RESULTS AND DISCUSSION

B.2.1. Drag Coefficient - Linear Shear Flow

The drag coefficient for a sphere resting on a surface has been previously studied, and a relationship based on the Reynolds number has been established [334]

$$C_D = 1.7009 \times \frac{24}{Re}(1 + 0.104Re^{0.75}) \tag{B.4}$$

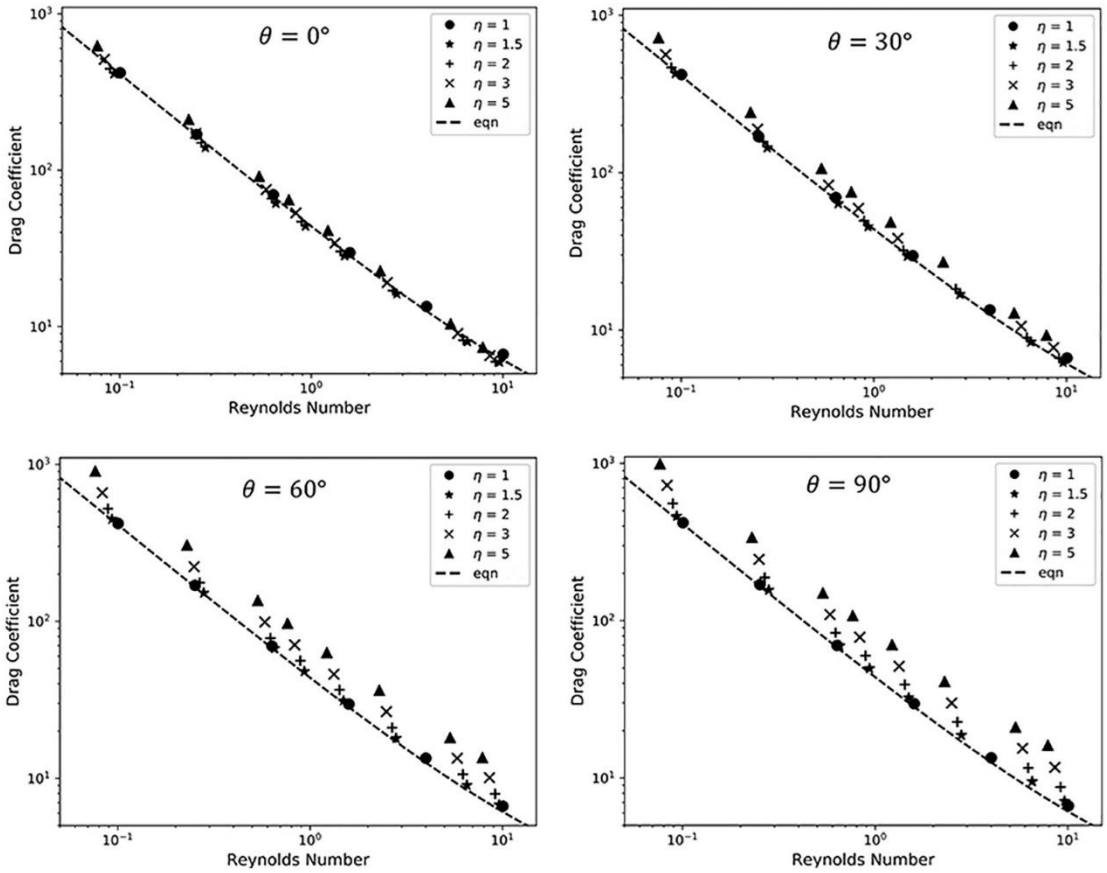

Figure B.2. Drag coefficient from DNS against particle Reynolds number for the incidence angle of 0^0, 30^0, 60^0 and 90^0 at all aspect ratios. The effect on aspect ratio on deviation from the spherical relation is most prominent at an angle of 90^0.

For prolate spheroids, then it is natural to use the existing expression for spherical particles with correction factors for orientation and aspect ratios. To validate the approach, spherical particles were modelled and compared to Eq.(B.4), with an excellent agreement, as shown in Figure B.2. When examining the effect of aspect ratio on drag coefficient at each angle, also shown in Figure B.2, it appears that only a slight adjustment to the spherical relation is necessary for θ = 0 (the volume equivalent diameter accounts for much of the variation due to the elongation of the particle); but the effect of aspect ratio increases with the angle θ. This is expected as at an angle of 0° the frontal projection of the particle is circular and the flow field in the spanwise plane would

be similar, as the incidence angle increases the flow field in the spanwise direction will deviate from the spherical case, requiring an adjustment for aspect ratio.

B.2.2. Drag Coefficient - Uniform Flow

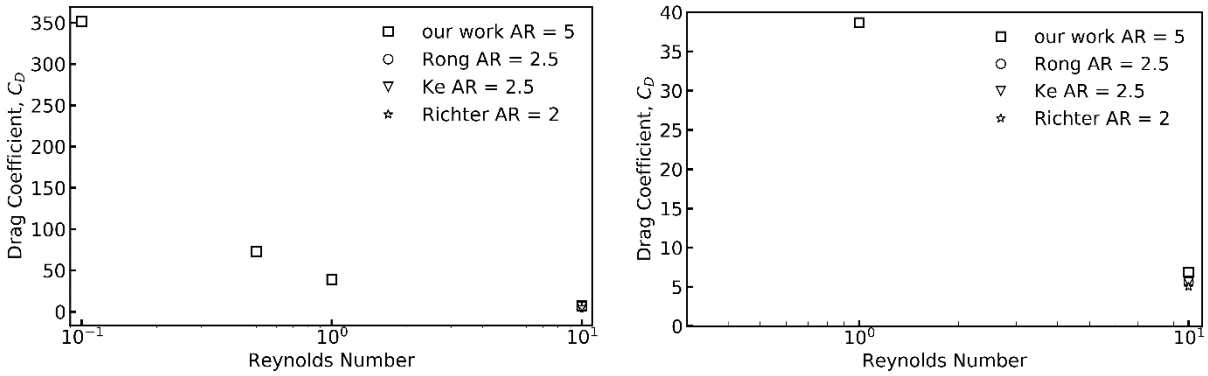

Figure B.3. Drag coefficient from DNS against particle Reynolds number for the incidence angle of 90^0 at AR = 5 and it is compared with drag coefficient from state of art [335-337].

Figure B.3 shows the variation of drag coefficient with Reynolds number and comparison of drag coefficient with the previous reports. As the Reynolds number increases, the drag coefficient decreases as expected. The drag coefficient for AR = 5 at Re = 10 in the present study is higher than the drag coefficients reported in the literature for AR = 2 and 2.5. This can be explained by the fact that for particle oriented perpendicular to the flow direction i.e incidence angle 90^0, a higher aspect ratio leads to a larger area affected by the particle thus increasing the viscous and pressure drag. Table B.1 summarizes the drag coefficient in the current study and state of the art. The drag coefficient increases by 12.3% when the AR of the particle changes from 2 to 2.5 and it increases by 37.2 % when the AR of the particle changes from 2 to 5.

Table B.1. Comparison of drag coefficients between state of the art and present work for Re = 10.

	Drag Coefficient
Our work AR = 5	6.89
Richter AR = 2	5.02
Rong AR = 2.5	5.64
Ke AR = 2.5	5.58